Coherent attosecond light sources based on high-order harmonic generation: influence of the propagation effects

VNiVERSiDAD D SALAMANCA

CAMPUS DE EXCELENCIA INTERNACIONAL

Carlos Hernández García

Departamento de Física Aplicada. Área de Óptica.
Grupo de Investigación en Óptica Extrema (GIOE)

Universidad de Salamanca

A thesis submitted for the degree of

Doctor in Physics at Universidad de Salamanca

supervised by Prof. Dr. Luis Plaja Rustein

Salamanca, January 2013

LUIS PLAJA RUSTEIN, Profesor Titular del Área de Óptica del Departamento de Física Aplicada de la Universidad de Salamanca, CERTIFICA:

> Que la presente Memoria, "**Coherent attosecond light sources based on high-order harmonic generation: influence of the propagation effects / *Fuentes de luz coherentes de attosegundo basadas en la generación de armónicos de orden elevado: influencia de los efectos de propagación***" ha sido realizada bajo su dirección en el Área de Óptica del Departamento de Física Aplicada de la Universidad de Salamanca por el Licenciado Carlos Hernández García y constituye su Tesis Doctoral para optar al grado de Doctor en Física con Mención Internacional.

Salamanca, 12 de diciembre de 2012.

A mis padres y hermano,
A Cristina

Agradecimientos

Si estás leyendo estas palabras es que tu interés por mi trabajo, mi persona, o la simple y vana curiosidad te ha traído hasta aquí. Siento de antemano mi redacción, las letras nunca fueron lo mío. Probablemente ésta es la parte de la tesis que me resulta más difícil de escribir, pero no puedo dejar pasar la oportunidad de expresar mi gratitud por el apoyo recibido, de una u otra manera, por tanta gente durante esta etapa de mi vida, sin importar si llegan a leer estas líneas.

En primer lugar, he de agradecer la inconmensurable labor realizada por Luis Plaja, el principal responsable de, no sólo este trabajo, sino también de despertar en mi un gran interés por la ciencia. Su contínuo estímulo, ilusión y dedicación hacia mi, han sido claves a lo largo de estos años. Sin duda, presumiré de director de tesis durante toda la vida.

En segundo lugar he de dar las gracias a Luis Roso por la confianza depositada en mi al introducirme en el mundo de los láseres intensos y por sus fructíferas conversaciones sobre ciencia. Sin duda le estoy muy agradecido por acogerme en 'El Fotón Charro', un grupo de incalculable valor humano. Doy las gracias a todos y cada uno de sus componentes, por hacerme pasar muy buenos momentos en el día a día. De todos ellos voy a nombrar a los que han contribuido de forma directa en esta tesis: a José Antonio Pérez, por su valiosa colaboración aportando cálculos 'single-atom' y 3D TDSE; a Cruz Méndez, Íñigo Sola y Óscar Varela por la paciencia que tuvieron conmigo en el laboratorio; a Enrique Conejero, por ayudarme a dar los primeros pasos en mi doctorado; y a los editores de 'El láser, la luz de nuestro tiempo', con quienes compartí gratas experiencias. Al resto de componentes del Área de Óptica y del Centro de Láseres Pulsados (CLPU) con los que he tenido la suerte de convivir, muchas gracias. He

aprendido muchas cosas –y espero seguir aprendiendo– de todos y cada uno de vosotros, científica y humanamente.

Me gustaría también dar las gracias a la gente de Boulder: a Andreas Becker y Agnieszka Jaron-Becker, a los que estoy enormemente agradecido por acogerme en su grupo de investigación en JILA y por depositar su confianza en nuestro trabajo previo; a Margaret Murnane y Henry Kapteyn por darme la oportunidad única de colaborar con ellos; y a Tenio Popmintchev por nuestra estrecha colaboración. Finalmente, he de afirmar que mi primera visita a Boulder no habría sido tan exitosa sin la incalculable ayuda de mi amigo Antonio Picón, siempre tan atento. Muchas gracias también al resto de amigos de Boulder que hicieron mis dos estancias muy llevaderas.

Me gustaría también agradecer al Grup dÒptica Quàntica de la Universitat Autònoma de Barcelona por su cálida acogida en mis visitas, así como a Martin Kretschmar, de la Universidad de Hannover, por su reciente colaboración científica, y al Grupo de Robótica de la Universidad de Salamanca.

Ya en el plano puramente personal, deseo expresar mi enorme gratitud a mi familia, especialmente a mis padres y hermano, por su cariño e incondicional apoyo y por haberme dado todo tipo de facilidades para llegar hasta aquí. Jamás encontraré la forma de agradecer todo lo que habéis hecho por mi. Sin duda alguna, este título es también vuestro, estoy muy orgulloso de vosotros. También me gustaría agradecer el apoyo de mis amigos, con los que he disfrutado de tan buenos momentos. Y por último, a Cristina, por hacer realidad mis sueños.

Acknowledgements

If you are reading these words, it means that your interest in my work, my person, or simply your curiosity, has brought you here. First of all I would like to apologize for my writing. Probably this is the part of the thesis that I find most difficult to write, but I can not pass up the opportunity to express my gratitude for the support received from many people during this stage of my life, no matter if they read these words or not.

First, I must thank the immeasurable work of Luis Plaja, primarily responsible for, not only this work, but also for boosting my interest in science. His continuous encouragement, enthusiasm, and dedication to me, were very important during these years. Undoubtedly, I'll be very proud of my thesis supervisor during my whole lifetime.

Secondly I would like to thank Luis Roso for trusting in me since the very beginning, for introducing me in the world of intense lasers, and for his fruitful conversations about science. I am very grateful too for hosting me in 'El Fotón Charro', an incredibly nice group of people. I thank each and every one of its components, which with I had a great time in a daily basis. From all of them, I will name here those who have contributed directly to this thesis: José Antonio Pérez, for its valuable collaboration, providing single-atom and 3D TDSE calculations; Cruz Méndez, Íñigo Sola and Óscar Varela for their patience with me in the lab; Enrique Conejero, for helping me during the first steps of my PhD; and the editors of 'El láser, la luz de nuestro tiempo', with whom I shared pleasant experiences. To the rest of the people of the Optics group at the University of Salamanca and at Centro de Láseres Pulsados (CLPU), thank you very much. I have learnt a lot –and I hope to continue learning– from each and every one of you, scientific, and humanely.

I wish to acknowledge the people from Boulder: Andreas Becker and Agnieszka Jaron-Becker, whom I am extremely grateful for hosting me in his research group at JILA, and for trusting in our previous work; Margaret Murnane and Henry Kapteyn, for giving me the unique opportunity to collaborate with their group; and Tenio Popmintchev for our strong collaboration. Finally, I must say that my first visit to Boulder would not have been so successful without the invaluable help of my friend Antonio Picón, always so helpful. Thank you very much to the rest of Boulder friends who made my two visits so warm.

I would also like to express my gratitude to the Grup dÒptica Quàntica at the Universitat Autònoma de Barcelona for their warm hospitality during my visits, as well as to Martin Kretschmar, from Universität Hannover, for his recent scientific collaboration, and to the Robotics Group of the University of Salamanca.

From a personal point of view, I wish to express my deep gratitude to my family, especially to my parents and to my brother, for their affection and unconditional support, and for giving me everything I needed to get here. I will never find a way to thank for all you did for me. Undoubtedly, this achievement is also yours, I'm very proud of you. I would also like to acknowledge the support of my friends, with whom I've enjoyed such good times. And finally, to Cristina, for making my dreams come true.

"Si perdemos, continuaremos siendo el mejor equipo del mundo.
Si ganamos, seremos eternos"

Pep Guardiola

"If we lose, we'll continue being the best team in the world.
If we win, we'll be eternal"

Pep Guardiola, Soccer Coach

Contents

List of Publications

Publications upon which this report is based:

1. High-order harmonic propagation in gases within the discrete dipole approximation.
   C. Hernández-García, J. A. Pérez-Hernández, J. Ramos, E. Conejero, L. Roso and L. Plaja
   Physical Review A **82**, 033432-1-11 (2010)

2. New methods for computing high-order harmonic generation and propagation.
   J. A. Pérez-Hernández, C. Hernández-García, J. Ramos, E. Conejero, L. Plaja and L. Roso,
   Book Chapter: *Progress in Ultrafast Intense Laser Science VII (pp 145-162), Springer (2011)* ISBN 978-3-642-18326-3

3. Off-axis compensation of attosecond pulse chirp.
   C. Hernández-García, and L. Plaja
   Journal of Physics B: At. Mol. Opt. Phys. **45**, 074021 (2012)

4. Bright Coherent Ultrahigh Harmonics in the keV X-ray Regime from Mid-Infrared Femtosecond Lasers.
   T. Popmintchev, M.-C. Chen, D. Popmintchev, P. Arpin, S. Brown, S. Ališauskas, G. Andriukaitis, T. Balčiunas, O. Mücke, A. Pugzlys, A. Baltuška, B. Shim, S. E. Schrauth, A. Gaeta, C. Hernández-García, L. Plaja, A. Becker, A. Jaron-Becker, M. M. Murnane, and H. C. Kapteyn
   Science **336**, 1287 (2012)

5. Zeptosecond keV X-ray waveforms driven by mid-infrared laser pulses.
   C. Hernández-García, J. A. Pérez-Hernández, T. Popmintchev, M. M. Murnane,

H. C. Kapteyn, A. Jaron-Becker, A. Becker and L. Plaja
submitted to *Nature Photonics* (2012).

6. Signature of the transversal coherence length in high-order harmonic generation.
   Carlos Hernández-García, Íñigo J. Sola and Luis Plaja
   submitted to *Optics Express* (2012).

7. Spatial contributions of electron trajectories to high-order harmonic radiation originating from a semi-infinite gas cell.
   Martin Kretschmar, Carlos Hernández-García, Daniel S. Steingrube, Luis Plaja, Uwe Morgner and Milutin Kovačev.
   submitted to *Physical Review A* (2012).

Other work carried out in the predoctoral period and not mentioned in this report:

1. Role of the longitudinal piston error in a tiled-grating compressor in second and high-order harmonic generation.
   C. Hernández-García, C. Méndez, I. Arias, J. R. Vázquez de Aldana, O. Varela, I. J. Sola and L. Roso
   Applied Physics B **108**, 773-777 (2012).

Introduction

During more than two decades, the field of ultrafast intense laser science has boosted our understanding of matter subjected to strong laser fields. Unlike other non-perturbative fields of physics, the worldwide availability of intense laser technology has provided a fruitful interplay between theory and experiments on a daily basis. The present work is a clear example of this interplay.

Intense electromagnetic radiation induces a strong non-linear response in matter. The atomic electrons acquire energy from the driving laser, which can be subsequently released in the form of high frequency coherent radiation, in a process known as high-order harmonic generation (HHG). The lack of conventional lasers at these high frequencies drives the technological interest of HHG as a basis for coherent short wavelength sources. Until very recently, intense laser technology was limited to near-infrared wavelengths (around 800 nm), consequently, the harmonic conversion was limited to the far ultraviolet (XUV). Nowadays, thank to the development of parametric conversion techniques, the current limit falls in the soft X-rays region.

However, it was early recognized that the potential applications of HHG extend beyond the obvious applications of coherent high-frequency radiation. In the spectral region near the cut-off frequency, the spectrum has the form of a comb of harmonics with similar intensities and, most interestingly, with a smooth spectral phase distribution. Therefore, after filtering the low-frequency spectrum, the resulting radiation corresponds to a train of ultrashort XUV pulses, with typical durations of hundreds of attoseconds (1 as=10^{-18} s), and spaced regularly every half of the driving laser period. After their experimental confirmation, these are considered the shortest bursts of coherent radiation ever created. This technology is in his birth, but already has demonstrated multiple applications in the time resolution of the ultrafast (attosecond) dynamics of physical, chemical and biological systems.

The aim of this thesis is to make an original contribution to this field. The conducting line followed in this study consists on developing theoretical methods to compare directly with the experiments. This strategy is twofold. First of all, theory is used to understand the experimental results. For that purpose we have make our own experiments (under the guidance of Dr. Íñigo J. Sola) to directly compare our simulations, but we have also collaborated with two experimental groups to compare with their results. Secondly, theory is applied to predict new physics and to determine some direction towards which experiments could be done.

The starting point of this thesis is the single-atom HHG calculations, developed previously at the University of Salamanca, and explained here along chapter 1. Hence, our first objective was to implement a propagation scheme for the high-order harmonics, making the theory comparable to the experiments. For this, we have implemented a novel propagation technique based on the discrete dipole approximation. This technique and the fundamentals for understanding high-order harmonic propagation are developed in chapter 2. Our novel method was published in *Physical Review A* **82**, 033432-1-11 (2010).

In chapter 3 we study the propagation of high-order harmonics from near-IR fields in rare gases. As a first test, we have analyzed theoretically and experimentally the change of the phase-matching conditions when moving the gas jet along the propagation axis. Once our method was validated experimentally, we proposed a route to obtain narrower attosecond pulses by detecting them at a certain angle form the propagation axis, published in *Journal of Physics B: At. Mol. Opt. Phys.* **45**, 074021 (2012). Afterwards, we present a study of the transversal coherence length, by comparing our theoretical analysis with our experiments, in a work that was recently submitted to *Optics Express,* (2012). Finally, we have implemented a semi-infinite gas cell geometry in order to explain the experiments carried by M. Kovačev's group at Universität Hannover (Germany). The joint work was recently submitted to *Pyhsical Review A,* (2012).

In chapter 4 we have implemented our method to obtain ultra high-order harmonics driven by mid-IR lasers, in collaboration with the theoretical group of A. Becker and A. Jaron-Becker at JILA, University of Colorado (USA). The main result was the demonstration of the temporal coherence of the keV X-rays obtained by the experimental group of M. Murnane and H. Kapteyn at JILA, University of Colorado (USA),

that led a joint collaboration with Technical University of Vienna (Austria), Cornell University (USA) and us. The result was published in *Science* **336**, 1287 (2012). In further exploration of the X-ray bursts driven by mid-IR laser sources, we have derived a route for obtaining waveforms in the zeptosecond regime (1 zs=10^{-21} s). This work, which is also a collaboration with the theoretical and experimental groups at JILA, has been submitted to *Nature Photonics,* (2012).

1

High-Order Harmonic and Attosecond Pulse Generation

The refinement of mode-locking techniques [1, 2] and the development of chirped-pulse amplification [3] opened in the late 1980s the new frontier of high energy laser-matter interaction. Intense fields have also, and quite unexpectedly, extended the limits of ultrashort laser pulses to durations below the femtosecond barrier. Even though it is presently at an early stage of development, attosecond metrology has revolutionized physics, giving experimental evidences to fundamental questions on how ionization, molecular charge transfer and other phenomena take place.

This chapter is aimed as a fundamental introduction to strong field phenomena, with special emphasis in those aspects relevant with high-order harmonic generation (HHG) and attosecond pulse production. We have divided it in three sections. First of all we describe some fundamentals of HHG. After a small historical review, we shall introduce the different possible nonlinear ionization processes, and the classical model of HHG. Section 1.1 will conclude with the analysis of attosecond pulse generation from the HHG spectrum. In section 1.2 we will turn into the quantum description of HHG, describing the Strong-Field Approximation (SFA) approach and the saddle point approximation. Finally, in section 1.3 we will describe the extended SFA theory (SFA+), which was developed previously in our group and that has been used along this thesis to compute the single-atom HHG.

1.1 Fundamentals of High-Order Harmonic Generation

When matter interacts with sufficiently intense fields, its dynamics becomes non-linear. As a result, the excited charges (mainly electrons) radiate at frequencies not contained in the driving field. If the interaction extends over many cycles, interference leads to the emission of radiation at integer multiples of the driving field frequency, known as harmonics. The radiated spectra is, therefore, composed of a comb of equally spaced peaks. Harmonic generation with ultraintense fields is characterized by the abnormal the extension of the spectra towards short wavelengths. In addition, a second and equally relevant characteristic of strong-field harmonic generation is the phase locking of the higher harmonics, which leads to the generation of attosecond pulses. Reviews of high-order harmonic generation and attosecond physics can be found in [4, 5, 6, 7, 8, 9, 10].

1.1.1 A brief history of High-Order Harmonic Generation

One of the major challenges since the invention of the laser in 1960 [11] has been to extend coherent radiation to the extreme regions of the optical electromagnetic spectrum, in particular, at higher frequencies. For that purpose, harmonic generation offers a direct route. The first experimental evidence of harmonic generation was demonstrated by Franken *et al.* in 1961 [12]. In this pioneering work, a ruby laser with wavelength $\lambda = 694$ nm was aimed to generate its second harmonic (347 nm) in a quartz crystal. As a linear phenomenon, the quest for the highest harmonic orders is closely linked to the development of laser sources of high intensity. Non-perturbative harmonics, i.e. those whose efficiency does not decrease exponentially with their order, were reported in the late 1980s [13, 14], using krypton-fluoride ($\lambda = 248$ nm) and neodymium-glass ($\lambda = 1064$ nm) lasers respectively. Harmonics with orders greater than the 109th were observed very early for incident wavelengths in the near infrared range using neon as a target [15]. At the very beginning, this behavior was attributed to multiphoton excitation of atomic subshells, but later, a nice classical interpretation was proposed by Corkum, relating the harmonic generation with ionization in the so-called three step model [16].

The most relevant aspects of high-order harmonic generation and propagation were stablished during the 1990s, following intensive experimental and theoretical activities.

The close interplay between theory an experiments has boosted the development of the field. A particularly relevant case is the discovery of the natural phase locking of the highest harmonics, which was predicted theoretically almost a decade earlier than found experimentally. This phase locking conveys the production of high-frequency radiation in the form of coherent sub-femtosecond pulses [17]. It was not until 2001, when two different groups demonstrated experimentally the first evidence of attosecond pulse generation (1 as = 10^{-18} s) [18, 19]. The new era of attosecond physics was born.

The development and refining of experimental techniques has gradually extended the limits of harmonic production and attosecond pulse generation. For instance, we have been giving theoretical support to the experimental demonstration of ultra-high harmonic generation above the 5000th order [20], extending its coherent behavior from the vacuum ultraviolet to the soft X-ray region ($<$ 1.6 keV). In addition, a new record for the shortest coherent pulses (67 attoseconds) has been very recently reported [21].

1.1.2 Strong-field ionization

Atomic photoionization is a phenomenon that has drawn physicists' attention for almost a century, and which is still very much alive. After being crucial for the introduction and acceptance of quantum theory, it is still nowadays an extraordinary tool to unveil and characterize the details of laser-matter interaction.

The ionization of a quantum system is nonlinear when the condition $\hbar\omega_0 < I_p$ is fulfilled, where ω_0 is the frequency of the incident radiation and I_p is the atomic ionization potential, i.e. the energy necessary to extract the the most energetic bound electron of the system [22]. Although this process violates the earliest conception of the photoelectric effect [23], the possibility of a simultaneous absorption of various electromagnetic quanta was proposed by Göppert-Mayer in 1931 [24].

Multiphoton processes are of course not restricted to ionization (which is a transition from a bound to a continuum level) since can also occur in any transition between bound states, changing Bohr's third postulate from its initial form $\hbar\omega_0 = E_f - E_i$ to the multiphoton one $K\hbar\omega_0 = E_f - E_i$, K being the integer number of photons absorbed by the system. In perturbation theory, the possibility of having multiphoton transitions is justified by the uncertainty principle for energy and time, $\delta\omega\delta t \geq \hbar$, which permits the system to pass through virtual states during a time δt with an energy defect $\delta\omega$.

1. HIGH-ORDER HARMONIC AND ATTOSECOND PULSE GENERATION

Let us now review the different flavors in which intense field ionization takes place (reviews of the interaction of atoms with intense fields, including many references, can be found in [22, 25, 26, 27, 28, 29]).

Tunneling ionization

Let us consider, for the sake of simplicity, an electron in the fundamental state of the hydrogen atom. The electron is strongly bounded to the nucleus by a Coulomb potential, as represented in Fig. 1.1a. When a linearly polarized field is applied to the atom, the Coulomb potential is modified, forming a potential barrier through which the electron can tunnel to the continuum (see Fig. 1.1b).

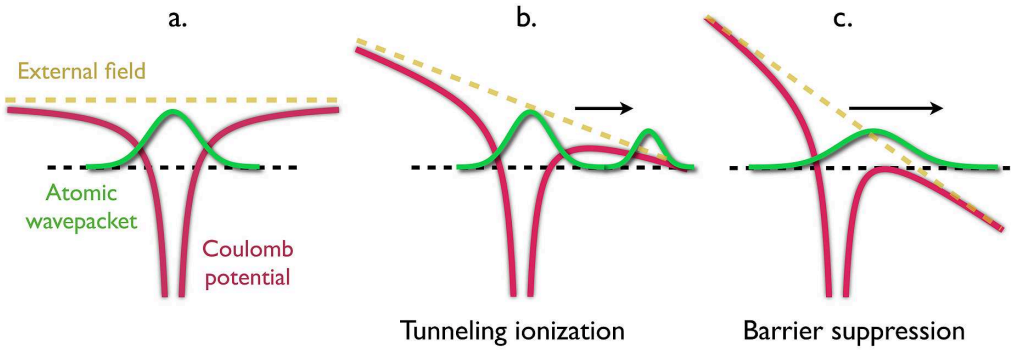

Figure 1.1: **a** Scheme of the evolution of the atomic wavepacket in the absence of an external field, **b** when the field permits tunneling ionization and **c** when the field is so intense that there is barrier suppression.

The tunneling time can be estimated simply as the ratio of the distance between the points where the potential barrier crosses the state energy of the electron, to the velocity of the electron inside the barrier [30, 31]. Let us simplify the tunnel picture neglecting the Coulomb potential (see Fig. 1.2). If we assume the electron (with charge q) to be initially at $z = 0$, with an energy ϵ_0, the tunneling exit coordinate is given by the condition $\epsilon_0 = -qE_0 z$, where E_0 is the electric field's amplitude, and therefore

$$z_0 = \frac{|\epsilon_0|}{qE_0} \tag{1.1}$$

If we now assume a constant velocity through tunneling whose absolute value is given by $\sqrt{2m\epsilon_0}$, the tunneling time can be computed as

$$\tau_t = \frac{z_0}{v_0} = -i\frac{\gamma}{2\omega_0} \tag{1.2}$$

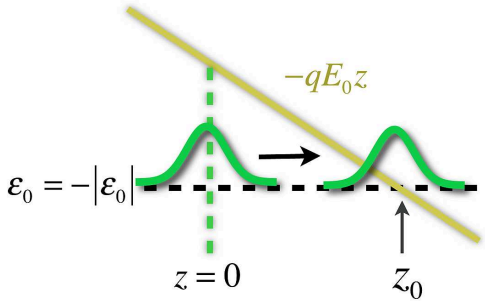

Figure 1.2: Scheme of the simplified tunnel picture neglecting the Coulomb potential. The tunneling exit coordinate, z_0, is given by the condition $\epsilon_0 = -qE_0z$.

where γ is the so-called Keldysh adiabaticity parameter [32] defined as

$$\gamma = \frac{\omega_0(2mI_p)^{1/2}}{qE_0} = \sqrt{\frac{I_p}{2U_p}} \tag{1.3}$$

$U_p = qE_0^2/4m\omega_0^2$ is the ponderomotive energy, which is the mean kinetic energy of a free electron in the electromagnetic field, and $I_p = |\epsilon_0|$ is the ionization potential. The Keldysh parameter can be expressed in terms of the tunneling time and the laser period (T) as $\gamma \approx 4\pi|\tau_t|/T$. Intuitively, we shall expect tunneling ionization to be relevant when the electron has enough time to cross the barrier before the oscillating electromagnetic field changes its sign. Therefore, the condition for efficient tunneling corresponds to a Keldysh parameter well below the unity. It can be then assumed that the electron tunneling is fast enough to approximate the electromagnetic field to a static field. This remarkable property is fundamental for the development of attophysics.

In order to compute the ionization rate in the tunneling regime, we will resort to the Amosov-Delone-Krainov (ADK) theory [33], as will be explained in Chapter 2.

Multiphoton ionization (MPI)

When $\gamma \gg 1$ –that is, the ionization potential is much higher than the ponderomotive energy, which happens for relatively high frequencies or for weak fields– ionization is dominated by multiphoton absorption (MPI). In this case, we can graphically describe the process as the absorption of the minimum number of photons (K) needed to promote the electron to the continuum. As a result, the electron is ionized with a kinetic energy $K\hbar\omega_0 - I_p$, always less than the photon energy.

For weak fields, the ionization rate (probability of ionization in a time unit) is given by the perturbative formula

$$w = \sigma^{(K)} I^K, \tag{1.4}$$

where $\sigma^{(K)}$ is the multiphoton cross section, which depends on the frequency and the polarization of the field, and also on the atomic structure, but not on the field intensity (I). When $K = 1$, Eq. (1.4) describes the single-photon photoelectric effect, whose dependence on the field intensity is linear. In the case of intense fields, the perturbative picture breaks down, and the multiphoton ionization can result in electrons with energies corresponding to the absorption of a photon number greater than the minimum necessary (K), a phenomenon referred as above-threshold ionization (ATI). The first experiments on multiphoton ionization were performed in 1977 by Lompré *et al.* [34], whilst above-threshold ionization was first reported by Pierre Agostini *et al.* in 1979 [35]. From a fundamental viewpoint, the appearance of peaks in the photoelectron spectrum, each with a width smaller that one photon energy, implies, from the time-energy uncertainity principle, that multiphoton ionization is a process that takes place along many cycles of the driving field.

Ionization from barrier suppression

The limiting case of tunneling for the highest intensities is the so-called barrier suppression ionization (BSI), which is depicted in Fig. 1.1c. This kind of ionization takes place when the field amplitude is so high that the potential barrier lies below the bound electron's energy, the electron wavepacket being free to escape from the ion. For even higher intensities, and contrary to what one would expect intuitively, the ionization rate is predicted to decrease and a stabilization regime can be reached, in which a large amount of the population remains trapped in the bound states. Both barrier suppression ionization and stabilization [36] have not been yet unambiguously recognized in experiments as they require ultraintense laser pulses with turn-on less than one cycle.

1.1.3 High-order harmonic generation in atoms. Basic characteristics

Let us now review the main characteristics of the harmonic spectrum generated by an atom irradiated by an intense laser pulse. As we shall see, the highest harmonic

frequencies are obtained in the limit of intense fields and low frequencies, therefore in the tunneling ionization regime.

The spectrum has certain peculiar features which have been observed in the earliest experiments [13, 14, 37] and also in the first theoretical simulations [38]. A typical spectrum is composed of a few low order harmonics whose intensities decrease exponentially, in accordance with the perturbative scaling, followed by a wide region of harmonics with similar intensities (*plateau*). The plateau ends sharply at a cut-off frequency given by the law

$$\hbar\omega_{max} = I_p + 3.17U_p. \tag{1.5}$$

where U_p is the ponderomotive energy. The appearance of a plateau is a remarkable property, since conveys the efficient emission of shorter wavelengths. Beyond the cut-off frequency, the intensity of the harmonics decreases again quickly and higher order harmonics are hardly visible. In Fig. 1.3 we represent a scheme of the typical HHG spectrum. The scaling of the harmonic q with the intensity is $I^{q'}$, with $q' < q$ at the plateau and cut-off regions, revealing their non-perturbative origin [39]. In contrast, the low-order harmonics scale with the perturbative power law I^q.

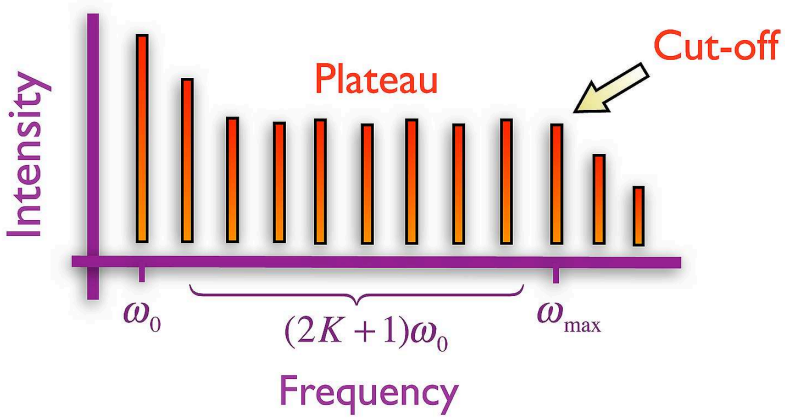

Figure 1.3: Scheme of the HHG spectrum in the tunneling ionization regime, composed by peaks with frequencies an odd multiple of that of the fundamental field (harmonics). The spectrum consists of a few low order harmonics whose intensities decrease exponentially, following the perturbative scaling, followed by a wide region of harmonics with similar intensities (*plateau*). The plateau ends sharply at a cut-off frequency. (Intensity is represented here in logarithmic scale).

Given the fact that the radiation emitted in the harmonic generation is coherent, there is a fundamental interest in extending the cut-off frequency to higher energies. From the dependences of the ponderomotive energy, $U_p \propto \lambda_0^2 I$, and the cut-off law in Eq. (4.1), there are two basic strategies for increasing the extension of the harmonics spectra: either to increase the intensity (I) or/and to increase the wavelength of the driving field (λ_0).

However, there are physical restrictions that limit the maximum photon energy of the harmonic spectra. First, if we increase the laser intensity beyond a critical point, we move to the barrier suppression regime. In this case, the maximum frequency does not follow anymore the law (4.1), and the spectral plateau is degraded. Second, the efficiency for the generation of the highest harmonic orders has been shown to decrease drastically with the wavelength [40, 41]. In addition, harmonics are always generated in macroscopic media, and therefore phase-matching conditions in the propagation play an essential role. This will decrease the efficiency of the harmonics when both increasing the intensity or the wavelength of the driving laser field. Nevertheless, it is possible to define the experiments under optical phase-matching conditions [42]. It is in this optimal situation in which the ultrahigh conversion of > 5000 photons mentioned above was demonstrated [20].

At present, the basic properties of the harmonic spectra generated by intense fields are well understood. The theoretical treatment of the process admits different levels of description, that range from the classical to semiclassical and full quantum. In the following section we will review the details of the classical description of high-order harmonic generation. Afterwards, in section 1.2, we shall develop the quantum description of the process, and derive the semiclassical quantum-orbit model.

1.1.4 Simpleman's model of HHG

The simpleman's model refers to the classical theory for describing HHG. The approach is based on three assumptions. First of all, the ionization process depends only on the instantaneous value of the electromagnetic field. Secondly, right after ionization, the electron is located at the coordinate origin with zero velocity. These are reasonable assumptions in the tunneling regime since zero is the mean value of the velocity and the coordinate of the bound state previous to ionization. The third assumption consists in considering the dynamics subsequent to ionization as corresponding to a classical

free electron in the electromagnetic field, thus neglecting the influence of the Coulomb potential. This model was first proposed by van Linden and Muller [43], and Gallagher [44] to study above-threshold ionization, and later used by Corkum [16] and Kulander and Schafer [45] to explain the plateau in the harmonic spectrum, and is also known as the simpleman's or three-step model.

Let us, therefore, assume an electron which is ionized at the coordinate origin at the instant t_0, with zero velocity, and that evolves under a monochromatic external field linearly polarized in the x direction, with the form $E(t) = E_0 \sin \omega t$. Integrating Newton's law, the classical equations of motion are

$$\ddot{x}(t) = -\frac{eE_0}{m} \sin(\omega t) \tag{1.6}$$

$$\dot{x}(t) = \frac{eE_0}{m\omega} [\cos(\omega t) - \cos(\omega t_0)] \tag{1.7}$$

$$x(t) = \frac{eE_0}{m\omega^2} [\sin(\omega t) - \sin(\omega t_0) - \omega(t - t_0) \cos(\omega t_0)] \tag{1.8}$$

where e is the absolute value of the electron's charge. We can see that the velocity includes two distinct terms, a drift term, $v_{drift} = -(eE_0/m\omega) \cos(\omega t_0)$, and a quiver term, $v_p = (eE_0/m\omega) \cos(\omega t)$, which describes the oscillation in the external field. The drift term makes the trajectory to depend strongly on the initial phase of the electric field, ωt_0.

According to the three-step model [16, 45], the generation of the most energetic harmonics can be understood in terms of simple semiclassical arguments (see Fig. 1.4). In a first step, the atomic electron appears in the continuum after tunneling through the Coulomb barrier. After the release, in a second step, the electron is accelerated by the electric field and driven back towards the parent ion. Then, the high frequency radiation is emitted in a last step, in which the electron recombines to the ground state of the parent ion. At this latter moment, the electron emits a photon whose energy equals the electron's total energy: kinetic plus ionization potential.

In order to obtain the maximum photon energy that can be generated, we have to look at the kinetic energy, which is given by $T(t) = m\dot{x}^2(t)/2$. It can be found from Eqs. (1.7) and (1.8) that the maximum energy of an electron returning to the nucleus is $T_{max} = 3.17U_p$, being U_p the ponderomotive energy. As a consequence, we recover the cut-off law (4.1) for the maximum photon energy.

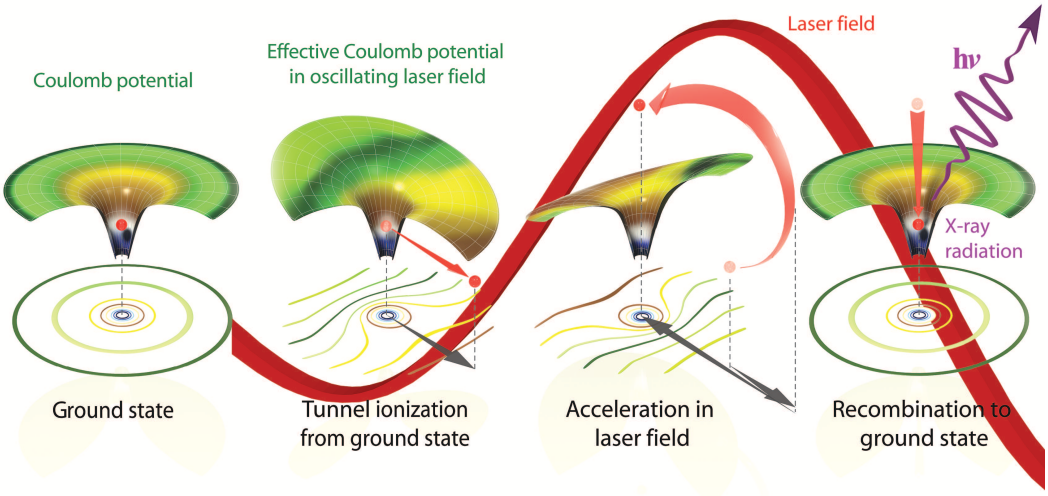

Figure 1.4: Classical schematic of HHG, by the three-step model. The electric field of an intense laser extracts an electron from an atom by tunnel ionization through the potential barrier formed by the Coulomb potential. The laser field then accelerates the electron, which is driven back to the ground state of the parent atom, liberating its excess energy as a high-energy photon. Figure courtesy of T. Popmintchev [9].

Let us now study in detail the dynamics represented by Eqs. (1.6)-(1.8). In Fig. 1.5a we have depicted some electron trajectories for different ionization times. The grey-dashed line represents the electric field in arbitrary units units (arb. u.) whereas the green line represents the nucleus position, at the coordinate origin. In figure 1.5b we have plotted the recollision kinetic energy of the particles as a function of the recollision (green points) and ionization time (red points). The maximum recollision energy takes the well-known value, $T_M = 3.17U_p$, for the trajectory represented in blue, with an excursion time of approximately 0.63 times the period of the laser pulse. Further recollisions do not raise this maximum energy. Noticeably, in every half cycle of the laser pulse, there are two possible electron trajectories leading to the same kinetic energy at recollision, and therefore two possible paths for the generation of the same harmonic (each named accordingly to the excursion time as *short* and *long* trajectory). We have represented in Fig. 1.5a three pairs of short and long trajectories with energies at recollision of $3.0U_p$, $2.5U_p$ and $1.5U_p$. In Fig. 1.5b we can observe that for the short trajectory contributions, the less energetic harmonics are emitted earlier than the more energetic, thus imprinting a positive chirp in the harmonic radiation. This behavior is

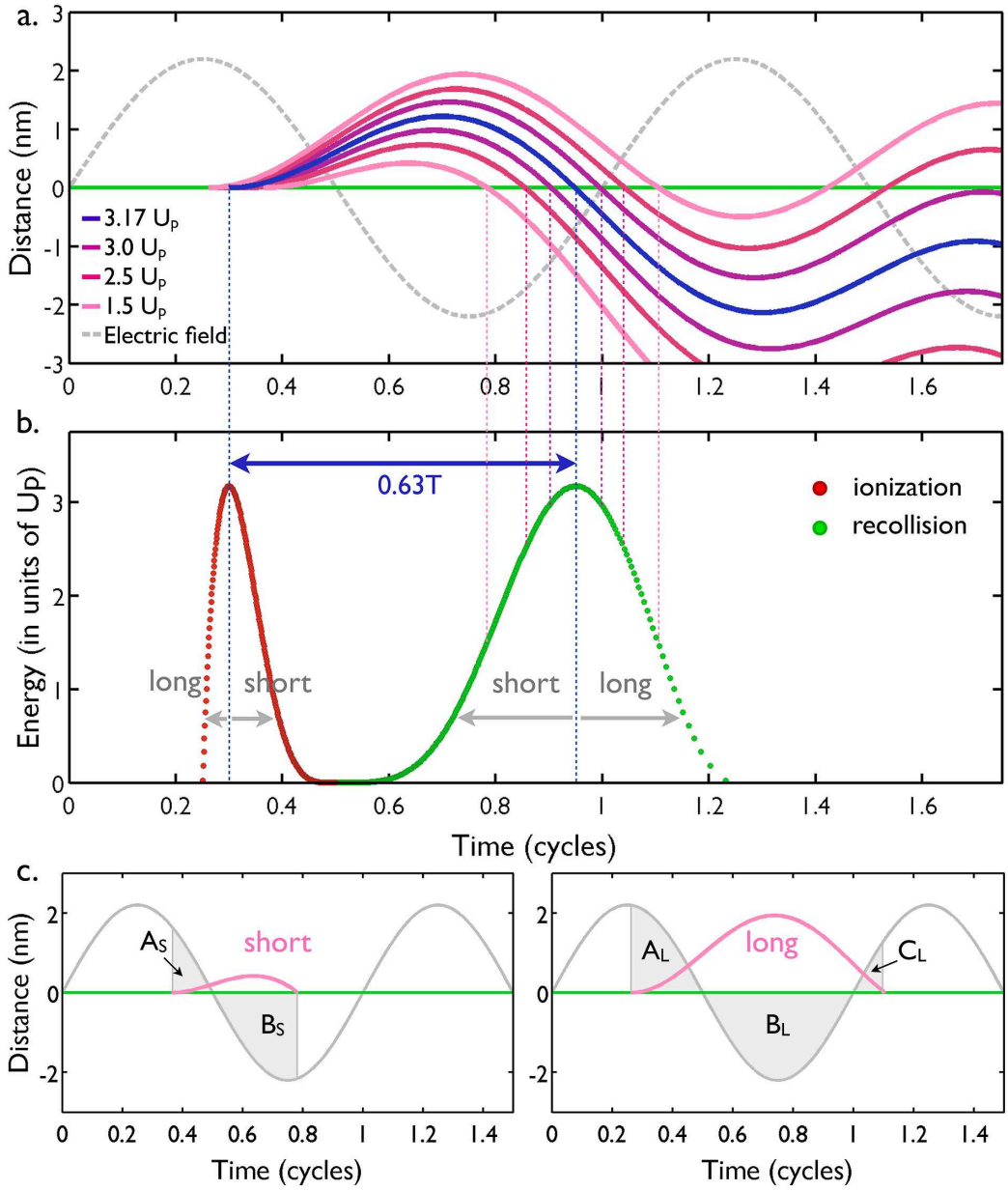

Figure 1.5: **a** Sample of electronic trajectories in a monochromatic laser field of $\lambda_0 = 800$ nm and peak intensity 1.57×10^{14} W/cm^2. The grey-dashed line represents the electric field in arbitrary units, whereas the green line, the nucleus position. Three pairs of short and long trajectories are represented for energies at recollision of $3.0U_p$ (purple), $2.5U_p$ (dark pink) and $1.5U_p$ (light pink), whereas the most energetic trajectory, raising $3.17U_p$ at recollision, is represented in blue. The vertical axis represents the distance from the nucleus. **b** Returning kinetic energy of the particles at the instant of the first recollision in **a**. The green points represent the recollision time, whereas the red points the ionization time. The blue arrow shows the excursion time for the most energetic trajectory, $0.63T$, where T is the laser period. In **c** we present a pair of short and long trajectories, of energy $1.5U_p$. The grey-shaded regions represent the integration of the electric field over time, i.e., the velocity of the electron.

reversed for the long trajectories, that imprint a negative chirp.

In Fig. 1.5c we present a pair of short and long trajectories, corresponding to a kinetic energy at recollision of $1.5U_p$. The grey-shaded regions represent the integration of the electric field over time, i.e., the velocity of the electron. Therefore, the energy at recollision for the short trajectory will be given by $A_S + B_S$, whereas for the long one, $A_L+B_L+C_L$. It is straightforward to observe that in this case, $A_S+B_S = A_L+B_L+C_L$, and as a consequence, both trajectories lead to the same kinetic energy at recollision.

It is noticeably that a very simple classical picture provides such a complete description of the harmonic generation process. This model can also be extended to other regimes. In the case of multiphoton ionization, the relevant difference is that the initial velocity will be given by the excess energy in the ionization process, i.e. $v_0(t_0) = [2(K\hbar\omega_0 - I_p - U_p)/m]^{1/2}$. This new contribution to the drift velocity shifts the trajectories and hence fewer particles with high kinetic energy return to the core. In any case, the ponderomotive energy is typically smaller in the multiphoton regime, therefore the highest harmonic order is smaller than in tunneling ionization. For the case of barrier suppression, the atom becomes quickly ionized, and there is no possibility of recombination except in a small fraction of the first laser period. However, it has been proposed that, for laser pulses with non adiabatic turn-on, and of high peak intensity (deep barrier suppression regime), the energy of the recolliding electron can be high enough to generate photons in the soft X-ray regime [46].

1.1.5 Attosecond pulses

One of the most exciting perspectives of high-order harmonic generation by intense lasers is the possibility of synthesize XUV pulses of sub-femtosecond duration [17, 47, 48, 49]. An attosecond pulse train (1 as = 10^{-18} s) is obtained by the selection of the higher frequency part of the harmonic spectrum which conform the plateau region. For the correct synthesis, the spectrum should approach two conditions: on one side its structure should approach that of a frequency comb, in which the harmonic intensities are similar; on the other side, the relative phase between the harmonics should be nearly constant (phase locking) [17]. Fortunately, these two conditions are approached in the typical harmonic spectra generated during the interaction of intense fields with matter. However, as we will see in chapter 3, the macroscopic conditions of the HHG experiments play an important role for the final phase locking of the different harmonics.

The first experimental evidence of an attosecond pulse train was achieved by selecting five consecutive harmonics generated in argon, obtaining 250 as pulses [18]. Almost simultaneously, isolated pulses with duration of 650 as were generated by spectrally filtering a few cut-off harmonics produced by an ultrashort laser pulse [19]. At present, after postcompression of the attosecond pulses, isolated pulses of temporal durations < 100 attoseconds have been measured experimentally [21, 50].

Let us now analyze the main characteristics of attosecond pulse generation. In the previous section, we have presented the harmonic spectrum obtained in the tunneling ionization regime, in which several harmonics are emitted with similar intensity conforming the plateau region. If these harmonics were emitted in the Fourier limit (i.e. with constant relative phase), the pulse duration would scale inversely with the bandwidth of the coherent spectrum.

Nevertheless, the HHG mechanism itself prevents the harmonics to be emitted in the Fourier limit. Since the different electronic trajectories rescatter at different times (see Fig. 1.5), a chirp is imprinted in the emitted radiation. The emission from the short trajectories is positively chirped (the lower harmonics are emitted before the higher), while the emission from the long trajectories exhibits a negative chirp (the higher harmonics are emitted before the lower) [51, 52]. This chirp is referred in the literature as *atto-chirp*.

We present in Fig. 1.6b the HHG spectrum obtained from the interaction of an hydrogen atom with a 800 nm, 5.8 cycles full width at half maximum (FWHM), 1.57×10^{14} W/cm^2 peak intensity laser pulse, represented in Fig. 1.6a. In Figs. 1.6c-e we present the attosecond pulse trains computed from the inverse Fourier transform of the complex harmonic spectrum, windowed by a rectangular mask of ten photons bandwidth ($10\omega_0$) for three positions of the window's center: (c) at the lower energy plateau, (d) at the high-energy plateau, and (e) involving harmonics above the cut-off region. Note that an attosecond pulse is obtained in each half-cycle of the incident laser pulse. The width of the attosecond pulses becomes narrower, and the contrast increases, when selecting the higher energy part of the plateau region (d), as phase locking conditions are better. In the cut-off region (e), longer attosecond pulses are obtained, as only a couple of harmonics have similar intensity.

It is possible to obtain an isolated attosecond pulse using few-cycle driving pulses [19, 49], since high order harmonics are then generated in a single rescattering event. As

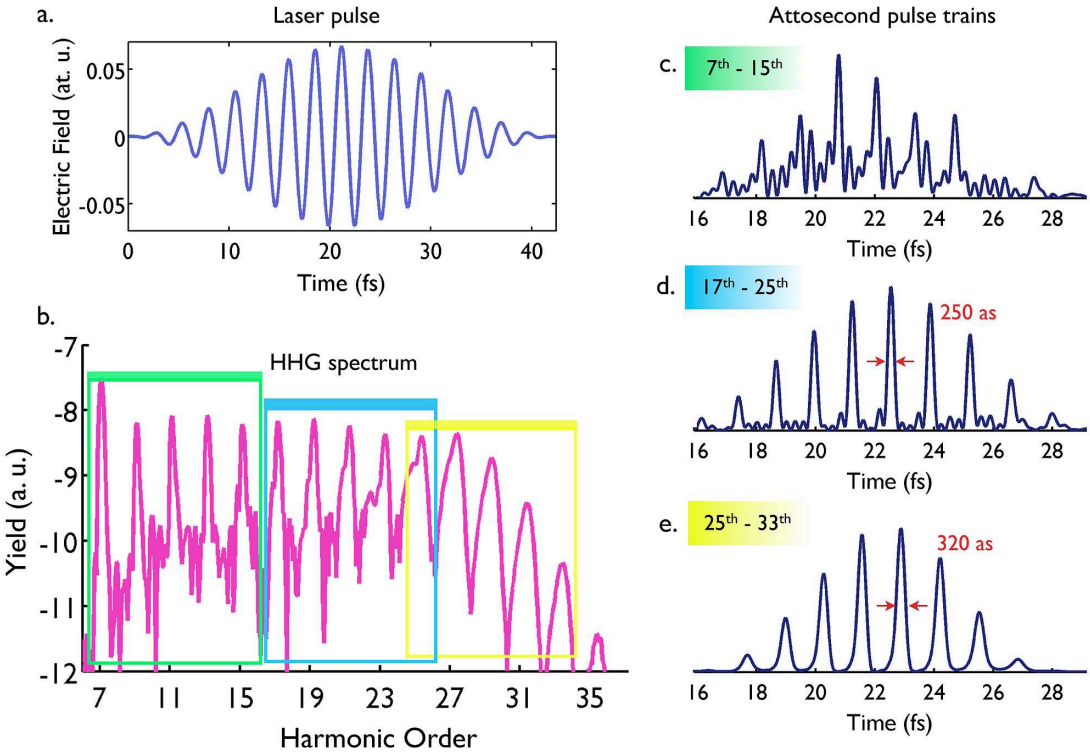

Figure 1.6: Attosecond pulse trains obtained from the HHG spectrum from a hydrogen atom (panel **b**) driven by the laser pulse represented in panel **a**, 800 nm in wavelength, 5.8 cycles (15 fs) FWHM and of peak intensity 1.57×10^{14} W/cm^2. The HHG spectrum is calculated with the quantum SFA+ theory in hydrogen (see section 1.3). Attosecond pulse trains are presented after performing the Fourier transform considering a fixed bandwidth of five harmonic orders: **c** 7th to 15th, **d** 17th to 25th and **e** 25th to 33th.

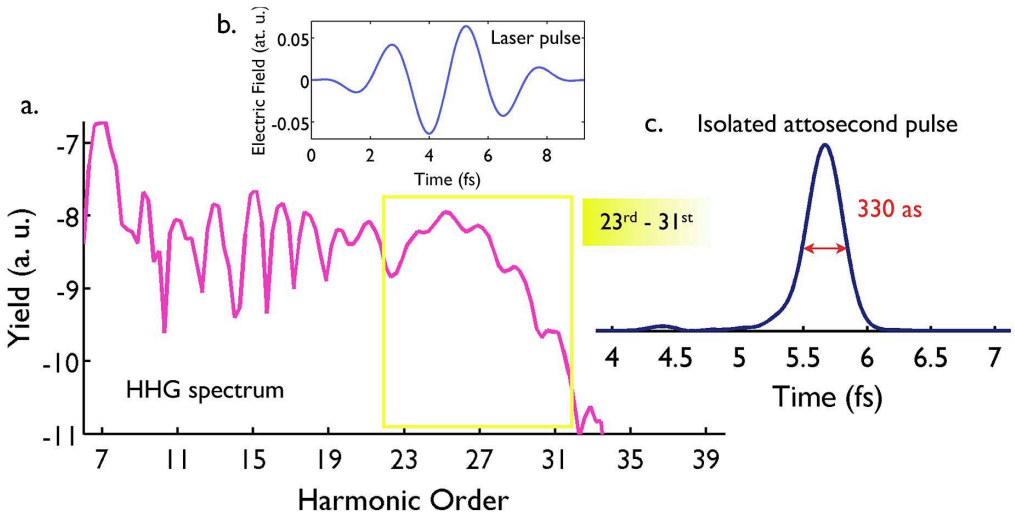

Figure 1.7: **a**. HHG spectrum driven by the laser pulse of panel **b**, 800 nm in wavelength, 1.3 cycles (3.4 fs) FWHM and of peak intensity 1.57×10^{14} W/cm^2. The HHG spectrum is calculated with the quantum SFA+ theory in hydrogen (see section 1.3). An isolated attosecond pulse (panel **c**) is produced by performing the Fourier transform over the spectral bandwidth (yellow line) between harmonics 23rd to 31st.

an example, in Fig. 1.7a we present the HHG spectrum obtained from the interaction of an hydrogen atom with a 800 nm, 1.3 cycles FWHM, 1.57×10^{14} W/cm^2 peak intensity laser pulse, represented in 1.7b. By selecting the spectral bandwidth between harmonics 23rd to 31st in the cut-off region, an isolated attosecond pulse is produced (Fig. 1.7c). Other techniques have been applied for isolating a single attosecond pulse [47, 53, 54], whereas the extraction of the different attosecond pulses from the train has also been reported recently [55, 56, 57].

1.2 Quantum description of High-Order Harmonic Generation

There is a fundamental interest in developing theoretical methods to describe the non-perturbative interaction of ultraintense lasers with atoms. In its full depth, the theoretical description of an atomic electron submitted to an intense electromagnetic field corresponds to the integration of the time-dependent Schrödinger equation (TDSE), which has to be done numerically. Nowadays the exact 3D solution is only feasible for

one and two-electron systems, taking some tens of minutes in the first case, while being a formidable task for supercomputers for the second. Even for the single electron, the exact solution of the propagation equations in macroscopic targets, involving a huge number of atoms, is far from the present and near-future computing capabilities. In this scenario, the development of approximated models becomes mandatory. Among them, the S-matrix formulation combined with the Strong-Field Approximation (SFA) constitute an accredited strategy to approach the problem [58]. The first studies in this direction where aimed to the computation of ionization rates and the description of the photoelectron spectrum [59, 60, 61], but these techniques were progressively extended to treat new phenomenology, as the multielectron ionization [62] or high-order harmonic generation [63, 64, 65]. In this latter case, the *standard* approach combines SFA with a saddle point method to compute the harmonic spectra very efficiently in terms of computing time. As a result of the saddle point integration, the standard theory offers a semiclassical description in terms of electronic trajectories, which also constitutes an extraordinary tool for the physical understanding of high-order harmonic generation.

1.2.1 Strong Field Approximation theory of HHG

Let us start considering the description of an isolated atom interacting with an intense electromagnetic field. In the single-active electron approximation, and assuming a nucleus with infinite mass, the system's dynamics is described by the time-evolution of the electronic wavefunction, according to the one-particle Schrödinger equation,

$$i\hbar\frac{\partial}{\partial t}|\psi(t)\rangle = [H_a + V_i(t)]\,|\psi(t)\rangle \tag{1.9}$$

where $H_a = p^2/2m - Zq^2/r$ is the atomic Hamiltonian (with $q = -|e|$, Z the atomic number, and p the canonical momentum) and $V_i(t) = -(q/mc)A(t)p_z + q^2/(2mc^2)A^2(t)$, in the velocity gauge –being $A(t)$ the vector potential of the electric field– for a linearly polarized field in the dipole approximation. The exact integral solution can be written in terms of propagators as

$$-i|\psi(t)\rangle = G_a^+(t,t_0)|\psi(t_0)\rangle + \frac{1}{\hbar}\int_{t_0}^{t} dt' G^+(t,t')V_i(t')G_a^+(t',t_0)|\psi(t_0)\rangle \tag{1.10}$$

G^+ being the Green's function of the whole problem, and G_a^+ the one associated with the field-free case. Let us now consider a splitting of the Hilbert space into two subspaces,

one for the bound states of the atom, Q, and one for the continuum, P. In association, we define the corresponding projectors $\hat{Q}$ and $\hat{P}$. By definition, $\hat{Q}+\hat{P}=1$, $\hat{Q}\hat{P}=\hat{P}\hat{Q}=0$, $\hat{Q}^2=\hat{Q}$, $\hat{P}^2=\hat{P}$, therefore $|\psi(t_0)\rangle=\hat{Q}|\psi(t_0)\rangle$, $|\psi(t_0)\rangle$ being the initial bound state (note that this does not imply that the subspace Q contains only this state). Also, by definition, $\left[H_a,\hat{Q}\right]=0$, whereas $\hat{P}G_a^+(t',t_0)|\psi(t_0)\rangle=0$, and $\hat{Q}G_a^+(t',t_0)|\psi(t_0)\rangle=G_a^+(t',t_0)|\psi(t_0)\rangle$. Using these relations, Eq. (1.10) leads to two coupled equations (one for the bound part of the wavefunction and other for the free part)

$$\begin{aligned}
-i\hat{Q}|\psi(t)\rangle &= G_a^+(t,t_0)|\psi(t_0)\rangle \\
&+ \frac{1}{\hbar}\int_{t_0}^{t} dt'\hat{Q}G^+(t,t')\hat{Q}V_i(t')\hat{Q}\; G_a^+(t',t_0)|\psi(t_0)\rangle \\
&+ \frac{1}{\hbar}\int_{t_0}^{t} dt'\hat{Q}G^+(t,t')\hat{P}V_i(t')\hat{Q}\; G_a^+(t',t_0)|\psi(t_0)\rangle \qquad (1.11)\\
-i\hat{P}|\psi(t)\rangle &= \frac{1}{\hbar}\int_{t_0}^{t} dt'\hat{P}G^+(t,t')\hat{Q}V_i(t')\hat{Q}\; G_a^+(t',t_0)|\psi(t_0)\rangle \\
&+ \frac{1}{\hbar}\int_{t_0}^{t} dt'\hat{P}G^+(t,t')\hat{P}V_i(t')\hat{Q}\; G_a^+(t',t_0)|\psi(t_0)\rangle \qquad (1.12)
\end{aligned}$$

The first condition of the SFA consists in considering the electrons promoted to the continuum to have no possibility to recombine, therefore $\left[H,\hat{P}\right]\simeq 0$. As a result $\hat{Q}G^+(t,t')\hat{P}=0$, and the third term in the rhs of Eq. (1.11), and the first term in the rhs of Eq. (1.12) vanish, leading to the following set of equations

$$\begin{aligned}
-i\hat{Q}|\psi(t)\rangle &= G_a^+(t,t_0)|\psi(t_0)\rangle \\
&+ \frac{1}{\hbar}\int_{t_0}^{t} dt'\hat{Q}G^+(t,t')\hat{Q}V_i(t')\hat{Q}\; G_a^+(t',t_0)|\psi(t_0)\rangle \qquad (1.13)\\
-i\hat{P}|\psi(t)\rangle &= \frac{1}{\hbar}\int_{t_0}^{t} dt'\hat{P}G^+(t,t')\hat{P}V_i(t')\hat{Q}\; G_a^+(t',t_0)|\psi(t_0)\rangle \qquad (1.14)
\end{aligned}$$

Now the second term in the rhs of Eq. (1.13) describes the non-ionizing excitation of the ground-state at t' and its subsequent evolution until t in the combined influence of the atom and the field. Therefore Eq. (1.13) describes the evolution of the bound part of the wavefunction as the superposition of the bare (field free) evolution and the bound-state excitations (here referred as field-dressing, a contribution wich will be important for the extended theory, SFA+, as we shall see later). A second condition of the standard SFA consists in neglecting these excitations, i.e. setting $\hat{Q}V_i(t')\hat{Q}=0$ in Eq. (1.13), therefore considering that the field interaction leads invariably to ionization.

As a consequence, under the SFA conditions, Eq. (1.10) leads to the following two coupled equations

$$-i\hat{Q}|\psi(t)\rangle = G_a^+(t,t_0)|\psi(t_0)\rangle \tag{1.15}$$

$$-i\hat{P}|\psi(t)\rangle = \frac{1}{\hbar}\int_{t_0}^{t} dt'\hat{P}G^+(t,t')\hat{P}V_i(t')\hat{Q}\; G_a^+(t',t_0)|\psi(t_0)\rangle \tag{1.16}$$

Now we turn into the computation of the radiation spectrum. Although the harmonic conversion efficiency is typically orders of magnitude smaller than unity, the use of intense lasers ensures a sufficient number of radiated photons to allow for a classical description of the harmonic field. The single-atom radiation, therefore, is proportional to the dipole acceleration (see section 2.4) $a(t) = \langle\psi(t)|\hat{a}|\psi(t)\rangle$, that can be evaluated according to the Ehrenfest theorem: $\hat{a} = -(q/m)\nabla V_c$ (V_c being the Coulomb potential, $-Zq^2/r$ in our case). The higher-frequency harmonics correspond to the most energetic photons, thus involving the higher energy transitions, i.e. free to bound. Therefore, we may use Eqs. (1.15) and (1.16) and approximate the acceleration as

$$\begin{aligned} a(t) &\simeq \langle\psi(t)|\hat{Q}\hat{a}\hat{P}|\psi(t)\rangle + c.c. = \\ &= \frac{1}{\hbar}\int_{t_0}^{t} dt_1\langle\phi_0|G_a^-(t_0,t)\hat{a}\hat{P}G^+(t,t_1)\hat{P}V_i(t_1)\hat{Q}G_a^+(t_1,t_0)|\phi_0\rangle + c.c. \end{aligned} \tag{1.17}$$

where the initial bound state is defined as the atomic ground state $|\phi_0\rangle$. The operators $\hat{P}V_i(t_1)\hat{Q}$ and $\hat{P}G^+(t,t_1)\hat{P}$ can be evaluated according to the third assumption in the SFA, that consists in considering the electrons as free particles in the continuum, thus neglecting the Coulomb interaction during their evolution. If we consider a planewave basis, $\{\mathbf{k}\}$, for the subspace defined by $\hat{P}$, we have

$$\hat{P} \simeq \int d\mathbf{k}|\mathbf{k}\rangle\langle\mathbf{k}| \tag{1.18}$$

and therefore,

$$\hat{P}V_i(t_1)\hat{Q} \simeq \int d\mathbf{k}V_i(\mathbf{k},t_1)|\mathbf{k}\rangle\langle\mathbf{k}|\hat{Q} \tag{1.19}$$

with $V_i(\mathbf{k},t_1) = -(q/mc)A(t_1)k_z + q^2A^2(t_1)/(2mc^2)$. In addition,

$$\hat{P}G^+(t,t_1)\hat{P} = -i\frac{C_F}{r^n}\exp\left[-(i/\hbar)\int_{t_1}^{t} d\tau\hat{P}H(\tau)\hat{P}\right] \tag{1.20}$$

where we have introduced the Coulomb factor [66] $C_F/r^n = \left(2Z^2/n^2E_0r\right)^n$. Since the ionized electrons are considered as free particles, we have

$$\hat{P}H(\tau)\hat{P} \simeq \int d\mathbf{k}\;\epsilon(\mathbf{k},\tau)|\mathbf{k}\rangle\langle\mathbf{k}| \tag{1.21}$$

where $\epsilon(\mathbf{k},\tau) = \hbar^2k^2/2m - (\hbar q/mc)A(\tau)k_z + q^2A^2(\tau)/(2mc^2)$. Therefore, Eq. (1.20) describes the evolution of the free particle in the electromagnetic field (Volkov wave). With these definitions, the acceleration calculated in the standard SFA, Eq.(1.18), can be written as $a(t) = \int d\mathbf{k} a(\mathbf{k},t) + c.c.$ where

$$a(\mathbf{k},t) = -\frac{i}{\hbar}C_F \int_{t_0}^{t} dt_1 e^{i\epsilon_0(t-t_1)/\hbar} e^{-i\frac{1}{\hbar}\int_{t_1}^{t}\epsilon(\mathbf{k},\tau)d\tau} \langle\phi_0|\hat{a}|\mathbf{k}\rangle V_i(\mathbf{k},t_1)\langle\mathbf{k}|r^{-n}|\phi_0\rangle \tag{1.22}$$

At this point we can define the action as

$$S(\mathbf{k},t,t_1) = \int_{t_1}^{t} [\epsilon(\mathbf{k},\tau) - \epsilon_0]\, d\tau \tag{1.23}$$

so the acceleration can be written as

$$a(\mathbf{k},t) = -\frac{i}{\hbar}C_F \int_{t_0}^{t} dt_1 e^{-i\frac{1}{\hbar}S(\mathbf{k},t,t_1)} \langle\phi_0|\hat{a}|\mathbf{k}\rangle V_i(\mathbf{k},t_1)\langle\mathbf{k}|r^{-n}|\phi_0\rangle \tag{1.24}$$

Eq. (1.24) can be nicely interpreted as a sum of probability amplitudes of the following processes: (i) $V_i(\mathbf{k},t_1)\langle\mathbf{k}|r^{-n}|\phi_0\rangle$ corresponds to the electron's transition amplitude from the ground state to the continuum at a time t_1 with a momentum $\mathbf{k}$; (ii) the wavefunction propagates from t_1 to t in the continuum acquiring a phase factor $e^{-iS(\mathbf{k},t,t_1)/\hbar}$; and (iii), the electron recombines at t with the probability amplitude $\langle\phi_0|\hat{a}|\mathbf{k}\rangle$.

Finally, the time integral leading to $a(\mathbf{k})$ can be computed very effectively numerically by integrating the set of (uncoupled) one dimensional differential equations, each associated with a particular Volkov wave $\mathbf{k}$, that results from differentiating Eq. (1.22) [41]

$$\frac{d}{dt}a(\mathbf{k},t) = \frac{i}{\hbar}\left[\epsilon_0 - \epsilon(\mathbf{k},t)\right] a(\mathbf{k},t) - \frac{i}{\hbar}C_F\langle\phi_0|\hat{a}|\mathbf{k}\rangle V_i(\mathbf{k},t)\langle\mathbf{k}|r^{-n}|\phi_0\rangle \tag{1.25}$$

1.2.2 Saddle Point Analysis

Although Eq. (1.25) represents a computationally efficient method to compute the exact SFA dipole acceleration, the physical insight of the process remains hidden. Therefore, it is still of interest to resort to the semiclassical approach, based in the saddle-point approximation, developed by M. Lewenstein *et al.* [63]. From equation (1.24) the acceleration can be written as

$$a(t) = -\frac{i}{\hbar}C_F \int_{t_0}^{t} dt_1 \int d\mathbf{k} e^{-i\frac{1}{\hbar}S(\mathbf{k},t,t_1)} \eta(\mathbf{k},t_1) \tag{1.26}$$

where $\eta(\mathbf{k},t_1)=\langle\phi_0|\hat{a}|\mathbf{k}\rangle V_i(\mathbf{k},t_1)\langle\mathbf{k}|r^{-n}|\phi_0\rangle$ includes the ionization and recombination matrix elements. The harmonic spectrum is computed form the Fourier transform of Eq. (1.26),

$$a(\omega)=-\frac{i}{\hbar}C_F\int dt\int_{t_0}^{t}dt_1\int d\mathbf{k}e^{-i\frac{1}{\hbar}S(\mathbf{k},t,t_1)+i\omega t}\eta(\mathbf{k},t_1) \tag{1.27}$$

For computing the acceleration spectrum we have to integrate over three variables: (i) the momentum $\mathbf{k}$, in a three-dimensional space, (ii) the ionization time t_1, and (iii) the returning time t. First, we implement the saddle point approximation in the momentum integral. From Eq. (1.26), one can observe that the complex exponential of the action $S(\mathbf{k},t,t_1)$ oscillates much faster than $\eta(\mathbf{k},t_1)$. As a consequence, the relevant contributions to the momentum-space integral result from the neighborhood of the stationary points of the semiclassical action, i.e.

$$\nabla_{\mathbf{k}}S(\mathbf{k},t,t_1)=0 \tag{1.28}$$

The stationary momentum corresponds to $k_x^{st}=0$, $k_y^{st}=0$ and $k_z^{st}=\frac{q}{c\hbar(t-t_1)}\int_{t_1}^{t}A(\tau)d\tau$. As the velocity is given by $\mathbf{v}(\tau)=\hbar\mathbf{k}/m-qA(\tau)/(mc)$, Eq. (1.28) implies $\mathbf{r}(t)-\mathbf{r}(t_1)=0$, i.e., the stationary points of the semiclassical action correspond to those $\mathbf{k^{st}}$ in which the electron born at time t_1 returns to the same position at time t. We can now perform a Taylor expansion on the action around the stationary points, as

$$\begin{aligned}S(\mathbf{k},t,t_1) &\simeq S(\mathbf{k^{st}},t,t_1)+\frac{1}{2}\sum_{i\neq j}\frac{\partial S(\mathbf{k},t,t_1)}{\partial k_i k_j}\Big|_{st}(k_i-k_i^{st})(k_j-k_j^{st})+\\ &+\frac{1}{2}\sum_{i}\frac{\partial^2 S(\mathbf{k},t,t_1)}{\partial k_i^2}\Big|_{st}(k_i-k_i^{st})^2=\\ &=S(\mathbf{k^{st}},t,t_1)+\frac{\hbar^2}{2m}(t-t_1)\left[k_x^2+k_y^2+(k_z-k_z^{st})^2\right]\end{aligned} \tag{1.29}$$

and, approximating $\eta(\mathbf{k},t_1)\simeq\eta(\mathbf{k^{st}},t_1)$, the acceleration becomes

$$\begin{aligned}a(\omega) &= -\frac{i}{\hbar}C_F\int dt\int_{t_0}^{t}dt_1 e^{-i\frac{1}{\hbar}S(\mathbf{k^{st}},t,t_1)+i\omega t}\eta(\mathbf{k^{st}},t_1)\int d\mathbf{k}e^{-i\frac{\hbar}{2m}(t-t_1)\left[k_x^2+k_y^2+(k_z-k_z^{st})^2\right]}=\\ &= -\frac{i}{\hbar}C_F\int dt\int_{t_0}^{t}dt_1\left[\frac{2\pi m}{i\hbar(t-t_1)}\right]^{3/2}e^{-i\frac{1}{\hbar}S(\mathbf{k^{st}},t,t_1)+i\omega t}\eta(\mathbf{k^{st}},t_1)\end{aligned} \tag{1.30}$$

Applying the saddle-point approximation in the ionization time, i.e., $\partial S(\mathbf{k^{st}},t,t_1)/\partial t_1=0$, we find a stationary value for the ionization time

$$\epsilon(\mathbf{k^{st}},t_1^{st})=\epsilon_0\rightarrow\frac{1}{2m}\left[\hbar\mathbf{k^{st}}-\frac{q}{c}A(t_1^{st})\right]^2=-I_p \tag{1.31}$$

that means that the kinetic energy at the ionization time equals the energy of the bound state and, therefore, is negative (as $I_p = |\epsilon_0|$). If I_p is zero, the electron leaving the nucleus at time $t - t_1^{st}$ should have a velocity equal to zero (recovering the simple man's model of section 1.1.4). However, since $I_p \neq 0$, the initial velocity is imaginary, which expresses the fact that the atom can not be described classically. In addition, condition (1.31) leads also to a complex ionization time t_1^{st}. The imaginary part of t_1^{st} is interpreted as the time the electron needs to tunnel the Coulomb barrier [33], whereas the real part of t_1^{st} is interpreted as the ionization time in which the electron appears in the continuum. The difference between the semiclassical and classical pictures of tunneling has been recently confirmed experimentally [67]. Applying this second saddle point condition, the acceleration spectrum becomes

$$a(\omega) = -\frac{i}{\hbar} C_F \sum_j \int dt \left[\frac{2\pi m}{i\hbar(t - t_{1,j}^{st})}\right]^{3/2} e^{-i\frac{1}{\hbar}S(\mathbf{k^{st}}, t, t_{1,j}^{st}) + i\omega t} \eta(\mathbf{k^{st}}, t_{1,j}^{st}) \tag{1.32}$$

where we sum over the ionization times that fulfills condition (1.31). Finally, we can perform the saddle-point approximation for the returning time t, i.e.

$$\frac{\partial S(\mathbf{k^{st}}, t, t_1^{st}) - \hbar\omega t}{\partial t} = 0 \rightarrow \epsilon(\mathbf{k^{st}}, t^{st}) = \hbar\omega - \epsilon_0 \tag{1.33}$$

This latter equation express the energy conservation law at the time of recombination, where the energy of the emitted photon corresponds to the kinetic energy of the recolliding electron plus the ionization potential $I_p = |\epsilon_0|$. As a conclusion, the saddle-point approximation method recovers the classical description of HHG (see section 1.1.4), except that takes into account the tunneling process and its influence on the electron kinetic energy at the moment of recombination.

Semiclassical Analysis. Trajectories and phase of the harmonics

The first condition derived from the saddle-point approximation (1.28) implies that an electron ionized at time t_1 returns to the same position at time t. In principle, the electron can be ionized at any position as long as the ground-state wavefunction has not negligible probability. However, the acceleration at rescattering is maximum at the nucleus position. As a consequence, to a good approximation, the saddle point condition represents trajectories born in the nucleus position, that return to the same position to emit a photon, i.e. closed loops.

On the other hand, condition (1.33) imposes a limit to the energy of the emitted harmonic. Classically, the maximum kinetic energy of the closed-loop trajectories is $3.17U_p$, thus (1.33) contains the empirical cut-off formula (4.1). However, the definition of a complex ionization time leads to a correction:

$$\hbar\omega_{max} = I_p F(I_p/U_p) + 3.17U_p. \tag{1.34}$$

where $F(I_p/U_p)$ is a function that takes values in the range between 1.32 and 1.24 [63].

The saddle approximation gives a nice physical interpretation of the HHG process in terms of semiclassical trajectories. As it was shown in section 1.1.4, in each half cycle of the laser pulse there are two electron trajectories leading to the same kinetic energy at recollision, named as *short* and *long* trajectories, accordingly to their excursion time. Eq. (1.32) implies that the phase associated to each trajectory contribution generating an harmonic q is given by the semiclassical action acquired during the excursion time, i.e.,

$$\phi_q^i = \frac{1}{\hbar} S(\mathbf{k}^{\mathbf{st,i}}, t^{st,i}, t_1^{st,i}) + \omega t^{st,i} \tag{1.35}$$

This phase can be approximated by the product of the ponderomotive energy U_p (i.e. the mean energy of the free electron in the oscillating field) and the excursion time $\tau_q^i = t^{st,i} - t_1^{st,i}$, as

$$\phi_q^i \simeq -\frac{1}{\hbar} U_p \tau_q^i = -\alpha_q^i I \tag{1.36}$$

The factor α_q^i is proportional to the excursion time, so it is larger for long (L) trajectories than for the short (S) ones ($\alpha_q^L > \alpha_q^S$) [64]. Since the quantum orbit phase is translated to the harmonic radiation, the final harmonic emission reflects the interference between the contributions of the short and long trajectories [68, 69].

Let us now concentrate on the spectral properties of the harmonic emission, separating the contributions from short and long trajectories. As the phase of the harmonics depends on the laser pulse intensity I, there is an intrinsic chirp in the harmonic emission due to the time-dependent intensity over the laser pulse envelope [70]. The contribution of a single trajectory to the time-dependent acceleration is given by

$$a(t) = \int a(\omega) e^{-i\omega t} d\omega = \int |a(\omega)| e^{i\phi(\omega, t^{st})} e^{-i\omega t} d\omega \tag{1.37}$$

therefore, the instantaneous frequency of the harmonic is given as

$$\omega(t) = \frac{\partial}{\partial t}\left[\omega t - \phi(\omega, t^{st})\right] \simeq \omega + \alpha(\omega)\frac{\partial I}{\partial t} \tag{1.38}$$

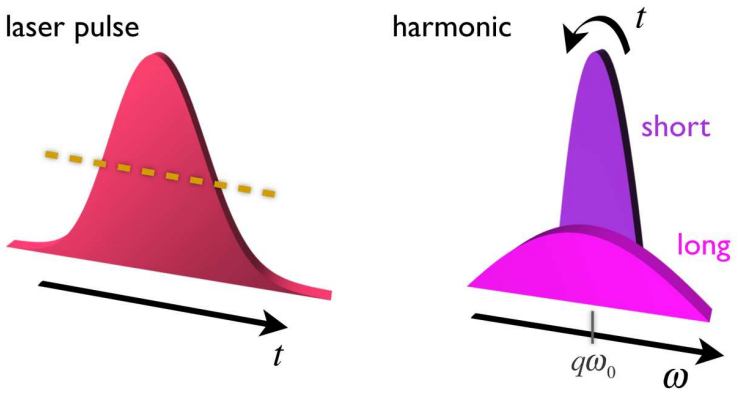

Figure 1.8: Scheme of the chirp induced on the harmonic emission peak. The region over the dashed line of the driving pulse has enough intensity to generate the qth-order harmonic, first the higher frequencies and later the lower ones. The long trajectory distribution is wider than the short one.

Hence the harmonics are generated with a temporal chirp, that depends on the temporal distribution of the laser pulse intensity, and the particular path followed by the rescattered electron. For instance, considering the harmonic peak with frequency $q\omega_0$, the higher frequencies are generated in the first place, during the leading part of the pulse, whereas lower frequencies are generated at the pulse tail (see scheme in Fig. 1.8). This chirp, intrinsic to the harmonic peak, is different to the atto-chirp described in section 1.1.5, that results from the relative phase of consecutive harmonics, also referred as extrinsic phase [52].

From Eq. (1.38) we observe that the short-trajectory contribution is dominant near the central part of the harmonic peak, whereas the long contribution spreads over a wider spectral window, as $\alpha_q^L > \alpha_q^S$. As a result, short trajectories induce a smaller intrinsic chirp (narrow harmonic spectrum) whereas long trajectories causes a larger intrinsic chirp (wider harmonic spectrum) [71, 72]. In addition, we already know that the efficiency of the short paths is higher than the long ones, as the dipole acceleration is inversely proportional to the excursion time –see Eq. (1.32)–. Those two features lead to the spectral distributions shown schematically in Fig. 1.8. The chirp in the harmonic emission was firstly observed by Bellini *et al.* [73] by measuring the coherence time of the harmonics. To measure the coherence time is equivalent to determine the spectral width of the harmonics, since it is inversely proportional to the bandwidth.

1.3 Computing high-order harmonic generation within the SFA+

The standard model in which SFA is combined with a saddle point method [63] succeeds in predicting the mode locking of the highest order harmonics, chirps and modulation of the yields with the intensity [69]. However, despite of these achievements, studies on the scaling of the harmonic yield with wavelength point out departures between the predictions of this model and the exact TDSE [40, 74, 75]. It was recently shown that, for the quantitative improvement of the model predictions, the standard SFA has to be relaxed to incorporate the field-induced dynamics on the ground state, at least during the rescattering event [41, 76]. This approach has been developed in our group, an we refer it as SFA+. In addition to include some part of the ground-state dressing, SFA+ does not resort to the saddle-point approximation, therefore including the full quantum description of the high-order harmonic generation process.

The extension developed in the SFA+, consists on taking into account $\hat{Q}V_i(t')\hat{Q} \neq 0$ in Eq. (1.13) [41], including the possibility of atomic bound-state excitations, thus softening the constraints of standard SFA. As a consequence, the acceleration is given by

$$a(t) \simeq \langle\psi(t)|\hat{Q}\hat{a}\hat{P}|\psi(t)\rangle + c.c. = a_b(t) + a_d(t) + c.c. \tag{1.39}$$

where a_b and a_d are two interfering contributions to the total acceleration, associated with transitions between the continuum to the bare ground state or to its field-dressing (not considered in the standard SFA). Respectively [41],

$$a_b(t) = \frac{1}{\hbar}\int_{t_0}^{t} dt_1 \langle\phi_0|G_a^-(t_0,t)\hat{a}\hat{P}G^+(t,t_1)\hat{P}V_i(t_1)\hat{Q}G_a^+(t_1,t_0)|\phi_0\rangle \tag{1.40}$$

$$a_d(t) = \frac{1}{\hbar^2}\int_{t_0}^{t} dt_2 \langle\phi_0|G_a^-(t_0,t_2)\hat{Q}V_i(t_2)\hat{Q}G^-(t_2,t)\hat{Q}\hat{a}\times \int_{t_0}^{t_2} dt_1 \hat{P}G^+(t,t_1)\hat{P}V_i(t_1)\hat{Q}G_a^+(t_1,t_0)|\phi_0\rangle \tag{1.41}$$

The operators $\hat{P}V_i(t_1)\hat{Q}$ and $\hat{P}G^+(t,t_1)\hat{P}$, were already described in section 1.2.1, so $a_b(t)$ corresponds to the dipole acceleration computed in the standard SFA, and can be written as $a_b(t) = \int d\mathbf{k} a_b(\mathbf{k},t)$ where $a_b(\mathbf{k},t)$ is given by Eq. (1.22).

The evaluation of the operators of the field-dressing part, $\hat{Q}V_i(t_2)\hat{Q}$ and $\hat{Q}G^-(t,t_2)\hat{Q}$, is not straightforward in the general case. However, some simplifications arise for the

particular study of high-order harmonic generation. High-order harmonics are generated from the transitions from continuum to bound states that take place during the process of rescattering of the ionized electron with the parent ion. Instead of assuming this process as instantaneous, let us consider that the harmonic generation at time t is triggered by the collision of the ionized electron taking place over the small time interval, $t-\delta t_s$ to t. Assuming the bound state wavefunction to be the ground state at the beginning of this interval, Eq. (1.13) predicts its evolution during the temporal lapse of rescattering, by setting the the lower limit t_0 of the time integral to the initial time before rescattering $t-\delta t_s$,

$$\begin{aligned} -i\hat{Q}|\psi(t)\rangle &\simeq G_a^+(t,t_0)|\phi_0\rangle \\ &+ \frac{1}{\hbar}\int_{t-\delta t_s}^{t} dt'\hat{Q}G^+(t,t')\hat{Q}V_i(t')\hat{Q}\; G_a^+(t',t_0))|\phi_0\rangle \end{aligned} \tag{1.42}$$

and

$$\begin{aligned} a_d(t) &\simeq \frac{1}{\hbar^2}\int_{t-\delta t_s}^{t} dt_2\langle\phi_0|G_a^-(t_0,t_2)\hat{Q}V_i(t_2)\hat{Q}G^-(t_2,t)\hat{Q}\hat{a}\times \\ &\int_{t_0}^{t_2} dt_1\hat{P}G^+(t,t_1)\hat{P}V_i(t_1)\hat{Q}G_a^+(t_1,t_0)|\phi_0\rangle \end{aligned} \tag{1.43}$$

The dynamics of the bound excitations during the time lapse δt_s is given by the operator $\hat{Q}G^-(t_2,t)\hat{Q}$ which is, in turn, a function of the total Hamiltonian $H(t)=H_a+V_i(t)$. The rescattering event is defined by the overlap of the free electron wavefunction with the coordinate origin, where the potential singularity is located. With this definition, dividing the spatial width of the expanded wavepacket by its rescattering velocity, the scattering time lapse for the most energetic electrons can be evaluated as [41]

$$\delta t_s \simeq (3\pi/2\omega_0)\sqrt{|\epsilon_0|/3.17U_p} \tag{1.44}$$

where U_p is the ponderomotive energy. For large U_p, this time lapse is small enough to approximate the time-dependent operator $V_i(t)$ in Eqs. (1.42) and (1.43) by its time average over δt_s

$$\Delta_s = \langle V_i(t)\rangle = (1/\delta t_s)\int_{t-\delta t_s}^{t}\left[-(q\hbar/mc)A(\tau)k_z + (q^2/2mc^2)A^2(\tau)\right]d\tau \tag{1.45}$$

where k_z is a relevant momentum of the state, than can be evaluated as [41]

$$k_z = -\frac{2}{\hbar}\sqrt{mU_p}\frac{\sin\omega_0\delta t_s}{\omega_0\delta t_s}\left[1-\sqrt{1-\frac{1}{6}\left(1+\frac{\epsilon_0}{U_p}+\frac{\sin 2\omega_0\delta t_s}{2\omega_0\delta t_s}\right)\left(\frac{\sin\omega_0\delta t_s}{\omega_0\delta t_s}\right)^{-2}}\right] \tag{1.46}$$

Therefore $\hat{Q}G^{-}(t_2,t)\hat{Q}$ can be approximated by $i\exp\left[i(\epsilon_0+\Delta_s)(t-t_2)\right]$, where we assume that the mean energy of the ground state after interacting with $\hat{Q}V_i(t_2)\hat{Q}$ is $\simeq\epsilon_0$. On the other hand, one should look also for a simplified form of the interaction operator $\hat{Q}V_i(t_2)\hat{Q}$. A first choice would be to replace it by the time-averaged form Δ_s, but it proves not to be a sufficiently accurate approximation. We shall, therefore, consider the factorization $V_i(t)=H(t)-H_a\simeq p^2/2m+\Delta_s-H_a$. The Coulomb term in $H(t)$ is neglected as we assume the ground-state excitations to have minimal probability near the origin (which is a reasonable assumption for a p state). With these approximations, and after some algebra [41], the dressing contribution to the acceleration can be written in terms of the bare acceleration as

$$a_d(\mathbf{k},t)\simeq-\left[1+\frac{k^2/2m-\epsilon_0}{\Delta_s}\right]a_b(\mathbf{k},t) \tag{1.47}$$

Therefore the total acceleration is given by

$$a(t)=-\int d\mathbf{k}\frac{\hbar^2k^2/2m-\epsilon_0}{\Delta_s}a_b(\mathbf{k},t)+c.c. \tag{1.48}$$

Note that the opposite sign of a_d relative to a_b, see Eq. (1.47), leads to the destructive interference between the bare and dressing contributions to the acceleration. This is a main result of the SFA+ approach, as the standard SFA considers only the bare contribution, a_b. The degree of interference changes with the laser parameters and affects the harmonic yield. In particular, through this interference, SFA+ gives a proper account of the scaling of the harmonic intensities with the laser wavelength [41].

Since the time integral leading to the standard SFA acceleration, $a_b(\mathbf{k})$, can be computed by integrating the set of (uncoupled) one dimensional differential equations –see Eq. (1.25)–, there is not an additional computation difficulty in evaluating the SFA+ acceleration (1.48).

In order to gain insight on the validity of SFA+, we show in Fig. 1.9 –extracted from [76]– the results for the computations of the harmonic spectra in hydrogen for three different laser parameters. The plots in the figure correspond to the direct outcome from the Fourier transform of the dipole acceleration, i.e. no relative shift or scalings have been used. The result of the exact computation of the 3D TDSE is plotted using blue lines, while the result of the SFA+ computation is plotted using filled green areas, and the orange line corresponds to the computation in the SFA approach, i.e. not including ground-state dressing, $a_d(t)$. We recall that here the SFA computations are

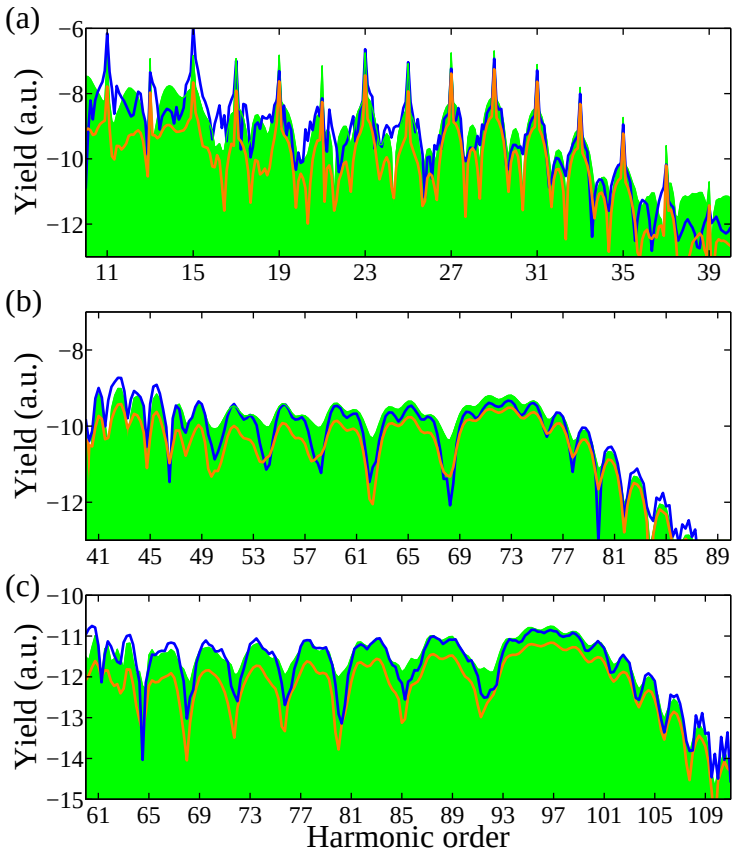

Figure 1.9: Comparison of the harmonic spectra computed from the exact numerical integration of the TDSE (blue line), the SFA model (orange line) and SFA+ model (green filled area) for different laser parameters: **a** 9 cycle pulse of trapezoidal shape, with half period turn-on and turn-off and constant intensity in between, with intensity $\simeq 1.58 \times 10^{14}$ W/cm^2 and wavelength 800 nm, **b** 4 cycle full temporal length (1.4 cycles FQHM) sin^2 envelope with intensity $\simeq 1.58 \times 10^{14}$ W/cm^2 and wavelength 1.2 μm, and **c** 4 cycle full temporal length sin^2 envelope (1.4 cycles FWHM) with intensity $\simeq 9 \times 10^{13}$ W/cm^2 and wavelength 1.6 μm. Figure extracted from [76].

carried on using Eq. (1.25), i.e. also without resort to the saddle point method. The field intensities are changed from 1.58×10^{14} W/cm^2 in part (a) and (b) to 9×10^{13} in (c), wavelengths correspond to (a) 800 nm, (b) 1.2 μm and (c) 1.6 μm, the field envelopes are 9 cycle trapezoidal (half -cycle turn-on and turn-off) in (a) and 4-cycle full temporal length sine squared in (b) and (c). More comparisons including, for instance, carrier-envelope phase offsets are found in [41, 77, 78]. As a general trend, the SFA+ method offers a more accurate description of the high-order harmonic plateau than the SFA, and for a wider frequency interval. For the longer pulses (Fig. 1.9a), the effect of ionization shows up, and the SFA+ model gives harmonic yields slightly higher than the TDSE.

We may notice that both models, SFA and SFA+, become progressively inaccurate for the lowest harmonics. These correspond to low-energy transitions, involving excited states in the atom, and are not fully accounted into the dressing term of SFA+, while are ruled out completely in the standard SFA. A rough estimation is to consider the law $|\epsilon| + 3.17U_p$ valid also for the maximum frequency reachable from excited states. In such case, the influence of the excited states extends in the harmonic spectrum up to a maximum energy $|\epsilon_0| - |\epsilon|$ below the cut-off frequency, being ϵ the energy of the lowest excited state. Therefore, one can consider that the frequency window extending $|\epsilon_0| - |\epsilon|$ below the cut-off is produced solely by the transitions involving the ground state, and, therefore, will be properly addressed by SFA and SFA+. For the case of hydrogen, this window is of about 10 eV. Therefore, for the 800nm case of Fig. 1.9a, this defines a region window of validity for the SFA and SFA+ approaches from the cut-off at the 29th harmonic, down to the 23th harmonic. The figure seems to corroborate this discussion, as the description of the harmonic spectrum by the SFA+ model in this window is excellent. We shall note, also, that the estimation of this window is quite conservative, as the model description can be accurate in a wider spectral region if the population of the excited states is small, for instance for longer wavelengths (Figs. 1.9b and 1.9c).

The results presented here were obtained in hydrogen. Along this thesis we will perform SFA+ also in argon, xenon and helium. For that purpose, we will perform our simulations in the single-electron approximation using the Roothaan-Hartree-Fock wavefunction [79] for the ionization and rescattering matrix elements for each gas component. The acceleration operator for hydrogen in Eq. (1.48) will be replaced ac-

cordingly with the gradient of the Coulomb potential of the corresponding element ion [80].

1.3.1 Transversal saddle-point approximation

In order to speed up the calculations of the single-atom high-order harmonic generation by linearly polarized fields, we combine the SFA+ and saddle point approaches by implementing a saddle-point approach in the momentum space plane, *transversal* to the field polarization [81]. With this we shall increase the computational time, while still keeping a full quantum description along the polarization axis, where the relevant dynamics takes place. To this aim we use Eq. (1.26), and turning into cylindrical coordinates and exploiting the symmetry around the polarization axis, the acceleration can written as

$$a_b(t) = -\frac{i}{\hbar} C_F \int_{t_0}^{t} dt_1 \int\int 2\pi k_\rho dk_\rho dk_z e^{-i\frac{1}{\hbar}S(\mathbf{k},t,t_1)} \eta(\mathbf{k},t_1) \tag{1.49}$$

Now we implement the saddle point approximation in the transversal momentum, k_ρ, i.e. $\nabla_{k_\rho} S(\mathbf{k},t,t_1) = 0$, that corresponds to $k_\rho^{st} = 0$. The Taylor expansion on the action around the stationary points, gives

$$S(\mathbf{k},t,t_1) \simeq S(k_z,k_\rho^{st},t,t_1) + \frac{\hbar^2}{2m}(t-t_1)k_\rho^2 \tag{1.50}$$

Therefore the acceleration can be approximated as

$$\begin{aligned} a_b(t) &= -\frac{i}{\hbar} 2\pi C_F \int_{t_0}^{t} dt_1 \int dk_z e^{-i\frac{1}{\hbar}S(k_z,k_\rho^{st},t,t_1)} \eta(k_z,k_\rho^{st},t_1) \int k_\rho dk_\rho e^{-i\frac{\hbar}{2m}(t-t_1)k_\rho^2} = \\ &= -\frac{2\pi m C_F}{\hbar^2(t-t_1)} \int_{t_0}^{t} dt_1 \int dk_z e^{-i\frac{1}{\hbar}S(k_z,0,t,t_1)} \end{aligned} \tag{1.51}$$

since

$$\int k_\rho dk_\rho e^{-i\frac{\hbar}{2m}(t-t_1)k_\rho^2} = \frac{m}{i\hbar(t-t_1)} \tag{1.52}$$

We now take as an approximation for the excursion time $t - t_1 \simeq 0.63T$, where T is the laser period. As it was shown in Fig. 1.5, this is valid for the harmonics in the cut-off region. The acceleration is therefore written as,

$$a_b(t) \simeq -\frac{\pi m C_F}{\hbar^2 0.63T} \int_{t_0}^{t} dt_1 \int dk_z e^{-i\frac{1}{\hbar}S(k_z,k_\rho^{st},t,t_1)} \tag{1.53}$$

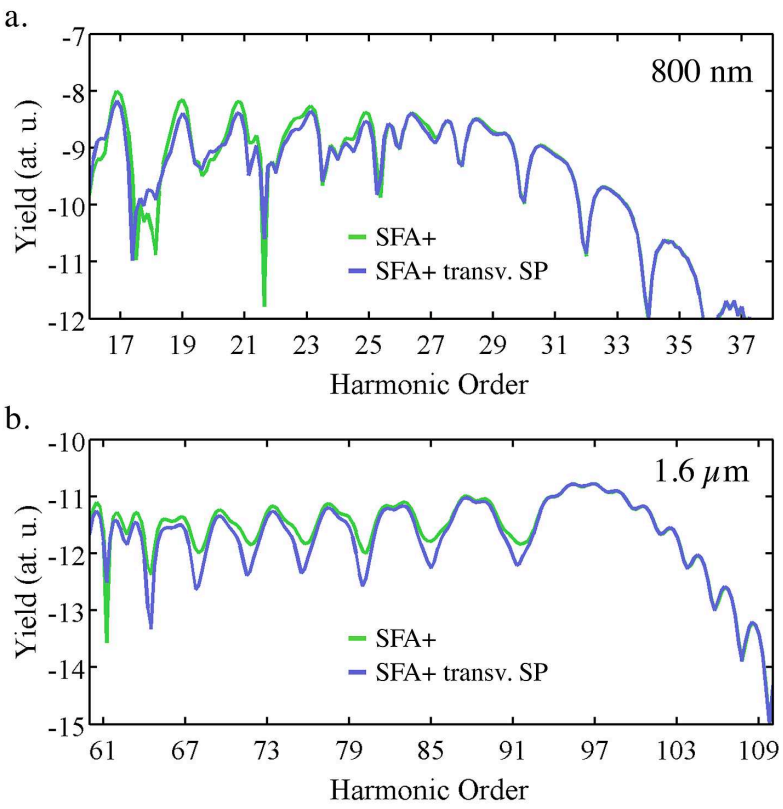

Figure 1.10: Comparison of the harmonic spectra computed from the SFA+ model (green line), and the SFA+ model combined with the transversal saddle point approximation (blue line) for different laser parameters: **a** 8 cycle full temporal length $\sin^2$ envelope (2.9 cycles FWHM) with intensity $\simeq 1.58 \times 10^{14}$ W/cm^2 and wavelength 800 nm, and **b** 4 cycle full temporal length $\sin^2$ envelope (1.4 cycles FWHM) with intensity $\simeq 8.75 \times 10^{13}$ W/cm^2 and wavelength 1.6 μm.

As a result, implementing the saddle point approximation in the transversal plane we transform the three-dimensional integral in the momentum space in one-dimensional, thus reducing the computational time. In Fig. 1.10 we show the harmonic spectra in hydrogen for two different laser parameters, comparing the result of the SFA+ computation (green line), and the combination of the SFA+ with the saddle point approximation in the transversal plane (blue line), where $a_b(t)$ is computed using Eq. (1.53). In Fig. 1.10a the laser pulse is modeled as a $\sin^2$ function, 8 cycles full temporal length (2.9 cycles FWHM), 800 nm and peak intensity 1.58×10^{14} W/cm^2, whereas in Fig. 1.10b the laser pulse is 4 cycles full temporal length (1.4 cycles FWHM), 1.6 μm, and peak intensity 8.75×10^{13} W/cm^2. As a general trend, the saddle point approximation in the transversal plane is in good agreement with the complete SFA+ theory, being perfectly matched in the cut-off region.

1.3.2 Time-frequency analysis

One of the most interesting deliverables of the saddle point analysis is its nice interpretation of HHG in terms of semiclassical trajectories. It is very useful to know when the electron is ionized and when recollides in order to control the HHG process as well as to understand how the attosecond pulses are obtained. Unfortunately, this classical interpretation is missed when considering the full quantum description of HHG, as given by the SFA+ or the TDSE. However, it is still possible to have some insight from these calculations, using a time-frequency analysis (TFA).

In the TFA, we select an spectral window in the harmonic spectrum and take its Fourier transform. By shifting the window to cover all the harmonic spectrum, it is possible to resolve the time in which the different harmonics are generated. Nevertheless, due to the uncertainity principle, we have to be careful when interpreting the results of the TFA, as the width of the spectral window determines the resolution in time: the narrower the spectral window is, the less resolution we obtain in the temporal domain.

In Fig. 1.11 we present the time-frequency analysis for the HHG spectrum driven by a 1.3 cycles FWHM, 800 nm laser pulse, which corresponds to the same case as shown in Fig. 1.7. We consider a gaussian spectral window whose FWHM is $3\omega_0$ (see blue dashed line in plot 1.11b). In the TFA (1.11c) we can identify when is generated each harmonic. For instance, it allows to identify the harmonics generated by the

short (positive slope) and the long (negative slope) trajectory contributions. In figure 1.11c we have plotted in black dots the recollision energies of the classical trajectories obtained from Eq. (1.8), using the condition (4.1), with the correction to the ionization potential given in (1.34), with $F(I_p/U_p) = 1.28$. We see that the TFA is in excellent agreement with the classical predictions for the rescattering energy of the electronic trajectories.

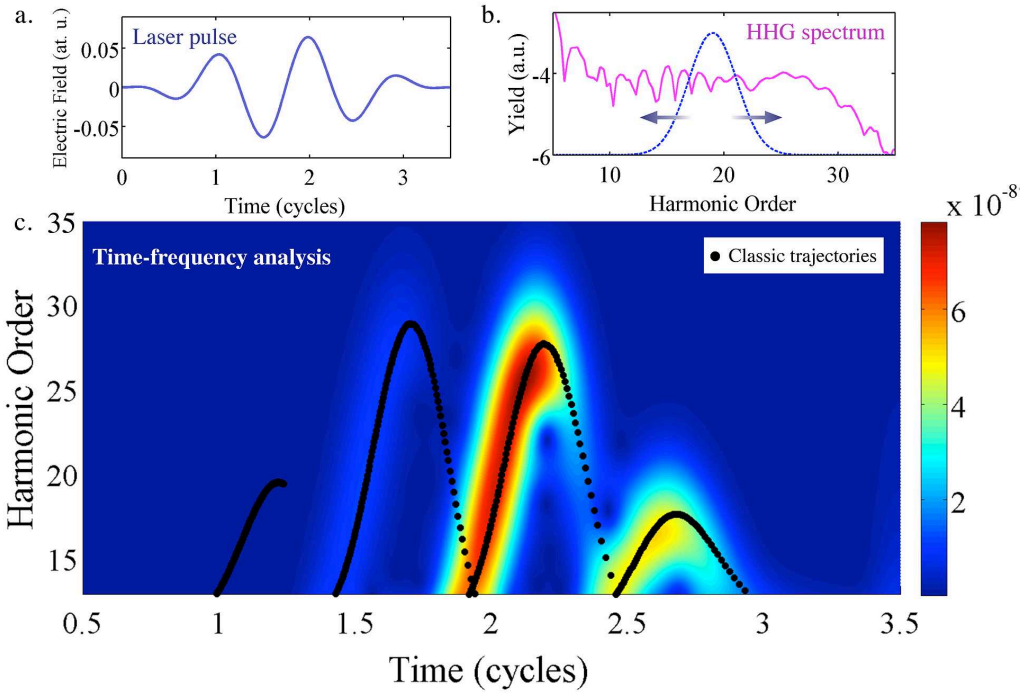

Figure 1.11: Time-frequency analysis for the HHG spectrum showed in **b** driven by the laser pulse of panel **a**, 800 nm in wavelength, 1.3 cycles FWHM (3.4 fs FWHM) and of peak intensity 1.57×10^{14} W/cm^2. We consider a Gaussian spectral window whose FWHM is $3\omega_0$ (see blue dashed line in **b**). In the time-frequency analysis, **c**, the black dots represent the classical trajectories given by (1.34), with $F(I_p/U_p) = 1.28$.

We can also observe in Fig. 1.11 that the efficiency of the harmonic generation via shorter paths is greater than via longer paths. This is in agreement with the exact solution of the TDSE [78] and is interpreted in terms of the spreading of the wavefunction of the recoiling electron, which is greater for the longer trajectories. For the sake of clarity we present in Fig. 1.12 the time-frequency analysis for the HHG spectrum

driven by a 5.8 cycles FWHM, 800 nm laser pulse, which corresponds to the same case as shown in Fig. 1.6. Again, the agreement between the classical trajectories –for the exact cut-off law (1.34), with $F(I_p/U_p) = 1.28$– and the TFA is excellent.

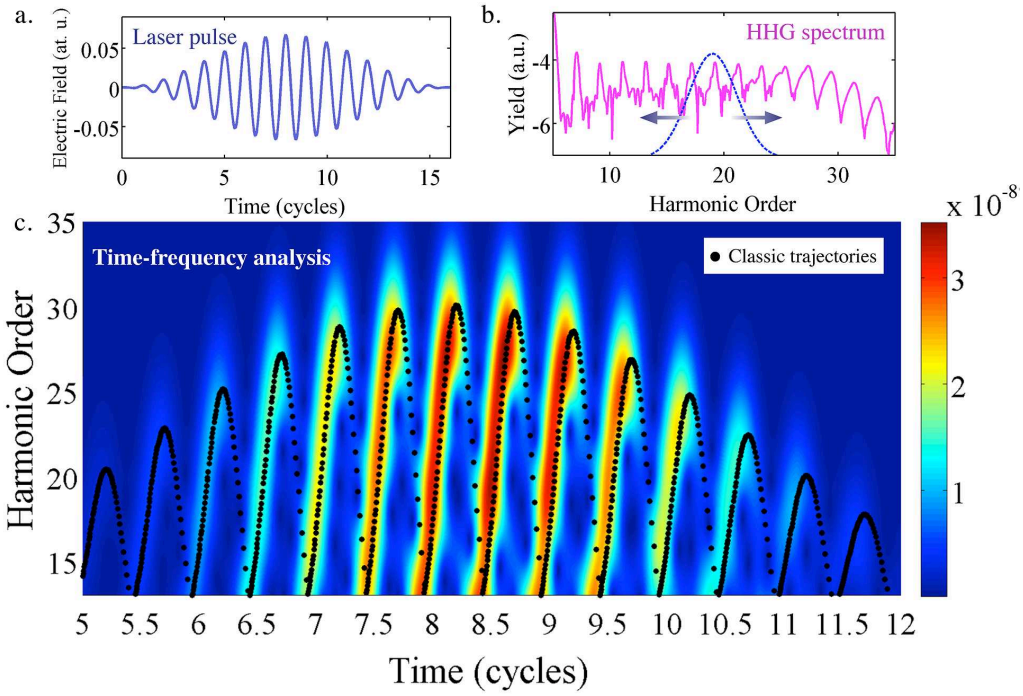

Figure 1.12: Time-frequency analysis for the HHG spectrum showed in **b** driven by the laser pulse of panel **a**, 800 nm in wavelength, 5.8 cycles FWHM (15.5 fs FWHM) and of peak intensity 1.57×10^{14} W/cm^2. We consider a gaussian spectral window whose FWHM is $3\omega_0$ (see blue dashed line in **b**). In the time-frequency analysis, **c**, the black dots represent the classical trajectories given by (1.34), with $F(I_p/U_p) = 1.28$.

1. HIGH-ORDER HARMONIC AND ATTOSECOND PULSE GENERATION

2

Computing high-order harmonic propagation

The aim of this chapter is to establish the connection between the harmonic radiation emitted from a single atom and the emission of a macroscopic sample. The appropriate description of experiments involving high-order harmonic generation (HHG) has to include a faithful reproduction not only of the single radiator (atom or molecule) spectrum but also of the propagation of the harmonics in the medium and its far field distribution at the detectors. The fundamental aspects of the computations of high-order harmonic propagation were discussed by Anne L'Huillier *et al.* in two seminal articles [82, 83].

From the fundamental viewpoint, the harmonic radiation emitted by a macroscopic target corresponds to the coherent addition of the elementary contributions of every atom or molecule in the sample. For a number of reasons that we will see in this chapter, this coherent addition is not generally optimal, since the phases of the elementary radiators are not matched. This limitation was recognized very early, theoretically [84] and experimentally [70, 85], as a fundamental issue limiting the efficiency of HHG from macroscopic samples. On the other hand phase-matching is shown to depend on the different parameters of the experiment (including atomic species, beam shape, target configuration, etc.), consequently offering several degrees of freedom for the optimization of the harmonic yield.

Theoretically, the computation of HHG from macroscopic targets is a formidable task due to the disparity of the scales involved (few tens of nanometers for the shorter

harmonic wavelengths and propagation distances up to few millimeters). In the previous chapter, we presented some efficient methods, available in our group, to compute the harmonic radiation from an isolated atom. In this chapter we shall present a new method for the computation of the high-order harmonic propagation in rare gases.

We have divided this chapter in five sections. First of all, we will briefly deduce the wave equations for the radiation electromagnetic field from the Maxwell's equations. Following, in section 2.2, we will review the relevant aspects of field propagation in linear media, introducing the Gaussian beam. In section 2.3, we will study the case of non-linear media, on one hand analyzing the different contributions to phase-matching, geometrical and intrinsic, and, on the other hand, the effect of ionization (free charges and neutral-atom depletion) in the propagation of the fundamental field. We shall also review the conditions for optimal phase-matching, and the experimental set-up developed at JILA, University of Colorado. In section 2.4, we will introduce our original method for computing high-order harmonic propagation, based on the wave equation propagator. Finally, in section 2.5 we will introduce the Discrete Dipole Approximation, that we use to speed up the computations, and analyze the convergence of this approach.

2.1 Wave equations for the transversal electromagnetic field

Let us begin considering the Maxwell's equations

$$\nabla \times \mathbf{E} = -\frac{1}{c}\frac{\partial}{\partial t}\mathbf{H} \tag{2.1a}$$

$$\nabla \times \mathbf{H} = \frac{4\pi}{c}\mathbf{J} + \frac{1}{c}\frac{\partial}{\partial t}\mathbf{E} \tag{2.1b}$$

$$\nabla \cdot \mathbf{E} = 4\pi\rho \tag{2.1c}$$

$$\nabla \cdot \mathbf{H} = 0 \tag{2.1d}$$

where $\mathbf{E}$ is the electric field, $\mathbf{H}$ the magnetic field, c is the speed of light, and ρ is the charge density. Without any loose in accuracy, we can decompose the fields in a transversal ($\perp$) and a longitudinal ($||$) component ($\mathbf{E} = \mathbf{E}_\perp + \mathbf{E}_{||}$), satisfying $\nabla \times \mathbf{E}_{||} = 0$ and $\nabla \cdot \mathbf{E}_\perp = 0$. With this factorization, we obtain the following Maxwell's equations

for the longitudinal field,

$$\nabla \cdot \mathbf{E}_{||} = 4\pi\rho \tag{2.2a}$$

$$\nabla \cdot \mathbf{H}_{||} = 0 \tag{2.2b}$$

$$\nabla \times \mathbf{H}_{||} = \frac{4\pi}{c}\mathbf{J}_{||} + \frac{1}{c}\frac{\partial}{\partial t}\mathbf{E}_{||} \tag{2.2c}$$

Performing the temporal derivative of $\nabla \cdot \mathbf{E}_{||}$ and taking into account that $\nabla \times \mathbf{H}_{||} = 0$, Eqs. (2.2a) and (2.2c) lead to the charge continuity equation

$$\frac{\partial \rho}{\partial t} + \nabla \cdot \mathbf{J}_{||} = 0 \tag{2.3}$$

Therefore the longitudinal part describes the Coulomb, non radiative, field. On the other hand, the Maxwell's equations for the transverse components read as

$$\nabla \times \mathbf{E}_{\perp} = -\frac{1}{c}\frac{\partial}{\partial t}\mathbf{H}_{\perp} \tag{2.4a}$$

$$\nabla \times \mathbf{H}_{\perp} = \frac{4\pi}{c}\mathbf{J}_{\perp} + \frac{1}{c}\frac{\partial}{\partial t}\mathbf{E}_{\perp} \tag{2.4b}$$

Now, applying the rotational to $\nabla \times \mathbf{E}_{\perp}$, and taking into account the identity $\nabla \times (\nabla \times \mathbf{E}_{\perp}) = \nabla(\nabla \cdot \mathbf{E}_{\perp}) - \nabla^2 \cdot \mathbf{E}_{\perp}$, one can obtain the wave equation for the transversal electric field

$$\nabla^2 \mathbf{E}_{\perp}(\mathbf{r}, t) - \frac{1}{c^2}\frac{\partial}{\partial t^2}\mathbf{E}_{\perp}(\mathbf{r}, t) = \frac{4\pi}{c^2}\frac{\partial}{\partial t}\mathbf{J}_{\perp}(\mathbf{r}, t) \tag{2.5}$$

The general problem of radiation propagation amounts to solve this wave equation for the transversal electric field. From its structure we can see that the source of the electromagnetic field is given by the temporal derivative of the current density, $\mathbf{J} = \mathbf{J}_b + \mathbf{J}_f$, where the subindex b and f stand for *bound* and *free* charges respectively. Traditionally, bound charges are not considered as current generators, but as *polarizers* of the medium. Therefore, it is common to express the bound charge current density using the medium polarizability, $\mathbf{P}$, as $\mathbf{J}_b = \frac{\partial}{\partial t}\mathbf{P}$, so we can rewrite 2.5 as

$$\nabla^2 \mathbf{E}_{\perp}(\mathbf{r}, t) - \frac{1}{c^2}\frac{\partial}{\partial t^2}\mathbf{E}_{\perp}(\mathbf{r}, t) = \frac{4\pi}{c^2}\frac{\partial}{\partial t}\mathbf{J}_{\perp,f}(\mathbf{r}, t) + \frac{4\pi}{c^2}\frac{\partial^2}{\partial t^2}\mathbf{P}_{\perp}(\mathbf{r}, t) \tag{2.6}$$

2.2 Propagation in linear media

In this section we will review some fundamental aspects of propagation in linear media. In first place, we shall focus to the monochromatic case, introducing the empirical formulae for the refractive index, that we will be employed later in our computations. Also we shall introduce the Gaussian beam as a particular solution of the wave equation representing a focused beam.

2.2.1 Monochromatic propagation in linear media

Let us now consider $\mathbf{E}(\mathbf{r},t)$ as a linear polarized monochromatic field with a period $2\pi/\omega$. The response of the neutral media to a monochromatic wave is characterized by the susceptibility $\chi(\omega)$,

$$\mathbf{P}(\mathbf{r},t) = \chi(\omega)\mathbf{E}(\mathbf{r},t) \tag{2.7}$$

On the other hand, the response of the free charges is characterized by the conductivity $\sigma(\omega)$, which in the case of linear optics corresponds to

$$\mathbf{J}_f(\mathbf{r},t) = \sigma(\omega)\mathbf{E}(\mathbf{r},t) \tag{2.8}$$

Fourier transforming Eq. (2.6) we find

$$\nabla^2\mathbf{E}(\mathbf{r},t) + \frac{\omega^2}{c^2}n_r^2(\omega)\mathbf{E}(\mathbf{r},t) = 0 \tag{2.9}$$

where we have defined the refractive index, $n_r(\omega)$, as

$$n_r^2(\omega) = 1 + 4\pi\left[\chi(\omega) + i\frac{\sigma(\omega)}{\omega}\right] \tag{2.10}$$

This quantity encloses all the information about the linear response of the medium to the electromagnetic field. The dependence of the refractive index with the frequency is the defining characteristic of a dispersive medium, in which monochromatic waves of different frequencies travel with different velocities. In the case of this study, where we consider gas targets, we can approximate the refractive index as

$$n_r(\omega) \simeq 1 + 2\pi\left[\chi(\omega) + i\frac{\sigma(\omega)}{\omega}\right] \tag{2.11}$$

Assuming the bound electrons as harmonic oscillators, and the free charges as evolving only under the influence of the electromagnetic field, we can write the susceptibility and conductivity as

$$\sigma(\omega) = i\omega n_f q^2 \frac{m\omega^2 - i\omega b}{m^2\omega^4 + \omega^2 b^2} \tag{2.12}$$

$$\chi(\omega) = \frac{n_b}{m} q^2 \frac{m(\bar{\omega_0}^2 - \omega^2) + i\omega b}{m^2(\bar{\omega_0}^2 - \omega^2)^2 + \omega^2 b^2} \tag{2.13}$$

where n_b and n_f are the density of bound and free charges respectively, $\bar{\omega_0}$ is the frequency of the harmonic oscillator, and b represents a frictional force, that includes the collisions as a dissipative mechanism. In the case of rare gases we can neglect this latter term, so we can easily find the conductivity in terms of the plasma frequency, $\omega_p^2 = 4\pi n_f e^2/m$, as

$$\sigma(\omega) = i\frac{\omega_p^2}{4\pi\omega} \tag{2.14}$$

Since matter shows more than one resonance, this simple model is not accurate enough to reproduce the optical response of most media, therefore empirical formulas are commonly used. The Sellmeier equation gives an empirical relationship between the real part of the refractive index and wavelength for different media [86], and is a development of the Cauchy's equation for modelling dispersion. In its most general form, the Sellmeier equation is given as

$$n_r^2(\lambda) = 1 + \sum_i \frac{B_i \lambda^2}{\lambda^2 - C_i} \tag{2.15}$$

where B_i and C_i are coefficients determined experimentally, representing an absorption resonance of strength B_i at a wavelength $\sqrt{C_i}$. As an example, we present the empirical dependence of the susceptibility with the wavelength for three gases used along this work: argon, helium and xenon [87]. In all of them, the susceptibility was calculated at T=273 K and P=1 atm, ie, at a density of $n_b \simeq 2.7 \times 10^{19}$ atoms/cm^3. In the case of argon, the susceptibility becomes

$$\chi_0^{Ar} = \frac{1}{2\pi} C_1^{Ar} \left(\frac{C_2^{Ar}\lambda^2}{C_3^{Ar}\lambda^2 - 1} + \frac{C_4^{Ar}\lambda^2}{C_5^{Ar}\lambda^2 - 1} + \frac{C_6^{Ar}\lambda^2}{C_7^{Ar}\lambda^2 - 1} \right) \tag{2.16}$$

being $C_1^{Ar} = 0.012055$, $C_2^{Ar} = 0.2075$, $C_3^{Ar} = 91.012$, $C_4^{Ar} = 0.0415$, $C_5^{Ar} = 87.892$, $C_6^{Ar} = 4.3330$ and $C_7^{Ar} = 214.02$. For helium,

$$\chi_0^{He} = \frac{1}{2\pi} \frac{C_1^{He}}{C_2^{He} - \lambda^{-2}} \tag{2.17}$$

being $C_1^{He} = 0.01470091$ and $C_2^{He} = 423.98$. Finally, for xenon the susceptibility becomes

$$\chi_0^{Xe} = \frac{1}{2\pi} C_1^{Xe} \left(\frac{C_2^{Xe}\lambda^2}{C_3^{Xe}\lambda^2 - 1} + \frac{C_4^{Xe}\lambda^2}{C_5^{Xe}\lambda^2 - 1} + \frac{C_6^{Xe}\lambda^2}{C_7^{Xe}\lambda^2 - 1} \right) \tag{2.18}$$

being $C_1^{Xe} = 0.012055$, $C_2^{Xe} = 0.26783$, $C_3^{Xe} = 46.301$, $C_4^{Xe} = 0.29481$, $C_5^{Xe} = 50.578$, $C_6^{Xe} = 5.0333$ and $C_7^{Xe} = 112.74$.

Let us now study the propagation of the field in a linear isotropic medium. In this case, the field polarization is not relevant, and we look for solutions of the scalar wave equation of the form $E(\mathbf{r}, t) = U(\mathbf{r})e^{i\omega t}$. Substituting in the wave equation (2.5) we obtain the Helmholtz equation for the complex amplitude, $U(\mathbf{r})$,

$$\nabla^2 U(\mathbf{r}) + k^2 U(\mathbf{r}) = 0 \tag{2.19}$$

where it is defined the wavenumber as $k(\omega) = k_0 n_r(\omega)$ being $k_0 = \omega/c$ the propagation vector of the electromagnetic field in vacuum. The simplest solution of the Helmholtz equation in a homogeneous medium is the plane wave, $U(\mathbf{r}) = U_0 e^{-i\mathbf{k}\cdot\mathbf{r}}$, where U_0 is a complex constant called the complex envelope and $\mathbf{k}$ is called the wavevector.

Assuming the plane wave to travel along the propagation axis z, the phase of the field, $\phi_0 = -n_{r,R}(\omega)kz + \omega t$ (being $n_{r,R}$ the real part of the refractive index), travels in time with the phase velocity, v_{ph},

$$v_{ph}(\omega) = \frac{c}{n_r(\omega)} \tag{2.20}$$

If we now look at the intensity of the propagating wave,

$$I(z) \propto |E(\mathbf{r}, t)|^2 = I_0 e^{-\alpha z} \tag{2.21}$$

we can define the absorption coefficient as $\alpha = 2kn_{r,I}$, being $n_{r,I}$ the imaginary part of the refractive index. The inverse quantity, $1/\alpha$, is known as the absorption length.

In the paraxial approximation, we may write $U(\mathbf{r}) = A(\mathbf{r})e^{-ikz}$, assuming that $A(\mathbf{r})$ varies slowly along the propagation coordinate z. Substituting $U(\mathbf{r})$ in Eq. (2.19), and neglecting the higher derivatives of the amplitude, we find the Paraxial Helmholtz equation,

$$\nabla_T^2 A(\mathbf{r}) - i2k\frac{\partial A(\mathbf{r})}{\partial z} = 0 \tag{2.22}$$

where $\nabla_T^2 = \partial^2/\partial x + \partial^2/\partial y$ is the transverse Laplacian operator. One solution of the Paraxial Helmholtz equation is the Gaussian beam [88],

$$U(\mathbf{r}) = A_0 \frac{W_0}{W(z)} \exp\left(-\frac{\rho^2}{W^2(z)}\right) \exp\left(-ikz - ik\frac{\rho^2}{2R(z)} + i\zeta(z)\right) \tag{2.23}$$

with $\rho = \sqrt{x^2 + y^2}$ and where the beam parameters are

$$W(z) = W_0\sqrt{1 + \left(\frac{z}{z_0}\right)^2} \tag{2.24a}$$

$$R(z) = z\left[1 + \left(\frac{z_0}{z}\right)^2\right] \tag{2.24b}$$

$$\zeta(z) = \tan^{-1}\left(\frac{z}{z_0}\right) \tag{2.24c}$$

where $W(z)$ is the beam width, being W_0 the beam waist, related to the Rayleigh range, z_0, as $W_0 = \sqrt{\lambda z_0/\pi}$. $R(z)$ is the radius of curvature of the wavefront and $\zeta(z)$ is the Gouy phase (see more at 2.3.1). The waist diameter, $2W_0$, is also called the spot size, whereas twice the Rayleigh range is known as the depth of focus or confocal parameter. On the other hand, it is also possible to find the vector solution for the Gaussian beam [88], describing the space-dependent field polarization as

$$\mathbf{E}(\mathbf{r}) = E_0\left(-\hat{\mathbf{x}} + \frac{x}{z + iz_0}\hat{\mathbf{z}}\right)\mathbf{U}(\mathbf{r}) \tag{2.25}$$

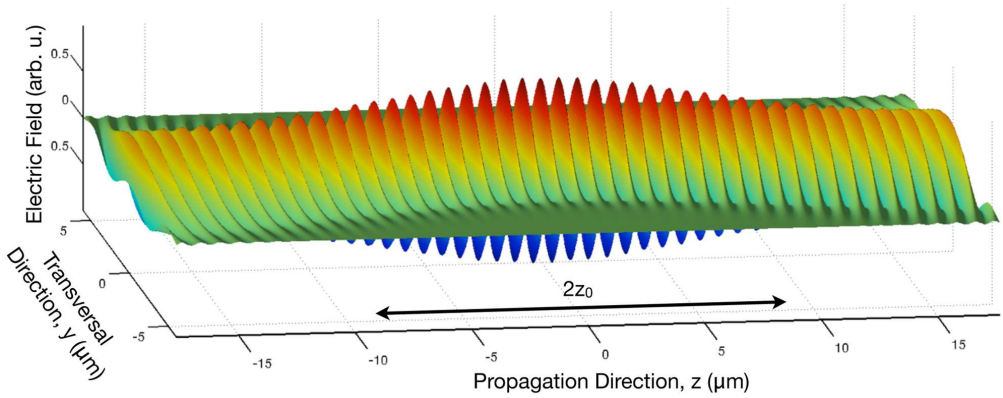

Figure 2.1: Electric field of a Gaussian beam –real part of $U(\mathbf{r})$–, where λ=0.8 μm, W_0=1.5 μm and z_0=8.8 μm.

2.2.2 Pulse propagation in linear media

In general, we can represent a pulsed field as a monochromatic wave modulated in amplitude an phase by an envelope,

$$E(z,t) = A(z - v_g t)e^{i[k(z-v_{ph}t)+\phi_{CEO}]} \tag{2.26}$$

where v_g is the group velocity and ϕ_{CEO} is the carrier-envelope offset. When considering the propagation of pulses of light in dispersive media, the velocity at which the envelope travels is different from the phase velocity. The speed with which the pulse propagates is called the group velocity, and is given by

$$v_g = \left[\frac{\partial k(\omega)}{\partial \omega}\Big|_{\omega_0}\right]^{-1} \tag{2.27}$$

being ω_0 the central frequency of the electromagnetic pulse. Both group velocity and phase velocity are related as

$$\frac{1}{v_g} - \frac{1}{v_{ph}} = \frac{\omega_0}{c}\frac{\partial n_r(\omega)}{\partial \omega}\Big|_{\omega_0} \tag{2.28}$$

so in an ideal non-dispersive medium (refractive index independent of the wavelength), the phase and group velocities are identical. Let us now consider the propagation of the envelope of the pulse between two different points (z_0 and z_1) inside a medium. The electric field in z_0, at a time t_0, is given by

$$E(z_0,t_0) = A(z_0 - v_g t_0)e^{i[k(z_0-v_{ph}t_0)+\phi_{CEO}]} \tag{2.29}$$

where $A(z_0 - v_g t_0)$ is the envelope of the field, and v_g and v_{ph} are the group and phase velocities. On the other hand, the electric field at another point z_1 is given by

$$E(z_1,t_1) = A(z_1 - v_g t_1)e^{i[k(z_1-v_{ph}t_1)+\phi_{CEO}]} \tag{2.30}$$

If $t_1 = t_0 - (z_1 - z_0)/v_g$, then the field amplitude at this two situations must be the same. Therefore, multiplying and dividing by the phase of the field at t_0, we can write

$$\begin{aligned} E(z_1,t_1) &= A(z_0 - v_g t_0)e^{i[k(z_0-v_{ph}t_0)+\phi_{CEO}]}e^{ik(z_1-z_0)(1-v_{ph}/v_g)} \\ &= E(z_0,t_0)e^{ik(z_1-z_0)(1-v_{ph}/v_g)} \end{aligned} \tag{2.31}$$

Therefore, if $v_{ph} \neq v_g$, the envelope accumulates a carrier-envelope phase during the propagation of the pulse. Note that, at this level of approximation, the form of the pulse envelope form does not change due to dispersion.

If the pulse propagates in an absorbing medium, the pulse absorption can be sufficiently well described using the absorption coefficient for the central frequency. On the other hand, the wavenumber of the fundamental field is shifted from its vacuum value to

$$k^2 = k_0^2[1 - \omega_p^2/\omega_0^2 + 4\pi\chi(\omega_0)] \tag{2.32}$$

When considering electromagnetic pulses, the ionization becomes time-dependent so the refractive index changes in time. Let us first concentrate in the effect of the increase of the free charges in the media. In this case, the wavenumber of the fundamental field is shifted from its vacuum value to $k_1^2 \simeq k_0^2(1 - \omega_p^2/\omega_0^2)$, ω_p being the plasma frequency [89]. As a consequence, the time-dependent ionization will lead to a time-dependent wavenumber, and Eq. (2.26) must be written as,

$$E(z,t) = A(z - v_g t)e^{i[\int_{-\infty}^{z-v_g t} k_1(x,y,\xi,t)d\xi - k_0 v_{ph} t + \phi_{CEO}]} \tag{2.33}$$

The spatial phase of the field can be approximated by the integral over the propagation direction

$$\int_{-\infty}^{z-v_g t} k_1(x,y,\xi,t)d\xi \simeq k_0 z - \frac{2\pi e^2}{{\omega_0}^2 m} P_f(\mathbf{r}, t - z/v_g) \int_{-\infty}^{z-v_g t} n_0(x,y,\xi)d\xi \tag{2.34}$$

being $n_0(\mathbf{r})$ the atomic density distribution and $P_f(\mathbf{r},\tau)$ the ratio for ionized electrons, that we calculate as follows

$$P_f(\mathbf{r},\tau) = 1 - e^{-\int_{-\infty}^{\tau} w_{ADK}(\mathbf{r},t')dt'} \tag{2.35}$$

where $w_{ADK}(\mathbf{r},t')$ is the ionization rate, calculated from the Amosov-Delone-Krainov (ADK) equation [33]. For hydrogen this reads

$$w_{ADK}(\mathbf{r},t') = \frac{2e^2}{\pi}\left[\frac{3}{\pi|E(\mathbf{r},t')|}\right]^{1/2} e^{-\frac{2}{3|E(\mathbf{r},t')|}} \tag{2.36}$$

Now let us turn our attention to the effect of the decrease of neutral atoms due to ionization. As well as the effect of the free charges, the effect of the neutral atoms in the refractive index becomes time-dependent during the electromagnetic pulse propagation. From the equation of the wavenumber (2.32), one can derive that the phase of the electromagnetic field is shifted as:

$$E(z,t) = A(z - v_g t)e^{i[\int_{-\infty}^{z-v_g t} k(x,y,\xi,t)d\xi - k_0 v_{ph} t + \phi_{CEO}]} \tag{2.37}$$

including the effects of the increase of free charges and the decrease of neutrals as

$$\begin{aligned}\int_{-\infty}^{z-v_g t} k(x,y,\xi,t)d\xi &= k_0 z - \frac{2\pi e^2}{{\omega_0}^2 m} P_f(\mathbf{r}, t-z/v_g)\int_{-\infty}^{z-v_g t} n(x,y,\xi)d\xi \\ &+ 2\pi k_0[1-P_f(\mathbf{r},t-z/v_g)]\int_{-\infty}^{z-v_g t}\chi(x,y,\xi,\omega)d\xi \quad (2.38)\end{aligned}$$

being $\chi(\mathbf{r},\omega)$ the susceptibility due to the neutral atoms in the medium, whose dependence on the spatial coordinate $\mathbf{r}$ is given by the atomic density $n(\mathbf{r})$.

2.3 Propagation in non-linear media

The non-linear response of a medium induces the generation of harmonics as well as modifications in the propagation of the fundamental field. In conventional non-linear optics, the optical response of an isotropic medium to a monochromatic wave of frequency ω_0 can be described expressing the polarization as a perturbative power series in the field strength as

$$\mathbf{P} = \chi^{(1)}(-\omega_0,\omega_0)\mathbf{E} + \chi^{(2)}(-2\omega_0,\omega_0)\mathbf{E}^2 + \chi^{(3)}(-3\omega_0,\omega_0)\mathbf{E}^3 + ... \quad (2.39)$$

where $\chi^{(1)}(-\omega_0,\omega_0)$ is the linear susceptibility and $\chi^{(2)}(-2\omega_0,\omega_0)$, $\chi^{(3)}(-3\omega_0,\omega_0)$ are the second- and third-order non-linear susceptibilities, respectively. The even-order non-linear processes only occur in non-centrosymmetric media [90]. As a consequence, in atoms, the high-order harmonic generation process leads only to odd harmonics of the fundamental field.

The main non-linear effects of the neutral media on the fundamental field are the Kerr effect and self-phase modulation [90], both induced by the third-order susceptibility. For low-density gases these effects can be neglected. On the other hand, the time-dependent ionization, and the presence of free charges in the medium can be of importance even in this case. Harmonic generation results from a wave-mixing process in which the qth-order response of the material generates a new field from the combination of q photons of the fundamental. For a linearly polarized field, the general equation for the propagation of a harmonic in an isotropic medium is given by

$$\nabla^2 E_q(\mathbf{r},t) + \left(\frac{q\omega_0}{c}\right)^2 E_q(\mathbf{r},t) = -4\pi\left(\frac{q\omega_0}{c}\right)^2 P_q(\mathbf{r},t) \quad (2.40)$$

E_q being the electric field associated to the qth-order harmonic. The polarization of the medium can be split into linear and non-linear contributions, $P_q = P_q^L + P_q^{NL}$. The linear term is the response of the atom to the propagating field of frequency $q\omega_0$,

$$P_q^L = \chi^{(1)}(-q\omega_0, q\omega_0)E_q \tag{2.41}$$

Defining the wavenumber of the qth-order harmonic as

$$k_q = q\frac{\omega_0}{c}n_{r,q}(q\omega_0) = q\frac{\omega_0}{c}\sqrt{1+4\pi n_b\chi^{(1)}(-q\omega_0, q\omega_0)} \tag{2.42}$$

where $n_{r,q}$ is the refractive index at the harmonic frequency, equation (2.40) reduces to

$$\nabla^2 E_q(\mathbf{r},t) + k_q^2 E_q(\mathbf{r},t) = -4\pi\left(\frac{q\omega_0}{c}\right)^2 P_q^{NL}(\mathbf{r},t) \tag{2.43}$$

Therefore, the non-linar polarization P_q^{NL} is the source of the harmonic field. Note that the right hand side term is null by definition for the fundamental harmonic (q=1).

The non-linear polarization encloses all possible wave mixing processes involving the fundamental frequency and the harmonics, that give a $q\omega_0$ oscillation as a result. We will consider here only the contribution of the driving field to the qth-order polarization,

$$P_q^{NL} = \chi^{(q)}(-q\omega_0, \omega_0)E_1^q \tag{2.44}$$

where E_1 is the fundamental field. As a result, the qth-order non-linear polarizability propagates with a wavenumber qk_1.

The interference of the linear and non-linear response leads to a space-dependent enhancement or suppression of the polarizability. For instance, for a Gaussian beam focused in vacuum, the qth-order polarizability is given by

$$\begin{aligned} P_q &= P_q^L + P_q^{NL} = \\ &\chi_L A(z)e^{-ik_q z - ik_q\frac{\rho^2}{2R(z)} + i\zeta(z)} + \chi_{NL}A^q(z)e^{-iq\omega_0 z/c - iq\omega_0/c\frac{\rho^2}{2R(z)} + iq\zeta(z)} \simeq \\ &e^{-i(k_q - \partial\zeta(z)/\partial z)z}\left(\chi_L A(z)e^{-ik_q\frac{\rho^2}{2R(z)}} + \chi_{NL}A^q(z)e^{i\Delta k_q z - iq\omega_0/c\frac{\rho^2}{2R(z)}}\right) \end{aligned} \tag{2.45}$$

where we have defined the phase-mismatch along the propagation direction as $\Delta k_q = k_q - q\omega_0/c + (q-1)\partial\zeta(z)/\partial z$. In general, the phase-mismatch is defined as $\Delta k_q = k_q - qk_1$, and takes into account other contributions to the polarizability. In Fig- 2.2 we plot an example of the spatial distribution of (a) the linear polarization P_q^L, and (b) the total polarization P_q, for a Gaussian beam. As can be seen, the interference of the linear

and non-linear response to the harmonic field causes the vanishing of the polarizability at some spatial regions. The harmonic generation is, therefore, confined to the bright regions in between, whose characteristic size is the coherence length, defined as

$$L_q^{coh} = \left| \frac{\pi}{\Delta k_q} \right| \tag{2.46}$$

The optimal harmonic yield from the macroscopic target is obtained when the the linear and non-linear polarization waves have their phases matched, i.e. when $\Delta k_q = 0$.

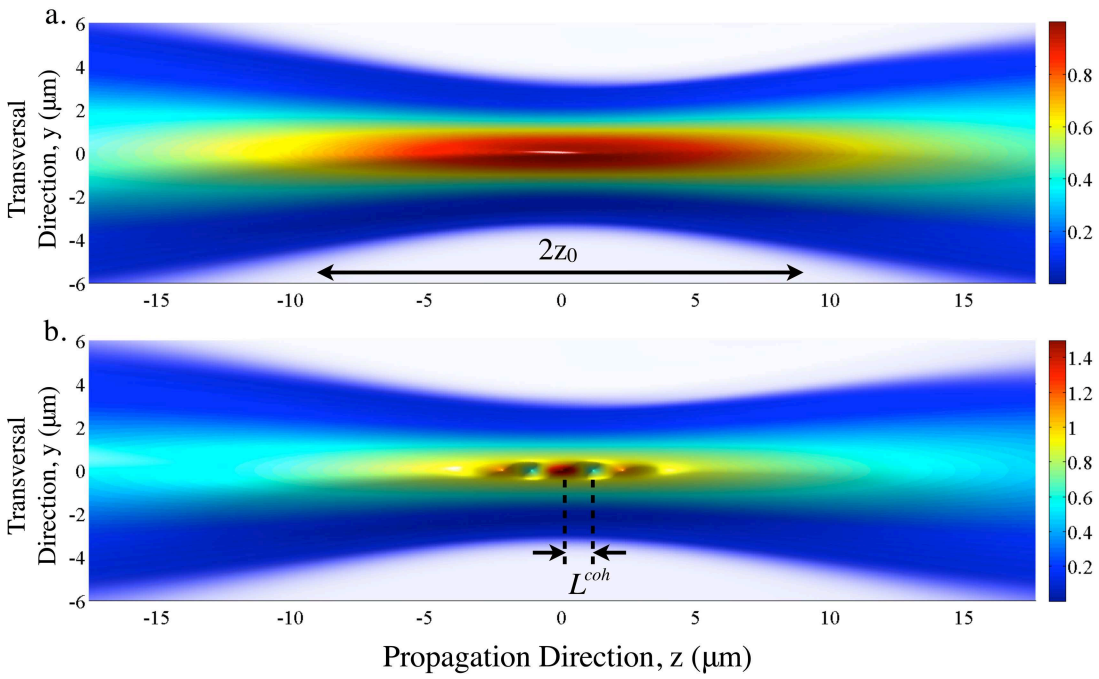

Figure 2.2: **a** Absolute value of the linear polarization, P_q^L for the 37th harmonic in a Gaussian beam of parameters λ=800 nm, W_0=1.5 μm, and z_0=8.84 μm. In plot **b** we show the absolute value of the total polarization, $P_q = P_q^L + P_q^{NL}$. The parameters used in these plots are unrealistic for the sake of clarity, the susceptibilities being $\chi_L = 1$ and $\chi_{NL} = 0.5$, the refractive indexes n_1=1.0001 and n_{37}=1.005, and A_0=1.

Let us now introduce a very simple model that we will use in the following to explore the different aspects of phase-matching. We shall consider two atoms, located at the propagation axis of a plane wave (see Fig. 2.3, where the two atoms are located at z_1 and z_2). If we place a detector at a distance z_D, the field there corresponds to the

interference of the fields generated at each atom, and propagated to the detector, i.e.

$$E_{det} = e^{iqk_1 z_1} e^{ik_q(z_D - z_1)} + e^{iqk_1 z_2} e^{ik_q(z_D - z_2)} \propto \cos(\Delta k_q L/2) \tag{2.47}$$

where $L = z_2 - z_1$ and Δk_q is the phase-mismatch. With this simple model, we can easily verify that the coherence length is the distance between two atoms whose emitted radiation interferes destructively, as it is sketched in Fig. 2.4.

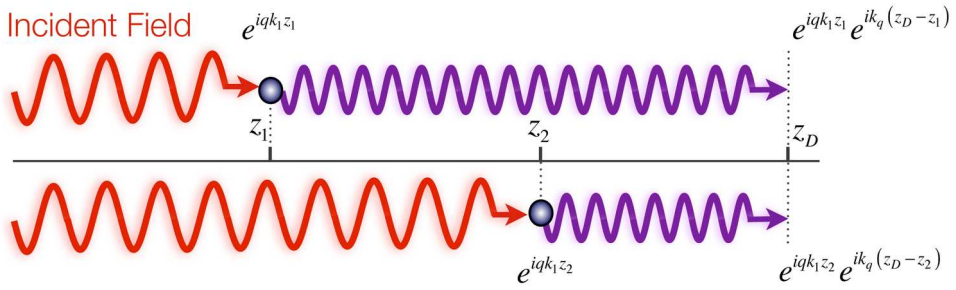

Figure 2.3: Scheme of our simple model to study phase-matching. The harmonic radiation is generated by two atoms at positions z_1 and z_2. The detector is located at the coordinate z_D.

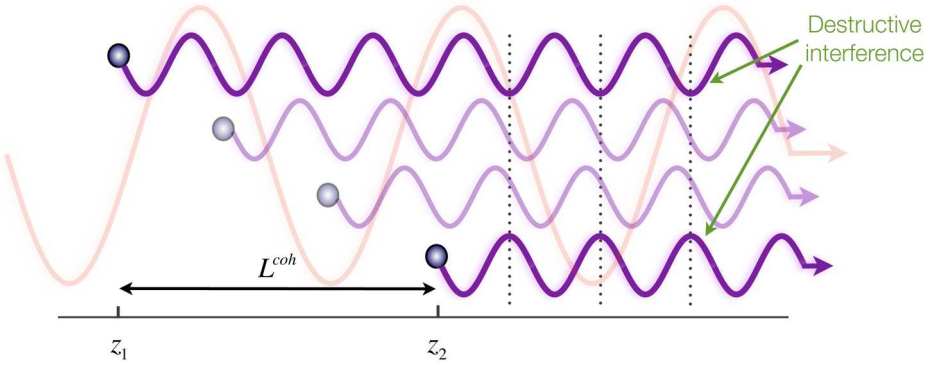

Figure 2.4: Scheme of one-dimensional phase-matching of harmonic radiation generated at different atom positions. The radiation emitted from the atoms located at z_1 and z_2 interferes destructively, so the coherence length corresponds to their separation.

In a typical experiment of HHG, the phase-mismatch function has four main contributions:

$$\Delta k_q \simeq \Delta k_q^{geom} + \Delta k_q^{f} + \Delta k_q^{b} + \Delta k_q^{int} \tag{2.48}$$

where Δk_q^{geom} results from the spatial phase variations arising from the focusing geometry, Δk_q^{f} is associated to the presence of free charges in the medium, Δk_q^{b} is due to the polarization of the neutrals and Δk_q^{int} corresponds to the harmonic phase, intrinsic to the generation process.

As we will see later in this chapter, phase-matching is automatically included in our calculations, as we solve the wave equation numerically. We, however, assume that the phase velocity of the harmonic field is that of the vacuum, although we include the possibility of absorption. Let us now explore the different contributions to phase-matching in order to, first, have a in-depth understanding of the process that otherwise remains hidden in our exact computation and, second, to demonstrate that the assumption for the harmonic field phase velocity is essentially correct. We shall study those contributions separately in the following subsections.

On the other hand, it is a challenge to define experimental conditions in which the mismatch is reduced to a minimum. Even under optimal phase-matching conditions, the efficiency of the harmonic generation can be strongly limited by the absorption in the medium. In section 2.3.4 we shall address the phenomenon of harmonic reabsorption whereas in 2.3.5 we will analyze a technique for achieving this optimal phase-matching condition ($\Delta k_q \simeq 0$) in a hollow waveguide.

2.3.1 Geometrical contributions to phase-matching

Now we study the contributions to the phase-matching arising from the characteristics of the experimental setup (focusing geometry and detection angle). Therefore, we decompose the geometrical phase-mismatch factor as:

$$\Delta k_q^{geom} \simeq \Delta k_q^{Gouy} + \Delta k_q^{angle} \tag{2.49}$$

where Δk_q^{Gouy} is the contribution of the Gouy phase of a Gaussian beam, and Δk_q^{angle} results from the detection of the harmonics at different divergence angles.

Gouy phase

A Gaussian beam propagating through its focus experiences a π phase-shift with respect to a plane wave, known as the Gouy phase [91]. As described by Eq.(2.24c), the spatial dependence of the Gouy phase has the form $\zeta(z) = \tan^{-1}(z/z_0)$. Assuming a narrow target, we may approximate the Gouy phase linearly, therefore resulting in a correction to the propagating vector for the fundamental field, $k_1 = \omega/c - d\zeta/dz \simeq \omega/c - 1/z_0$, and for the generated harmonic $k_q = q\omega/c - d\zeta/dz \simeq q\omega/c - 1/z_0$. Therefore the phase-mismatch can be approximated to

$$\Delta k_q^{Gouy} = k_q - qk_1 = \frac{q-1}{z_0} \tag{2.50}$$

Since $\zeta(z)$ is antisymmetric with respect to the focus, phase-matching conditions when the target is located before and after the focus will become substantially different. Moreover, the more focalized is the beam, the more important is the effect of the Gouy phase, and on the reverse, we can neglect this effect for targets whose width is very short compared to the Rayleigh distance of the beam.

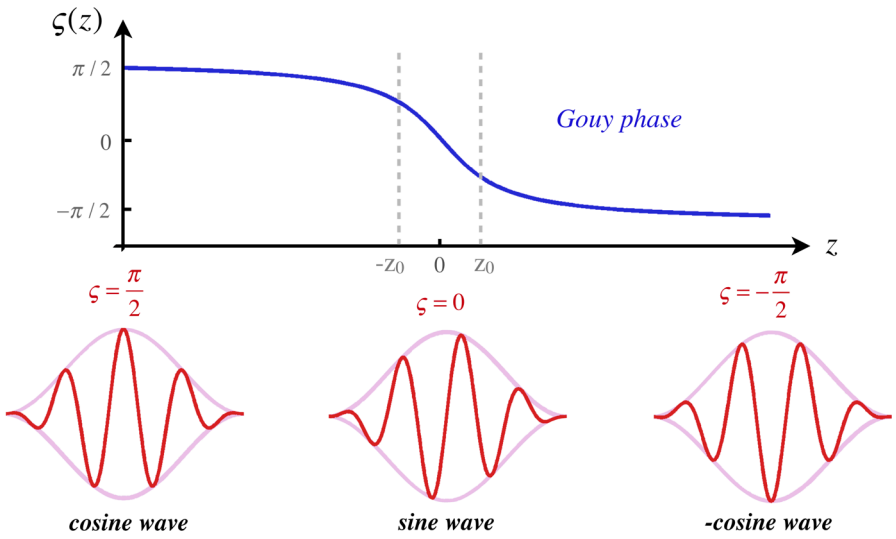

Figure 2.5: Effect of the Gouy phase (blue line) in the carrier-envelope phase during the pulse propagation. The waveform of the electric field changes from an initial cosine function at $z << 0$, to a sine function in the focus position ($z = 0$), and a minus cosine function at $z >> 0$. The spatial variation becomes significant within the Rayleigh range (from $-z_0$ to z_0).

In addition to phase-matching, the effect of the Gouy phase is also specially significant for few-cycle pulses, as modifies the carrier-envelope phase [92]. In Fig. 2.5 we can observe how the Gouy phase shifts the carrier-envelope phase continuously through one Rayleigh distance around the focus: the waveform of the electric field changes from an initial cosine function at $z << 0$, to a sine function in the focus position ($z = 0$), and a minus cosine function at $z >> 0$.

Angle of detection

The harmonics radiated from the atoms located at different places in the target travel to the detector through different optical paths. The relative difference between those paths changes with the angle of detection. For the sake of simplicity, let us consider again the two-atom model presented before (see Fig. 2.6). If we consider off-axis detection under an angle θ, then

$$E_{det} = e^{iqk_1z_1}e^{ik'_q(z_D-z_1)} + e^{iqk_1z_2}e^{ik'_q(z_D-z_2)} \propto \cos(\Delta k'_q)L \tag{2.51}$$

where

$$k'_q = k_q\cos\theta \simeq k_q - \frac{q\omega}{2c}\theta^2 \tag{2.52}$$

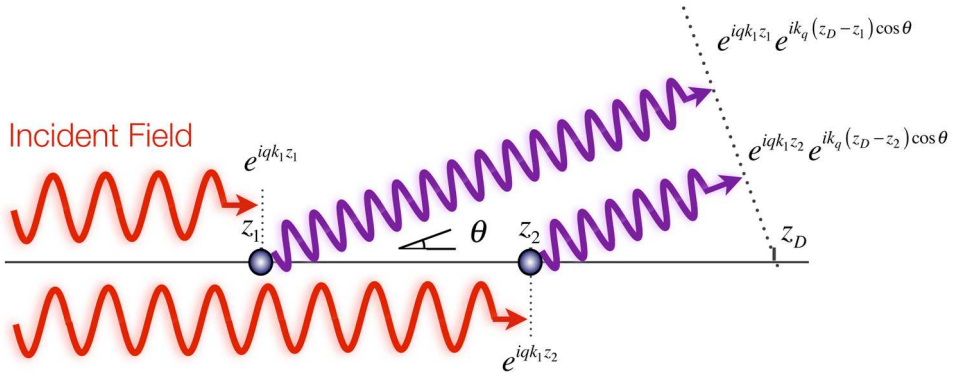

Figure 2.6: Scheme of phase-matching considering two different atoms in the target, when the radiation is detected at an angle θ from the propagation axis.

The phase-mismatch function now becomes

$$\Delta k_q^{angle} = k_q - qk_1 = -\frac{q\omega_0}{2c}\theta^2 \tag{2.53}$$

As we will see in the next chapter, the angle of detection plays an important role when selecting short and long trajectory contributions from the high-order harmonic generation process.

In conclusion, once we have included the effect of the Gouy phase and the angle of detection, we can rewrite Eq. (2.49) as

$$\Delta k_q^{geom} \simeq \frac{q-1}{z_0} - \frac{q\omega_0}{2c}\theta^2 \tag{2.54}$$

2.3.2 Contribution of free charges and neutrals to phase-matching

The contributions of free charges and neutrals can be treated similarly by considering them the result of quantum transitions between free states or between bound states, respectively. For low-density media we use the approximation form (2.11)

$$n_r \simeq 1 + 2\pi(\chi_b + \chi_f) \tag{2.55}$$

being χ_b and χ_f the susceptibilities associated with neutrals and free charges, respectively. The phase-mismatch associated to each of these contributions alone can be written as

$$\Delta k_q^i = k_q - qk_1 = \frac{2\pi}{\lambda_q}\left[n_r(\lambda_q) - n_r(\lambda_0)\right] \simeq \frac{4\pi^2}{\lambda_q}\left[\chi_i(\lambda_q) - \chi_i(\lambda_0)\right] \tag{2.56}$$

where the label i corresponds to f in the case of free charges, and b in the case of neutrals. Therefore, the coherence length of each process can be estimated as

$$L_{q,i}^{coh} = \left|\frac{\pi}{\Delta k_q^{mat}}\right| = \left|\frac{\lambda_q}{4\pi}\frac{1}{\chi_i\left(\lambda_0\right) - \chi_i\left(\lambda_q\right)}\right| \tag{2.57}$$

In the following, we will see that $\chi_i(\lambda_q) \ll \chi_i(\lambda_0)$, therefore the linear propagation of the harmonic can be considered as in vacuum, while the phase-mismatch is mainly due to the up-conversion of the phase accumulated by the fundamental field during its propagation.

Free charges: effect of free-free transitions

From Eq. (2.57), the coherence length due to the effect of the free charges in the material is given by

$$L_{q,f}^{coh} = \left|\frac{\lambda_q}{4\pi}\frac{1}{\chi_f\left(\lambda_q\right) - \chi_f\left(\lambda_0\right)}\right| \tag{2.58}$$

where the susceptibility associated to the free-free transitions corresponds to, $\chi_f = -\omega_p^2/(4\pi\omega^2)$, being ω_p the plasma frequency, which is expressed as $\omega_p^2 = 4\pi n_f e^2/m$, and being n_f, the density of free electrons. Therefore, the coherence length due to free-free transitions reads as

$$L_{q,f}^{coh} = \left| \frac{q\pi mc^2}{e^2 n_f \lambda_0 (q^2-1)} \right| \tag{2.59}$$

In Table 2.1 we show the coherence lengths for three different situations: high-order harmonic generation driven by vacuum ultraviolet, –VUV (267 nm)–, near-infrared –near-IR, (800 nm)– and mid-infrared –mid-IR, (3.9 μm)– laser sources. The harmonic orders considered in each case are the 11th, 27th and 5000th respectively. We use three different atomic densities for the target, $10^{18}, 10^{19}$ and 10^{20} atoms/cm^3, and assume typical ionization levels of 10% (VUV), 5% (near-IR) and 0.1% (mid-IR). For instance, assuming a 5% ionization during the pulse propagation of harmonics generated by near-IR laser sources in a gas jet of 10^{18} atoms/cm^3, the effect of free charges in the propagation of the 27th harmonic begins to be relevant at propagation lengths above approximately 1 mm.

λ \ n_b	10^{18}at/cm^3	10^{19}at/cm^3	10^{20}at/cm^3
VUV ($267\ nm, q = 11, P_i = 10\%$)	3.829 mm	382.9 μm	38.29 μm
NIR ($800\ nm, q = 27, P_i = 5\%$)	1.034 mm	103.4 μm	10.34 μm
MIR ($3.9\ \mu m, q = 5000, P_i = 0.1\%$)	57.2 μm	5.72 μm	572 nm

Table 2.1: Coherence length due to free-free transitions for the propagation of the qth-order harmonic of a fundamental field of wavelength λ, through a medium of density n_b, assuming a ionization ratio P_i ($n_f = P_i n_b$), in three different regimes of HHG.

We shall now see that the effect of the free-free transitions in the linear propagation of the high-harmonic is negligible, i.e. $\chi_f(\lambda_q) << \chi_f(\lambda_0)$. In this case, the phase-mismatch becomes $\Delta k_q^f \simeq -\frac{4\pi^2}{\lambda_q}\chi_f(\lambda_0)$, and Eq. (2.59) can be approximated as

$$L_{q,f}^{coh} \simeq \left| \frac{\pi mc^2}{e^2 n_f q \lambda_0} \right| \tag{2.60}$$

With this approximation, the values of the coherence lengths of table 2.1 are reduced in less than 1% at 267 nm and 0.1% at 800 nm. In the mid-IR regime (3.9 μm), there is no appreciable variation. Therefore, we demonstrate that propagation of the harmonic field can be approximated to the vacuum.

Neutrals: effect of bound-bound transitions

From Eq. (2.57), the coherence length due to the effect of the bound-bound transitions in the material is given by

$$L_{q,b}^{coh} = \left| \frac{\lambda_q}{4\pi} \frac{1}{\chi_b(\lambda_q) - \chi_b(\lambda_0)} \right| \tag{2.61}$$

In the absence of resonances, we can estimate χ_b according to the perturbative formula [93],

$$\chi_b \simeq \frac{n_b e^2}{m} \frac{f_{12}}{\omega_{12}^2 - \omega^2} \tag{2.62}$$

where n_b is the density of atoms in the ground state, 1 labels the ground state, 2 the final level of the lowest energetic transition, and f_{12} the oscillator strength. Then, the coherence length due to bound-bound transitions corresponds to

$$L_{q,b}^{coh} = \left| \frac{\pi m c^2 \lambda_q}{e^2 n_b f_{12} \lambda_{12}^4} \frac{\left(\lambda_0^2 - \lambda_{12}^2\right)\left(\lambda_q^2 - \lambda_{12}^2\right)}{\lambda_q^2 - \lambda_0^2} \right| \tag{2.63}$$

If we consider the $1s-2p$ transition of the hydrogen atom, $f_{12} = 0.1388$ and $\lambda_{12} = 121.5$ nm [94]. In Table 2.2 we compute the coherence length for the three cases analyzed in this section. As an example, in the propagation of harmonics generated by near-IR laser sources in a gas jet of 10^{18} atoms/cm^3, the effect of neutrals in the propagation of the 27th harmonic for the example above begins to be relevant at propagation lengths above approximately 150 mm. Note that depending on the element, the effect of the neutrals can be relevant even at lower densities, near absorption edges.

λ \ n_b	10^{18}at/cm^3	10^{19}at/cm^3	10^{20}at/cm^3
VUV ($267\ nm, q = 11$)	1.01 cm	101 mm	10.1 mm
NIR ($800\ nm, q = 27$)	1.48 cm	148 mm	14.8 mm
MIR ($3.9\ \mu m, q = 5000$)	424 μm	42.4 μm	4.24 μm

Table 2.2: Coherence length due to bound-bound transitions in the propagation of the qth-order harmonic of the fundamental field of wavelength λ, through an hydrogen gas medium of density n_b, for the typical cases considered in this thesis

Since the frequency of the harmonic, $q\omega$, is greater than the ionization potential, the bound-bound transitions will mainly affect the propagation of the fundamental field

and not the harmonic, $\chi_b(\lambda_q) << \chi_b(\lambda_0)$, and thus Eq. (2.63) can be approximated as

$$L_{q,b}^{coh} \simeq \left| \frac{\pi m c^2 \lambda_q}{e^2 n_b f_{12}} \frac{\left(\lambda_{12}^2 - \lambda_0^2\right)}{\lambda_0^2 \lambda_{12}^2} \right| \tag{2.64}$$

With this approximation, the values of the coherence lengths of Table 2.2 are increased in less than 3% at 267 nm and 5% at 800 nm. In the mid-IR regime (3.9 μm), there is no appreciable variation. Therefore, as in the case of free charges, the influence of the neutrals in the linear propagation of the high-order harmonics can be neglected.

2.3.3 Intrinsic phase-matching

The intrinsic phase corresponds to the phase of the harmonics generated assuming a driving field unaffected by propagation. In section 1.2.2 we already discussed that each harmonic is mainly produced by two recollision paths. Each trajectory contribution has associated a phase given by the semiclassical action acquired during the excursion time (1.35). This phase is proportional to the laser intensity through a factor α_q^i, that depends on the particular trajectory (i) followed by the ionized electron. Therefore, the phase of the qth-order harmonic can be written as $\phi_q^i \simeq -\alpha_q^i I$.

The contribution of the intrinsic phase to the mismatch function is therefore given by the spatial dependence of the laser pulse intensity, i.e.

$$\Delta k_q^{int} = k_q - q k_1 \simeq \frac{\partial \alpha_q^i}{\partial I} \frac{\partial I}{\partial z} I + \alpha_q^i \frac{\partial I}{\partial z} \tag{2.65}$$

If the harmonic falls in the plateau region for the intensity range considered along the propagation axis, one can approximate $\partial \alpha_q^i / \partial I \simeq 0$, i.e., the excursion time of the electron does not change with the intensity, thus following the same trajectory. In that case, the phase-mismatch can be reduced to

$$\Delta k_q^{int} \simeq \alpha_q^i \frac{\partial I}{\partial z} \tag{2.66}$$

being higher for long trajectories rather than short, as $(\alpha_q^L > \alpha_q^S)$.

2.3.4 Absorption

Phase-matching plays a very important role in the efficiency of the generation of high-order harmonics. In principle, if one could achieve perfect phase-matching, the harmonic yield would increase monotonically with the target size. Nevertheless, even in

this case, the final efficiency would be limited by the absorption in the medium. In HHG driven by near-infrared laser sources, the radiation is emitted in the extreme ultraviolet (EUV) region of the spectrum, where the majority of gases are absorbing. Therefore, reabsorption of the harmonics saturates the efficiency of the harmonic generation [95].

In order to estimate the absorption length, we resort in the theoretical and experimental results available in the literature [96, 97, 98]. The absorption length can be defined as $L_{abs} = 1/(\sigma n_b)$, where n_b is the gas density and σ is the photoabsorption cross section. In table 2.3 we present the absorption lengths for hydrogen, helium, argon and xenon calculated from [96, 97, 98]. For example, the absorption length for the 27th harmonic driven by a 800 nm laser, in a gas of density 10^{18} atoms/cm^3 is 3.5 mm for helium, 4.5 mm for argon and 5 mm for xenon.

Gas	λ \ n_b	10^{18}at/cm^3	10^{19}at/cm^3	10^{20}at/cm^3
H	VUV (267 $nm, q = 11$)	6.73 cm	6.73 mm	0.673 mm
	NIR (800 $nm, q = 27$)	3.73 cm	3.73 mm	0.373 mm
	MIR (3.9 $\mu m, q = 5000$)	3.86 km	386 m	38.6 m
Ar	VUV (267 $nm, q = 11$)	1.00 cm	1.00 mm	100 μm
	NIR (800 $nm, q = 27$)	4.57 mm	457 μm	45.7 μm
	MIR (3.9 $\mu m, q = 5000$)	15.4 cm	1.54 cm	2.54 mm
He	VUV (267 $nm, q = 11$)	5.44 mm	544 μm	54.4 μm
	NIR (800 $nm, q = 27$)	3.51 mm	351 μm	35.1 μm
	MIR (3.9 $\mu m, q = 5000$)	111 m	11.1 m	1.11 m
Xe	VUV (267 $nm, q = 11$)	7.35 mm	735 μm	73.5 μm
	NIR (800 $nm, q = 27$)	5.07 mm	507 μm	50.7 μm
	MIR (3.9 $\mu m, q = 5000$)	12.7 mm	1.27 mm	127 μm

Table 2.3: Absorption lengths for H, Ar, He and Xe atoms computed from data extracted from [96, 97, 98].

Nevertheless, we have to be careful with estimations of table 2.3, as the absorption may vary significantly with the photon energy due to the presence of absorption edges. For example, argon presents resonances in the EUV region that can lead to total absorption of harmonics below 23rd [99]. In figure 2.7 we plot the transmission after 500 μm propagation through a gas of density 10^{18} atoms/cm^3 for hydrogen (pink), argon (green), helium (blue) and xenon (red) gases (data extracted from [98]). We observe

that the reabsorption of harmonics below the 25th (800 nm) is very significant in argon and xenon, so depending on the desired photon energy, the election of the medium is critical.

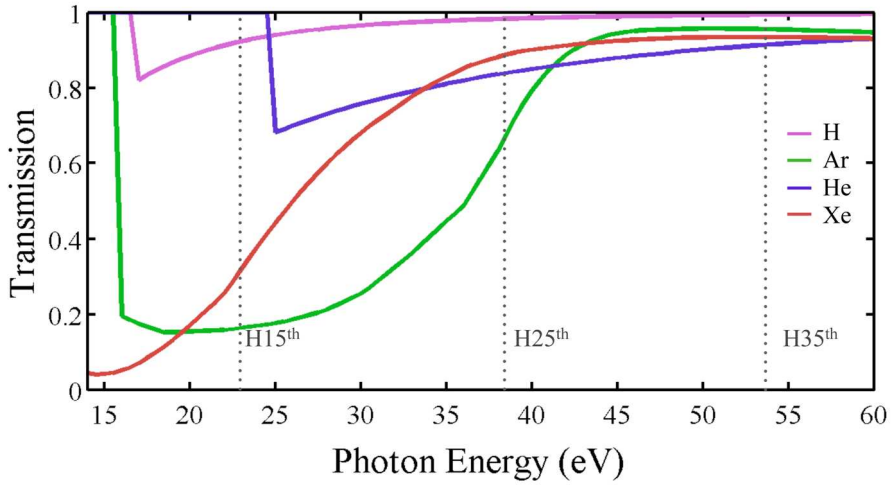

Figure 2.7: Transmission through 500 μm of a gas with density 10^{18} atoms/cm^3 in the case of hydrogen (pink), argon (green), helium (blue) and xenon (red). We indicate the energy of the15th, 25th and 35th harmonics for a 800 nm driving laser. Data obtained from [98].

2.3.5 Optimal phase-matching

One of the challenges to obtain efficient high-order harmonics is the achievement of optimal phase-matching conditions, i.e. $\Delta k_q \simeq 0$ [100]. Typically, optimal phase-matching corresponds to a coherent length longer than the medium length. In the absence of perfect phase-matching, quasi-phase-matching (QPM) techniques have been successfully used by periodically readjusting the relative phase between the fundamental and non-linear radiation in intervals corresponding to the coherence length [101, 102, 103, 104, 105, 106].

Kapteyn and Murnane proposed an alternative technique for achieving optimal phase-matching conditions in a hollow waveguide [42, 99]. The driving laser is focused into a gas-filled hollow waveguide, which ensures a non-diverging, near-plane-wave, propagation [42]. As a consequence, in terms of phase-matching, one avoids the effect

of the Gouy phase and that of the variation of the intrinsic phase of the harmonics, as the laser peak intensity is constant along the direction of propagation. Therefore, phase-matching is given by the two surviving contributions: the effect of free charges and neutral atoms. The phase-mismatch function then becomes

$$\Delta k_q^{waveguide} \simeq -\frac{4\pi^2}{\lambda_q}\left[\chi_f(\lambda_0)+\chi_b(\lambda_0)\right] \simeq q\left(\frac{n_f e^2\lambda_0}{mc^2}-\frac{4\pi^2 n_b \chi_b^0}{\lambda_0\eta_0}\right) \tag{2.67}$$

where, with this approximation, the bound charge susceptibility χ_{bb}^0, is calculated at a density η_0 using the empirical Sellmeier equation (2.15). The free and bound charge densities can be expressed in terms of the ionization probability P_f and the atomic density n_0 as $n_f = P_f n_0$ and $n_b = (1-P_f)n_b$.

Since the contributions of the free charges and neutrals are opposite in sign in Eq. (2.67), they can compensate to achieve perfect phase-matching, i.e. $\Delta k_q = 0$. Imposing this condition to Eq. (2.67) we find the optimal ionization probability as

$$P_f^{opt} = \frac{\chi_b^0}{\eta_0}\left(\frac{e^2\lambda_0^2}{4\pi mc^2}+\frac{\chi_b^0}{\eta_0}\right) \tag{2.68}$$

As the ionization probability depends on the intensity of the driving field, Eq. (2.68) describes an optimal intensity for each wavelength that will ensure perfect phase-matching along the waveguide. Since the ionization probability is time-dependent, the optimal phase-matching is a transient condition.

Let us now look at the driving electric field at consecutive positions along the waveguide in a frame moving with the phase velocity. In Fig. 2.8 we represent an 800 nm electric field at the entrance (light red line) ant at the output (dark red line) of a hollow waveguide 8 mm in length, filled by an helium gas of density 10^{19} atoms/cm^3, treating separately the effects of neutrals and free charges. In 2.8a, where only neutrals' effects are considered, the phase of the electric field is shifted in the waveguide, due to the refractive index of the gas. On the other hand, if only free charges' effects are considered (see 2.8b) the time-dependent ionized population imprints a negative chirp in the propagated electric field.

If we now take into account both the effect of neutrals and free charges in the propagation of the fundamental field, we can choose an intensity to fulfill perfect phase-matching conditions at the peak of the laser pulse, as can be observed in Fig. 2.8c. As a consequence, there is a temporal window in which the optimal phase-matching

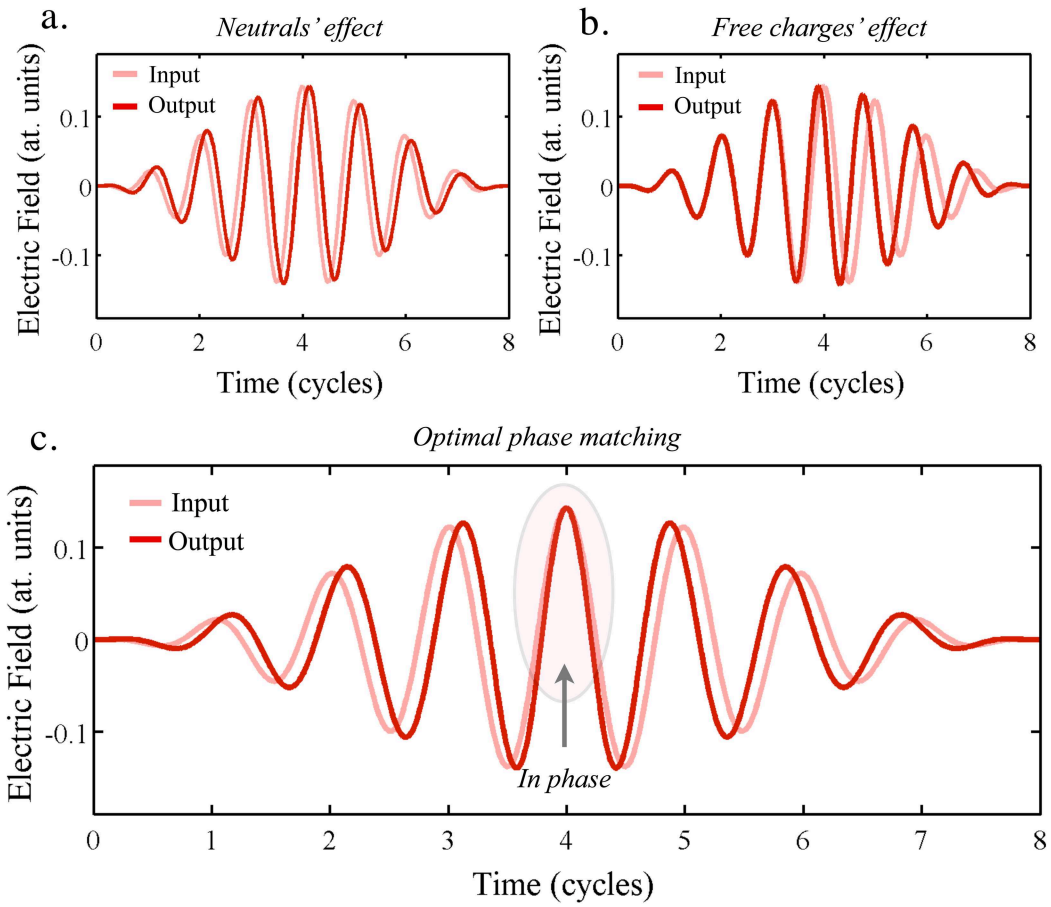

Figure 2.8: Electric field at the input (light red) and at the output (dark red) of a hollow waveguide considering **a** only neutral's effects, **b** only free charges' effects, and **c** both of them. The hollow waveguide is 8 mm in length, and filled by an helium gas of density 10^{19} atoms/cm^3. The laser pulse envelope is modeled as a $\sin^2$ function, 8 cycles full temporal length (2.9 cycles FWHM). The laser wavelength is 800 nm, whose optimal phase-matching intensity is 7.2×10^{14} W/cm^2. The neutrals effect produce a temporarily constant phase shift in the electric field (panel **a**), whereas free charges due to ionization imprints a negative chirp (panel **b**). In plot **c**, where both effects are considered, there is a temporal region in which optimal phase-matching conditions are achieved.

conditions holds. The width of this temporal window depends on the density (or pressure) of the gas inside the waveguide.

In Fig. 2.9 we plot the intensity for achieving perfect phase-matching inside a helium-filled waveguide versus the wavelength (from VUV to mid-IR). Optimal phase-matching conditions are fulfilled at the central part of the driving laser pulse. We can observe that the optimal intensity decreases when increasing the wavelength. This technique was recently used in the obtention for the first time of keV X-rays from HHG driven by mid-IR laser sources [20], where a laser pulse of 3.9 μm in wavelength and peak intensity of $\simeq 3 \times 10^{14}$ W/cm^2 was used.

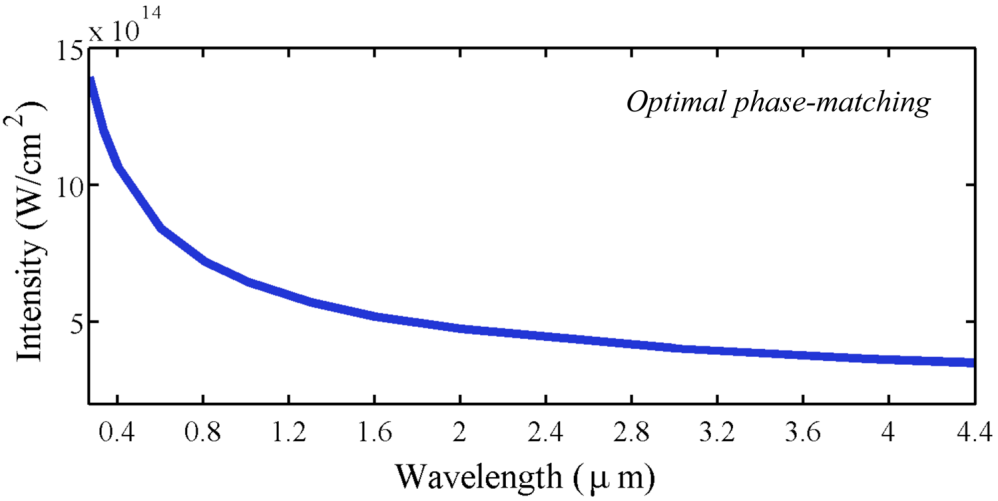

Figure 2.9: Optimal intensity for achieving perfect phase-matching inside a helium-filled waveguide at the central part of a driving laser pulse, whose envelope is modeled as a $\sin^2$ function, with 8 cycles full length duration (2.9 cycles FWHM).

2.4 Integral solution of the wave equation: A numerical method for computing high-order harmonic propagation

The details for the computation of high-order harmonic propagation have been studied extensively, for instance, by Anne L'Huillier's group [37, 82, 83]. Their approach consists in applying the paraxial approximation and the slowly varying envelope approximation to the wave equation, thus obtaining the differential equation (2.43), that is solved for each frequency component. Other groups have extensively used this approach for their computations of high-order harmonic propagation [107, 108, 109].

We have developed an alternative method in which, instead of solving numerically Eq. (2.5), we consider its integral solution [89]: $\mathbf{E}(\mathbf{r},t) = \mathbf{E}_0(\mathbf{r},t) + \mathbf{E}_i(\mathbf{r},t)$, where $\mathbf{E}_0(\mathbf{r},t)$ is the external field as it propagates in vacuum, and $\mathbf{E}_i(\mathbf{r},t)$ is the field radiated by the accelerated charges in the target,

$$\mathbf{E}_i(\mathbf{r},t) = -\frac{1}{c^2}\int d\mathbf{r}' \frac{1}{|\mathbf{r}-\mathbf{r}'|}\left[\frac{\partial}{\partial t'}\mathbf{J}_\perp(\mathbf{r}',t')\right]_{t'=t-|\mathbf{r}-\mathbf{r}'|/c} \tag{2.69}$$

Note that this expression assumes the generated radiation to propagate with the vacuum velocity (c) for all frequencies. We have seen before in this chapter that this is a reasonable assumption for the high-order harmonics. However, the above formula can not be applied for the propagation of the fundamental field. For this case, the differential equation should be used (2.43), which for the fundamental field assumes a linear response of the medium.

From the microscopic viewpoint, we may decompose the target into a discrete sum of elementary contributions, associated to each charge in the sample. The transversal far field radiated by the jth charge, placed at point $\mathbf{r}_j$ in the target, can be found from (2.69) and reads as [89],

$$\mathbf{E}_i^j(\mathbf{r}_d,t) = \frac{1}{c^2}\frac{q_j}{|\mathbf{r}_d-\mathbf{r}_j(0)|}\mathbf{s}_d \times [\mathbf{s}_d \times \mathbf{a}_j\,(t-|\mathbf{r}_d-\mathbf{r}_j(0)|/c)] \tag{2.70}$$

where $\mathbf{a}_j$ is the charge's acceleration, evaluated at the retarded time, and $\mathbf{s}_d$ is the unitary vector pointing to a virtual detector located at $\mathbf{r}_d$ (see figure 2.10). Note that we are using the dipole approximation, as the charge displacement during the interaction is assumed to be small in comparison to the wavelength of the radiation

field (including its harmonics), therefore $\mathbf{r}_j(t) \simeq \mathbf{r}_j(0)$. This condition is fulfilled in atomic gas targets, as harmonics are generated by charges in the vicinity of the parent ion.

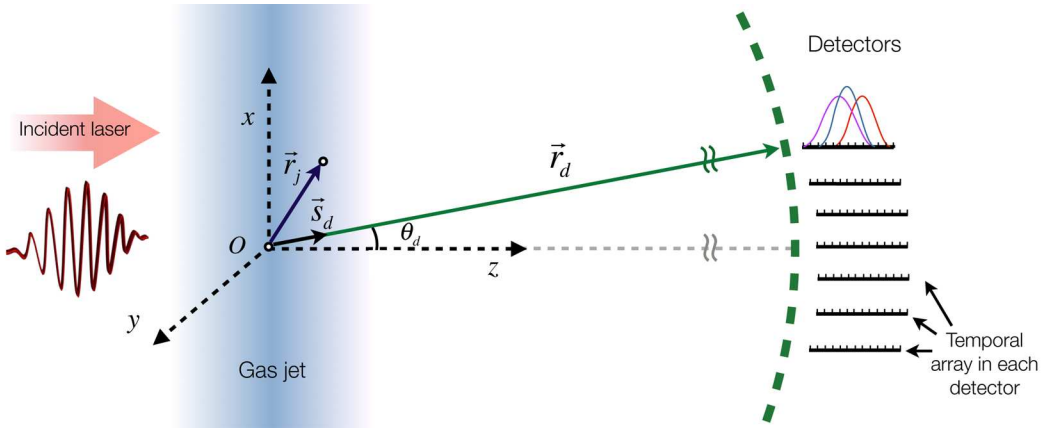

Figure 2.10: Scheme of our method to compute high-order harmonic propagation. The target (a gas jet) consists on a discrete number of elementary radiators, each placed at a coordinate $\mathbf{r}_j$. The detection of the radiation takes place at a distance $|\mathbf{r}_d|$ from the center of the target, O, using elementary detectors, each one characterized by the angle θ_d. For each of these detectors we consider a temporal array where the field contributions emitted by the different radiators are added.

In order to compute the charge's acceleration at the retarded time, $\mathbf{a}_j(t - |\mathbf{r}_d - \mathbf{r}_j(0)|/c)$ we have to take into account the position of each charge in the sample, as well as the angle of detection. As shown in Fig. 2.10, our detection scheme consists on a discrete number of far-field angular detectors placed at a distance $|\mathbf{r}_d|$ from the center of the sample, O, and at a certain angle θ_D respect to the propagation direction z. To compute the final phase at the detector, we consider the total time delay as the sum of the delays of the fundamental field reaching the elementary radiator position (t_{pre}) and the delay of the harmonic field when propagating from the radiator to the detector (t_{post}). Following the coordinate system described in figure 2.10, we can compute each propagation time as:

$$t_{pre,j} = z_j/v_g \tag{2.71}$$

$$t_{post,j} = (|\mathbf{r}_d| - \mathbf{r}_j \cdot \mathbf{s}_d)/c \tag{2.72}$$

where v_g is the group velocity –see Eq. (2.27)–. As a reference, we define the propagation times for a charge placed at the center of the sample, O, as $t_{pre,0} = 0$ and $t_{post,0} = |\mathbf{r_d}|/c$. For any other charge j, we can define the time of arrival to the detector as

$$\tau_j = t_{pre,j} + t_{post,j} = z_j/v_g + (|\mathbf{r}_d| - \mathbf{r}_j \cdot \mathbf{s}_d)/c \tag{2.73}$$

To compute the total harmonic yield, we sum up the radiation from the different charges at the target, propagated to the detector position. For each detector we create a large temporal array, placing the radiation emitted at a charge j corresponding to its time τ_j. As a reference, the radiation emitted from an emitter placed at the center of the target, O, is placed at the center of each detector array. Then, for each charge j, we compute the temporal delay relative to this central emitter as $\delta_j = \tau_0 - \tau_j$, where $\tau_0 = t_{pre,0} + t_{post,0}$. Since the array defined at the detector consists on a set of discrete time values, $n \times \Delta_t$, we need to accommodate the delays to this temporal grid (see Fig. 2.11). We do this in two steps: first we find the point in the grid i which is closest to the actual time delay τ_j. Since this time delay will not be exactly a point of the temporal grid, there is a residual temporal delay $\Delta\tau_j = \tau_j - i\Delta_t$ that is not properly taken into account. Therefore, in a second step, we correct for this remaining difference, by Fourier transforming the emitter's field signal at the detector's array and multiplying the resulting spectrum by the phase shift $e^{i\omega\Delta\tau_j}$. With this last step, we ensure a smooth representation of the field delays in the detector array. Otherwise, the round of the actual delay to the closest point in the temporal grid will add noise to the final spectrum.

Our integral method takes into account automatically the geometrical contributions to the phase-matching of the harmonics. On the other hand, the contributions to phase-matching given by the intrinsic phase of the harmonic generation process, are also present as a result of the single-atom HHG computation. The single-atom module in our code uses the SFA+ (see section 1.3) to compute the dipole acceleration.

From the previous section (see tables 2.1, 2.2) we see that the most relevant effects in the propagation of the fundamental field are the dephase generated by the presence of free charges, and the neutral atoms. Table 2.1 points out the necessity of including plasma effects in the propagation of the fundamental field, if one wants to consider propagation lengths of the order of one centimeter (near-IR regime). For that reason

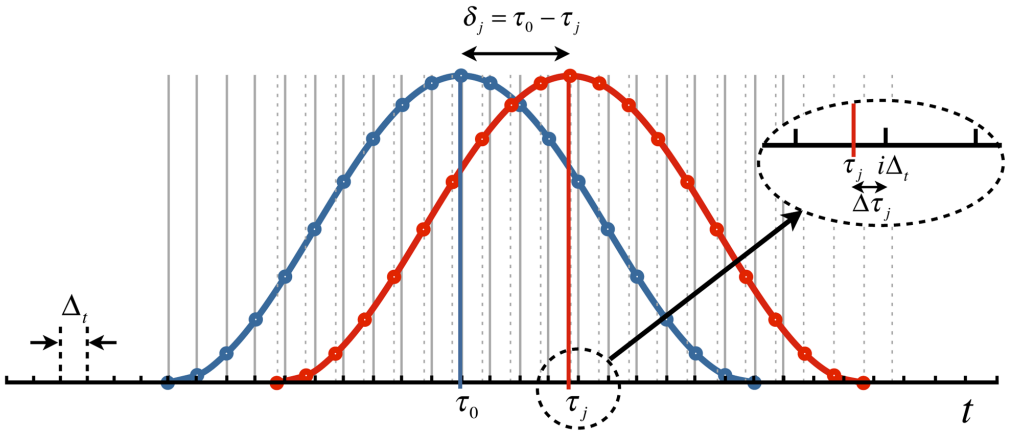

Figure 2.11: Description of the temporal array at the detectors. The blue line represents the envelope of the radiation arriving from the virtual charge placed at the center of the target, O, whereas the red line corresponds to the radiation from a charge j. In a first step the latter one is placed at the position of the array corresponding to $i\Delta_t$, but, in order to retain the whole information about the temporal propagation, the envelope is afterwards multiplied by $e^{i\omega\Delta\tau_j}$ in the spectral domain.

we include the change in the phase of the fundamental field as described in Eq. (2.34), using the ADK theory to compute the ionization probabilities –see Eq. (2.36)–.

On the other hand, table (2.2) points out the necessity of including the effect of neutral atoms in the propagation of the fundamental field if, for example, one wants to consider propagation lengths of the order of 1 mm at densitites of 10^{19} atoms/cm^3 in the near-IR regime in hydrogen. Depending on the element, the effect of the neutrals can be relevant even at lower densities, near absorption edges. In addition, the dispersion induced by the neutral atoms in the fundamental field is specially important in waveguide geometries [104, 110]. We include this effect in the fundamental field using the Sellmeier formula presented in Section 2.2.1 for different gases, taking into account that the gas jet is inhomogeneous and that the neutral density is time-dependent –see Eq. (2.38)–.

Once we have included the contributions to the refractive index due to the free charges and the neutral atoms, we also take into account the possibility of a group velocity different from the phase velocity, as explained by Eq. (2.66). Finally, we include absorption of the harmonics using Beer's law [98].

2.5 Discrete Dipole Approximation

2.5.1 Theoretical model

Even for low pressure densities (10^{18} atoms/cm^3), the number of target radiators in a typical interaction region is extremely high (of the order of 10^{12}). This means that, despite the use of efficient models for the computation of the single-atom dipole acceleration, the evaluation at every single radiator of the target becomes a formidable task. To overcome this limitation we shall use the Discrete Dipole Approximation (DDA) [111, 112], where the interaction volume is split into discrete spherical cells, each containing a macroscopic number of elementary radiators. Next we will see that it is possible to give a compact formula for the radiation of a finite cell, provided we know the dipole acceleration of an atom at its center. Therefore, for every macroscopic cell we will need only to compute one single-atom response. As the number of cells required to map the whole target is reasonable (about 10^5), this method reduces drastically the load of in computing macroscopic HHG.

In order to find an expression for the radiation of a finite spherical cell, the following conditions should be met:

(i) The number of dipoles enclosed in each cell is large enough to approximate the density by a continuous distribution. We shall then define a lower limit for the cell's size to enclose about 10 dipoles in each dimension, i.e. $d > 10 \times [1/n(\mathbf{r}_j)]^{1/3}$, d being the cell's diameter, $n(\mathbf{r}_j)$ the atomic density, and $\mathbf{r}_j$ the coordinate of the cell's center. For a gas density of 10^{18} atoms/cm^3, this lower limit is about 100 nm.

(ii) To avoid parasitic diffraction we shall circumvent the definition of sharp edges at the cell limits, defining the cell as a localized Gaussian distribution, $n(\mathbf{r}_j)V_{cell}g(\mathbf{r}')$ (V_{cell} being the cell's volume), with

$$g(r') = \frac{\pi^{3/2}}{\sigma^3} e^{-r'^2/\sigma^2} \tag{2.74}$$

If we define the cell diameter, d, at the FWHM of the density distribution, σ is related to the diameter as $d = 2\sigma\sqrt{ln2}$. On the other hand, $\mathbf{r}'$ is a coordinate on the local reference frame with origin O' at cell's center $\mathbf{r}_j$ (see Fig 2.12).

(iii) The size of the cells is small enough to approximate the external field as a local plane wave with a uniform intensity distribution in the cell's volume. Denoting W_0 a characteristic length for the variation of the intensity distribution of the external

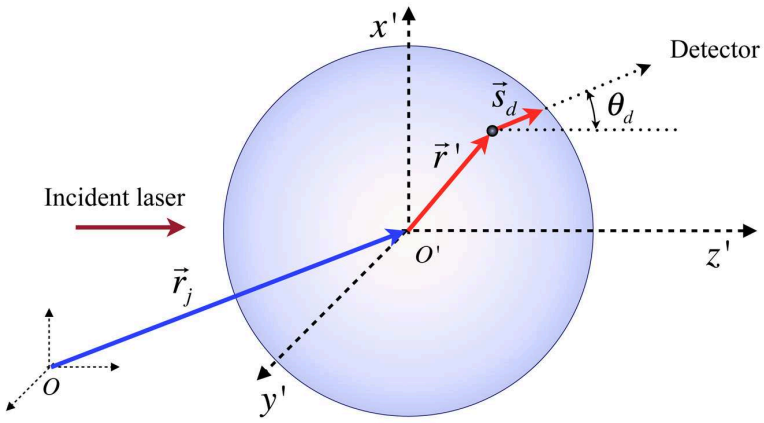

Figure 2.12: Scheme of the finite-size cell considered for the Discrete Dipole Approximation implementation. The direction towards the detector is defined by the vector $\mathbf{s}_d$. The local reference frame has its origin O' at the cell's center, $\mathbf{r}_j$, and it is oriented so that the z' axis coincides with the propagation direction of the local plane-wave field, and $\mathbf{s}_d$ has no y' component.

field, we shall define the upper limit of the cell's diameter as $d < 2W_0/10$. For the numerical results presented later in this section, we consider a Gaussian beam (see Eq. 2.23) whose beam waist is $W_0 = 30$ μm and, therefore, the cell's diameter d should not exceed 6 μm.

(iv) The total number of cells is determined by the ratio between the interaction region and the cell's volumes: $N_c \simeq V_{int}/V_{cell}$. In the practical case, however, the choice of the cell's location can be determined by a Monte Carlo method using the target's density distribution. Therefore, the computation can be stopped at any time, according to a convergence criteria, before scanning the total number of cells.

Denoting $\mathbf{E}_1(\mathbf{r}_j, t)$ the fundamental field at the center of the cell j, and assuming it as a local plane wave, the field at any neighbor point $\mathbf{r}'$ can be approximated by $\mathbf{E}_1(\mathbf{r}_j, t_{\mathbf{r}'})$, with $t_{\mathbf{r}'}$ the temporal lag associated to the distance from this point to O'. Since we choose the z' axis as the propagation direction of the local plane-wave, $t_{\mathbf{r}'} = t - z'/c$, the total field at the detector position $\mathbf{r}_d$ emitted by a single cell is given

by Eq. (2.70) as

$$\mathbf{E}_{i,j}(\mathbf{r}_d,t) \simeq \frac{n(\mathbf{r}_j)}{c^2|\mathbf{r}_d|}\int d\mathbf{r}' g(\mathbf{r}')\mathbf{s}_d \times \left[\mathbf{s}_d \times \mathbf{a}\left(\mathbf{r}_j, t-\frac{z'}{c}-\frac{|\mathbf{r}_d-\mathbf{r}'-\mathbf{r}_j|}{c}\right)\right] \tag{2.75}$$

where $\mathbf{a}(\mathbf{r}_j,t)$ is the dipole acceleration of an atom at O', that can be computed using the SFA+ approach. Note that this is a simplified form of the Mie rescattering theory [113], where the cells have diffused contours and, therefore, we do not include reflexions. In addition, in contrast to Mie theory, we assume the local propagation of the electromagnetic field inside the cell as a local plane wave.

For the case of isotropic radiators, the direction of the vector $\mathbf{a}(\mathbf{r}_j,t)$ is that of the driving field's polarization. The detector is assumed to be at an arbitrarily large distance from the interaction region, $|\mathbf{r}_d| >> |\mathbf{r}_j|$ (see Fig. 2.13).

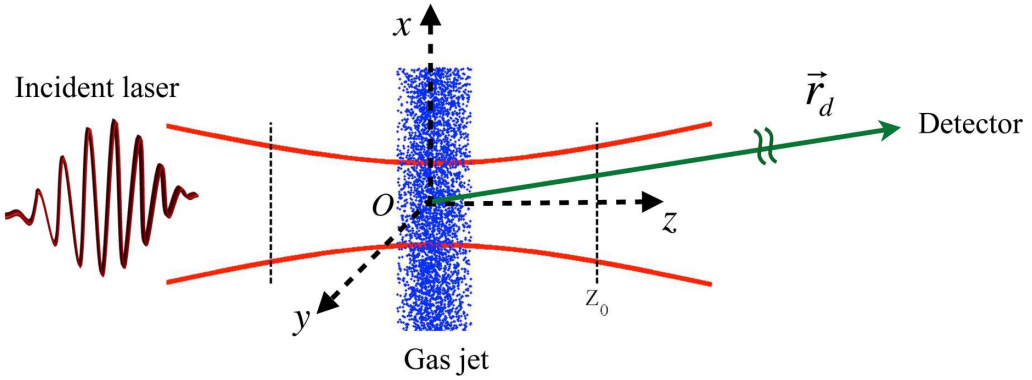

Figure 2.13: Scheme of the high-order harmonic experiment considered in this section, where a Gaussian beam is focused near the center of a gas jet. The coordinate origin, O, is located at the laser focus and the jet position is moved along the z axis.

With these assumptions, Eq. (2.75) can be integrated in the temporal frequency domain

$$\mathbf{E}_{i,j}(\mathbf{r}_d,\omega) \simeq \frac{n(\mathbf{r}_j)}{c^2|\mathbf{r}_d|}\int d\mathbf{r}' g(\mathbf{r}')\mathbf{s}_d \times \left[\mathbf{s}_d \times \mathbf{a}(\mathbf{r}_j,\omega)e^{i\omega(\frac{z'}{c}+\frac{|\mathbf{r}_d-\mathbf{r}'-\mathbf{r}_j|}{c})}\right] \tag{2.76}$$

Dropping constant terms, we have

$$\mathbf{E}_{i,j}(\mathbf{r}_d,t) \propto n(\mathbf{r}_j)\mathbf{s}_d \times \left[\mathbf{s}_d \times \mathbf{a}(\mathbf{r}_j,\omega)e^{-i\omega\frac{|\mathbf{r}_d-\mathbf{r}_j|}{c}}F(\theta_{d,j},\omega)\right] \tag{2.77}$$

where $F(\theta_{d,j},\omega)$ is a form factor defined as

$$\begin{aligned} F(\theta_{d,j},\omega) &= \lim_{|\mathbf{r_d}|\to\infty}\int d\mathbf{r}'g(\mathbf{r}')e^{i\omega(\frac{z'}{c}-\frac{|\mathbf{r}_d-\mathbf{r}'-\mathbf{r}_j|}{c}+\frac{|\mathbf{r}_d-\mathbf{r}_j|}{c})} \\ &= \int d\mathbf{r}'g(\mathbf{r}')e^{i\frac{\omega}{c}(z'-\mathbf{s}_d\cdot\mathbf{r}')} \end{aligned} \tag{2.78}$$

where $\mathbf{s}_d$ is the unitary vector pointing to the detector direction, and $\mathbf{s}_d \cdot \mathbf{e}_{z'} = cos\theta_{d,j}$, according with the chosen orientation of the local reference frame (see figure 2.12). Using the Gaussian distribution (2.74), the integral in (2.78) can be evaluated analytically, giving as a result

$$F(\theta_{d,j},\omega) \propto e^{\frac{1}{2}\frac{\omega^2}{c^2}\sigma^2(1-\cos\theta_{d,j})} \tag{2.79}$$

$\theta_{d,j}$ being the angle between the detector position and the propagation vector of the local field at the cell j. Note that Eq. (2.77) corresponds to the field emitted by a single radiator located at the cell's center $\mathbf{r}_j$, modulated by a form factor $F(\theta_{d,j},\omega)$ that takes into account the interfering contributions of the rest of the radiators in the macroscopic cell. In order to obtain the angle $\theta_{d,j}$, we compute $\cos(\theta_{d,j}) = \mathbf{k_j}\cdot\mathbf{s_d}$, being $\mathbf{k_j}$ the propagation vector of the local plane wave at the cell j. We assume the same propagation vector along the cell, whose value is computed at its center as $\mathbf{k_j} = \nabla\phi/|\nabla\phi|$, being ϕ the phase of the incident field at the center of the sphere.

Figure 2.14 shows the angular distribution of the high-order harmonic radiated spectra, in linear scale, (a) for a single radiator, and for cells of diameters (b) 10 nm, (c) 50 nm and (d) 500 nm. The radial axis corresponds to the harmonic order (starting at the 21st), whereas the angular scale is represented in degrees, $\theta = 0$ corresponding to the direction of propagation of the local plane wave fundamental field. Note that, as the cell's size increases, phase-matching is progressively restricted to the forward direction.

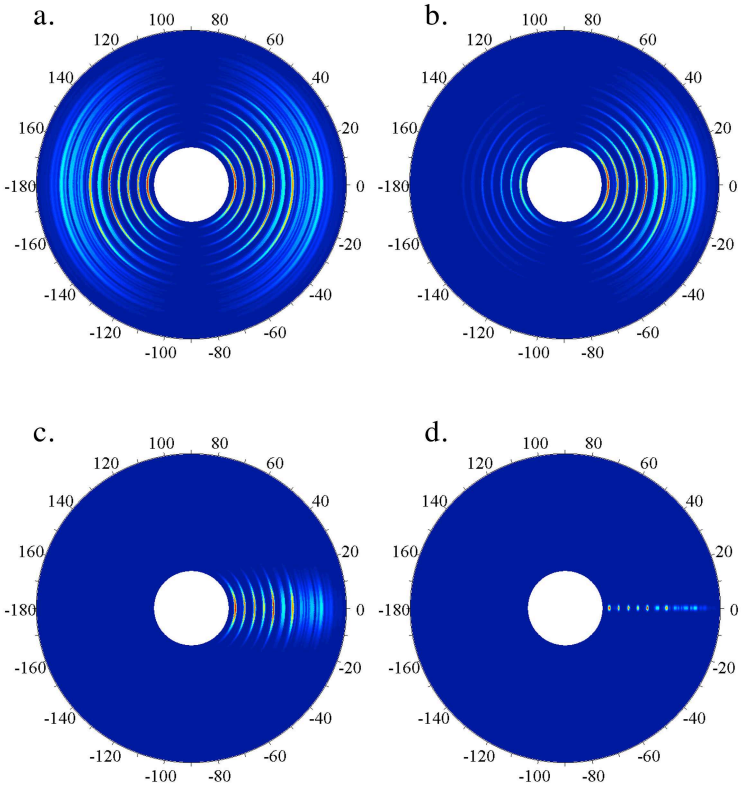

Figure 2.14: Angular distribution of the radiation spectra, in linear scale, **a** for a single radiator, and cells of **b** 10 nm, **c** 50 nm and **d** 500 nm diameter. The radial axis corresponds to the harmonic order (starting at the 21st). The angles are represented in degrees, $\theta = 0$ corresponding to the direction of propagation of the local plane wave fundamental field. The 800 nm laser pulse envelope is modeled as a $\sin^2$ function 8 cycles full temporal length and peak intensity 1.57×10^{14} W/cm^2.

2.5.2 Convergence and results

Let us now present some results of our calculation for the model experiment depicted in Fig. 2.13. We consider a low-pressure hydrogen gas jet interacting with an 800 nm laser pulse of 8 cycles (full temporal length) with a peak intensity of 1.57×10^{14} W/cm^2. For the description of the laser pulse, we have considered a Gaussian beam propagating in vacuum, but including the effect of the ionized electrons in the refractive index –as in Eq. (2.33)–. The beam waist is $W_0 = 30$ μm, and hence the Rayleigh range is z_0=3.5 mm. We shall define $z = 0$ as the focus position in the propagation axis z.

The gas jet, directed along the x-axis (perpendicular to the field propagation), is

modeled by a Gaussian distribution along the y and z dimensions, and a constant profile along its axial dimension, x. Therefore, the atom density distribution is given by

$$n(y,z) = n_0 e^{-\frac{(y-y_c)^2}{2\sigma_y^2}} e^{-\frac{(z-z_c)^2}{2\sigma_z^2}} \tag{2.80}$$

where n_0 is the maximum gas density over the interacting volume, and y_c, z_c are the coordinates of the center of the beam axis with respect to the laser focal point. The quantities σ_y and σ_z are the full width half maximum of the gas jet distribution in each direction respectively. Figure 2.15 shows the particular example where the gas jet is placed 2 mm before the focus of the beam (i.e. $z_c = -2$ mm), with $\sigma_z = 500$ μm. In the transversal direction, the parameters of the Gaussian distribution are $y_c = 0$ μm and $\sigma_y = 500$ μm. We implement the Monte Carlo method to determine the position of the cells in the sample.

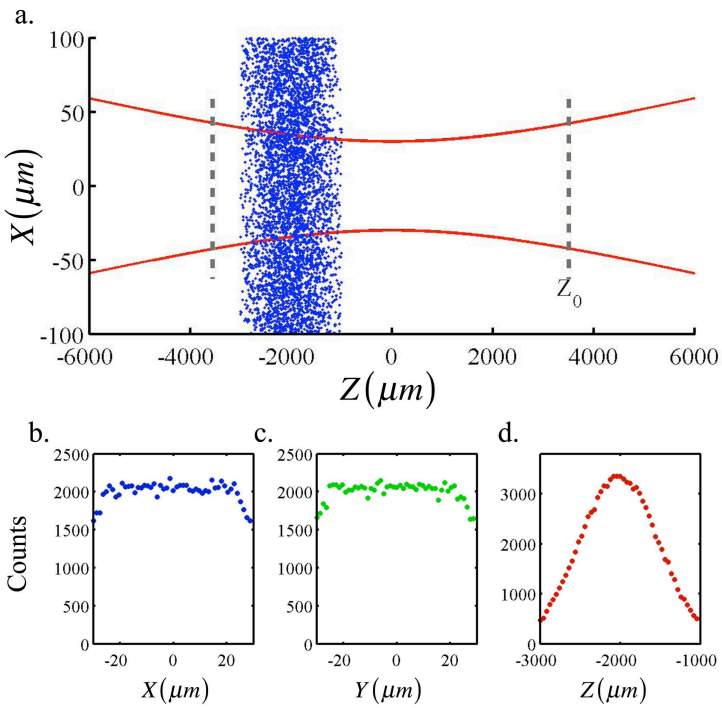

Figure 2.15: Cell distribution resulting from the Monte Carlo method using the Gaussian density (2.80) with the following parameters: $y_c = 0$, $z_c = -2$ mm, $\sigma_y = 500$ μm and $\sigma_z = 500$ μm. In **a** we plot the x-z distribution, while in **b** to **d** we plot the distributions along each dimension. The beam waist of the fundamental beam is $W_0 = 30$ μm and the Rayleigh range, marked with the dashed line in **a**, results z_0=3.5 mm.

As we discussed in section 2.5.1, for the particular example considered here, the diameter of the discrete cells must be enclosed in the interval 100 $nm < d < 6$ μm. Although the final result is independent on the actual choice within this interval, the use of smaller diameters dilates the computing time, as the same convergence goal is attained for a larger number of cells. This is illustrated in Fig. 2.16 where we present results for three different cell diameters. The first column shows the results of the bare problem, i.e. a collection of point dipoles, while columns 2 to 4 present the results of the DDA computations using cells with diameters 1, 2 and 3 μm respectively. The convergence of each case is illustrated through the different rows, which correspond to a different number of cells. Note that for 10^5 cells (6th row) all cases have converged, including the bare case. On the other hand, it becomes evident that using cells of larger diameter reduces the convergence time. In particular, for the choice of 3 μm it is sufficient to consider 10^4 cell's to obtain good results, that means a reduction of computing time of one order of magnitude in comparison with the bare dipole case.

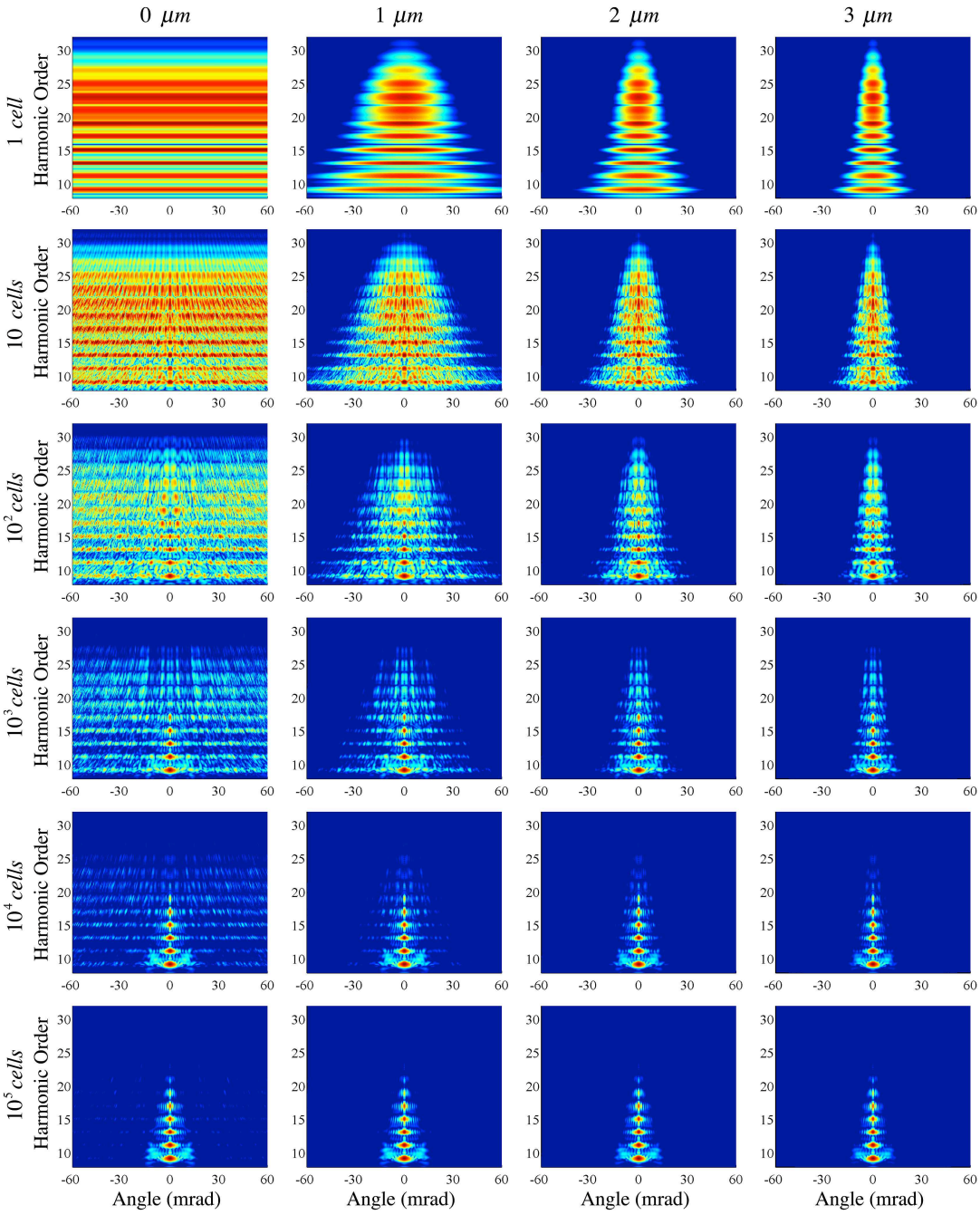

Figure 2.16: Angle-resolved high-order harmonic spectra for different numbers and sizes of the spherical cells within the DDA. On the column on the left, the simulation is done without the DDA approximation, that is, considering point atoms. On the others columns, from left to right, we have used spherical cells of diameters 1, 2 and 3 μm. The rows correspond to computations using different number of cells: in the first row we have 1 sphere, while 10, 10^2, 10^3, 10^4 and 10^5 spheres are considered in the following ones. The gas jet is placed 1 mm before the focus of the laser beam. The laser pulse is 8 cycles (full temporal length) at 800 nm with a peak intensity of 1.57×10^{14} W/cm^2.

3

Generation and propagation of high-order harmonics from near-IR fields in rare gas targets

There are three main geometrical setups for obtaining high-order harmonics from the laser-gas interaction. In the first observations of HHG, a tight focus was needed to reach an intensity high enough to ionize a noble gas atom [13, 14]. For that purpose, a near-infrared laser beam was focused perpendicularly to a gas jet of few millimeters width. With the advance of intense laser technology, short laser pulses were produced with enough energy to allow for loose focusing geometries [99, 114, 115]. In this case, the target extension can be increased, and gas cells and waveguides can be used, allowing to exploit the details of propagation phase-matching to optimize the efficiency of the HHG [9].

In this chapter, we study the high-order harmonic generation and propagation processes from near-infrared laser sources in gas jets and cells. We shall consider Ti:Sa laser systems, i.e., those with wavelength near 800 nm, and, as targets, low-density jets of hydrogen and argon, and cells filled with low-pressure xenon, the typical density being 10^{17}- 10^{18} atoms/cm^3 in both cases. Figure 3.1 shows schematically both configurations. We will use the SFA+ method [41] for computing the single-atom emission (see section 1.3), whereas for the harmonic propagation we will use the integral solution of Maxwell's equations combined with the DDA method (see section 2.5.1). The gas jets are modeled using a Gaussian distribution along the y and z dimensions, and a

3. GENERATION AND PROPAGATION OF HIGH-ORDER HARMONICS FROM NEAR-IR FIELDS IN RARE GAS TARGETS

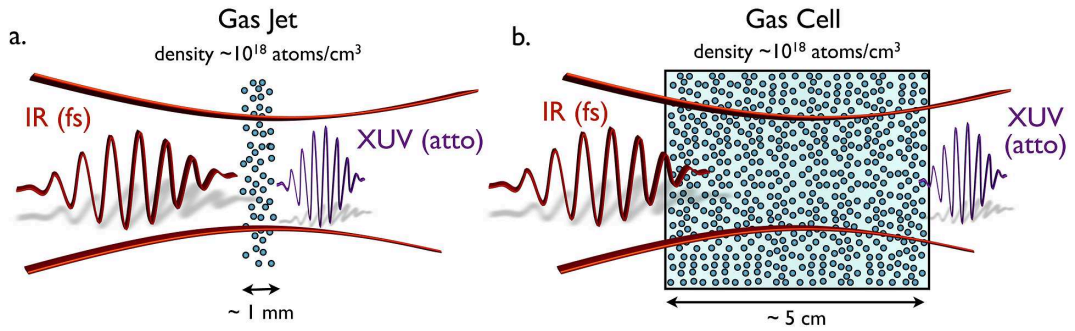

Figure 3.1: Scheme of the HHG process driven in **a** a gas jet and **b** a gas cell. The rare gas density is approximately 10^{18} atoms/cm^3, whereas the target size in a gas jet is below one millimeter, and in the gas cell of a few centimeters. .

constant profile along the axial direction, x, as given by Eq. (2.80). On the other hand, the gas distribution in a cell will be consider constant.

In the following we will present the original results of our theoretical methods, that will be compared with different experimental results, from ours and other groups.

We have divided this chapter in four sections. First of all we analyze the effect of the different contributions to phase-matching in a gas jet, using a tight focusing configuration. We will discuss on-axis and off-axis harmonic detection. In this latter case, quantum path interferences are known to play an important role in the angular far-field profile of the high-order harmonics. We shall then introduce our experimental setup for high-order harmonic generation and use the laboratory results to validate our simulations. In section 3.2 we will investigate theoretically the characteristics of the attosecond pulses obtained from HHG under different phase-matching conditions, in particular, the dependence of the pulse width with the angle of detection. In section 3.3 we will differentiate between longitudinal and transversal phase-matching. For this, we shall introduce the spatial map of the harmonic emission as an original theoretical tool to study the phase-matching process. By studying theoretically and experimentally the effect of aperturing the laser beam in the efficiency of the harmonic signal, we will identify the relevance of the transversal coherence length. Finally, in section 3.4 we will study the HHG process in a xenon semi-infinite gas cell, where not only phase-matching but absorption is relevant, and we will compare the theoretical results directly with the experiments made in the group of M. Kovačev in Universität Hannover, with which we have been collaborating.

3.1 Phase-matching for different target positions along the propagation axis

In this section we study the propagation of high-order harmonics generated in the interaction between a focused laser beam and a gas jet. First, we shall concentrate of the different aspects of the phase-matching process when detecting the harmonics on-axis. Secondly, we will study the dependence of phase-matching with the observation angle, that is, the angular profile of the emitted radiation. Finally we will present experimental results for different target positions along the propagation axis.

3.1.1 On-axis phase-matching

In a gas jet configuration, the typical width of the gas jet falls between 0.1 to 1 mm, and the gas densities between 10^{17} to 10^{18} atoms/cm^3. In this situation, the phase of the high-order harmonics can be facorized into three different contributions: (i) the Gouy phase associated to the Gaussian laser beam (see Section 2.3.1), (ii) the intrinsic phase, which depends mainly on intensity and is a consequence of the rescattering mechanism for harmonic generation in the single-atom (see Section 2.3.3), and (iii) the dephase produced in the fundamental field by the presence of free electrons (see Section 2.3.2), which is imprinted to the harmonics as a result of the non-linear process of harmonic generation. Therefore the phase-mismatch function for the qth-order harmonic detected on-axis –see Eq. (2.48)– can be approximated by

$$\Delta k_q \simeq \Delta k_q^{Gouy} + \Delta k_q^{int} + \Delta k_q^{f} \simeq \frac{q-1}{z_0} + \alpha_q^i \frac{\partial I(z)}{\partial z} + \frac{q e^2 n_f \lambda_0}{mc^2} \tag{3.1}$$

where z_0 is the Rayleigh distance, $I(z)$ the laser intensity distribution along the propagation axis, α_q^i a constant that depends on the rescattering trajectory that generates the harmonic (i), and n_f the density of free electrons in the gas.

Our computational method allows to naturally isolate the contributions of the different target points to the total harmonic spectrum. Therefore, it is possible to analyze the local phase of the field emitted. In addition, some physical contributions to phase-matching can be switched on and off (for instance, ionization). As a consequence, our theoretical tool allows us to analyze with detail the phase-matching phenomena in different situations.

Role of the Gouy and intrinsic phases

Let us isolate the Gouy and intrinsic contributions in the high-order harmonics, thus neglecting the influence of the free electrons in the phase-matching process. We consider a 800 nm laser pulse, whose envelope is modeled by a $\sin^2$ function, 8 cycles full temporal length (2.9 cycles FWHM) and 1.57×10^{14} W/cm^2 peak intensity. The pulse propagates as a Gaussian beam of waist $W_0 = 30$ μm, thus resulting in a Rayleigh range of z_0=3.5 mm. In Fig. 3.2 we plot the phase of the 21st harmonic (blue line) along the propagation axis, separated into two contributions, the Gouy phase (red line) and the intrinsic phase (green line). The comparison between these two contributions shows that, while the Gouy phase always decreases with the distance, the intrinsic phase, which depends on the intensity gradient, is symmetric with respect to the laser focal point. Therefore, the phase-mismatch resulting from the Gouy phase is always positive, while that coming from the intrinsic phase changes from positive to negative at the focus –see equation (3.1)–. As a consequence, when the target is located after the focus, the opposite behavior of the intrinsic and Gouy phases compensates, and results in an efficient phase-matching.

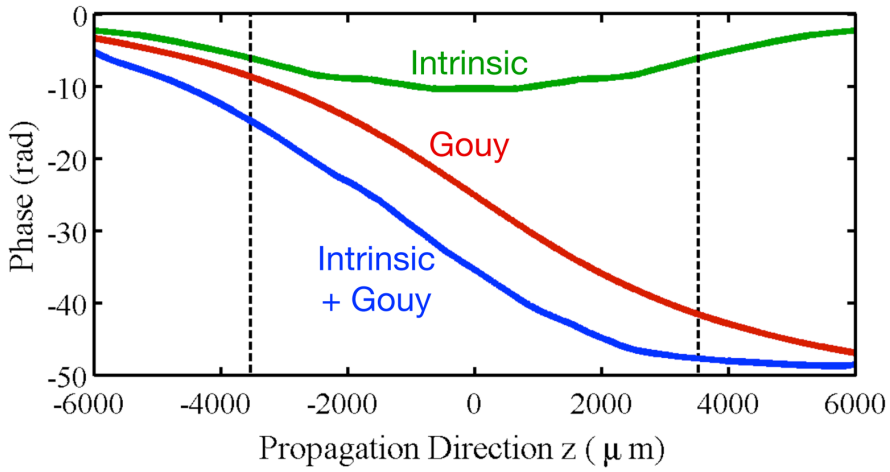

Figure 3.2: Spatial distribution of the Gouy (red line), intrinsic (green line), and both (blue line) phase contributions to the 21st harmonic generated in hydrogen along the propagation axis z, for a 800 nm laser pulse of 8 cycles full temporal length (2.9 cycles FWHM) and 1.57×10^{14} W/cm^2 peak intensity. The beam waist is $W_0 = 30$ μm and the Rayleigh range (dashed line) results z_0=3.5 mm.

In Fig. 3.3 we plot the phase of the 17th and 21st harmonics (blue line in 3.3a and 3.3b), and the local coherence length –i.e., the inverse of the spatial derivative of the phase (2.46)– along the propagation axis (pink line in 3.3c and 3.3d). We can observe for both harmonics how the coherence length is longer for $z > 0$, while shorter for $z < 0$, thus obtaining better phase-matching conditions when the gas jet is placed after the focus position.

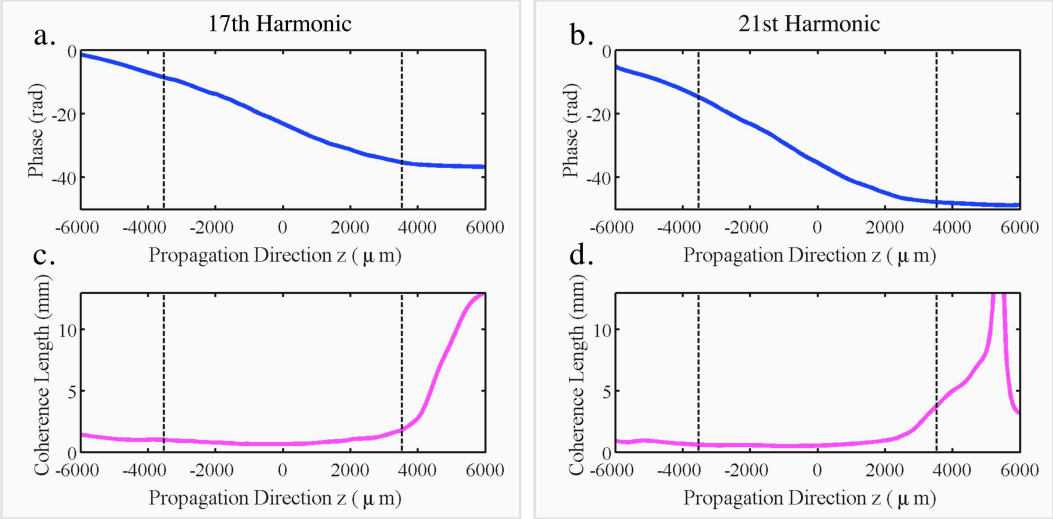

Figure 3.3: Spatial distribution of the Gouy and intrinsic phase contributions (blue line) to the 17th (left column) and 21st (right column) harmonics generated in hydrogen along the propagation axis z. In the plots below (pink lines) we show the local coherence lengths. The laser pulse is 8 cycles full temporal length (2.9 cycles FWHM), 800 nm in wavelength and 1.57×10^{14} W/cm^2 peak intensity. The beam waist is $W_0 = 30$ μm and the Rayleigh range (dashed lines) results z_0=3.5 mm.

Let us compute the harmonic spectra for these two different jet positions. For this, we shall consider an hydrogen gas jet, whose parameters were described in Fig. 2.15. We show in Fig. 3.4 the harmonic spectra centering the gas jet 4 mm after (purple line) and before (light blue line) the focus position. We can observe that for the higher-order harmonics ($q \geqslant 19$) there is a substantial enhancement of the yield when the gas jet is placed after the focus. This is explained by observing Figs. 3.3c and 3.3d, where the variation of the coherence length from before to after the focus increases for the higher-order harmonics.

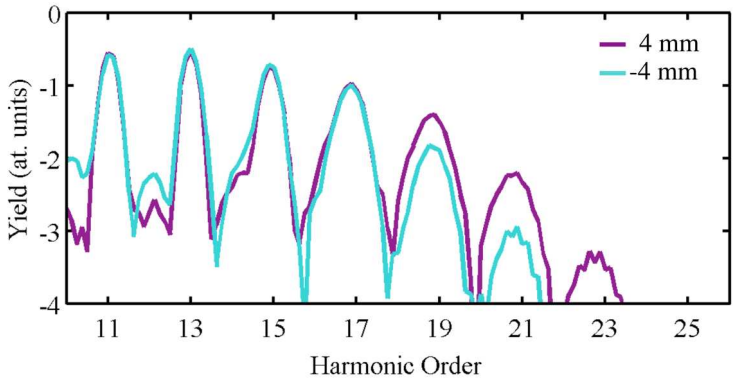

Figure 3.4: Harmonic spectra for a gas jet configuration where the target was centered 4 mm after (purple line) and before (light blue line) the focus position. The laser pulse is 8 cycles full temporal length (2.9 cycles FWHM), 800 nm in wavelength and 1.57×10^{14} W/cm^2 peak intensity. The beam waist is $W_0 = 30$ μm and the Rayleigh range results z_0=3.5 mm. The gas jet is modeled by a Gaussian distribution –see Eq. (2.80)– whose widths are $\sigma_y = 500$ μm and $\sigma_z = 500$ μm.

On the other hand, if the beam waist is increased, the Rayleigh range will be also increased, and the variation of the harmonics phase along the propagation axis would be lower for a fixed jet width, thus favoring phase-matching conditions. For that reason, long focal lengths are usually employed for efficient high-order harmonic generation.

Role of the free electrons

As described in section 2.3.2, the contribution of the free electrons in the refractive index of a rare gas has to be taken into account for propagation lengths of the order of a few millimeters or even below, becoming especially important if the gas jet is placed close to the focus of the beam, where the intensity is maximum. We implement in our code the time-dependent ionization in the pulse propagation through the gas jet as described in 2.2.2. Note that for the densities and propagation lengths discussed in this section, we can neglect the contribution to the refractive index from the neutral atoms.

In Fig. 3.5 we plot the phase of the 21st harmonic in two different situations. In 3.5a the gas jet is placed 2 mm before focus, while in 3.5b it is placed 2 mm after the focus. In both figures we have represented the different contributions to the phase: (red

line) the Gouy phase, (green line) the intrinsic phase, (blue-dashed line) the sum of the Gouy and the intrinsic phase, and (pink line) the total phase, including also ionization, i.e. the effect of the free electrons. Plots 3.5c and 3.5d show the local coherence length along the propagation length, corresponding to the cases (a) and (b) respectively. At the background, the grey line represents the atom distribution along the propagation axis, whose shape is the same as the one considered in the previous section, and peak density is 10^{18} atoms/cm^3.

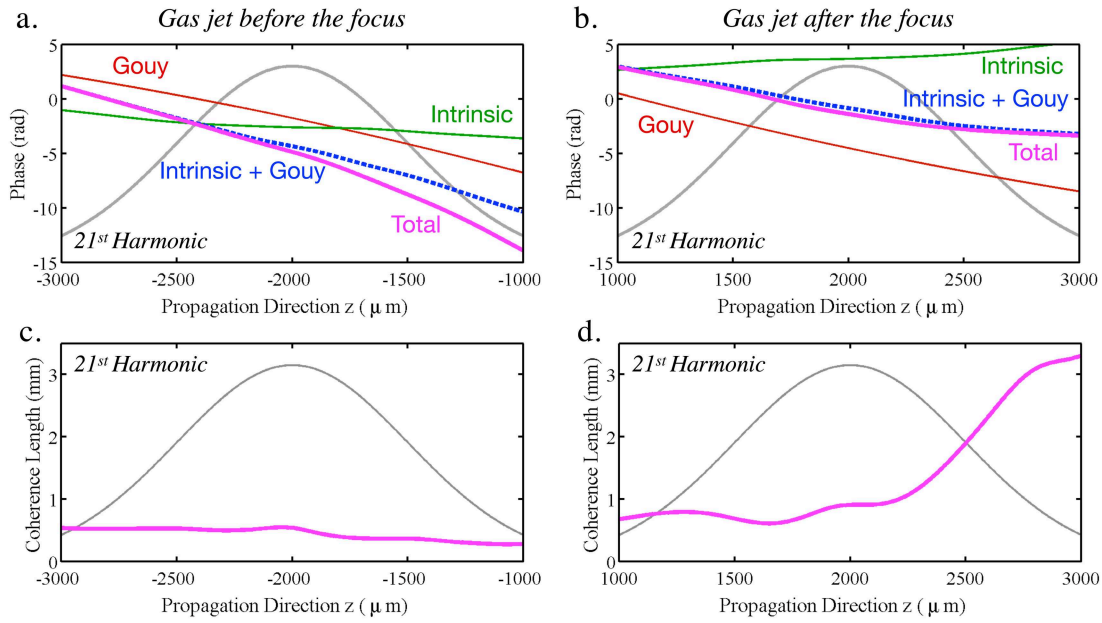

Figure 3.5: Spatial distribution of the phase of the 21st harmonic along the propagation axis z when the gas jet is placed **a** before, $z_c = -2$ mm, and **b** after the focus position, $z_c = 2$ mm. The different contributions to the phase are plotted as follows: (red) the Gouy phase, (green) the intrinsic phase, (dashed-blue) the sum of the Gouy and the intrinsic phase and (pink) the total phase, including also ionization, i.e. the effect of the free electrons. Plots **c** and **d** represent the local coherence length –i.e., the inverse of the spatial derivative of the phase– of the 21st harmonic along the propagation axis z when the gas jet is placed 2 mm before and after the focus respectively (pink lines). At the background, the light grey line represents the gas jet profile along the propagation axis, whose peak density is 10^{18} atoms/cm^3.

From Fig. 3.5a, we observe that, if the gas jet is located before the focus, the dephase induced by free charges has a strong contribution, increasing the spatial variation of the total phase along the propagation axis (blue line). On the other hand, when the gas jet is located after the beam focus (Fig. 3.5b), the addition of the phase induced by free charges to the total phase (pink line) does not affect this latter dramatically the total phase without it (dashed-blue line). Figures 3.5c and 3.5d show that the difference in coherence lengths before and after the focus is even higher.

Let us now analyze in detail the contribution of the ionization (i.e. free electrons) to the phase of the harmonics. At a fixed time t_f, the phase-shift imprinted by the ionized electrons in the propagation of the fundamental field (2.33) can be split into two terms that depend on the propagation distance: (i) the integration of the atomic density, $\int_{-\infty}^{z-v_g t_f} n_0(x,y,\xi)d\xi$, and (ii) the ratio for ionized electrons, $P_f(\mathbf{r}, t_f - z/v_g)$, whose dependence on the position is given by the electromagnetic field strength. In Fig. 3.6 we analyze both terms separately for three cases, where the gas jet is centered in the focus, 2 mm before and 2 mm after the focus position, fixing t_f at the end of the laser pulse. As the gas jet is the same, the integration of the atomic density over the propagation distance is the same for the three cases (see 3.6a), whereas the ratio for ionized electrons becomes different, as the intensity profile is different in all the cases (see 3.6b). These two terms are multiplied when obtaining the total phase of a given harmonic. We can observe how, when the gas jet is placed before the focus, both terms add up together, thus implying an increasing of the variation of the harmonic phase over the propagation distance (see 3.6c). In contrast, when the gas jet is placed after the focus (see 3.6e), both terms tend to compensate, so the harmonic phase is almost transparent to ionization.

Obviously, from the considerations above, one can deduce that an increase in the atomic density of the gas jet will enhance the effect of the ionization in the harmonic phases, thus increasing the difference between placing the jet before or after the focus position.

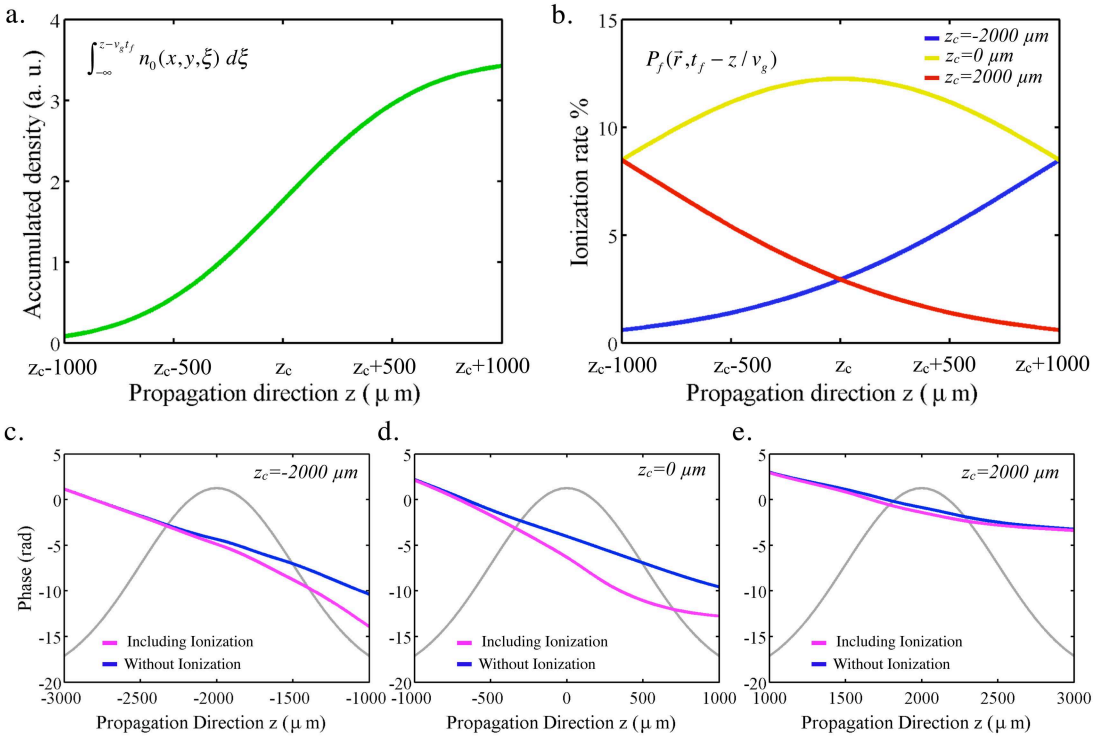

Figure 3.6: **a** Integration of the atomic density, $\int_{-\infty}^{z-v_g t_f} n_0(x,y,\xi)d\xi$, at the end of the laser pulse (t_f), for a gas jet centered at z_c and whose width in the longitudinal axis is given by $\sigma_z = 500\ \mu m$. **b** Ratio for ionized electrons, $P_f(\mathbf{r}, t_f - z/v_g)$, for a gas jet centered 2 mm before (blue line), 2 mm after (red line) and on (yellow line) the focus position. The phase of the 21st harmonic with (pink line) and without (blue line) ionization is represented for a gas jet placed **c** 2 mm before **e** 2 mm after and **d** on the focus position. The peak atomic density is 10^{18} atoms/cm^3.

3.1.2 Off-axis phase-matching: modifying the contrast of the quantum path interferences

As it was explained in section 1.1.4, in each half cycle of the laser pulse there are two possible electron trajectories leading to the same kinetic energy at recollision, and therefore two possible semiclassical paths for the generation of the same harmonic (each named accordingly to the excursion time as *short* and *long* trajectory). Accordingly to the Feynmann description, each semiclassical trajectory has associated a phase corresponding with the mechanical action. Since this phase is translated to the harmonic radiation, the final harmonic emission reflects the interference between the contributions

of the short and long trajectories. The first experimental evidence of the interference between different quantum paths was demonstrated by A. Zaïr *et al.* [69].

There are different approaches for controlling or selecting the trajectories. At the single-atom level, two-color laser fields have been used extensively for control the electron trajectories in order to enhance the harmonic emission [116, 117, 118] or improve the attosecond pulse generation [67, 119]. Other methods to control the quantum path dynamics use a polarization gate [53, 120] or the overlap of two replicas of the same laser pulse to extend the harmonic cut-off [121].

In addition, it is possible to control each quantum path contribution macroscopically as follows. The phase associated to each trajectory contribution (i) for the qth-order harmonic can be approximated by the product of the ponderomotive energy U_p by the excursion time τ_q^i, as $\phi_q^i \simeq -U_p\tau_q^i \simeq -\alpha_q^i I$. As a consequence, the phase of each trajectory contribution is proportional to the laser pulse intensity (I), by a factor of α_q^i. This factor is larger for long (L) trajectories rather than short (S) ones ($\alpha_q^L > \alpha_q^S$), i.e., the variation of the intrinsic phase of the long trajectories along the propagation axis is higher than the short ones [64].

It is already known [48, 71, 100] that when the target is positioned after the focus, phase-matching favours only short trajectories, becoming the dominant at all detection angles. In contrast, when the target is located before the focus, both trajectories are present, being the short ones the dominant on-axis, whereas as the angle of detection increases, the contribution of long trajectories becomes gradually important. Therefore, when the target is positioned before the focus, there is a range of detection angles in which the contributions of both trajectories to the harmonic spectrum are comparable. This effect is easily explained if we look at the phase-mismatch for each family of trajectories. In the one-dimensional approach, and neglecting the effect of neutral atoms, if we detect the qth-order harmonic at an angle θ from on-axis, the phase-mismatch function (see Eq. 2.48) becomes

$$\Delta k_q \simeq \frac{q-1}{z_0} + \alpha_q^i \frac{\partial I(z)}{\partial z} + \frac{qe^2 n_f \lambda_0}{mc^2} - \frac{q\omega_0}{2c}\theta^2 \tag{3.2}$$

The angle of detection θ adds a new degree of freedom for controlling phase-matching conditions. If we place the gas jet before the focus, the intrinsic phase-mismatch is positive, $\alpha_q^i \partial I(z)/\partial z > 0$, and can be compensated by the contribution of the angle of detection, which is negative, $-q\omega_0\theta^2/2c$. As ($\alpha_q^L > \alpha_q^S$), short trajectories

would be better phase-matched for low angles of detection, whereas long trajectories for higher angles. As a consequence, by changing the angle of detection one can change the phase-matching conditions separately for each family of trajectories, and thus control macroscopically the weight of each trajectory contribution. On the other hand, if the target is located after the focus, the intrinsic phase-mismatch is negative, $\alpha_q^i \partial I(z)/\partial z < 0$, so short trajectories will be always better phase-matched in the whole angular profile.

Figure 3.7 shows the angle-resolved high-order harmonic spectra as resulting from our simulations when the gas jet is placed 2 mm (a) before and (b) after the focus. In correspondence with the above discussion, on-axis we can observe an enhancement of high-order harmonics when the gas jet is placed after the focus. When looking at higher angles of detection, we can observe some rings appearing in the harmonic profile when the gas jet is placed before the focus position (see Fig. 3.7a). These structures correspond to situations in which both short and long trajectories interfere with the same weight. On the other hand, when the gas jet is placed after the focus (Fig. 3.7b), there is no interference structure, since the short trajectory contributions dominate at all angles. These results are in agreement with theoretical and experimental results presented by other authors, using also different methods for computing propagation [70, 85, 108, 122].

Another issue that we can observe in Fig. 3.7 is the reduction of the cut-off frequency due to propagation. As we have seen in section 1.1.3, the theoretical value for the maximum emitted frequency in single-atom high harmonic generation corresponds to $I_p + \kappa U_p$ being $\kappa = 3.17$ [123]. In hydrogen, with the parameters of our simulation, this corresponds to the 28th harmonic. Nevertheless, in figure 3.7 we can observe that propagation mismatch reduces the maximum harmonic below 28th, and near 21st. This value will correspond to $\kappa \simeq 2$, which is in good agreement with the experimental observation in [124].

For the sake of completeness we represent in Fig. 3.8 the angular profile of the high-order harmonics for five different positions of the gas jet with respect to the focus position. We can observe how the interference pattern between short and long trajectories disappears as we place the gas jet further after the focus position. In addition, the highest harmonics (17th to 27th) are substantially enhanced, and present a wider angular structure when placing the gas jet after the focus position.

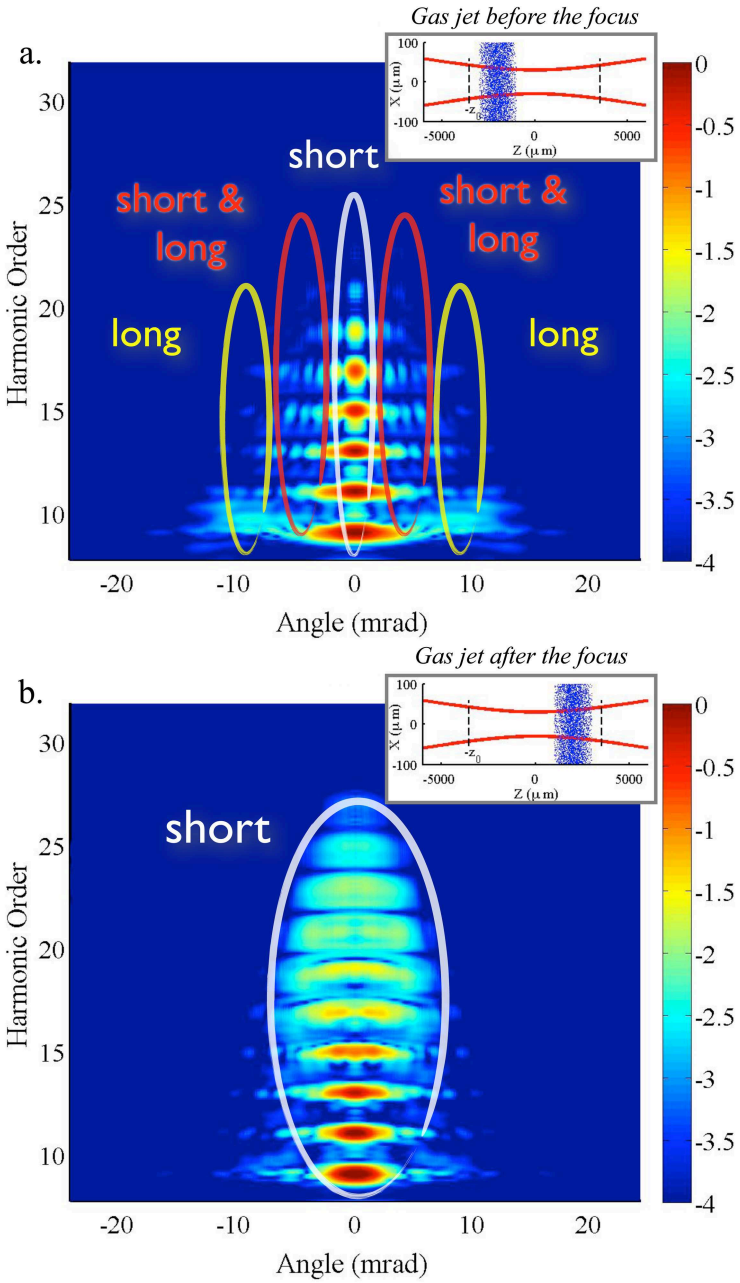

Figure 3.7: Angle resolved high-order harmonic spectra when the hydrogen gas jet is placed 2 mm **a** before and **b** after the focus of the laser beam (see the insets of the figures). The laser pulse is 8 cycles full temporal length (2.9 cycles FWHM) at 800 nm with a peak intensity of 1.57×10^{14} W/cm^2, with a beam waist of $W_0 = 30$ μm. The color scale represents the yield of the harmonics in arbitrary units (log. scale).

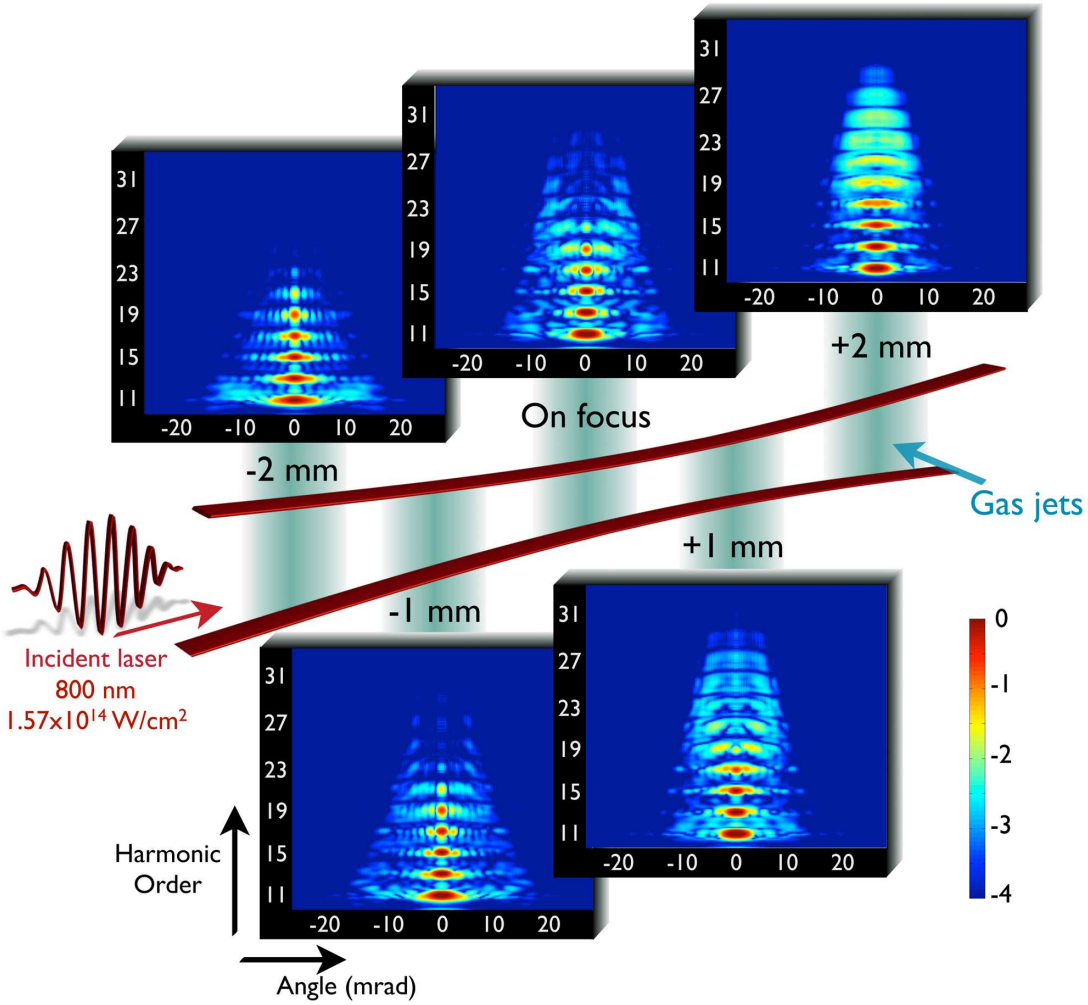

Figure 3.8: Angle resolved high-order harmonic spectra when the hydrogen gas jet is placed at positions -2 mm, -1 mm, 0 mm, 1 mm and 2 mm respect to the focus position. We represent the divergence angle (mrad) in the horizontal axis, whereas the harmonic order in the vertical axis. The laser pulse is 8 cycles full temporal length (2.9 cycles FWHM) at 800 nm with a peak intensity of 1.57×10^{14} W/cm^2. The beam waist is $W_0 = 30\ \mu m$. The color scale represents the yield of the harmonics in arbitrary units (log. scale).

In figure 3.9 we show the variation of the angular profile of a particular harmonic when the position of the gas jet is varied continuously along the propagation axis. The variation of the angular profile is represented for the (a) 17th, (b) 19th, (c) 21st and (d) 23rd harmonics. As discussed above, the ring structures appear for target positions before or at the focus, while after the focus the angular structure becomes smoother. The figure also describes the variations of the intensity of the radiated harmonics with the location of the target. As we can observe, the higher the harmonic is, the more contrast exists between the signal of the harmonic before and after the focus. While in the 17th harmonic this difference is not very important, as we increase the order of the harmonic, it becomes critical, as for example in the 23rd harmonic, where there is no signal before the focus.

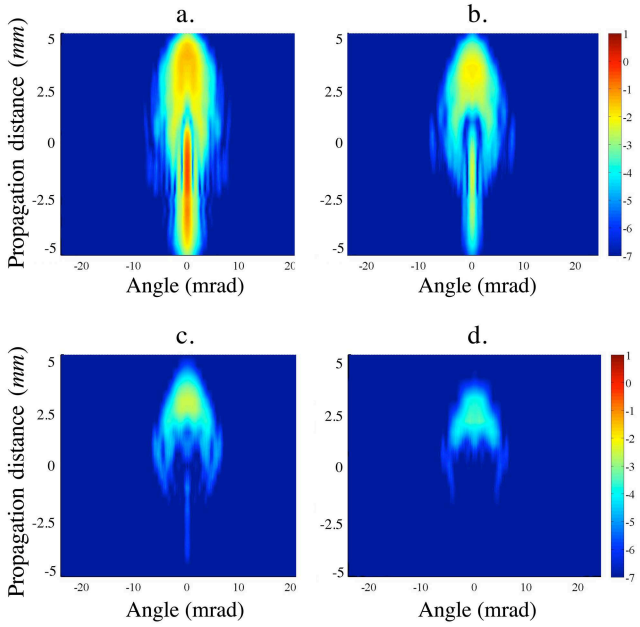

Figure 3.9: Spatial profile of the **a** 17th, **b** 19th, **c** 21st and **d** 23rd harmonics when the gas jet is placed in different positions relative to the focus position, along the propagation axis.

Finally, a further insight of this process can be gained performing the time-frequency analysis (see section 1.3.2) of the harmonic spectra at different detection angles presented in Fig. 3.7. We integrate the harmonics over a spatial window of 0.5 mrad in the far field profile for each detection angle. The time-frequency analysis is performed

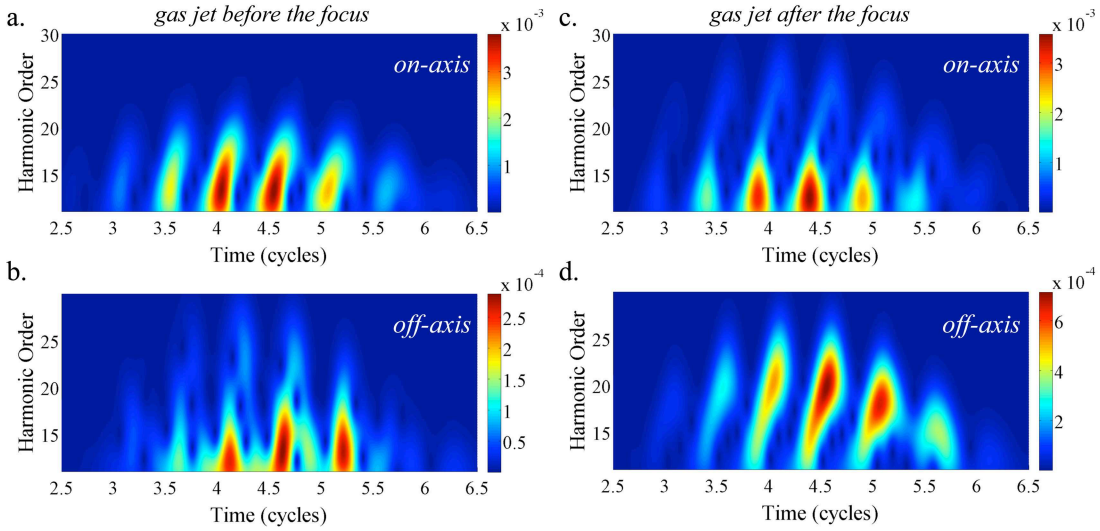

Figure 3.10: Time-frequency analysis of the filtered harmonics of the spectra presented in Fig. 3.7, when they are detected in a window on-axis (first row) and at 4.5 mrad (second row). From left to right, the gas jet is placed 1 mm before/after the focus position. The temporal axis is in units of the laser cycle. The laser pulse is 2.9 cycles FWHM, at 800 nm with a peak intensity of 1.57×10^{14} W/cm^2.

using a frequency window of length $3.5\omega_0$, ω_0 being the frequency of the fundamental field. On the left column of Fig. 3.10, we show the time-resolved emission of the high harmonics (a) on-axis and (b) at 4.5 mrad, when the gas jet is placed 2 mm before the laser focus. On the right column, the same angles are used but with the target 2 mm after the focus.

We can observe that when the harmonics are detected on-axis (Figs. 3.10a and 3.10c), the electron's recollision energy shows a roughly linear dependence on time, in which the lower harmonics are emitted before the higher ones, giving rise to a positive chirp typical from the harmonic spectrum emitted by short trajectories. This situation is also present in 3.10d, thus confirming that when the gas jet is placed after the focus position, the short trajectory contributions dominate for all detection angles. In contrast, in 3.10b we observe how the time-frequency structure is more complex, with contributions with both positive and negative slopes, thus confirming the existence of both short and long quantum paths. In addition, we can distinguish regions where the signal is minimum, coming from the interference between short and long trajectory contributions.

Ring structures in the angular profile of the harmonics

In the considerations above we have identified the spatial interference between the short and long trajectory contributions when changing the angle of detection. However, both contributions also interfere in the spectral domain. The spectral distribution of the qth-order harmonic generated with a driving laser field of frequency ω_0, is different for the short and long trajectory contributions (see section 1.2.2). For instance, the short contribution is dominant in the vicinity of the exact harmonic frequency $q\omega_0$, whereas, the long contribution is spread over a wider spectral window as causes a larger chirp in the spectrum. As a consequence, the interference of both trajectory contributions gives rise to the appearance of annular rings in the angular spectra of the harmonics.

In order to show these ring structures, we plot in Fig. 3.11a the angular profile of the high-order harmonics generated in an argon gas jet of density 10^{18} atoms/cm^3. The laser pulse is 32 cycles full temporal length (30 fs FWHM) at 800 nm with a peak intensity of 2×10^{14} W/cm^2, with a beam waist of $W_0 = 20$ μm. The gas jet is placed 1 mm before the focus position, favoring the interference between short and long trajectory contributions off-axis. As we can observe in detail in Fig. 3.11c, annular rings are observed in the angular profile, in excellent agreement with previous theoretical and experimental findings in the literature [71, 73, 125]. In Fig. 3.11b we plot the high-harmonic spectrum integrated over the detection angle, where we can distinguish the wider and lower distribution of the long paths (red dashed line) and the narrower and higher of the short paths (green dashed line).

On the other hand, ionization causes a blue-shift in the harmonic spectrum [126], due to the chirp imprinted during the propagation of the fundamental field in the medium. The blue-shift is larger for long contributions than short ones. As a consequence, the ring structures in the spatial profile of the harmonics are antisymmetric with respect to $q\omega_0$, as can be observed in Figs. 3.11a and 3.11c. This effect was not observed in previous sections, where the intensity and gas densities were not high enough to produce it.

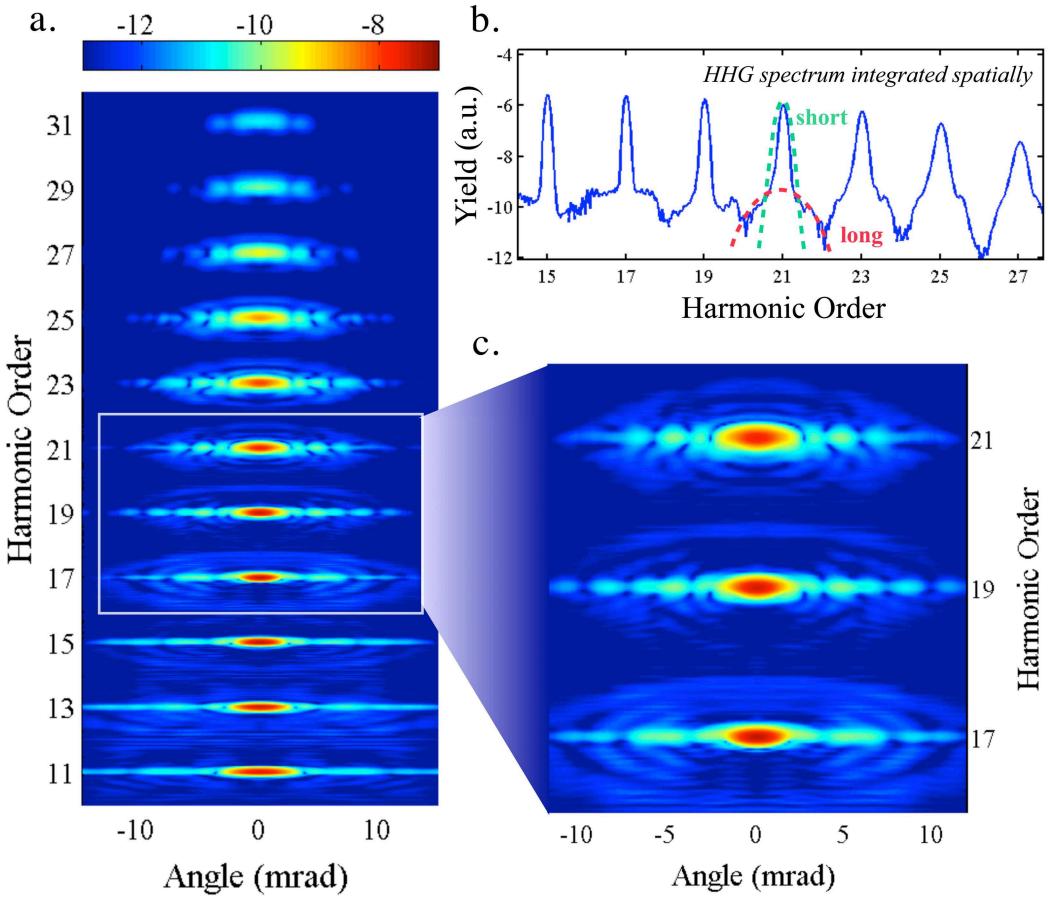

Figure 3.11: **a** Spatial profile of the high-order harmonics generated in an argon gas jet of density 10^{18} atoms/cm^3. The laser pulse is 32 cycles full length (30 fs FWHM) at 800 nm with a peak intensity of 5.9×10^{14} W/cm^2, with a beam waist of $W_0 = 30$ μm. The gas jet is modeled by a Gaussian distribution –see Eq. (2.80)– whose width is $\sigma_y = 100$ μm and $\sigma_z = 100$ μm, and it is placed 1 mm before the focus position. **b** High-harmonic spectrum (yield in log. scale) integrated over the spatial axis, showing the distribution coming from long (red dashed) and short (green dashed) trajectory contributions. A detail of plot **a** covering 17th to 21st harmonics is shown in plot **c**.

3.1.3 HHG along the propagation axis: theory vs experiments

In this section we present an experimental study of the phase-matching of high-order harmonics along the propagation axis, and we compare it with the results obtained with our theoretical method. For that purpose we have used a 100 fs Ti:Sa laser system (Spectra Physics, 800 nm, 10 Hz and up to 50 mJ pulse energy) belonging to the laser facility of the University of Salamanca and under the guidance of Dr. Íñigo J. Sola.

Figure 3.12 represents an scheme of the setup used in the experiment. Odd harmonics of the fundamental frequency are generated by focusing the compressed laser beam (of about 1 mJ pulse energy) with a 40 cm focal length lens into a pulsed argon jet exiting from a 500 μm nozzle inside a vacuum chamber (10^{-4} mbar). The relative distance between the focus position and the gas jet was continuously changed using a motorized linear stage. Previously, the focus position was identified by imaging the transversal beam distribution along the propagation axis. In addition, the interaction between the laser beam and the gas jet was aligned by imaging the inside of the vacuum chamber with a CCD camera (see Fig. 3.12c). Once the XUV radiation was generated, a thin aluminum filter (150 nm in thickness) was used to eliminate the remaining infrared laser pulse. In the next step, the harmonics were spatially selected by a slit before being characterized by a Rowland circle type XUV spectrometer (McPherson 248/310G) [127, 128]. The spectrometer consists of a reflective spherical grating, a microchannel plate coupled to phosphore screen and a CCD detector, all of them inside a vacuum chamber (10^{-6} mbar). In our measurements, the XUV radiation was angularly recorded in the CCD detector.

In the first row of Fig. 3.13 we show the experimental angular profile of the high-order harmonics for a gas jet placed 2 mm (a) before and (b) after the focus position. The measurements were obtained by integrating the 10 Hz signal over eight minutes in the CCD detector.

In order to compare the experiments with our theoretical results, we implement the SFA+ method for single-atom HHG, and the DDA propagation method, explained in the previous chapters, and used previously during this chapter. We do our simulations in argon, using the Roothaan-Hartree-Fock wavefunction [79] for the ionization and rescattering matrix elements. The acceleration operator for hydrogen in [41] is replaced

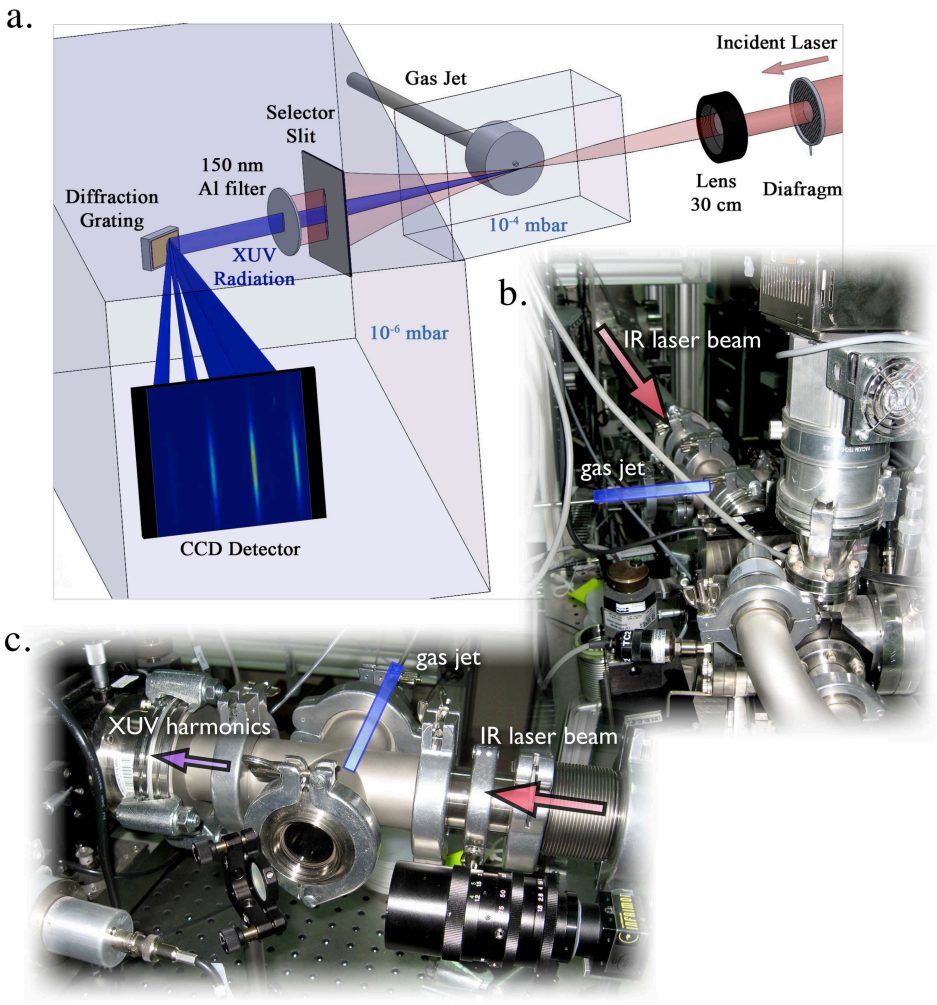

Figure 3.12: **a** Scheme of the experimental setup used for HHG. XUV radiation is generated by focusing (40 cm focal length) the laser pulse in an argon gas jet exiting from a 500 μm nozzle inside a vacuum chamber (10^{-4} mbar) whereas the remaining infrared laser pulse is eliminated by a 150 nm in thickness Al filter. The harmonics are spatially and spectrally characterized by a Rowland circle type XUV spectrometer inside another vacuum chamber (10^{-6} mbar). In panel **b** we show a picture of the experimental setup from the view of the detection system. In plot **c** we show a picture of the vacuum chamber in which the harmonics are generated. We used the 100 fs Ti:Sa laser system (Spectra Physics, 800 nm, 10 Hz and up to 50 mJ pulse energy) belonging to the laser facility at the University of Salamanca.

accordingly with the gradient of the Coulomb potential of the argon ion [80]. The 800 nm laser pulse was modeled by a $\sin^2$ function 32 cycles full temporal length (30.7 fs FWHM) with a peak intensity of 1.57×10^{14} W/cm^2. The laser pulse duration in the computations is approximately one fourth of the laser pulse of the experiment, due to the lack of computational time. However, this fact will not change substantially our results. The Gaussian laser beam (with waist $W_0 = 30$ μm, computed from the experimental focal length and beam waist) was focused into an argon gas jet of density 10^{18} atoms/cm^3. The gas jet is modeled by a Gaussian distribution –see Eq. (2.80)– whose widths are $\sigma_y = 500$ μm and $\sigma_z = 500$ μm.

In the second row of Fig. 3.13 we present the simulated angular profile of the high-order harmonics for a gas jet placed 2 mm (c) before and (d) after the focus position. As can be observed, the theoretical and experimental results are in agreement in two major aspects already discussed above. First, the cut-off of the spectrum is higher when the gas jet is placed after the focus, i.e., high-order harmonics are better phase-matched for a gas jet placed after the focus rather than before. Secondly, the divergence of the harmonics is also higher when the gas jet is placed after the focus. In contrast, we were not able to reproduce experimentally the fringes (or rings) coming from the interference between different quantum paths that should appear when the gas jet is placed before the focus position. We attribute this to the low stability of the laser system, as the average of the harmonics over eight minutes inhibits the appearance of the quantum path interference fringes in the angular profile of the harmonics. In conclusion, in Fig. 3.13 we present the first results of our theoretical methods compared directly to the experiments.

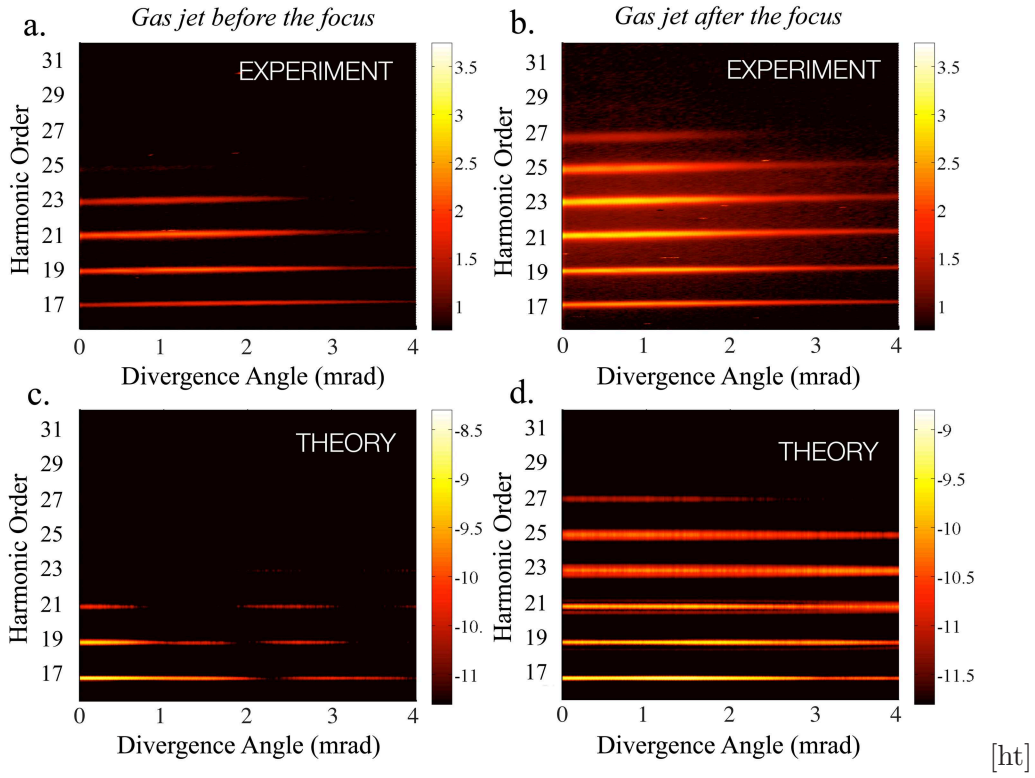

[ht]

Figure 3.13: Angle-resolved high-order harmonic spectra resulting form experiments and theory when the argon gas jet is placed 2 mm **a c** before and **b d** after the focus of the laser beam respectively. A 100 fs Ti:Sa laser system (Spectra Physics, 800 nm, 10 Hz) was used with a pulse energy of about 1 mJ. The compressed laser beam was focused with a 40 cm focal length into an argon gas jet exiting from a 500 μm nozzle. Theoretically, the 800 nm laser pulse was modeled by a $\sin^2$ function 32 cycles full temporal length (30.7 fs FWHM) with a peak intensity of 1.57×10^{14} W/cm^2, whereas the Gaussian laser beam ($W_0 = 30\ \mu m$) was focused into an argon gas jet of density 10^{18} atoms/cm^3. The color scale represents the yield of the harmonics in arbitrary units (log. scale).

3.2 Off-axis compensation of attosecond chirp

Attosecond XUV pulses can be synthesized selecting a window of the higher harmonic spectrum, using an appropriate filter. Physically, this corresponds to the isolation of the radiation bursts associated with the most energetic rescattering events, having typical durations well below the laser cycle. As the scatterings at different kinetic energies take place at different times (see section 1.1.4), the attosecond bursts are chirped and, therefore, its temporal duration is not the Fourier limit [50, 51, 52]. Also, since at least two different trajectories contribute to the same harmonic, the final time structure of the burst is complex. In addition, the macroscopic conditions of the experiment play an important role for the final phase-locking of the different harmonics [129, 130].

It has been reported the possibility of reducing the width of the high-order harmonic bursts selecting the contribution of a single trajectory using appropriate phase-matching conditions [122, 131, 132]. In this section we shall show that, for particular angles of detection where both the short and the long trajectories are relevant, the destructive interference of short an long paths can lead to a final attosecond burst with smaller duration than the corresponding to a single trajectory. Spectrally, this corresponds to an optimal compensation of the chirp of the attosecond pulse.

We have performed our computations assuming a fundamental field of 8 cycles full temporal length (2.9 cycles, 7.7 fs FWHM) $\sin^2$ envelope at 800 nm, with intensity at focus $\simeq 2.45 \times 10^{14}$ W/cm^2 and polarized along the x direction. The beam is assumed Gaussian, propagating along the z direction. The beam waist at focus is 22.5 μm and the confocal parameter $b = 3.98$ mm. The target is modeled as an argon gas jet flowing perpendicularly to the Gaussian beam. The gas jet profile is constant in the x direction, while Gaussian in y and z directions, with FWHM 500 μm, and peak density 10^{18} atoms/cm^3. For the angular resolved detection, we consider a window of 0.5 mrad in the far field profile, that would correspond experimentally to an annular gate. Figure 3.14 illustrates the scheme of this setup.

The attosecond pulses have been computed by Fourier transformation of the harmonic spectra detected at a particular angle, after filtering out of the low energy part. We have considered an aluminium plate filter, multiplying the total harmonic spectrum times the transmission function for this metal (obtained from [98]).

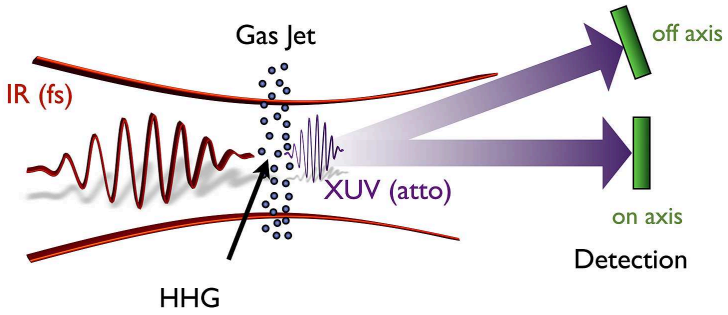

Figure 3.14: Scheme of the off-axis detection geometry used to demonstrate the angular chirping compensation of the attosecond bursts.

We plot in Fig. 3.15 the train of attosecond pulses resulting from the Fourier transform of the harmonic spectra obtained with our numerical simulation. We have considered two different situations: target placed before the laser focus (left column: plots 3.15a to 3.15c) and after the focus (right column: plots 3.15d to 3.15f). The first row in Fig. 3.15 –plots (a) and (d)– corresponds to the attosecond pulses detected on-axis, while the second row shows the off-axis detection –plots (b) and (e)–, where the spatial window was centered at 3.3 mrad. Finally, the third row –plots (c) and (f)– shows the width of the most prominent attosecond pulse as a function of the angle detection. The main conclusion of this section can be drawn by inspection of plots (a) and (b), comparing the attosecond pulse obtained on and off-axis. The reduction of the pulse width becomes apparent for the off-axis case, obtaining 184 attosecond pulses in contrast with 321 attosecond on-axis. This reduction has a physical explanation in the interference between the radiation bursts associated with the rescattering of short and long paths, which is more acute off-axis, where both trajectories have comparable weights, rather than on-axis, where short trajectories dominate. To support this conclussion, we should expect, in a situation where phase-matching favors only short paths at any angle, no reduction of the attosecond width with the angle of detection, as no other contribution cancels the positive chirp due to the short trajectories. As discussed previously in this chapter, this situation is found when the target is located after the laser focus position. The results of our simulations in this situation are shown in the plots at the right column of figure 3.15. Plots 3.15d and 3.15e (target after the focus) shows little variation in contrast with the cases 3.15a and 3.15b (target before

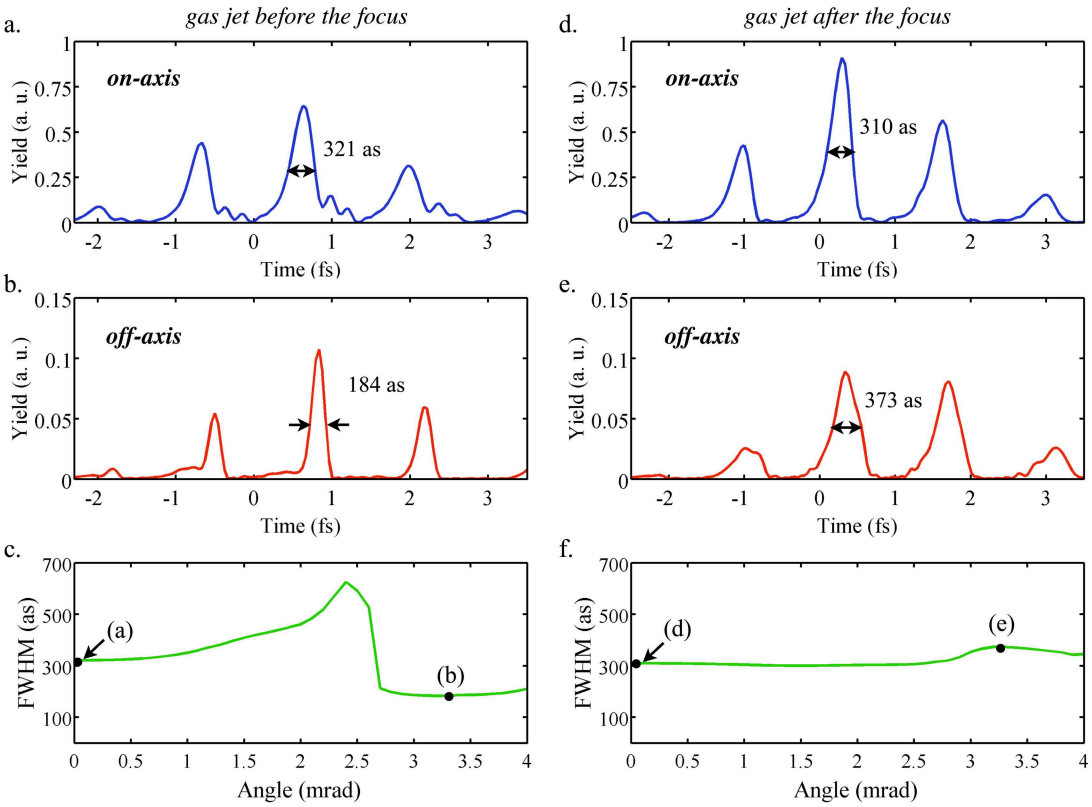

Figure 3.15: Temporal distribution of the attosecond train of pulses when the high-order harmonics are detected in a window **a** on-axis and **b** centered at 3.3 mrad, when the gas jet is placed 1 mm before the focus position. Figures **d** and **e** represent the same situation as **a** and **b**, but when the gas jet is placed 1 mm after the focus position. Figures **c** and **f** shows the FWHM of the pulses synthesized as a function of the detection angle, when the gas jet is located 1 mm before and after the focus respectively. The driving laser pulse is 8 cycles full temporal length (2.9 cycles, 7.7 fs FWHM) $\sin^2$, 800 nm, with intensity at focus $\simeq 2.45 \times 10^{14}$ W/cm^2.

the focus). Figure 3.15f shows that the attosecond pulse width remains practically insensitive to the angle of detection.

A further insight of this process can be gained performing a time-frequency analysis of the filtered spectrum at the detection angles depicted in figure 3.15. The time-frequency analysis is performed using a frequency window of length $3.5\omega_0$, ω_0 being the frequency of the fundamental field. On the left column of figure 3.16, we show the time-resolved emission of the high harmonics (a) on-axis and (b) at 3.3 mrad, when the gas jet is placed before the laser focus. On the right column, the same angles are used but with the target after the focus. Therefore, cases (a) (c) and (d) correspond to situations in which the short trajectory dominates. Accordingly to what we presented in Fig. 3.10, the electron's recollision energy shows a roughly linear dependence on time, in which the lower harmonics are emitted before the higher ones, giving rise to a positive chirp typical from the harmonic spectrum emitted by short trajectories. Plot 3.16b corresponds to the situation of 3.15b, off-axis detection leading to the shorter attosecond pulses. In this case, the interference between paths results in a modulation of the emission time of successive harmonics, producing vertical time-frequency structures. Thus, destructive interference tends to confine the harmonic radiation into a narrower window, reducing drastically the positive chirp associated to short trajectories alone.

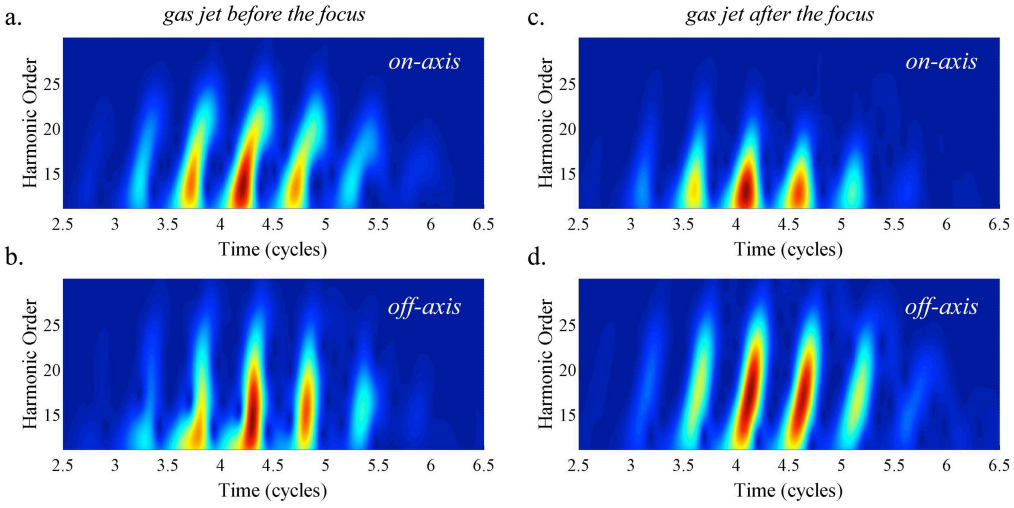

Figure 3.16: Time-frequency analysis of the filtered harmonics of the spectrum, when they are detected in a window on-axis (first row) and at 3.3 mrad (second row). From left to right, the gas jet is placed 1 mm before/after the focus position. The intensity is normalized in each graph. The temporal axis is in units of the laser cycle.

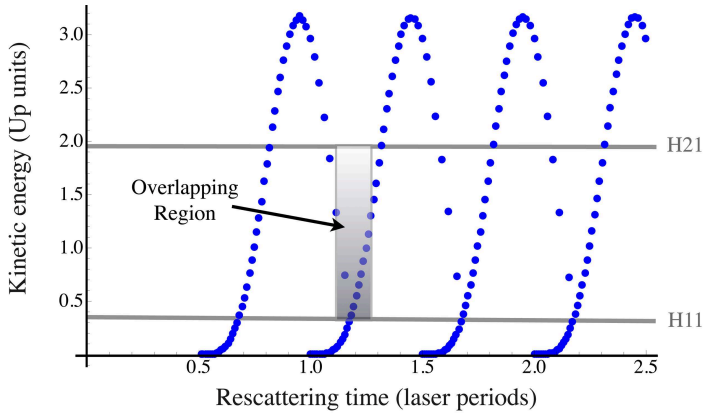

Figure 3.17: Classical temporal dependence of the electron's recollision energy for a constant envelope incident field. We have highlighted the time/energy region where long (negative slope) and short (positive slope) trajectories overlap for the energy range corresponding to harmonics from 11th to 21st. Long trajectories originated near a particular ionization maximum, overlap with the short trajectories ionized at the following maximum.

In order to understand the details of the interference between trajectories, we have plotted in Fig. 3.17 the temporal dependence of the electron's recollision energy, computed classically for a constant envelope incident field. We have highlighted a temporal region of about 0.15 laser periods (400 as) that includes the rescattering times where short (positive slope) and long (negative slope) trajectories overlap, for the energy range corresponding to harmonics from 11th to 21st. Note that this interference occurs between the short and long trajectories originated, respectively, at two consecutive ionization maxima. Consistently, the modulations of the time-frequency structures in 3.16b, appear also at that highlighted region in 3.17.

In Fig. 3.18 we present the attosecond pulse train and time-frequency structure from on-axis detection (0 mrad) to different angles off-axis (0.7, 1.3, 2.0, 2.6, 3.3 and 4.0 mrad), for a gas jet placed 1 mm before the focus position. In the time-frequency structures (right column) we observe how the interferences between short and long trajectory contributions appear slightly at 1.3 mrad, and change continuously when increasing the detection angle. As a consequence, the interference is optimal at 3.3 mrad where the time-frequency structure is vertical and thus the attosecond pulse width is the narrowest. On the other hand we can observe how the yield of the attosecond pulses decreases as the detection angle is increased (all plots in the left column are normalized to the same quantity).

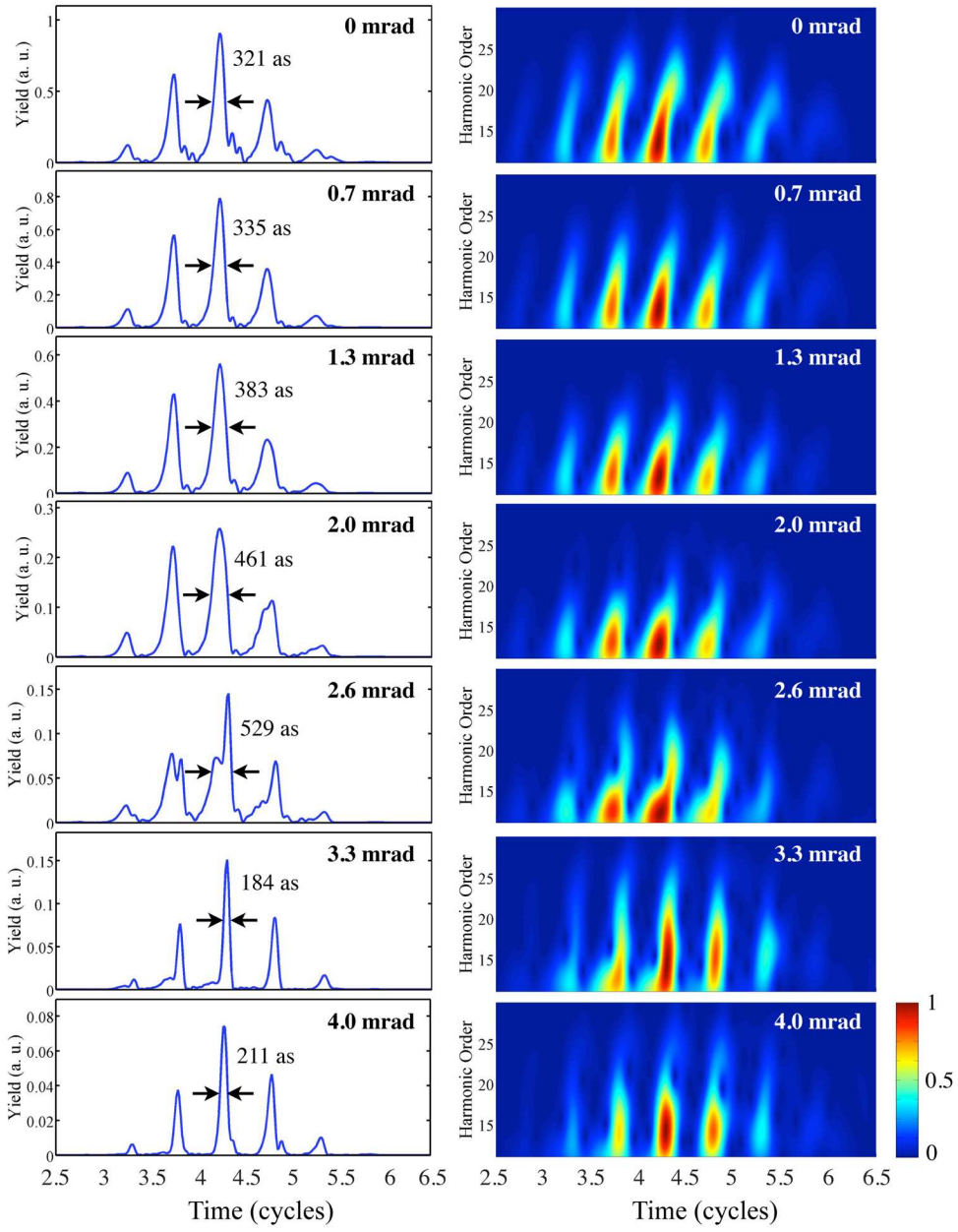

Figure 3.18: Temporal distribution of the attosecond train of pulses (left column) and time-frequency structure (right column) when the high-order harmonics are detected in a window on-axis in the first row, and centered at 0.7, 1.3, 2.0, 2.6, 3.3 and 4.0 mrad in the following rows. The gas jet is placed 1 mm before the focus position, and the laser pulse is 8 cycles full temporal length (2.9 cycles, 7.7 fs FWHM) $\sin^2$, 800 nm, with intensity at focus $\simeq 2.45 \times 10^{14}$ W/cm^2. Plots in the left column are normalized to the same quantity, whereas plots in the right column are normalized independently.

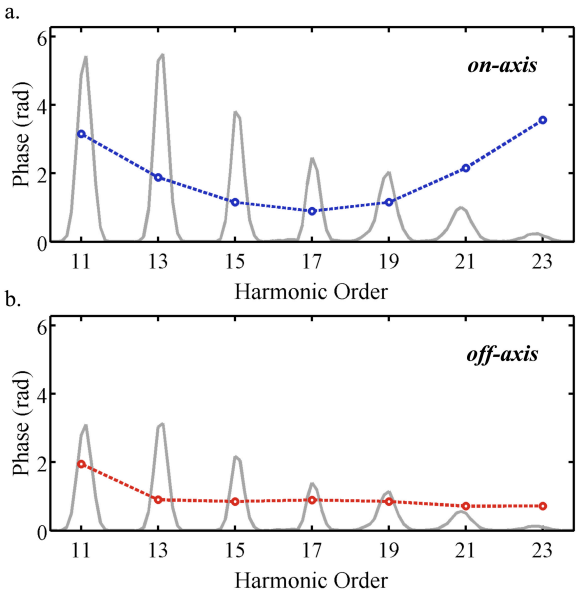

Figure 3.19: Quadratic term of the harmonic phase of the attosecond pulses when they are detected on-axis **a** and at 3.3 mrad **b**. At the background of both figures, we show the harmonic spectra.

In plots 3.19a and 3.19b we show the quadratic term of the spectral phase of the attosecond pulses showed in 3.15a and 3.15b respectively. When a spatial filter is placed on-axis to select the short trajectories, a positive chirp is present, in agreement to what was discussed before. In contrast, when filtering angularly the signal at 3.3 mrad (plot 3.19b) the superposition of the contributions of both trajectories results in a reduction of the spectral chirp, then phase-locking the different harmonics.

Consistently with our interpretation, we have found also narrower X-ray pulses for isolated attosecond bursts, therefore excluding the influence of multiple rescatterings in the pulse off-axis narrowing. For that purpose, in Fig. 3.20 we show the the train of attosecond pulses in the same conditions as in Fig. 3.15 but assuming a 4 cycle full temporal length (1.4 cycles, 3.8 fs FWHM) $\sin^2$, 800 nm fundamental field with intensity at focus $\simeq 2.45 \times 10^{14}$ W/cm^2, that is, half the temporal duration of the case presented in Fig. 3.15. Although the driving field is 1.4 cycles FWHM, there is still interference between the long and short trajectory contribution from two consecutive ionization maxima that leads to the pulse narrowing for harmonics detected off-axis.

We believe that this is a phenomenon potentially useful to reduce of the attosecond chirping and, thus, to obtain shorter pulses in the laboratory.

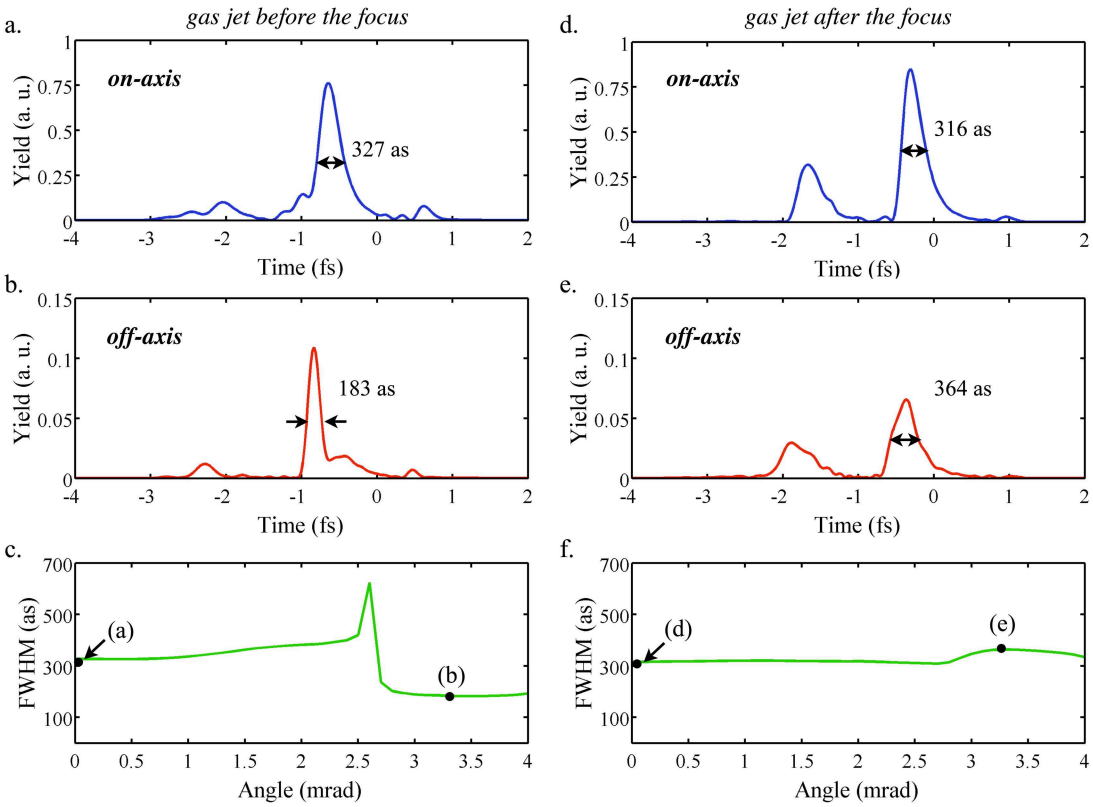

Figure 3.20: Temporal distribution of the attosecond train of pulses when the high-order harmonics are detected in a window **a** on-axis and **b** centered at 3.3 mrad, when the gas jet is placed 1 mm before the focus position. Plots **d** and **e** represent the same situation as **a** and **b**, but when the gas jet is placed 1 mm after the focus position. Plots **c** and **f** shows the FWHM of the pulses synthesized as a function of the detection angle, when the gas jet is located 1 mm before and after the focus respectively. The driving laser pulse is 4 cycles full temporal length (1.4 cycles, 3.8 fs FWHM) $\sin^2$, 800 nm, with intensity at focus $\simeq 2.45 \times 10^{14}$ W/cm^2.

3.3 Signature of the transversal coherence length on high-order harmonic propagation

In the previous sections we have described phase-matching in terms of a longitudinal coherence length, which corresponds to the distance between two atoms whose emitted radiation interferes destructively. However, there is also a transversal coherence length between the radiation coming from atoms placed in a plane perpendicular to the propagation axis. Here we will look at the conditions in which the transversal coherence length is more relevant than the longitudinal. In this section, first, we will present the concept of transverse coherence length. Secondly we will introduce the spatial maps of the harmonic detection as a novel tool for the analysis of HHG. Finally, we will present experimental and theoretical results for HHG driven by apertured laser beams in a gas jet. With the aid of the spatial maps we will identify the signature of the transversal coherence length in theory and experiments.

3.3.1 Transversal and longitudinal phase-matching

Let us first develop the concept of longitudinal and transversal phase-matching. Considering a detector at some distance $\mathbf{r}_d$, the contribution to the detected harmonic field of an atom located at $\mathbf{r}$ is given by

$$E_q(\mathbf{r}) \propto \left[|d_q^s(\mathbf{r})|e^{i\phi_q^s(\mathbf{r})} + |d_q^l(\mathbf{r})|e^{i\phi_q^l(\mathbf{r})}\right] e^{i(\mathbf{r}_d-\mathbf{r})\mathbf{k}_q} \tag{3.3}$$

where $|d_q^i(\mathbf{r})|$ is the spectral amplitude of the single-atom dipole and $\phi_q^i(\mathbf{r})$ its phase, for the long and short contributions ($i = l$ and $i = s$, respectively), and $\mathbf{k}_q$ is the propagation vector ($|k_q| = n_r(q\omega)q\omega/c$, ω being the frequency of the driving field and $n_r(\omega)$ the refractive index).

Assuming a driving field propagating along the z-axis, the phase-mismatch associated to each trajectory contribution for on-axis detection is defined as (see section 2.3)

$$\Delta\mathbf{k}_q^i = \mathbf{k}_q - \nabla\phi_q^i = k_q\mathbf{e_z} - \frac{\partial\phi_q^i}{\partial z}\mathbf{e_z} - \frac{\partial\phi_q^i}{\partial\rho}\mathbf{e}_\rho \tag{3.4}$$

We can now decompose the phase-mismatch into longitudinal ($\Delta k_q^{\parallel}$) and transversal

components ($\Delta k_q^{\perp}$) as:

$$\Delta k_q^{\parallel} = k_q \mathbf{e_z} - \frac{\partial \phi_1}{\partial z}\mathbf{e_z} \tag{3.5}$$

$$\Delta k_q^{\perp} = -\frac{\partial \phi_1}{\partial \rho}\mathbf{e}_\rho \tag{3.6}$$

and define the longitudinal coherence length as $L_{coh}^{\parallel} = \pi/\Delta k_q^{\parallel}$, and the transversal coherence length, $L_{coh}^{\perp} = \pi/\Delta k_q^{\perp}$.

Let us now consider a Gaussian beam driving field (2.23) propagating through a medium of refractive index $n_r(\omega)$. As we already saw in the previous chapter, there are different physical contributions to the dipole spectral phase $\phi_q^i(z)$. On one side there is an *extrinsic* contribution originated by the change in phase of the driving field as it propagates (Gouy phase, transversal phase and the dephase due to the presence of free charges and neutrals in the target), and, on the other hand, there is the intrinsic contribution to the dipole phase originated by the single-atom harmonic generation, which can be approximated as $\phi_{int}^i \simeq -\alpha^i I$, being (i) the electronic trajectory considered. Therefore, as we already stated in (3.1), we can express the longitudinal phase-mismatch as

$$\Delta k_q^{\parallel} \simeq q\frac{\omega}{c}\left[n_r(q\omega) - n_r(\omega)\right] + (q-1)\frac{\partial \zeta(z)}{\partial z} + \alpha_q^i \frac{\partial I}{\partial z} \tag{3.7}$$

where $\zeta(z)$ is the Gouy phase. Along the propagation axis, the phase-mismatch from the Gouy phase is always positive, while that coming from the intrinsic phase changes from positive to negative at the focus (see section 3.1). As a consequence, when the target is located after the focus, the opposite behavior of the intrinsic and Gouy phases compensates and results in an efficient longitudinal phase-matching.

On the other hand, the transversal phase-mismatch is given by

$$\Delta k_q^{\perp} \simeq -q\frac{\omega}{c}n(\omega)\frac{\rho}{R(z)} + \alpha_q^i \frac{\partial I}{\partial \rho} \tag{3.8}$$

where $R(z)$ is the radius of curvature of the Gaussian beam wavefront. For low density gases, there are mainly two contributions to the transversal phase-mismatch: the variation of the transversal phase and that of intrinsic phase. Both contributions are symmetric in the transversal plane. However, the sign of the transversal phase depends on the radius of curvature, which is positive before the focus, while negative after the focus position. As a consequence, when the target is located before the focus, the

opposite behavior of the intrinsic and transversal phases compensates, thus obtaining favorable transversal phase-matching conditions.

Note, therefore, that the efficiency of the detected signal will depend on the compromise between longitudinal and transversal phase-matching conditions, which behave opposite respect to the focus position, i.e., the longitudinal coherence length is longer after the focus, while the transversal is longer before the focus.

3.3.2 Spatial maps of the harmonic detection

In this section we present a novel tool for making a diagnosis of the high-order harmonic detection. One of the advantages of our propagation method is that allows to analyze the topology of the harmonic generation, i.e. the contribution of the different target regions to the far field phase and amplitude of the harmonic at the detector. Here we will use this possibility to generate maps of the amplitude and phase of these contributions to the total harmonic field at the detector.

Let us discuss briefly the information provided by the harmonic generation maps. For this, we shall focus first to the maps corresponding to the 19th harmonic for a hydrogen gas jet. Fig. 3.21 shows the cases of the gas jet located at (b) 2 mm before and (c) after the focus position. The laser pulse is assumed to be a $\sin^2$ envelope of 2.9 cycles FWHM (7.7 fs), 800 nm wavelength and peak intensity of 1.57×10^{14} W/cm^2. We have assumed a Gaussian beam (with waist $W_0 = 30\ \mu m$) focused into an hydrogen gas jet. The gas jet, directed along the x-axis (perpendicular to the field propagation), is modeled by a Gaussian distribution along the y and z dimensions (whose FWHM is 500 μm), and a constant profile along its axial dimension, x. For this example (with same parameters as in Fig. 3.7), we have taken hydrogen since, for this element, the harmonic absorption is negligible. The spatial map shows a background color which represents the amplitude of the local contribution to the harmonic far field at the detector, which in this case is located on-axis. This local contribution is obtained computing the single-atom HHG weighted by the local atom density, and multiplied by the cylindrical volume element, thus assuming cylindrical symmetry of the target. On the other hand, the arrows correspond to the polar representation of the field phase.

Note that these maps are conceptually different from those already presented in [100, 133], in which the background represents the local phase-mismatch and the arrows stand for the direction in which the harmonic emission is better phase-matched.

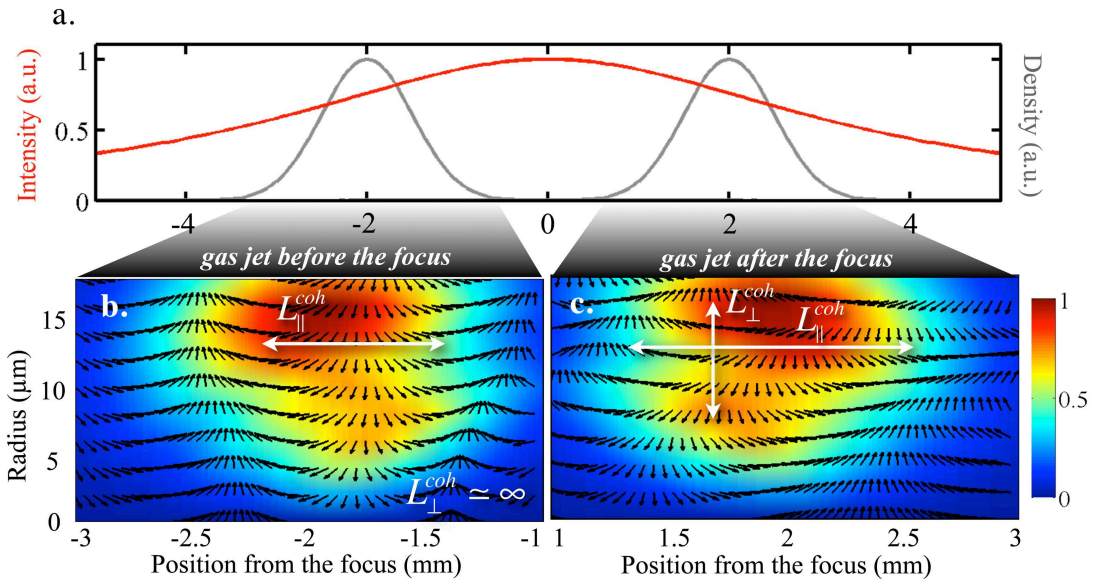

Figure 3.21: Spatial maps of the harmonic detection for the 19th harmonic for a hydrogen gas jet placed **b** 2 mm before and **c** after the focus position. We assume cylindrical symmetry, therefore each point in the map corresponds to the contribution of a ring at the target with a particular radius and located at a given distance to the focus. The colored background represents the amplitude of the contribution, while the phase is represented through the angle of the arrows. In **a** we present the intensity of the fundamental Gaussian beam (red line) and the gas density distribution (grey line) at the two positions presented here. The parameters of the laser pulse and hydrogen gas jet are the same as those in Fig. 3.7. Note that the cylindrical symmetry is only in the polar integration for the maps.

From our maps, it is possible to identify the longitudinal and transversal coherence length as the spatial distance between phase-arrows of opposite direction in the horizontal and vertical directions respectively. We represent those lengths as white left-right and up-down arrows. We observe that the longitudinal coherence length is longer when the gas jet is placed after the focus position, resulting from the compensation of the Gouy and intrinsic phase, as explained above. On the other hand, in the transversal direction, the compensation of the transversal phase and the intrinsic phase leads to a very large transversal coherence length before the focus (white arrow not shown in this case), while a finite transversal coherence length can be identified after the focus position.

Note that the spatial maps presented here are for on-axis detection. If we change

the detector angle, the optical paths to the detector change thus modifying the arrows' direction change, and, therefore, the associated coherence length.

3.3.3 Characterization of the detection of high-order harmonics driven by apertured laser beams

To demonstrate the signature of the transversal coherence length, we have performed experiments an theoretical computations of the variation of the harmonic yield as a function of the diameter of an apertured beam. This simple setup has been demonstrated to be useful to control various aspects relevant to phase-matching: the Gouy phase, the intrinsic phase and the free-charge density [134, 135]. In the seminal paper [134], Kazamias *et al.* demonstrated that a middle-sized aperture was the optimal to phase-match the harmonics, giving rise to an increase by a factor of 10 of the total harmonic yield. In this experiment, when aperturing, the variations of the phase-matching conditions could be attributed to changes in the Gouy phase gradient and in the density of free carriers. Therefore, the optimal aperture corresponds to the maximal compensation of these two contributions. Our experiment follows the same steps as Kazamias' but with parameters changed in order to reduce the variations of all the main sources of phase-mismatch (free charges, intensity gradient, Gouy-phase gradient) with exception of the wavefront curvature radius. Therefore, we select a case in which aperturing affects mainly to the transversal phase-matching. To reduce the total ionization and the intensity gradient, our laser beam energy has been lowered (0.5 mJ, 100 fs instead of 6 mJ, 30 fs). We have chosen also a Gaussian beam waist smaller (4.5 mm in our case, against the 11 mm in Kazamias' experiment) in order to reduce the clipping of the beam when the smallest aperture (4 mm) is used. We also use a shorter focal length to increase the transversal phase gradient and, therefore, the role of that transversal phase-matching. In few words, we have redesign the experiment so the effect of the aperture size in the longitudinal phase-matching is minimal. As we shall see, the experiment still shows a pronounced variation of the harmonic generation efficiency with the aperture size. We, then, will use our numerical codes to demonstrate that this variation can only be attributed to the increase of the transversal coherence length.

In the simulations we have considered a 800 nm laser pulse, 15.4 fs FWHM with energy 0.5 mJ. The argon gas jet, modeled as in Fig. 3.21 was 550 μm FWHM with density 10^{17} atoms/cm^3. The apertured fundamental field is computed by integrating

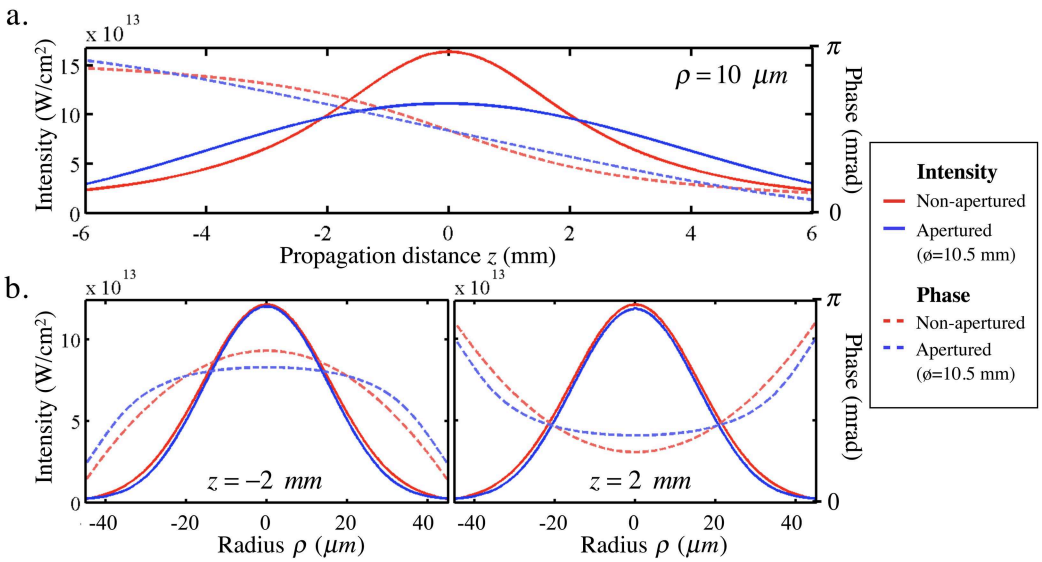

Figure 3.22: Intensity (solid lines) and phase (dashed lines) of the fundamental field, **a** along the propagation axis, at a radius $\rho = 10\ \mu m$, and **b** along the radial axis at (left) -2 mm and (right) 2 mm respect to the focus position. We performed simulations for a non-apertured laser beam (red) and a laser beam apertured (blue) by a 10.5 diameter diaphragm.

the Slowly-Varying-Envelope equation over the inhomogeneous gas target. The field found in this way is, then, used to compute the harmonic generation of the target. In Fig. 3.22 we represent the intensity (solid lines) and phase (dashed lines) of the fundamental field, (a) along the propagation axis, at a radius $\rho = 10\ \mu m$, and (b) along the radial axis at (left) -2 mm and (right) 2 mm respect to the focus position. We performed simulations for a non-apertured laser beam (red) and laser beam apertured (blue) by a 10.5 diameter diaphragm. When the gas jet is centered at -2 mm, we observe that the variation of the Gouy phase for the apertured and non-apertured beams remains similar. On the other hand, although there is a variation of the intensity gradient when aperturing, the absolute intensity is small, so the change in the intrinsic phase will be small. In addition, we observe that the gradient of the transversal phase is dramatically reduced when aperturing, thus increasing the transversal coherence length. As discussed before, the opposite sign of the transversal phase before the focus leads to the longer transversal coherence length. As a conclusion, from Fig. 3.22 we expect a small change in the longitudinal coherence length, while a noticeable increase

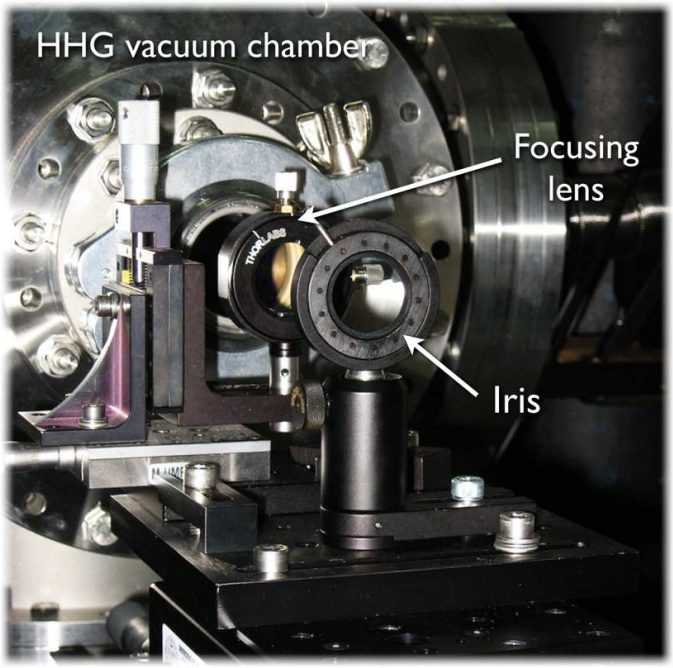

Figure 3.23: Picture of the experimental setup used for HHG driven by apertured laser beams, where a variable iris is placed before the focusing lens (40 cm focal length) in order to make an aperture in the laser beam to optimize phase-matching conditions. Both iris and focusing lens are mounted on a motorized linear stage in order to change the relative position between the gas jet and the focus.

of the transversal when aperturing the laser beam at those gas jet positions.

We have included in our experimental HHG setup (see Fig. 3.12a) a variable diaphragm before the focusing lens, as it is shown in Fig. 3.23. Both diaphragm and focusing lens are mounted on a motorized linear stage in order to change the relative position between the gas jet and the focus, keeping the distance between the diaphragm and the lens constant.

As a first test we compared the theoretical and experimental intensity profile of the apertured laser beam at different positions near the focus. Experimentally, we imaged the reflexion of the beam in a card that was mounted on a motorized linear stage, for different positions before and after the focus. In Fig. 3.24 we show the transversal intensity profile of a laser beam apertured with an iris of 11.5 mm in diameter. The images were taken at three different positions with respect to the focus (± 0.1 mm,

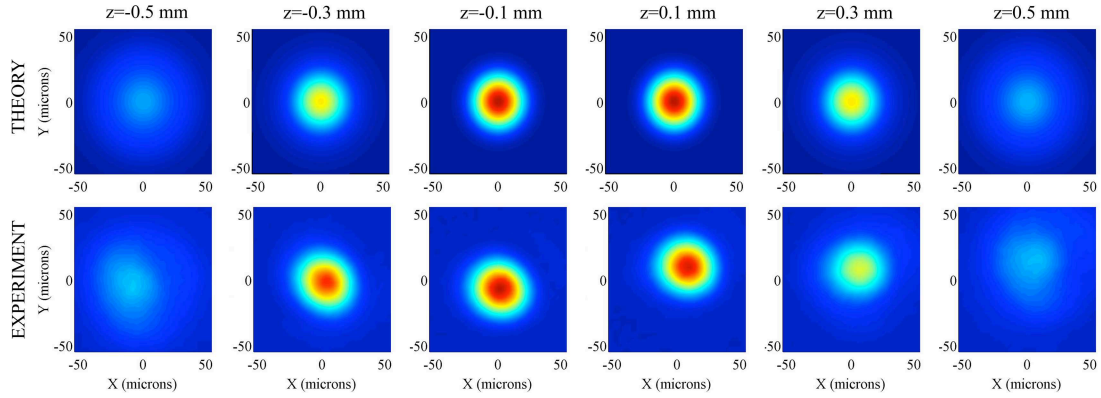

Figure 3.24: Transversal intensity profile –theoretical (first row) and experimental (second row)– of a laser beam apertured with an iris of 11.5 mm in diameter. The images were taken at three different positions with respect to the focus (± 0.1 mm, ± 0.3 mm and ± 0.5 mm).

± 0.3 mm and ± 0.5 mm). The agreement between the theoretical and experimental profiles is excellent.

The resulting laser beam (of about 0.5 mJ pulse energy) is focused with a 40 cm focal length lens into a pulsed argon jet exiting from a 500 μm nozzle inside a vacuum chamber (10^{-4} mbar). The waist (radius) of the laser beam before the lens was 4.5 mm. The generated XUV radiation was characterized by a Rowland circle type XUV spectrometer, as explained in section 3.1.3.

We have detected the harmonic signal for different iris diameters, from 7.5 mm to completely opened ($\sim$ 2 cm). The measurements were obtained by integrating the 10 Hz signal over eight minutes in the CCD detector. In Fig. 3.25 we show the detected harmonic signal for the 17th and 19th harmonics when the gas jet is placed at (a) (b) -2 mm, (c) (d) -1 mm, (c) (g) 1 mm, and (d) (h) 2 mm respect to the focus positions, respectively. The dots represent the experimental results, whereas the results of the simulations are presented in the dashed red lines.

The agreement between our theoretical and experimental results confirms that there is an optimal iris diameter in which the harmonic signal is higher, leading to an increase by a factor up to 8 in the harmonic yield. Also, as explained above, phase-matching conditions when the jet is located after or before the focus are different, therefore the enhancement turns out to be higher when the gas jet is placed before the focus. In any

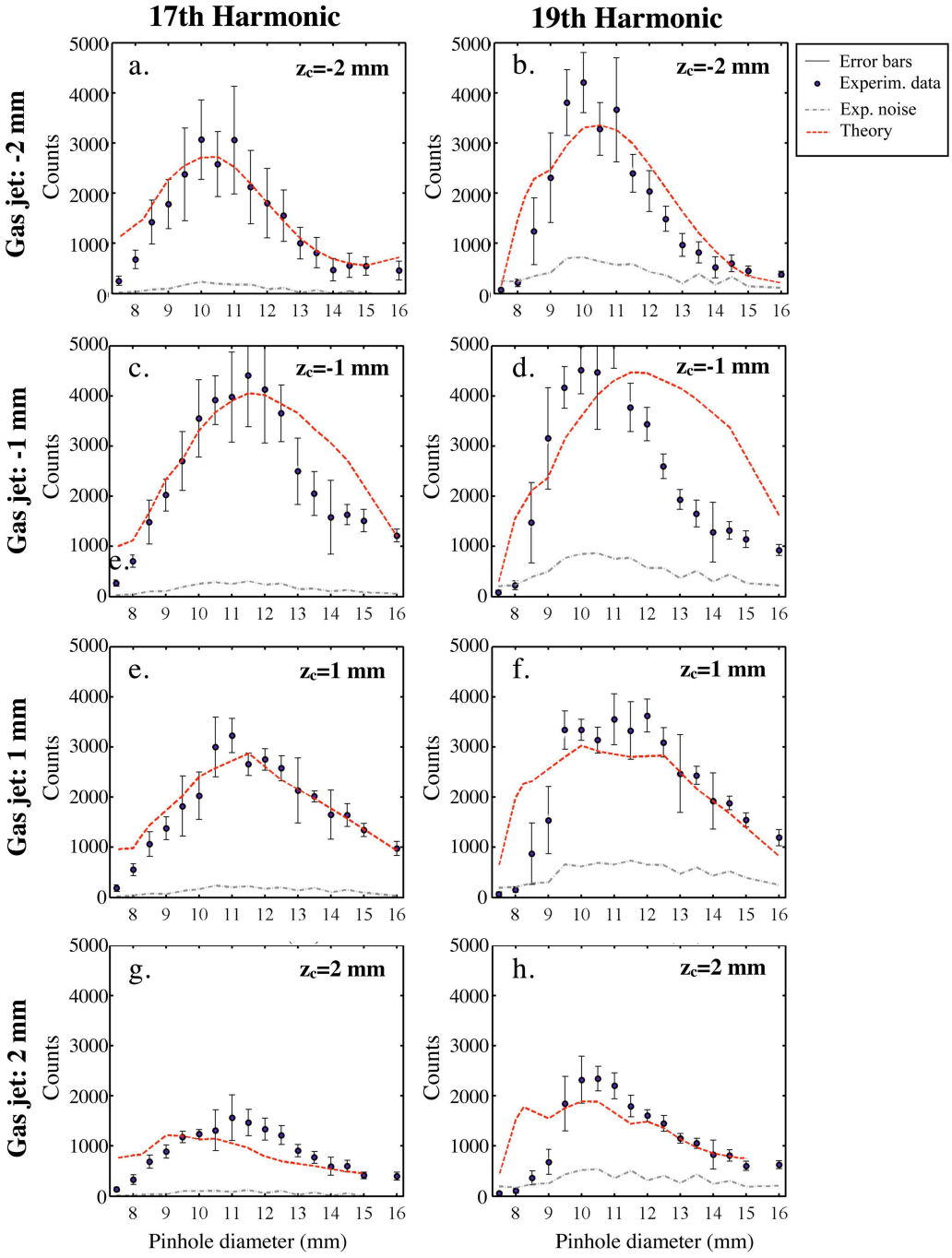

Figure 3.25: Detected signal versus the iris diameter for harmonics 17th (first row) and 19th (second row), when the gas jet is placed **a-c** 2 mm before, **b-f** 1 mm before, **c-g** 1 mm after, and **d-h** 2 mm after the focus position. The experimental signal is represented in black dots and error bars, being the dashed-grey line the background noise. Simulations (dashed red line) use a laser pulse of 15.4 fs FWHM and 0.5 mJ total energy. The argon gas jet is modeled as a Gaussian function of 550 μm in the propagation direction, with density 10^{17} atoms/cm^3.

case, the existence of an optimal aperture is a surprising fact, since our laser parameters are chosen to minimize the effect of the aperture in all the phase-matching contributions that are usually considered (i.e. those affecting the longitudinal coherence length). In Fig. 3.26 we present the spatial maps of the 19th harmonic for a driving laser beam non-apertured (left column) and apertured by a 10.5 mm iris diameter (right column), for a gas jet placed at the same positions as in Fig. 3.25. The iris diameter corresponds to the one in which the detected signal in the experiment was optimal.

There are two main conclusions to be drawn from these maps. On the first hand, for a gas jet placed at ±2 mm, the longitudinal coherence length associated to phase-matching remains very similar (left-right arrows), as expected from our parameter choice. As a consequence, the higher yield of the apertured beam can not be attributed to the optimization of the longitudinal phase-matching, as was the case in Kazamias' experiment [134]. Our simulations demonstrate that the enhancement of the yield when aperturing is a direct consequence of the transversal coherence length. In addition, as explained above, this effect is more acute before the focus, where the transversal coherence length is higher. This behavior can be also observed in our experimental results, in which the enhancement obtained when aperturing is substantially higher when the gas jet is placed at -2 mm than at 2 mm respect to the focus position (see Fig. 3.25).

On the other hand, if we move the target towards the focus (positions ±1 mm), the longitudinal coherence length plays an important role when aperturing. Both, transversal and longitudinal phase-matching, are relevant, and thus, the enhancement is due to those two factors.

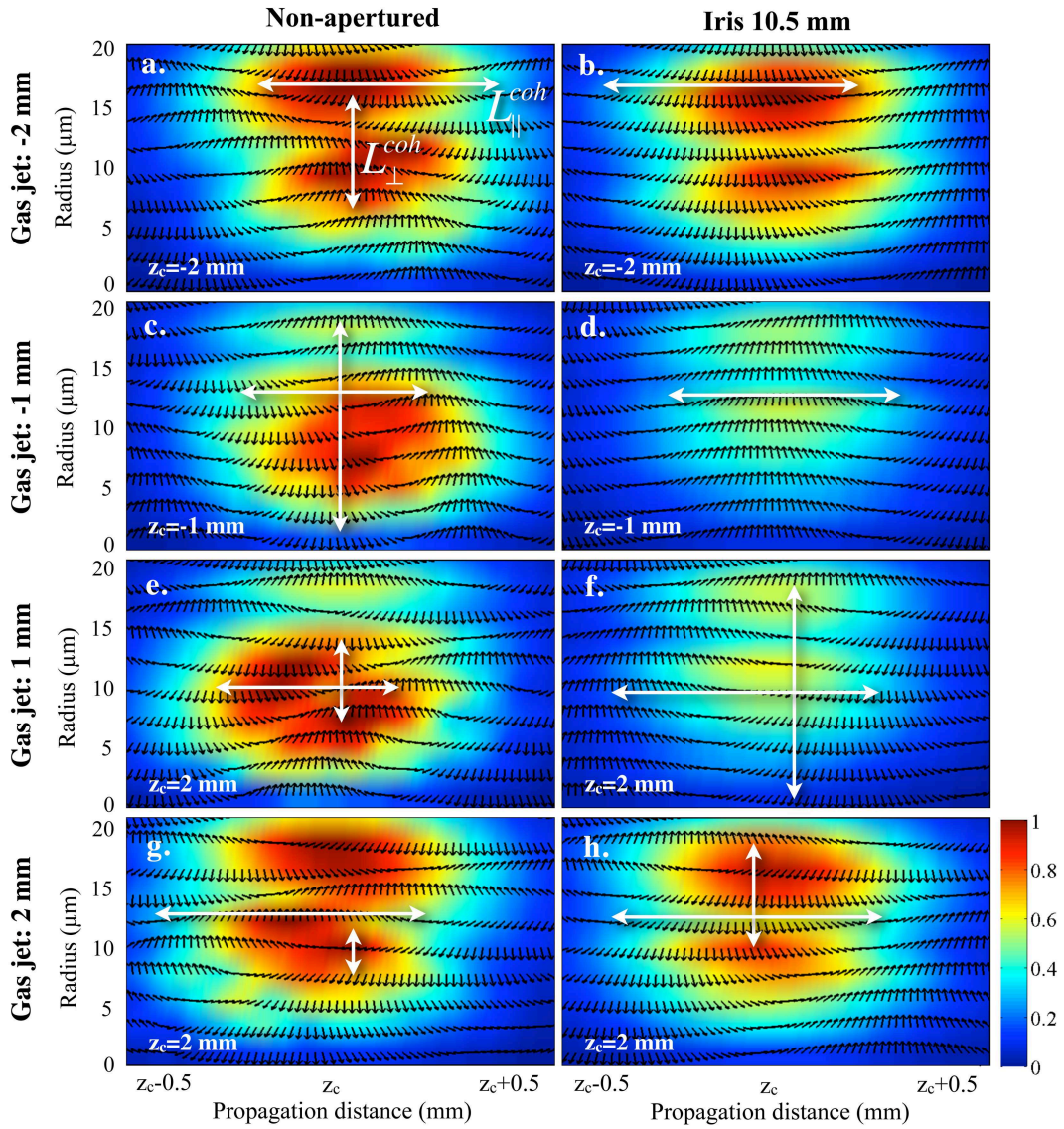

Figure 3.26: Spatial maps of the detected 19th harmonic for a driving laser beam non-apertured (left column) and apertured by a 10.5 mm iris diameter (right column), for a gas jet placed at **a b** -2 mm, **c d** -1 mm, **e f** 1 mm, and **g h** 2 mm respect to the focus position. The simulation parameters correspond to the same as in Fig. 3.25. The longitudinal and transversal coherence lengths are represented as white left-right and up-down arrows.

3.4 High-order harmonic generation driven in a semi-infinite gas cell

In the previous sections of this chapter we have studied the HHG process from gas jets, of lengths below 1 mm. Here we will study HHG in a 'semi-infinite' gas cell (SIGC), a geometry proposed in 2001 by Papadogiannis *et al.* [136]. The SIGC consists of an entrance window far away from the focal region to avoid any non-linear effects in the entrance area, and an exit composed by a metal plate with a laser-drilled pinhole, which assures an abrupt transition to vacuum. In particular, we are going to study theoretically the dependence of the harmonic radiation generated in a SIGC filled with xenon upon the pressure and the focus position. Our results will be compared with the experimental findings obtained in the group of M. Kovačev at the Universität Hannover.

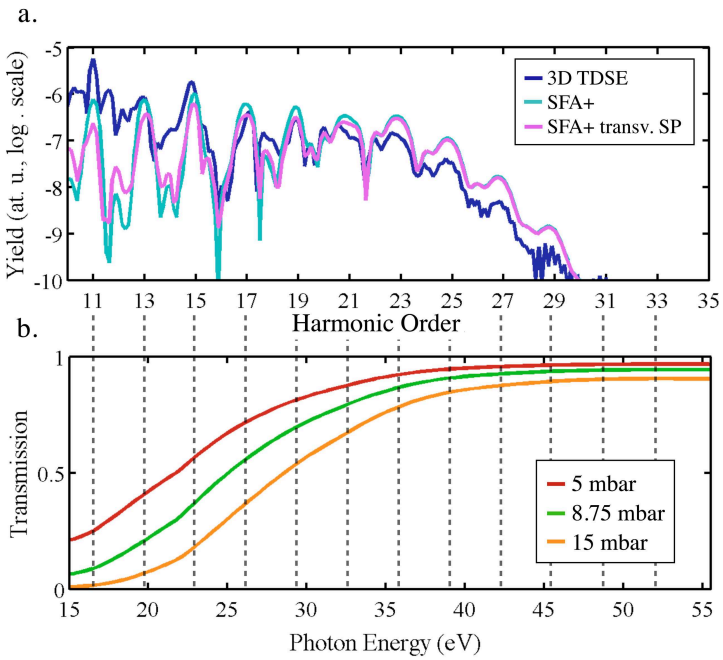

Figure 3.27: **a** Single-atom HHG spectra in xenon computed by (dark blue) 3D TDSE, (light blue) SFA+ and (pink) SFA+ with the transversal saddle point approximation. The driving laser pulse is modeled as a $\sin^2$ at 780 nm, 2.9 cycles (7.5 fs) FWHM, with peak intensity $\simeq 1.26 \times 10^{14}$ W/cm^2. **b** Transmission through 2 mm of xenon gas at a pressure of (red) 5 mbar, (green) 8.75 mbar, and (orange) 15 mbar (data obtained from [98]).

In Fig. 3.27a we present the single-atom HHG spectra in xenon computed by (dark blue) 3D TDSE, (light blue) SFA+ and (pink) SFA+ with the transversal saddle point

approximation. The laser pulse envelope is modeled as a $\sin^2$ function at 780 nm, 2.9 cycles (7.5 fs) FWHM, with peak intensity $\simeq 1.26\times10^{14}$ W/cm^2. In the following we will use the SFA+ approach including the saddle-point approximation in the momentum plane transverse to the polarization of the field (see section 1.3.1). This allows us to compute the single radiator yield within few seconds, and therefore, reduces the computational time needed for the long targets used in a gas cell configuration.

As it was shown in section 2.3.4, the absorption in xenon becomes a relevant process when propagating high-order harmonics over distances above one millimeter, in contrast to other gases as hydrogen or helium. In Fig. 3.27b we present the transmission through 2 mm of xenon gas at three different pressures: (red) 5 mbar, (green) 8.75 mbar, and (orange) 15 mbar. Comparing Figs. 3.27a and 3.27b, we can observe that low order harmonics (<15th) are strongly absorbed, whereas the xenon cell is transparent for the highest orders (> 21st). In this section we will focus our attention to the 17th harmonic, therefore, being the absorption a critical parameter on its propagation.

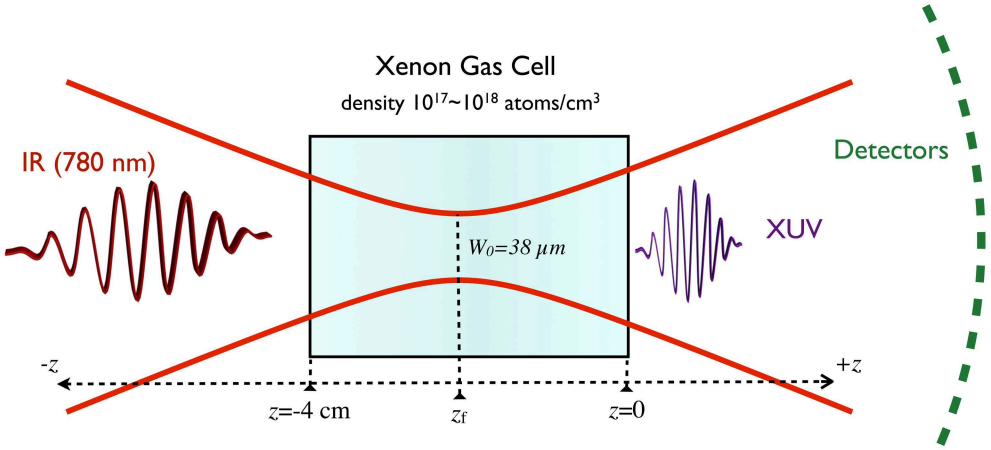

Figure 3.28: Schematic setup for the simulation of HHG driven in a semi-infinite gas cell (SIGC), modeled by an homogeneous xenon cell of variable density (10^{17}-10^{18} atoms/cm^3) and 4 cm in length. The coordinate origin is placed at the exit of the SIGC (z=0). The Gaussian laser beam, of waist $W_0 = 38$ μm is focused at z_f, and the laser pulse envelope is modeled as a $\sin^2$ function at 780 nm, 5.8 cycles (15 fs) FWHM, with peak intensity $\simeq 1.26 \times 10^{14}$ W/cm^2 .

In Fig. 3.28 we present a schematic setup of our simulation. The semi-infinite gas cell (SIGC) is modeled by an homogeneous xenon slab (i.e. cell) of variable density (10^{17}-10^{18} atoms/cm^3) and 4 cm in length. We use directly as an input a Gaussian laser

beam with waist $W_0 = 38\ \mu m$ (radius), and focused at the position z_f. The coordinate origin of our system is placed at the exit of the SIGC. The laser pulse envelope is modeled as a $\sin^2$ function at 780 nm, 5.8 cycles (15 fs) FWHM, with peak intensity $\simeq 1.26 \times 10^{14}$ W/cm^2. We compute the gas density from the pressure following the ideal gas law.

Before implementing high-order harmonic propagation, let us first study how the single-atom generation is limited by the absorption, depending on the pressure and the focus position in the SIGC. In Fig. 3.29 we present the single-atom HHG spectrum along the propagation axis, weighted by the absorption over the length remaining until the end of the cell ($z = 0$) as follows: from left to right, the focus position is changed, being z_f=-20 mm in the first column, and z_f=0 mm in the latest; from top to the bottom, the gas density is increased, from 0 mbar (i.e. no absorption) in the first row, to 15 mbar in the latest.

Let us concentrate on the 17th harmonic order, which is highlighted in each plot of Fig. 3.29. In the first row (no absorption), we can see that depending on the gas cell position, the 17th harmonic can be generated in the cut-off or plateau regions. This is detailed in Fig. 3.29a: near the focus position (z_f=-20 mm) the driving field's intensity is maximal and the 17th harmonic is generated in the plateau region of the spectrum, whereas away from the focus (z_f >-18 mm or z_f <-23 mm), the intensity is lower and the harmonic is generated at the cut-off. For the sake of clarity, the position where the harmonic is generated at the cut-off is indicated by red lines in the plots of Fig. 3.29.

Absorption plays a key role suppressing the harmonic radiated before the focus (which falls deeper inside the medium). The absorption strength will move the generation region out of the focus towards the exit of the cell, moving the harmonic generation from the plateau region to the cut-off region. For example, if the focus is placed at $z_f = -15$ mm, at 5 mbar, the 17th harmonic is essentially generated in the plateau region, whereas at 15 mbar, at the cut-off. This difference is essential to explain the characteristics of the signal arriving at the detector, as we will see later.

If we now take a look at the dependence of the complete spectrum upon the focus position in Fig. 3.29, our expectations are in agreement with previous findings by M. Kovačev's group [137], that demonstrated experimentally that focusing further into the gas cell leads to a suppression of the lower harmonic orders.

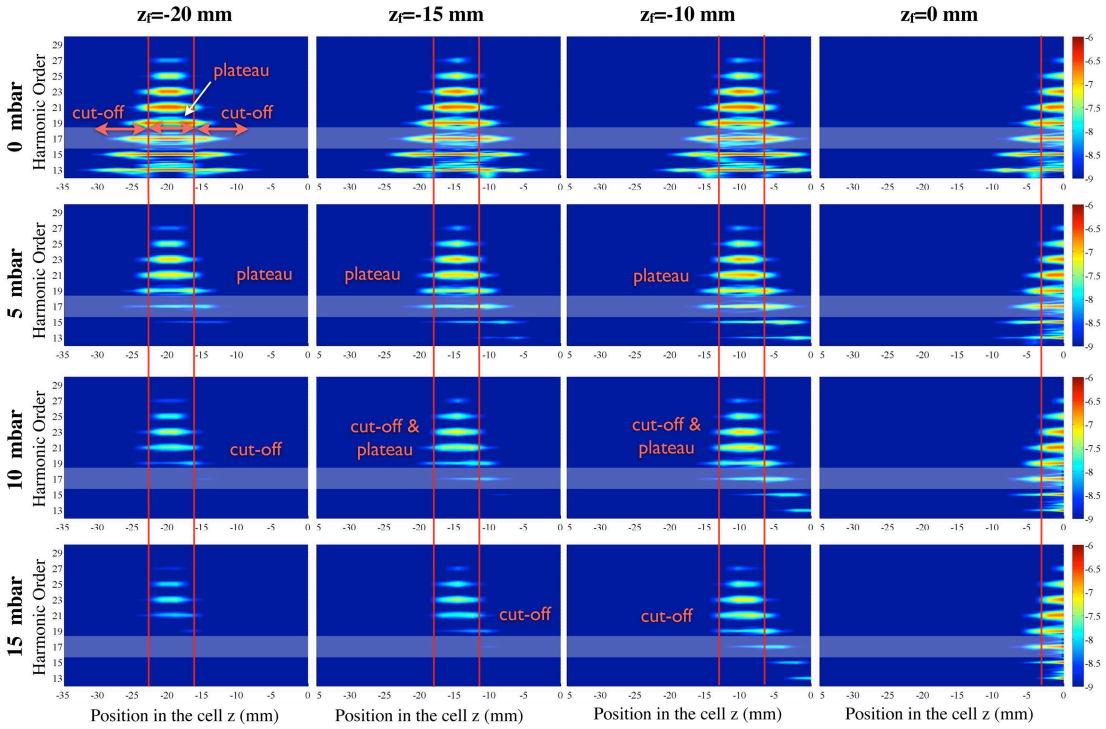

Figure 3.29: Single-atom HHG spectrum along the propagation axis weighted by the absorption over the length remaining until the end of the cell ($z = 0$). From left to right the focus position is changed, being z_f=-20 mm in the first column, and z_f=0 mm in the fourth; from top to the bottom the absorption increases with the gas pressure: from no absorption (0 mbar) in the first row, to the absorption corresponding to 15 mbar in the fourth.

Let us now study the phase-matching effects, including high-order harmonic propagation. In Fig. 3.30 we show the angular profile of the 17th harmonic at the detector, for a SIGC filled with xenon at 5 mbar (first column) and 15 mbar (second column) pressures, and at different focus positions: (a) (b) -10 mm, (c) (d) -15 mm and (e) (f) -20 mm. For the lowest pressure (5 mbar), the angular distribution is composed by three peaks, describing a central spot, surrounded by a ring structure. This structure is the result of the different phase-matching between short and long trajectories, as we saw for a gas jet configuration in section 3.1. Therefore, this result is in agreement with our previous discussion, as from Fig. 3.29 we have seen that the 17th harmonic is generated at the focus and, thus, corresponds to a harmonic inside the plateau. Correspondingly, at 15 mbar, the 17th harmonic is generated in the cut-off region, where

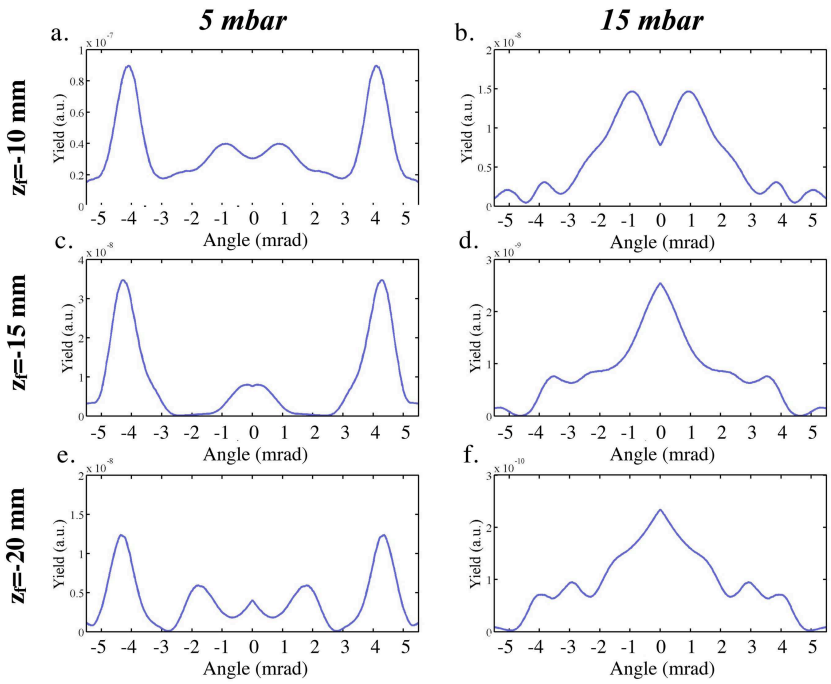

Figure 3.30: Spatial profile of the 17th harmonic generated in a xenon SIGC with 5 mbar (first column) and 15 mbar (second column) pressures, at different focus positions: **a b** -10 mm, **c d** -15 mm and **e f** -20 mm.

short and long trajectory contributions merge in a single one. This explains the uniform peak structure obtained in the right column of Fig. 3.30. The two-peaked structure in Fig. 3.30b can be explained as a intermediate situation, where the 17th harmonic is close to the cut-off region, and short and long trajectory contributions are about to merge into a single one, as it is obtained when moving the focus into the gas cell (Figs. 3.30d and 3.30f). Focusing closer to the exit of the SIGC will enable the generation of the 17th harmonic order from the central focal area leading to a splitting similar to the 5 mbar case.

Now we will compare our results with the present experimental findings from M. Kretschmar in M. Kovačev's group [138]. The laser system consists on a chirped-pulse amplification system (Dragon, KM Labs Inc.) that supplies 35 fs pulses with energy of 1 mJ, centered at a wavelength of 776 nm, at a repetition rate of 3 kHz. The SIGC consist of an approximately 50 cm long gas-filled chamber with an adjustable pressure in the range from 1 to 100mbar. The main difference with our simulations is in the laser

peak intensity, which in the experiment is estimated to be $\simeq 1 \times 10^{15}$ W/cm^2. This sets a limitation for the simulations, as this intensity falls into the barrier suppression regime, in which SFA+ is not reliable. In addition, that intensity makes the application of our propagation method very challenging. However, as it was shown experimentally in [137], the main contributions to the detected harmonic signal come from the regions in which the intensity is in the tunneling regime. For that reason, we have chosen in our simulations a peak intensity of $\simeq 1.26 \times 10^{14}$ W/cm^2.

As a consequence from our parameter choice, the pressure and focus position are different from the simulations compared to the experiments. However, we have found theoretical and experimental conditions that can be considered equivalent, as the absorption can be changed either by modifying the transmission coefficient (changing the pressure), or by changing the focus position (i.e. the propagation length towards the end of the cell). In the left column of Fig. 3.31 we plot the simulated profile of the 17th harmonic, when the focus is placed at z_d=-15 mm, for different gas pressures. On the other hand, in the right column of Fig. 3.31, we present the experimental profiles obtained at 25 mbar, for different focus positions. Under these conditions, the profile of the 17th shows a three peak structure obtained in the plateau region –plots (a) and (b)– that merges into a uniform profile coming from the cut-off region –plots (e) and (f)–. As a consequence, we can interpret the experimental results in the same way as we did for the simulations.

As we already saw in section 1.2.2, the coherence time gives us a direct measurement of the spectral width of the harmonics, and thus the chirp in the harmonic emission, which is different for short and long trajectories. Therefore, in a following step, the on-axis and off-axis spatial regions that appear in Fig. 3.31b were characterized experimentally by measuring its coherence time, using a Mach-Zender interferometric setup [138]. The coherence time was found to be (15.5 $\pm$ 2.9) fs in the on-axis region and (3.9 $\pm$ 0.6) fs in the off-axis region. As a consequence, the on-axis region is attributed to originate from short trajectory contributions, whereas the off-axis ring-structures from long ones.

We have performed a time-frequency analysis (TFA) over our simulated results to confirm this behavior. In Fig. 3.32a we show the HHG spectrum for the case of 5 mbar and $z_f = -15$ mm, shown in Fig. 3.31a. As we can observe, different harmonics show a different angular profile. To enhance the visibility of the 17th harmonic in the TFA,

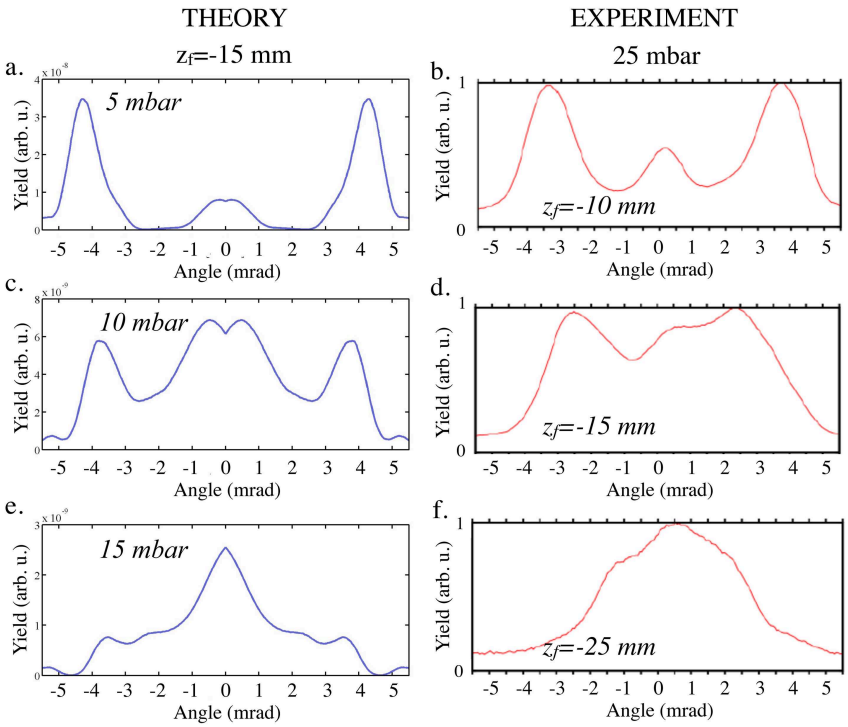

Figure 3.31: Comparison between the simulated and experimental spatial profile of the 17th harmonic. theory vs experiment. In the left column the simulated profile of the 17th harmonic is showed for a focus placed at z_d=-15 mm, and **a** 5 mbar, **c** 10 mbar and **e** 15 mbar. In the right column the experimental profile of the 17th harmonic in a 25 mbar gas cell is presented when the focus is placed at **b** -10 mm, **d** -15 mm and **f** -15 mm.

we have reduced artificially the amplitude of the 15th and 19th harmonics, so the 17th harmonic becomes the prominent one. Now, when performing a TFA with a Gaussian window of $2.5\omega_0$, the obtained information is mainly valid for the 17th harmonic. In Fig. 3.32b we show the TFA on-axis, whereas in 3.32c at 4.7 mrad off-axis, thus monitoring the central and outer peaks obtained in Fig. 3.31a. We can observe that the emission time of the 17th harmonic differs in $0.25T$ from on-axis to off-axis, thus corresponding to the short and long trajectory recollisions for an harmonic in the plateau region (see Fig. 1.5). As a consequence, we have confirmed also theoretically the short trajectory origin of the central peak and the long of the outer peaks.

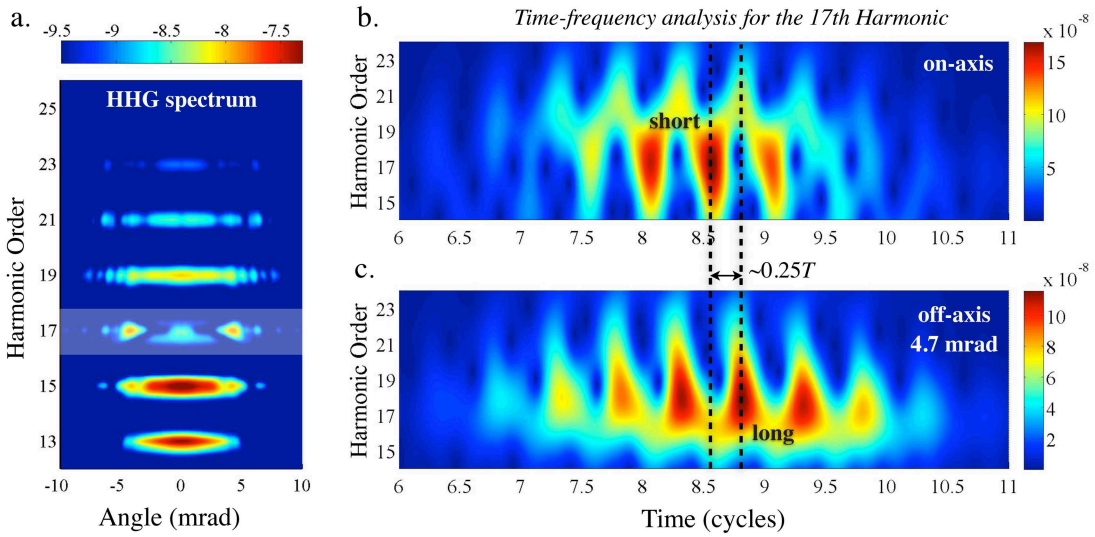

Figure 3.32: **a** HHG spectrum simulated in a 5 mbar gas cell, when the focus is placed at $z_f = -15$ mm. The time-frequency analysis is presented for the harmonics detected **b** on-axis and **c** 4.9 mrad off-axis. The HHG spectrum was modified in order to enhance the visibility of the 17th harmonic in the time-frequency analysis. The emission time of the 17th harmonic differs in $0.25T$ from on-axis to off-axis, being T the period of the laser field.

4

Generation and propagation of ultra high-order harmonic from mid-IR fields in waveguides

There is a basic interest in extending coherent radiation into the X-ray regime from the fundamental and the technological points of view. Coherent X-rays would allow us to develop new scenarios in high-energy physics, metrology, microscopy or femtochemistry. Due to recent developments in intense mid-infrared (mid-IR) laser technology [139], HHG has emerged as a potential tool to produce coherent X-rays up to the kilo-electron volt (keV) regime. Advances in the understanding of macroscopic phase-matching have made possible to generate bright, coherent, high-order harmonics in the keV region from these mid-IR lasers. This has been recently demonstrated by an international collaboration led by JILA (University of Colorado), and in which participated the Technical University of Vienna, Cornell University and us [20]. Although the brightness of HHG X-ray sources falls below those obtained with X-ray free electron lasers (XFEL), the degree of coherence is superior, and the spectral phase and pulse form are regular and repetitive. Moreover the whole source is table-top and, therefore, can be potentially adopted by many laboratories. In this chapter we will focus on the characterization of the temporal coherence of the HHG X-ray sources, by performing single-atom and propagation simulations of HHG driven by mid-IR sources.

On the other hand, as has been commented along this thesis, the quest to capture dynamical processes with ever finer time resolution on the time scale of atoms,

molecules and, more recently, of electrons, is one of the motivations behind the development of ultrashort light pulses [140, 141, 142, 143, 144, 145, 146, 147]. One of the main results of this chapter is to demonstrate that the temporal structure of keV high harmonic X-ray pulses differs substantially from those generated using near-infrared pulses, especially at high photon energies. In particular, we will show that, although the total width of the X-ray bursts spans femtosecond time scales, the pulse shows a sub-attosecond structure due to the interference of high harmonic emission from multiple re-encounters of the electron wavepacket with the ion. Regular zeptosecond waveforms can be produced and manipulated by simply changing the driver laser wavelength, the pulse length, the carrier-envelope offset, and inserting thin metal filters into the X-ray beam. Moreover, the waveform produced corresponds to a 1 fs long envelope modulated at 1.3 exahertz (EHz), which represents the highest frequency coherent waveform to date. This new mechanism thus provides a simple and realistic route for breaking the attosecond barrier, without any need to compensate for chirp.

We have divided this chapter into three sections. First of all, we will introduce the mechanism of high-order harmonic generation as an efficient tool for obtaining X-rays in the keV regime. Secondly, we will analyze the single-atom HHG calculations driven by mid-IR laser pulses, analyzing in detail its temporal structure. As a consequence, we will derive a route for obtaining pulse waveforms in the zeptosecond regime. Finally, we will include propagation effects in order to compare our spectra directly with the experiments, demonstrating the temporal coherence of the produced X-rays.

4.1 X-rays from ultra-high-order harmonic generation

As we already explained in section 1.1.3, from the cut-off law (4.1), we can find two strategies for extending the maximum photon energy in the HHG process: to increase the laser intensity and/or to increase the wavelength of the driving field. As an example, in order to reach 1.5 keV photons, we can combine laser intensity and wavelength following the blue line in Fig. 4.1.

In 2006, Seres *et al.* obtained keV harmonics using an 800 nm laser source, with an intensity close to 10^{16} W/cm^2 [148]. However, the efficiency of the generated radiation was very low due to phase-matching. As it was explained in the previous chapters,

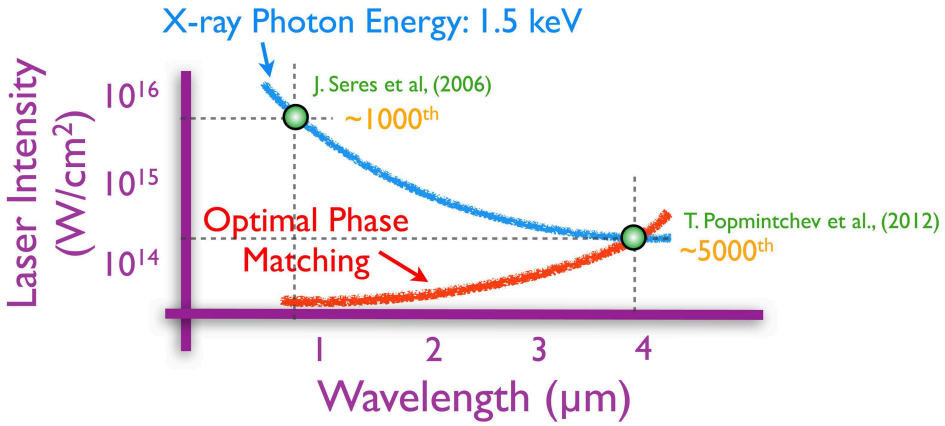

Figure 4.1: Choice of intensity and wavelength of the driving field in order to generate X-rays from HHG. The blue line indicates the intensity and wavelength required to obtain 1.5 keV photons, following the cut-off law. The red line indicates the pair intensity/wavelength where optimal phase-matching conditions are achieved. Two experiments have demonstrated the generation of keV X-rays: Seres *et al.* [148] at 800 nm and T. Popmintchev *et al.* [20] at 3.9 μm. In this latter case, a brightness four to five orders of magnitude higher was obtained.

phase-matching conditions during the propagation of the harmonics play an essential role in the efficiency of the detected signal.

We have already seen in section 2.3.5 that optimal phase-matching can be achieved if the harmonics are generated inside a waveguide [42, 99], fixing an optimal intensity for each wavelength (represented as a red line in Fig. 4.1). As a consequence, the scaling of the harmonic spectrum cut-off with the wavelength and the the compromise with the optimal phase-matching condition suggest that bright X-rays can be generated efficiently using mid-IR lasers. These sources require a refined development of optical parametric techniques (OP-CPA) for the mid-IR, which has been achieved recently [139]. In 2012, the international collaboration led by JILA (University of Colorado at Boulder) mentioned above, demonstrated the efficient generation of coherent X-rays: $>$ 1.6 keV radiation was obtained by combining up to 5000 photons of a mid-IR laser field (3.9 μm in wavelength and $\sim 3 \times 10^{14}$ W/cm^2 peak intensity) focused in an helium-filled waveguide [20].

In fact, optimal phase-matching is a stronger requirement when harmonics are generated with mid-IR fields. At the single-atom level, the efficiency for the generation of

the highest harmonic orders is known to decrease drastically when increasing the driver laser wavelength [40, 41] due to the spreading of the electron wavepacket during the HHG process. Fortunately, this decrease in the single-atom efficiency can be balanced by increasing the number of radiators in the macroscopic target under optimal phase-matching conditions [149, 150]. As a result, in the collaboration mentioned above [20], a brightness four to five orders of magnitude higher was obtained compared to the previous work of Seres *et al.* [148].

When selecting the atomic species with which ultra-high order harmonic generation has to be generated, one has to take into account the absorption cross-sections. For instance due to the presence of L-shell absorption edges in neon and argon (870 eV and 250 eV respectively), absorption at short wavelengths is much more pronounced than in helium. As a consequence, helium becomes the best atomic medium for ultra high-harmonic generation due to the absence of inner-shell absorptions [42].

We represent in Fig. 4.2 the transmission through one centimeter thickness of hydrogen (pink), argon (green), helium (blue) and neon (red), with density $\sim 10^{19}$ atoms/cm^3. In addition we indicate the energy of the 1000th, 3000th ad 5000th harmonics for a 3.9 μm driving laser.

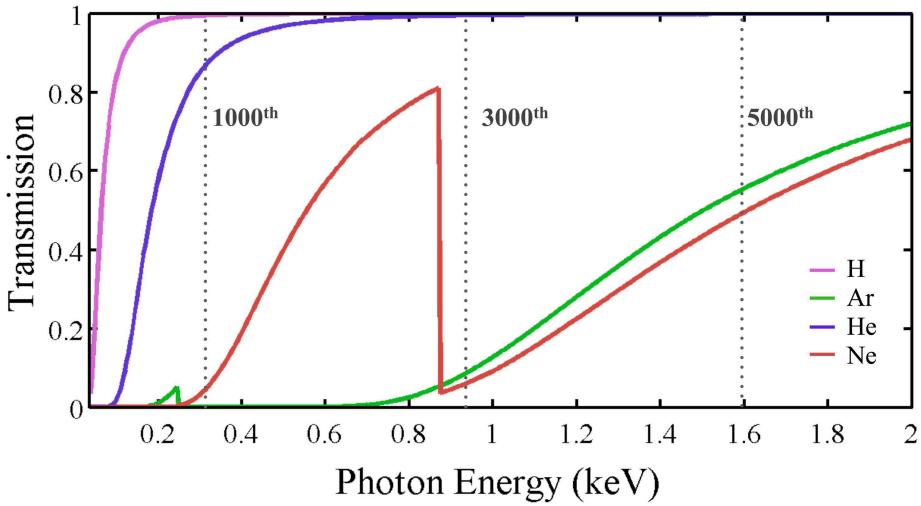

Figure 4.2: Transmission through a gas of density 10^{19} atoms/cm^3 along 1 cm for hydrogen (pink), argon (green), helium (blue) and xenon (red). We indicate the energy of the 1000th, 3000th ad 5000th harmonics for a 3.9 μm driving laser. Data obtained from [98].

4.2 Single-atom calculations: reaching the zeptosecond timescale

The shortest light pulses to date are produced from the broad harmonic spectrum resulting from the extreme nonlinear interaction of intense femtosecond lasers with atomic or molecular gases. Attosecond pulses and pulse trains are obtained using a filter to select the highest spectral contributions, that can support pulse durations <100 attoseconds [21, 50], as it was explained in section 1.1.5. Isolation of a single attosecond pulse from the train has also been reported recently [55, 56, 57].

From the Fourier indetermination, the minimum pulse duration that can be achieved using this scheme scales inversely with the width of the harmonic spectrum. Therefore, the enormous bandwidth of high harmonic X-ray emission driven by mid-IR lasers, offer us the possibility of obtaining extremely short pulses. Based on these ideas, here we present a new and realistic route for breaking the attosecond barrier, that is very attractive in its simplicity because it does not require the chirp compensation of the X-ray bursts. Our calculations show that the temporal structure of high harmonic X-ray pulses generated using mid-IR lasers, differs substantially from those generated using near-infrared lasers, especially at high photon energies. In particular, we show that, although the total temporal width of the X-ray bursts spans femtosecond time scales, they may exhibit a finer structure arising from the interference of X-ray emission due to multiple rescattering of the laser-driven electron wavepacket with the ion.

Other alternative approaches to reach atto-zeptosecond timescales have been proposed earlier [151], in the relativistic laser-plasma interactions at focused laser intensities above 10^{18} W/cm^2 [152, 153], four orders of magnitude higher than in the present proposal (10^{14} W/cm^2).

In the following, we will introduce the modifications to our theoretical method, needed to increase the efficiency of the computation in the mid-IR regime, and analyze in detail the single-atom spectra and temporal waveforms that may be obtained in this regime. We will see that those waveforms can be sculpted simply using thin metal filters of various thicknesses, and adjusting the pulse duration and carrier-envelope phase of the driving laser.

4.2.1 Computing single-atom HHG in the mid-IR regime

Calculating high-order harmonic spectra driven by mid-IR lasers is a challenging task, mainly because the excursion of the electron wavepacket in the laser field scales with the square of the laser wavelength (λ). As an example, in the near-IR regime (λ =800 nm, $I \simeq 3.6 \times 10^{14}$ W/cm^2) the maximum classical excursion of an electron in the continuum falls around 1 nm, whereas in the mid-IR regime considered in this chapter ($\lambda = 4$ μm, $I \simeq 1.6 \times 10^{14}$ W/cm^2), it is around 40 nm. On the other hand, the excursion time for the higher energy electron recollisions is 1.7 fs in the near-IR, whereas 8.4 fs in the mid-IR (assuming this excursion time to be $0.63T$, where T is the laser period). The most precise theoretical method to compute the HHG spectrum, namely the numerical integration of the 3D time-dependent Schrödinger equation (TDSE), requires an extremely large space-time grid in order to ensure the numerical convergence. For long driving laser wavelengths, therefore, it becomes mandatory to adopt simplified models that speed up the computations without missing the relevant information.

We use the SFA+ approach described in section 1.3 [41], including the saddle-point approach in the transverse momentum space (see 1.3.1). This allows us to compute the single radiator yield within minutes for driving laser wavelengths in the mid-IR regime.

Figure 4.3 shows, as a particular example, the results of the SFA+ calculation in comparison with the exact results of the 3D TDSE equation for a helium atom interacting with a laser field of wavelength 1.6 μm. We emphasize that no rescaling is done when comparing these spectra.

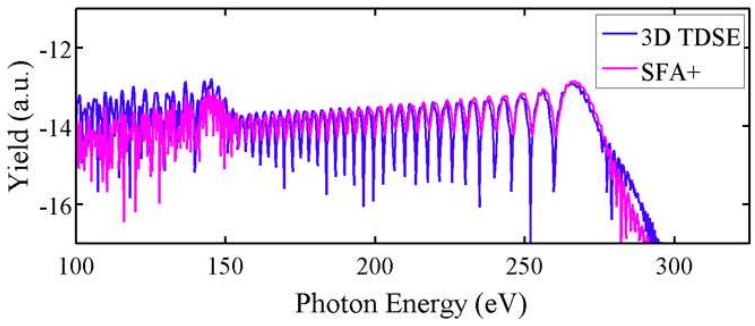

Figure 4.3: Single-atom HHG spectra in helium obtained using 3D TDSE (blue line) and SFA+ (pink line) models, where the laser pulse is assumed to be a $\sin^2$ envelope of 1.4 cycles FWHM (7.7 fs), 1.6 μm wavelength and peak intensity of 3.5×10^{14} W/cm^2.

4.2.2 Effects of high-order rescatterings

Let us now study in detail the single-atom HHG calculations in the mid-IR, using driving laser intensities and wavelengths chosen to fulfill the optimal phase-matching conditions. Figure 4.4 shows the results for the harmonic spectrum of the SFA+ calculation in helium driven by a laser of wavelength 3.9 μm and peak intensity 3.6×10^{14} W/cm^2. The laser pulse is sculpted by a $\sin^2$ envelope of 2.9 cycles FWHM (37.4 fs). The high-frequency part of the spectrum is computed after passing through a 0.1 μm thick Al filter. As becomes evident, the harmonic radiation clearly extends into the keV region (see inset on Fig. 4.4a). The corresponding electromagnetic field, which consists of a carrier wave at 1 keV photon energy, is represented in Figure 4.4a (blue line: intensity, red line: group delay, i.e. derivative of the spectral phase). To enhance visibility, the time resolution for the phase derivative has been chosen to average the additional fast oscillations that appear in the pulse train envelope.

The results show that the X-ray emission is composed of bursts of this carrier wave with temporal widths of about 2 fs. This temporal structure has the same electron-recollision origin as the attosecond pulse trains obtained using near-infrared laser wavelengths [48, 129, 154, 155]. The long durations of the bursts are a consequence of the wider time-interval in which energetic electron recollisions take place, that scale linearly with the driving laser wavelength. Interestingly, the atto-chirp is predicted to decrease as λ^{-1}. As a consequence, selecting a fixed HHG bandwidth, shorter X-ray pulses would be obtained when moving to longer mid-IR laser wavelengths [40]. However, under optimal phase-matching conditions, the generated phase-matched HHG bandwidth increases as $\lambda^{1.7}$, which effectively leads to the emission of chirped X-ray burst of femtosecond durations.

Most interesting and new is the fine structure of super-high-frequency oscillations that appears on some of the femtosecond HHG bursts. These structures are not observed using near-IR driving laser wavelengths around 0.8 μm, and are only present when mid-IR driving fields are used. In our simulations, they appear gradually during the interaction, and mainly influence the femtosecond X-ray bursts generated on the trailing part of the mid-IR pulse. As we will show later, the increasing contrast of the oscillations leads to the splitting of these femtosecond bursts into waveforms of a few attoseconds (or even hundreds of zeptoseconds) in duration.

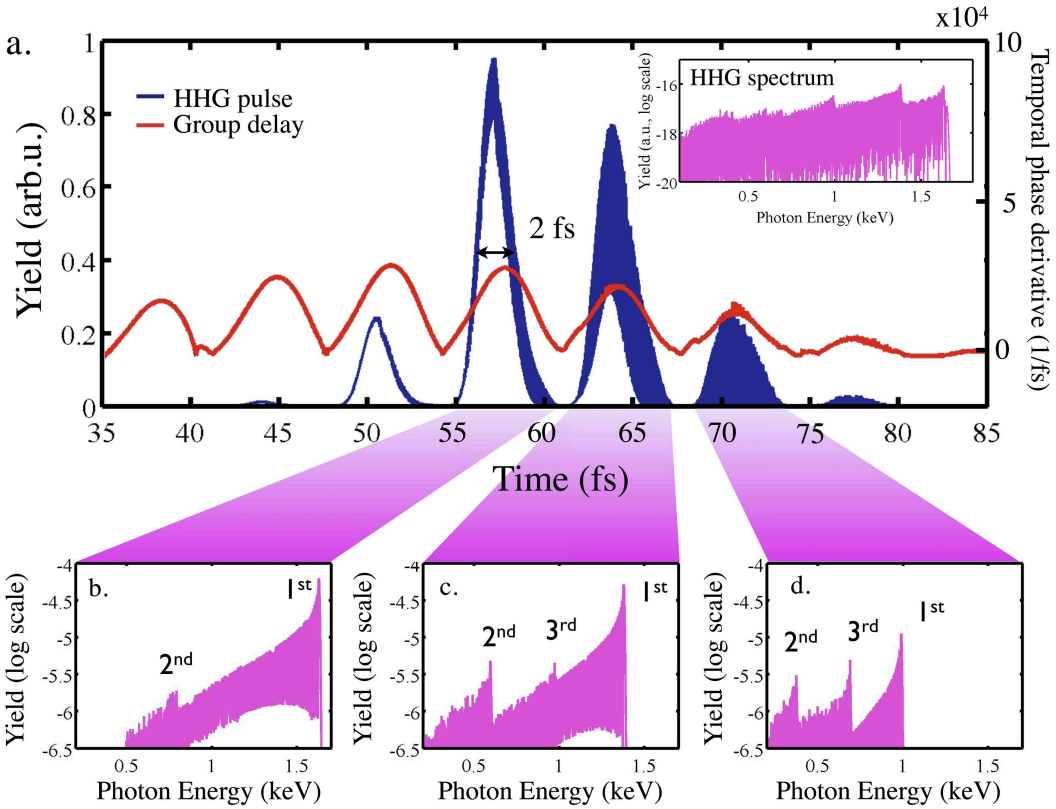

Figure 4.4: **a** Envelope of the X-ray bursts (blue line) and group delay (red line) obtained using a 3.9 μm wavelength laser, at an intensity of 3.6×10^{14} W/cm^2, and with a pulse duration of 2.9 cycles, (37 fs) FWHM. The HHG spectrum is shown in the inset (pink line). In the panels **b** to **c**, the spectral content of each burst is shown.

The physics underlying this waveform can be explained with the aid of the time-frequency analysis shown in Figure 4.5b. This plot shows the correlation of the HHG emission time with energy and, superimposed, the kinetic energy of the electrons at the moment of rescattering resulting from a classical trajectory analysis (black circles). The Gaussian spectral window to perform the time-frequency analysis was $13.5\omega_0$ in FWHM, being ω_0 the fundamental frequency. The three series of circles correspond to HHG emission from the first, second, or third consecutive rescatterings of the different electron trajectories with the parent ion. Examples of the classical trajectories leading to the three rescatterings are shown in Figure 4.4a for the HHG emission at 71 fs.

The appearance of a fine structure in the X-ray pulses in Fig. 4.4a is connected

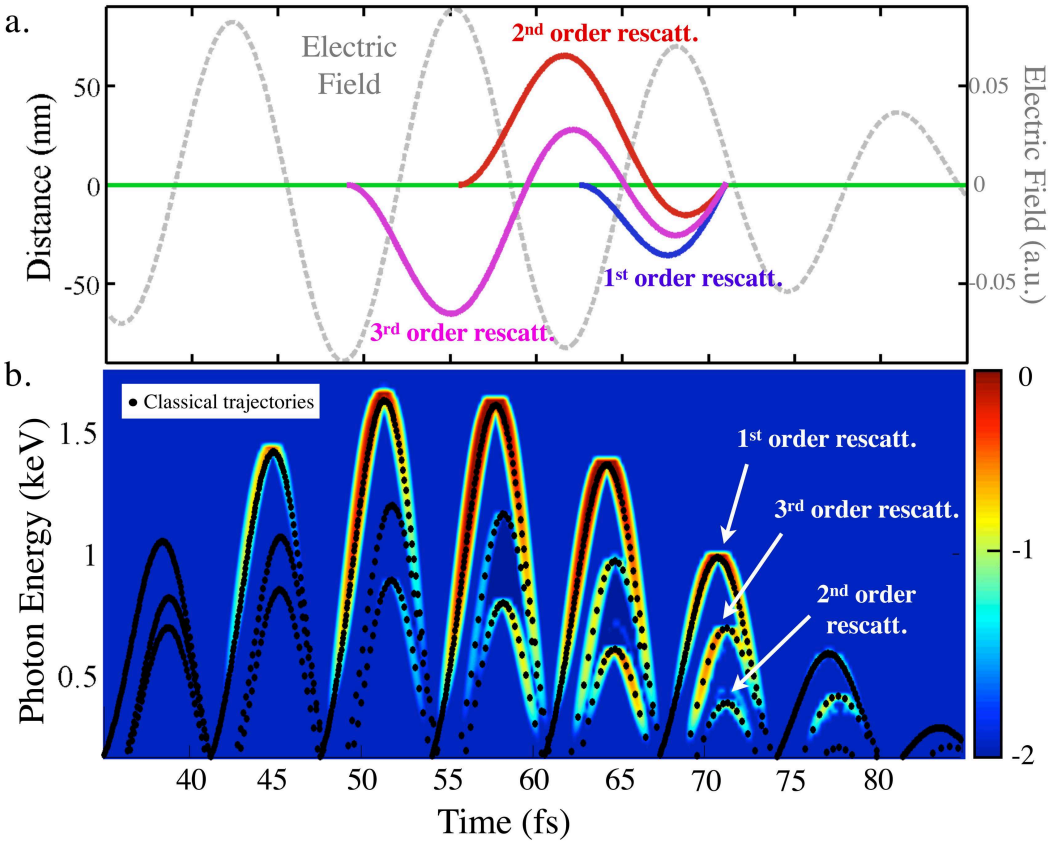

Figure 4.5: **a** Schematic of the driving field (grey-dashed line) and an example of the interfering trajectories contributing to one of the X-ray fs burst of Fig. 4.4a at time 71 fs. **b** Time-frequency analysis (logarithmic scale), of the HHG spectrum shown in Fig. 4.4a. The black-dotted lines represent classical calculations of the electronic rescattering energies of trajectories with different rescattering orders, which are more intense at the trailing part of the pulse. The Gaussian spectral window to perform the time-frequency analysis was $13.5\omega_0$ in FWHM

to the increase in relative strength of the HHG emission from the second and third rescatterings of the electron wavepacket with the ion, as the driving laser wavelength is increased. The interference structures become significant if the relative weights of HHG emission from the first and subsequent rescatterings are comparable. This occurs on the trailing edge of the laser pulse, where the efficiency loss associated with electron wavepacket spreading for the second and third rescatterings is compensated by the higher ionization rate when the electron was liberated into the continuum (the ionization times are nearer to the peak of the mid-IR laser pulse for these high-order rescatterings at the trailing edge). The different contributions of the multiple rescatterings can be identified in Figs. 4.4b-d, where we plot the spectral content of each fs burst. Note that the relevance of higher-order rescatterings for strong-field processes at longer wavelengths has been recently described in other contexts as well, theoretically [40] and experimentally [156], although its technological potential was not identified.

For the sake of clarity, we present in Fig. 4.6 the single-atom HHG calculations from helium driven by a longer laser pulse, 5.8 cycles FWHM (57 fs), i.e. twice the one considered previously. The laser wavelength remains 3.9 μm and the phase-matched peak intensity is now 3.3×10^{14} W/cm^2, similar to the recent demonstration of efficient generation of keV harmonics [20]. In 4.6a it is represented the carrier wave envelope (blue line) and its averaged temporal phase derivative (red line). From the time-frequency analysis in 4.6c, and the classical schematic representation in 4.6b, one can observe that, for this longer laser pulse, the fourth and the fifth rescattering orders become visible, leading to a more irregular structure of the fs X-ray bursts. Such high-order re-encounters of the electron with the nucleus were also observed experimentally in [156] for similar laser pulse durations.

Let us now identify the high-order rescattering effects in the exact 3D TDSE calculations. As mentioned above, resolving the 3D TDSE equation for those long wavelengths its very challenging. However, we have made calculations at 2 μm, where the high-order rescatterings are already present. In Fig. 4.7 we show the results of the SFA+ calculation in comparison with the exact results of the 3D TDSE equation for an helium atom interacting with a laser field of wavelength 2 μm, and pulse duration 2.9 cycles (19 fs) FWHM. Plot 4.7a shows the HHG spectra whereas the time-frequency analysis is presented for (b) the 3D TDSE and (c) SFA+ calculations. We can observe that the efficiency of the higher-order rescatterings is higher in the 3D TDSE than in the SFA+.

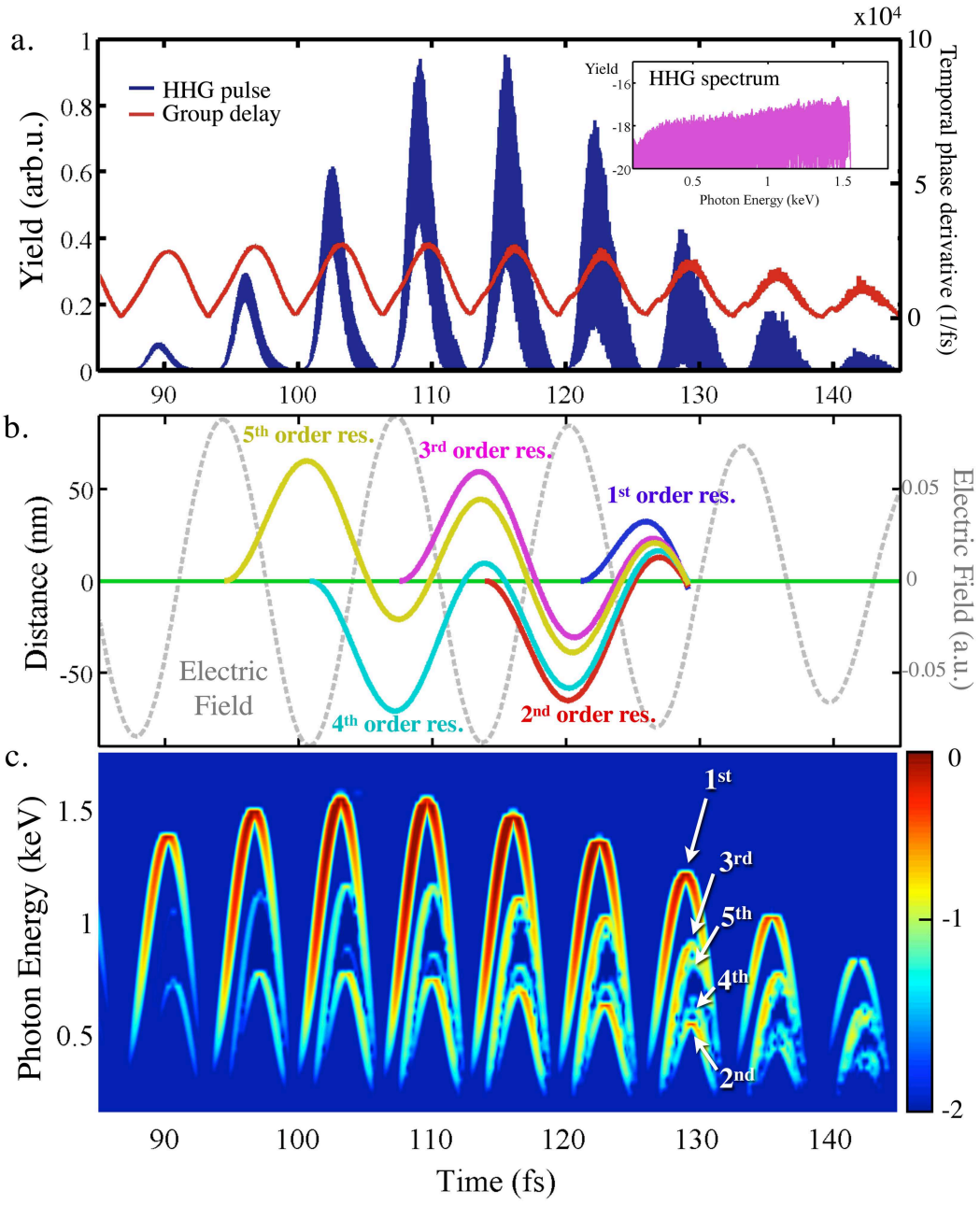

Figure 4.6: **a** Envelope of the X-ray bursts (blue line) and group delay (red line) obtained using a 3.9 μm wavelength laser, at an intensity of 3.3×10^{14} W/cm^2, and with a pulse duration of 5.8 cycles, (75 fs) FWHM. The HHG spectrum is shown in the inset (pink line). **b** Schematic of the driving field (grey-dashed line) and an example of the five interfering trajectories contributing to one of the X-ray fs bursts at 129 fs. **c** Time-frequency analysis (logarithmic scale), where the Gaussian spectral window used was $13.5\omega_0$ in FWHM.

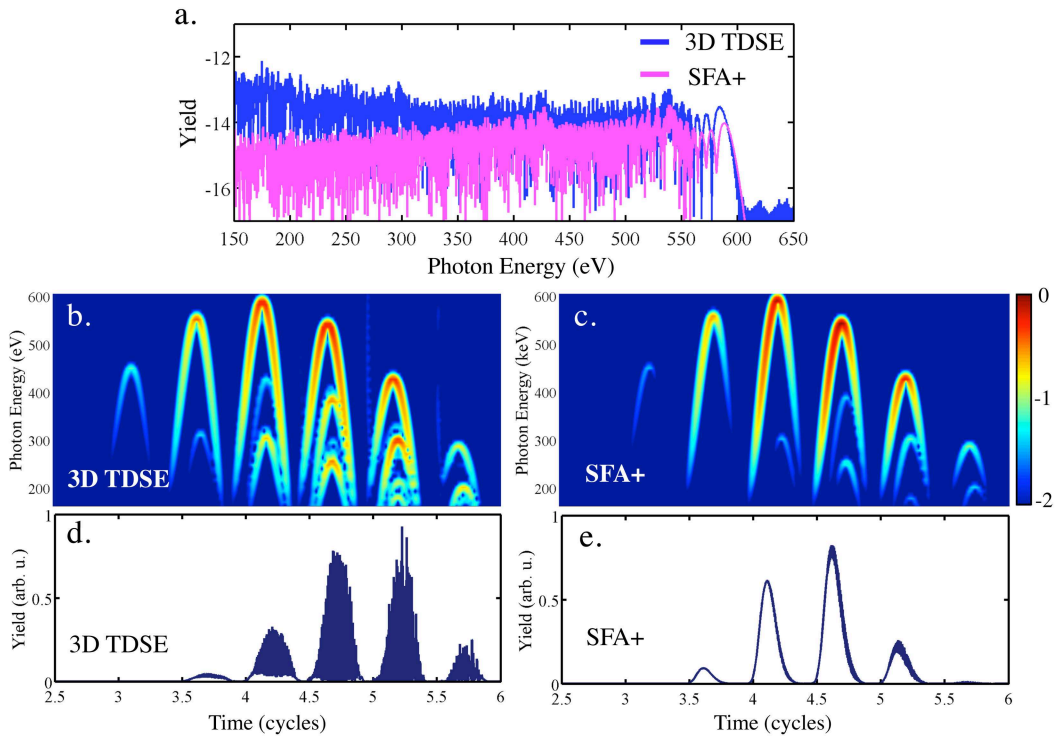

Figure 4.7: **a** HHG spectrum obtained with the 3D TDSE (blue line) and SFA+ calculations (pink line) obtained using a 2 μm wavelength laser, at a phase-matched intensity of 4.7×10^{14} W/cm^2, and with a pulse duration of 2.9 cycles, (19 fs) FWHM. The time-frequency analysis (in logarithmic scale) and envelope of the X-ray bursts are shown for **b** **d** the 3D TDSE and **c** **e** SFA+ calculations respectively.

This is translated into a more contrasted structure in the X-ray waveforms in the 3D TDSE case (plot 4.7d) than in the SFA+ (4.7e). As a consequence, for longer wavelengths we have to take into account that the efficiency of higher-order rescatterings increases when considering the exact 3D TDSE calculations.

In the following subsections we will filter temporally and spectrally the mid-IR HHG spectrum. First, by properly filtering the different rescattering orders, we will see that a fully contrasted waveform in the atto and zeptosecond timescales can be obtained. Secondly, by spectrally filtering the high-frequency part of the HHG spectrum we will find a route for manipulating the attosecond pulse train.

4.2.3 Filtering in the temporal-domain: Zeptosecond waveforms

In this section, we show that the contrast interference due to HHG emission from multiple rescattering events is significant enough to fully modulate the femtosecond X-ray bursts into a waveform of extremely short keV pulses. By properly filtering the different rescattering events, we will show that waveforms in the attosecond and even zeptosecond time scales can be achieved.

In Figure 4.8 we present the detailed structure of one of the femtosecond X-ray bursts (panel a) originated at the tail of the mid-IR pulse (of Fig. 4.5) used recently in experiments [20]. The temporal structures of the bursts obtained by using Al filters of different thicknesses, (c) 0.1 μm, (d) 0.5 μm, and (e) using a 0.1 μm Al filter combined with an artificial high-pass filter, are compared with each other. As can be seen from the spectra, the filters are chosen to select the contributions of the first (Al filter + high pass filter), the first and second (Al filter of 0.5 μm) and all three (Al filter of 0.1 μm) rescattering orders to the HHG spectra. The results clearly reveal the full modulation of the femtosecond burst into a waveform of pulses of about 5 attoseconds in duration, for this particular case. Note that each pulse in the train contains less than two cycles of the keV carrier wave.

The beating structure is not regular since there are HHG contributions from multiple rescattering processes (see 4.8c). A more regular pulse train can be obtained by increasing the thickness of the Al filter such that only the contributions of two rescatterings can interfere (4.8d). As expected for an interference pattern, the time between two consecutive bursts is given by $T = 2\pi/\Delta E$, where ΔE is the energy difference between the two dominant energetic contributions (here arising from the first and the third rescatterings). Finally, suppression of all but the first rescattering events leads to the disappearance of the fine structure in 4.8e, which unequivocally demonstrates that the interference effects are the origin for the attosecond fine structure in the femtosecond X-ray bursts.

We can now identify two conditions for the generation of atto/zeptosecond waveforms using this new approach: (i) the interference of two –*and only two*– electron wavepacket rescattering events in order to form a regular modulation, and (ii) comparable strengths of the two contributions to the HHG emission in order to achieve good contrast. Both requirements can be met using few-cycle mid-IR driven pulses, even

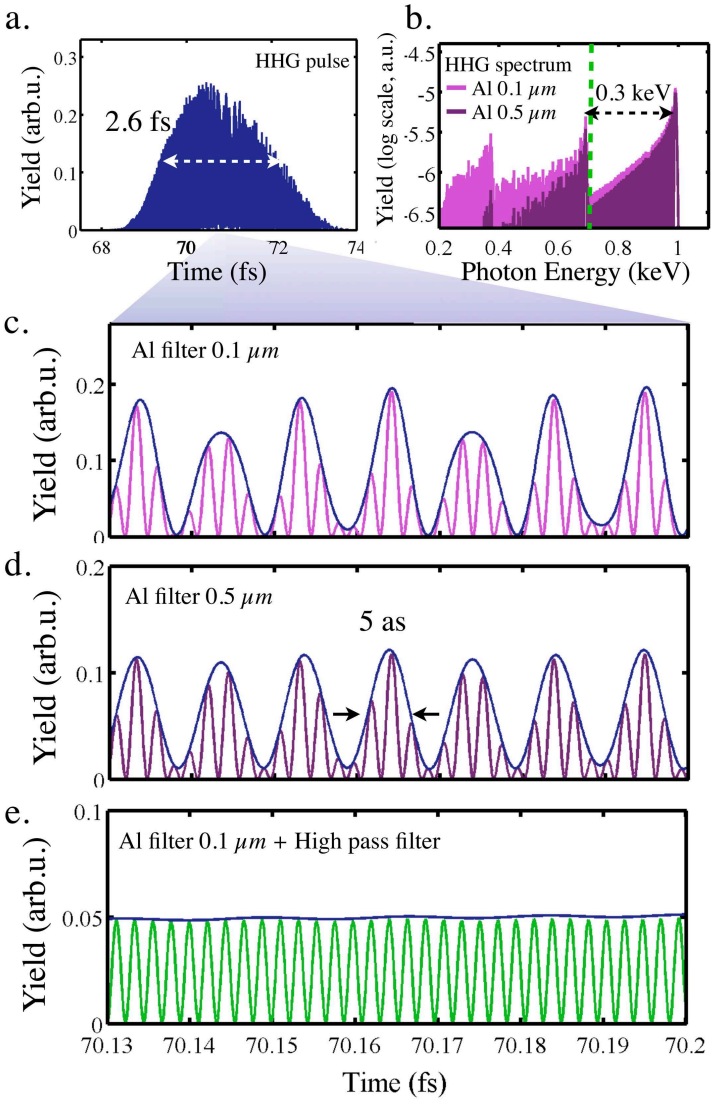

Figure 4.8: **a** Detailed structure of an X-ray burst from the tailing edge of the keV pulse train shown in Fig. 4.3 using an Al filter (0.1 μm thick), for a laser wavelength of 3.9 μm. The spectrum of the selected burst is shown in **b** for Al filters of 0.1 and 0.5 μm thickness. Plots **c** and **d** show a magnification of the temporal structure for the two Al filters respectively, whereas **e** corresponds to the X-ray field obtained by selecting only the highest frequency contributions to the spectra (above the greened dashed line in **b**).

without tailoring the spectra using filters (as was done for the results in Fig. 4.8d). The short duration of the driver pulse acts as a temporal window, restricting the number of rescattering events, while the relative efficiency of the rescattering events can be controlled using the carrier-envelope offset. With this understanding, we can now predict the optimal driving laser parameters to use in order to generate sub-attosecond waveforms. The number of rescattering events as well as their relative timing, and the energy of the returning electron for each rescattering, can be estimated using classical trajectory analysis. From these, the optimum driving pulse to meet condition (i) can be found and the width of the pulses in the train can be estimated as $T/2$. Predictions for $T/2$ as a function of the wavelength of a 1.5 cycle (FWHM) driver laser are shown in Fig. 4.9. The intensities of the driver pulses are chosen to match those for which optimal phase-matching is observed experimentally [9]. These simulations thus predict that the attosecond barrier will be broken for mid-IR wavelengths of about 7.7 μm.

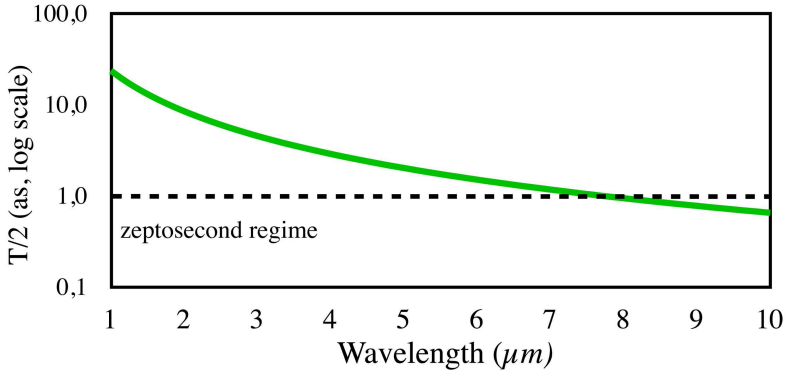

Figure 4.9: Predictions for the value of the width of each keV pulse in the train ($T/2$) as a function of laser wavelength.

Now, we perform simulations at wavelength λ= 9 μm in order to identify the zeptosecond (zs) waveform formation. We have considered a driving laser field of the form $\sin^2(\pi t/2\tau_p)\sin(2\pi ct/\lambda+\phi_{CEO})$ with intensity 3.4×10^{14} W/cm^2 (ideal for macroscopic phase-matched HHG at this laser wavelength), pulse duration τ_p= 43 fs (FWHM) and carrier-envelope offset ϕ_{CEO}=-π/8 (see Figure 4.10a). The results for the generated HHG spectrum (inset on left) after transmission through an 0.2 μm thick Al filter, are shown in Fig. 4.10b. There are two femtosecond bursts emitted, and the second burst is fully modulated into a zs waveform. In comparison with the 4 μm driver laser (shown

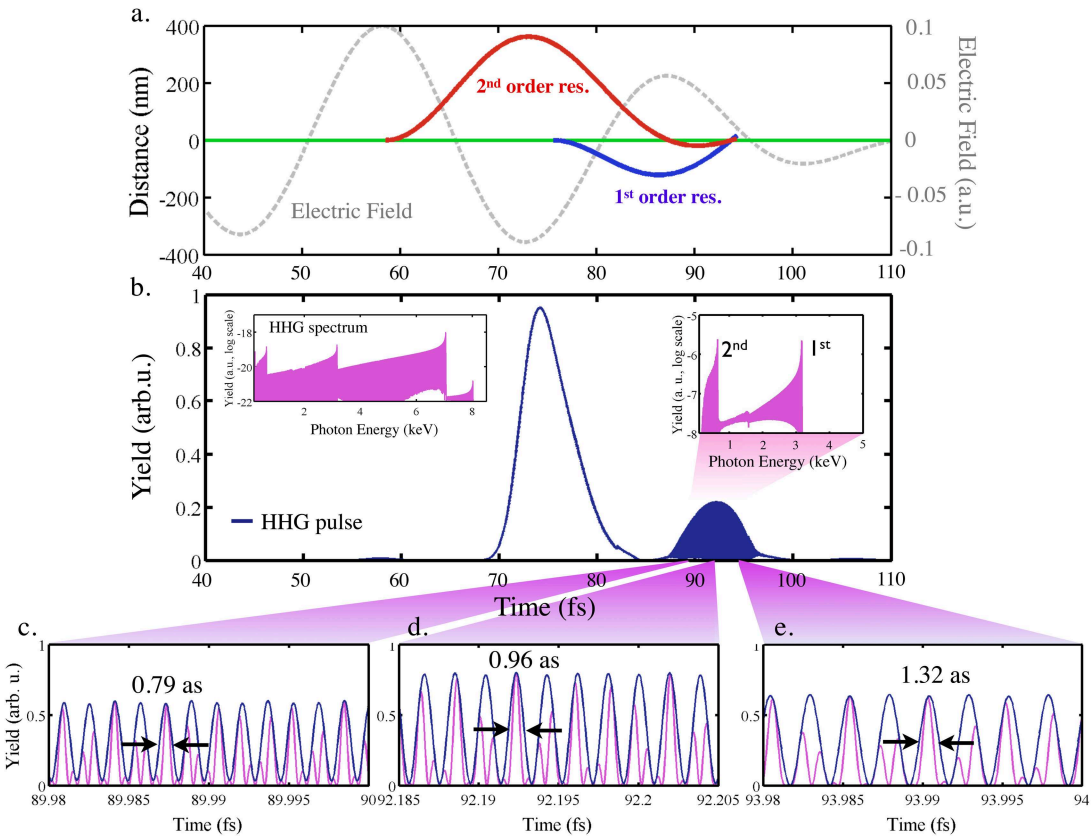

Figure 4.10: **a** Schematic of the driving field (grey-dashed line), 1.5-cycle mid-IR laser pulse with wavelength λ= 9 μm, macroscopic phase-matching intensity 3.4×10^{14} W/cm^2, pulse duration τ_p= 43 fs (FWHM) and carrier-envelope offset ϕ_{CEO}=-π/8. The first and second-order rescattering trajectories are drawn for a recollision time of 94 fs. **b** Envelope of the X-ray bursts obtained from the driving laser field. Left inset: high-order harmonic spectrum after an Al filter 0.2 μm. Right inset: spectral content of the second fs burst, showing the contributions of the first and second rescattering trajectories. Panels **c** to **e** detail the fine temporal structure of the second fs burst.

in Fig. 4.4), for a 9 μm driver laser, the spectral cut-off is increased to 8 keV, while the number of X-ray bursts emitted is smaller, as expected due to the few number of cycles in the laser field. The value for the carrier-envelope offset of the laser pulse is chosen to optimize the relative weight of the two rescattering contributions for the second burst (inset on right) and, hence, the contrast of the pulse-train in the waveform. Thus, the HHG emission presents interferences from only two rescattering events (see Fig. 4.10a), each with comparable efficiency, and as a result, a zeptosecond waveform is formed, as can be observed in Figs. 4.10c to e. The atto-to-zepto chirp associated with the temporal distribution of each of the two rescatterings leads to the emission of shorter keV pulses (0.72 as) on the leading edge (Fig. 4.10c), and longer pulses (1.32 as) on the trailing edge of the burst (Fig. 4.10e).

This new and straightforward route for generating as and zs waveforms is applicable to keV high harmonic emission driven by mid-IR lasers. We emphasize that the present scheme does not rely on compensating the atto-chirp, but rather makes use of the fact that the relative strength of HHG emission due to multiple rescatterings of the electron wavepacket becomes comparable using mid-IR laser wavelengths. By controlling the duration and carrier-envelope offset of driving laser pulses above 7 μm, the generation of a regular waveform consisting of trains of pulses with zeptosecond duration is realizable. Although one can expect to generate even shorter X-ray pulses at wavelengths much longer than 9 μm, one has to consider that at those wavelengths, the drift associated with the magnetic term in the Lorentz force, would lead to a separation of the electron trajectory by a distance too large to be compensated by the expansion of the free wavepacket and, therefore, to a reduction of the harmonic yield. The evidence of radiation bunches of zeptosecond scale opens the possibility of extending the applications of femtochemistry and attophysics to the zeptosecond time scale.

Control of the relative efficiency using the carrier-envelope offset

The relative efficiency of the different rescattering orders can be controlled by modifying the carrier-envelope offset of the driving pulse. In Fig. 4.11, we show the results of our numerical simulations for a driving laser of the form $\sin^2(\pi t/2\tau_p)\sin(2\pi ct/\lambda + \phi_{CEO})$, with wavelength λ= 9 μm, peak intensity 3.4×10^{14} W/cm^2, pulse duration τ_p= 43 fs (FWHM) for carrier-envelope offset of (a) ϕ_{CEO}=-π/2,(b) ϕ_{CEO}=-π/4, (c) ϕ_{CEO}=0, (d) ϕ_{CEO}=π/4. In each panel we show the envelope of the X-ray bursts (blue line) as

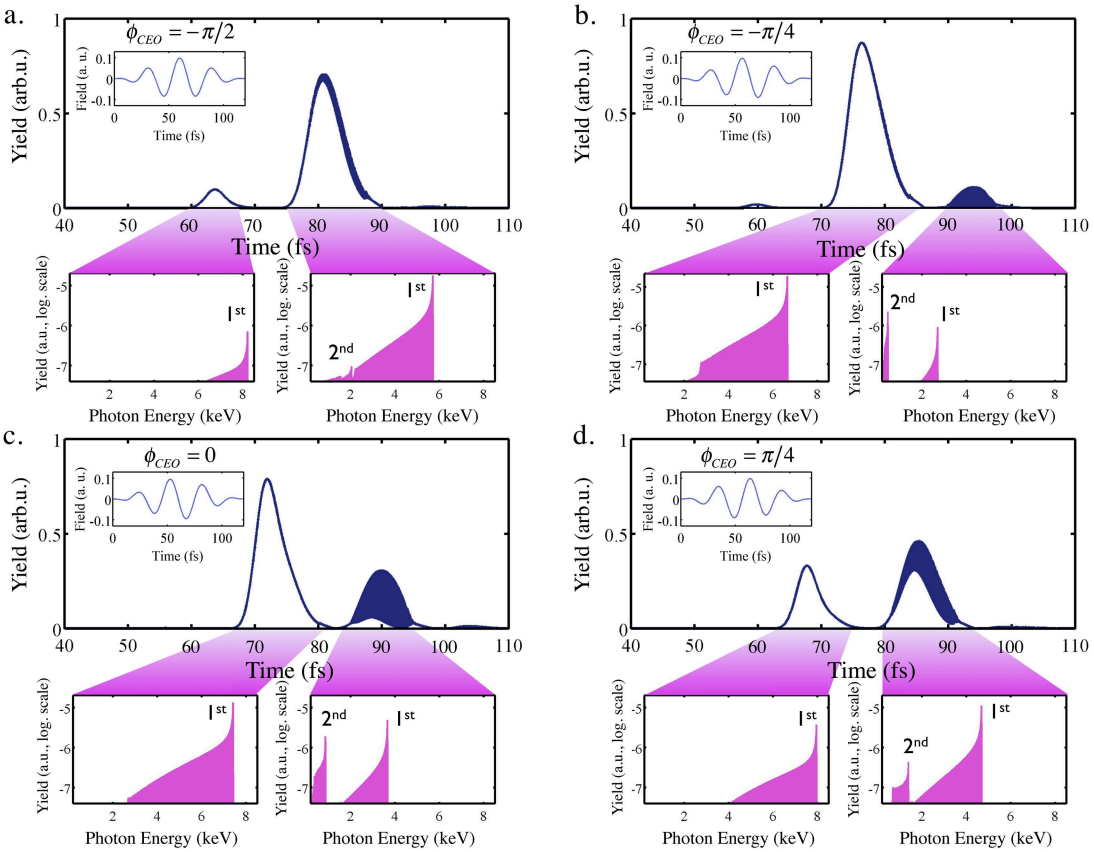

Figure 4.11: Numerical simulations for driving laser pulses of the form $\sin^2(\pi t/2\tau_p)\sin(2\pi ct/\lambda + \phi_{CEO})$, with wavelength λ= 9 μm, peak intensity 3.4×10^{14} W/cm^2, pulse duration τ_p= 43 fs (FWHM), and for carrier-envelope offset of **a** ϕ_{CEO}=-$\pi/2$, **b** ϕ_{CEO}=-$\pi/4$, **c** ϕ_{CEO}=0, **d** ϕ_{CEO}=$\pi/4$. In each panel we show the envelope of the X-ray bursts (blue line) as they appear from the high-order harmonic spectrum after transmission on an Al filter 0.2 μm thick, as well as the spectrum of the two main bursts (pink line).

they appear from the high-order harmonic spectrum after transmission on an Al filter 0.2 μm thick, as well as the spectrum of the two main bursts in each case. We can observe how the relative weight between the first and second rescattering contributions is modified as the carrier-envelope offset is changed. In panels (a) and (d), the relative weight is substantially different so the beating contrast of the train of zeptosecond pulses is low. In panels (b) and (c) the carrier-envelope phase chosen balances the relative weight to nearly equal, so that full contrast is achieved. The case shown in Fig. 4.10 corresponds to the intermediate of (b) and (c).

Propagation effects in the zeptosecond waveform

The complete simulation of the HHG process needs to take into account propagation in order to include phase-matching effects. For such long wavelengths (9 μm), computing HHG propagation is not feasible using current state-of-the-art theory. However, we have computed one-dimensional propagation for shorter wavelengths (2 μm), where the fine modulations arising from the high-order rescattering events are present with lower contrast.

We compute the field propagation from the single atom response using a scheme based on the discrete dipole approximation (see section 2.5) assuming a plane wave incident field. This assumption is based on the fact that we are implementing our calculations in the optimal phase-matching regime [42], i.e. there is only a particular intensity for which the harmonic fields propagate efficiently. Note that the intensity selection for the optimal phase-matching is advantageous to minimize the intensity dependence of the intrinsic phase. In addition, we include ionization, neutrals and group velocity effects in the fundamental field phase. Absorption was taken into account in the propagation of the harmonics.

In Figure 4.12a, we present the single-atom results of our numerical simulations for a driving laser of wavelength λ= 2 μm, peak intensity 4.7×10^{14} W/cm^2, and pulse duration 19 fs FWHM (2.9 cycles). There is an attosecond modulation over the femtosecond bursts related to the high-order rescattering events. In 4.12b we include propagation, where the target is modeled as an helium gas of density 10^{18} atoms/cm^3 and length 0.5 mm. It is observed that the modulations in the attosecond regime are preserved when considering propagation. Thus, we expect that the atto/zepto modulations are preserved when considering longer wavelengths and higher densities.

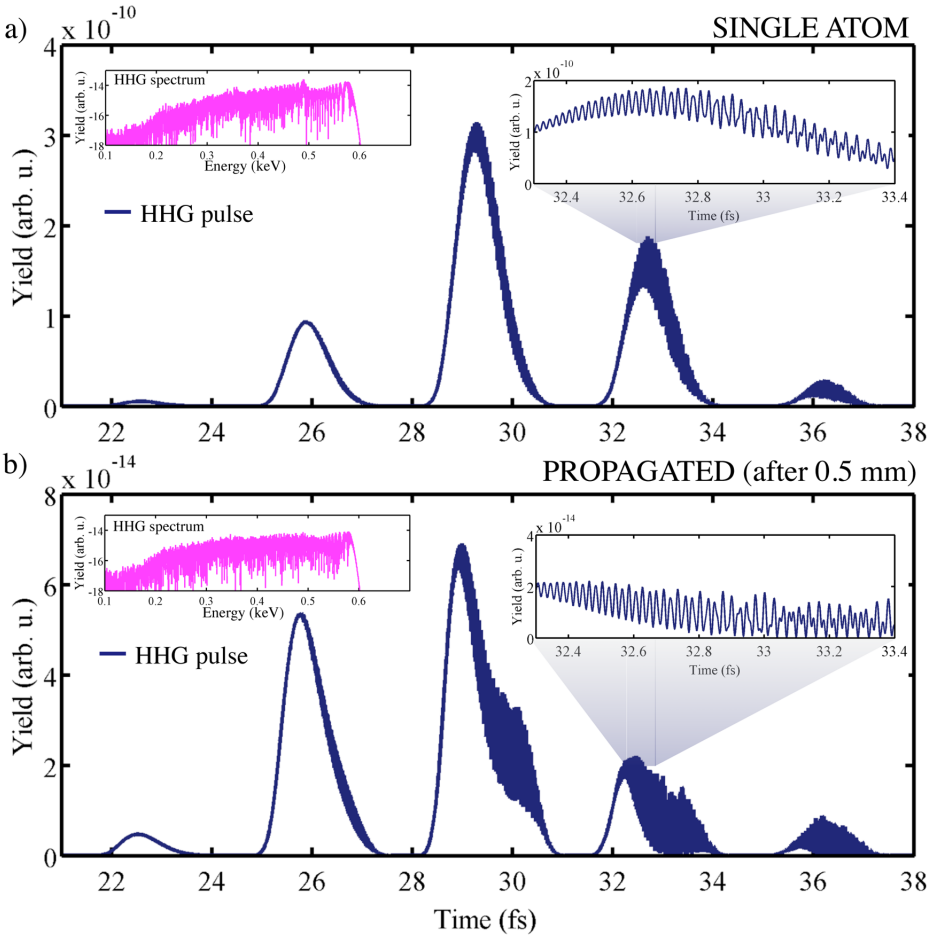

Figure 4.12: **a** Single atom HHG pulse (blue line) for a driving laser of wavelength λ= 2 μm, peak intensity 4.7×10^{14} W/cm^2, and pulse duration 19 fs FWHM (2.9 cycles). The pink line in the inset represents the HHG spectrum. In **b** we present the propagated HHG pulse and spectrum, where the target is modeled as an helium gas of density 10^{18} atoms/cm^3 and length 0.5 mm.

4.2.4 Filtering in the spectral-domain: Resolving different trajectory contributions.

Let us now describe how to control the X-rays in the temporal domain by applying n spectral filter. In principle it would be difficult to design specific filters that allow us such manipulation at the high frequencies presented here, but other systems such as a pair of gratings could be designed for that purpose.

The enormous broadband that offers the HHG spectrum obtained from mid-IR lasers, gives us the possibility of select different rescattering events by spectrally filtering the spectrum. In Fig. 4.13 we show a comparison of the capability of temporally controlling the produced X-ray bursts for two different wavelengths: (left column) 3.9 μm and (right column) 1.6 μm. Plots (a) and (b) show the HHG spectra obtained, using the corresponding phase-matching intensities at each wavelength, whereas plots (c) and (d) show the corresponding time-frequency analysis. As discussed above, high-order rescatterings are relevant at long wavelengths, thus being almost negligible at 1.6 μm. We now apply a spectral filter with a Gaussian distribution of 50 eV FWHM, centered at the photon energies corresponding to different multiples of the ponderomotive energy, U_p, as showed in (a) and (b). The central frequency of each filter is also indicated with dashed lines in the TFA. In Figs. 4.13e to 4.13p we present the envelope of the X-ray bursts (blue line) using the different filters, and its temporal phase derivative (red line).

There are interesting properties that can be extracted from the computed X-ray bursts. First, let us concentrate on the number of X-ray bursts obtained in each half-cycle. In the cut-off region (Figs. 4.13e and 4.13f, where the filter is centered at $3.1U_p$), one burst is obtained per half-cycle. As we move the filter towards the plateau region, each burst is split into two bursts per half-cycle, each one corresponding to the short and long trajectory contributions, as indicated by the slope of the temporal phase derivative (positive for the short ones, and negative for the long). This splitting is more precise for the longer wavelength. More interesting is the appearance of several bursts per half-cycle when the filter is centered at $1.5U_p$ and $1.1U_p$ for the 3.9 μm case (Figs. 4.13m and 4.13o). Each burst corresponds to different rescattering orders as indicated by the TFA. However, in the 1.6 μm case, the temporal structure with those filters becomes irregular (Figs. 4.13n and 4.13p). As a result, by properly filtering the HHG spectrum driven by mid-IR sources, one can obtain temporal structures corresponding to different rescattering orders, and thus, with different phase properties.

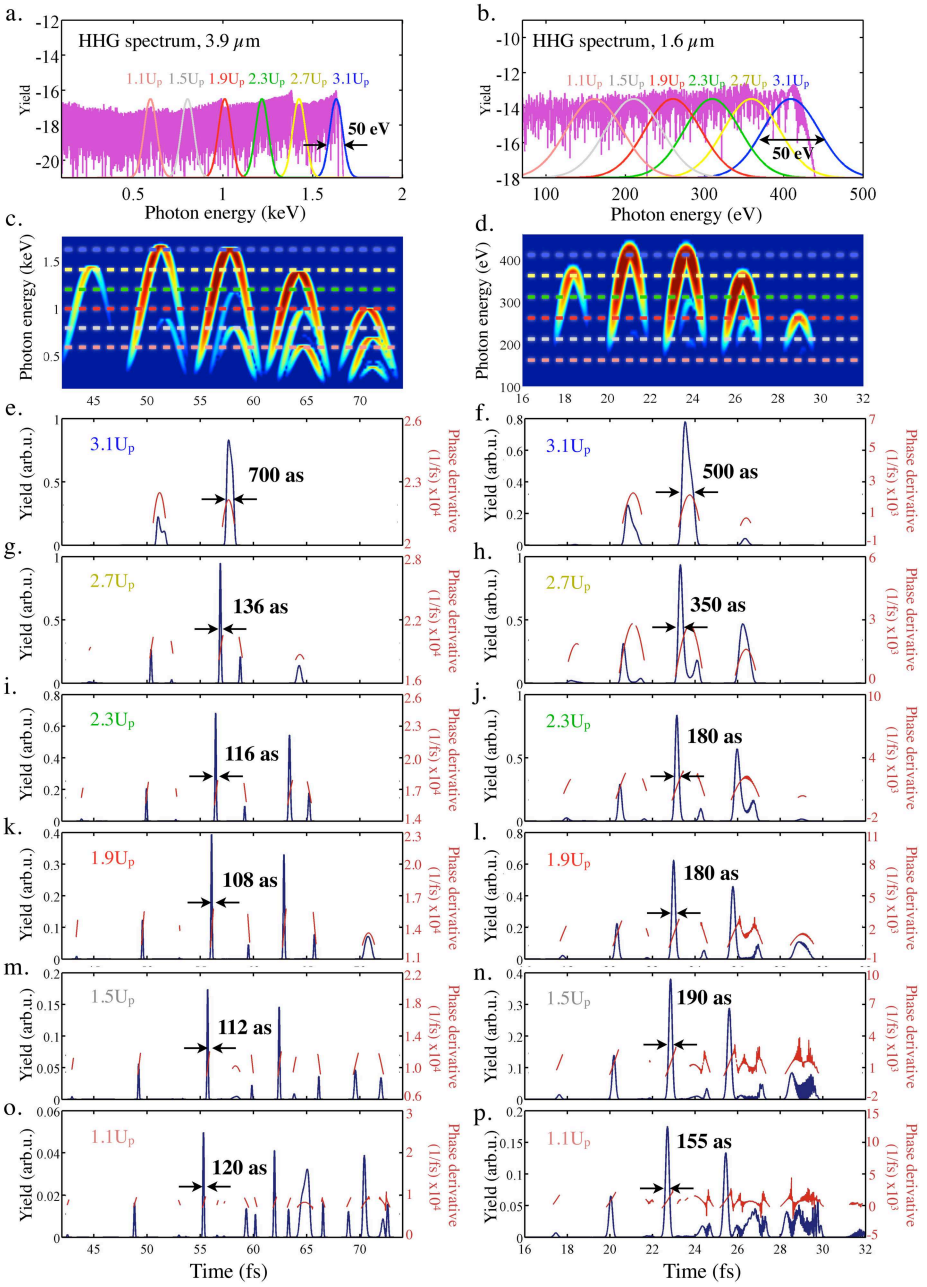

Figure 4.13: Control of the X-ray bursts obtained from HHG driven by (left column) 3.9 μm and (right column) 1.6 μm laser fields. The laser pulse envelope is modeled as a $\sin^2$ function of 2.9 cycles FWHM, with macroscopic phase-matching peak intensities, 3.6×10^{14} W/cm^2 at 3.9 μm and 5.2×10^{14} W/cm^2 at 1.6 μm. **a** and **b** show the HHG spectra, whereas **c** and **d** the corresponding time-frequency analysis. A spectral filter with a Gaussian distribution of 50 eV FWHM is applied, centered at different multiples of the ponderomotive energy, U_p, as showed in **a** and **b** with different colors. The central frequency of each filter is also indicated with dashed lines in the time-frequency analysis (TFA). In the rest of plots we present the envelope of the X-ray bursts obtained after applying the indicated filter.

Let us now concentrate in the width of the X-ray bursts. In principle, from 50 eV photon bandwidth, 82.5 attosecond pulses could be obtained in the Fourier limit. However, due to the chirp imprinted in the HHG process (red lines in Figs. 4.13e to 4.13p), the shortest pulses that we can achieve are longer than 100 as. In the single-atom regime presented here, the shortest attosecond pulses are produced in the plateau region, where the short and long trajectory contributions are well separated. Note that although the bandwidth of the filter is the same, longer X-ray pulses are obtained for the 1.6 μm case, as the chirp acquired over that bandwidth is higher.

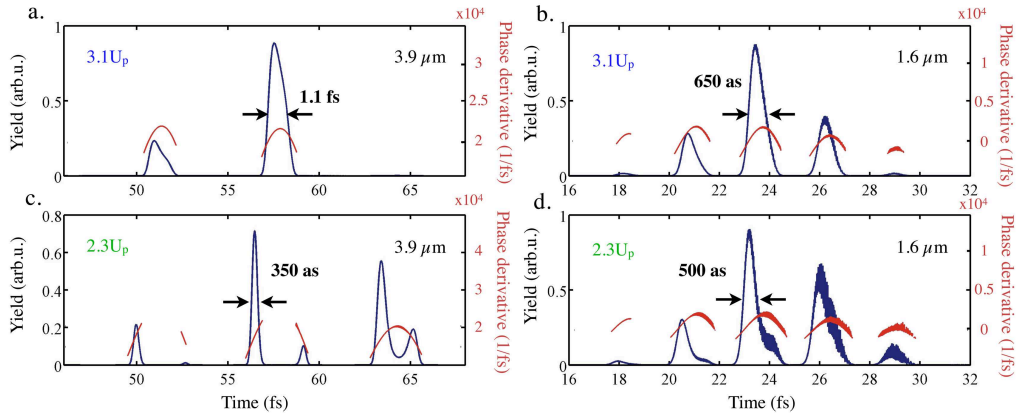

Figure 4.14: Temporal envelope of X-ray bursts obtained from HHG driven by (left column) 3.9 μm and (right column) 1.6 μm laser fields. The laser pulse is modeled as in Fig. 4.13. A spectral filter with a Gaussian distribution of 150 eV FWHM is applied, centered at different at **a b** $3.1U_p$, and **c d** $2.3U_p$.

In a next step, we increase the bandwidth of the spectral filter from 50 eV to 150 eV. In principle, one would expect to obtain shorter X-ray pulses, as in the Fourier limit, 27.5 as pulses would be obtained. In Fig. 4.14 we present the X-ray bursts for the 3.9 μm (left column) and 1.6 μm (right column) cases, after applying the spectral filters centered at $3.1U_p$ and $2.3U_p$. First, we observe that the splitting between short and long trajectory contributions is no longer achieved in the 1.6 μm, due to the broad bandwidth considered. Secondly and more interesting, the X-ray bursts obtained are even longer than in the previous case, where a narrower bandwidth was selected. This is a result of the chirp imprinted during HHG, that prevents from obtaining shorter pulses at the single-atom level. Post-compressing techniques or propagation effects would be needed to compensate that chirp, allowing to obtain shorter attosecond X-ray pulses.

4.3 Propagation effects in ultra high-order harmonics driven by mid-IR fields

Once we have studied the single-atom HHG driven by mid-IR laser sources, here we will include propagation effects. As stated before, implementing propagation in such long wavelengths is a challenging task, due to the large spatio-temporal grid required for the single-atom computations. However, we have included some approximations in order to reproduce the experimental results.

First, in the previous section we have analyzed the atto-to-zeptosecond structure that arises in the X-ray bursts due to the high-order rescatterings. When considering propagation, this effect becomes an issue to reach convergence. In order to avoid the high-order rescatterings we have implemented a spatial mask in the single-atom calculations that dimmes the higher-order electron rescatterings.

In Fig. 4.15a and 4.15c we show the single-atom HHG spectrum for 1 and 6 cycles $\sin^2$ envelope laser pulse, with a wavelength of 3.9 μm and a peak intensity of 4.1 and 3. 3 $\times 10^{14}$ W/cm^2 respectively. Figure 4.16a shows two cut-offs due to the different ionization peaks present in the incident few-cycle laser field. In both simulations, the highest harmonic cut-off reaches 1.6 keV, thus combining more than 5000 mid-IR photons. In figures 4.15b and 4.16d we plot the corresponding temporal HHG pulse (blue lines), showing a unique temporal burst in the 1-cycle case, whereas a train of fs pulses for the 6-cycles laser field. In both cases each burst has a FWHM of 2 fs. The parabolic shape of the first derivative of the temporal phase (green curves) shows contributions from both short (positive slope) and long (negative slope) electron trajectories, thus exhibiting a temporal chirp. As can be noticed, the signature of high-order rescatterings in the temporal domain has been removed.

In the experiment carried out by Kapteyn and Murnane's group and Baltuška's group, six-cycle (80 fs) FWHM, 10 mJ pulses, centered at a wavelength of 3.9 μm, were generated at 20 Hz as the idler output of an optical parametric chirped-pulse amplification laser system [139]. X-rays were generated by focusing the laser beam into a 200 mm diameter, 5 cm long, gas-filled hollow waveguide. High gas pressures of helium up to 35 atm were used to increase the photon flux. The HHG spectrum was then captured with the use of a soft X-ray spectrometer and X-ray charge-coupled device camera. An scheme of the setup is shown in Fig. 4.16. The phase-matched HHG

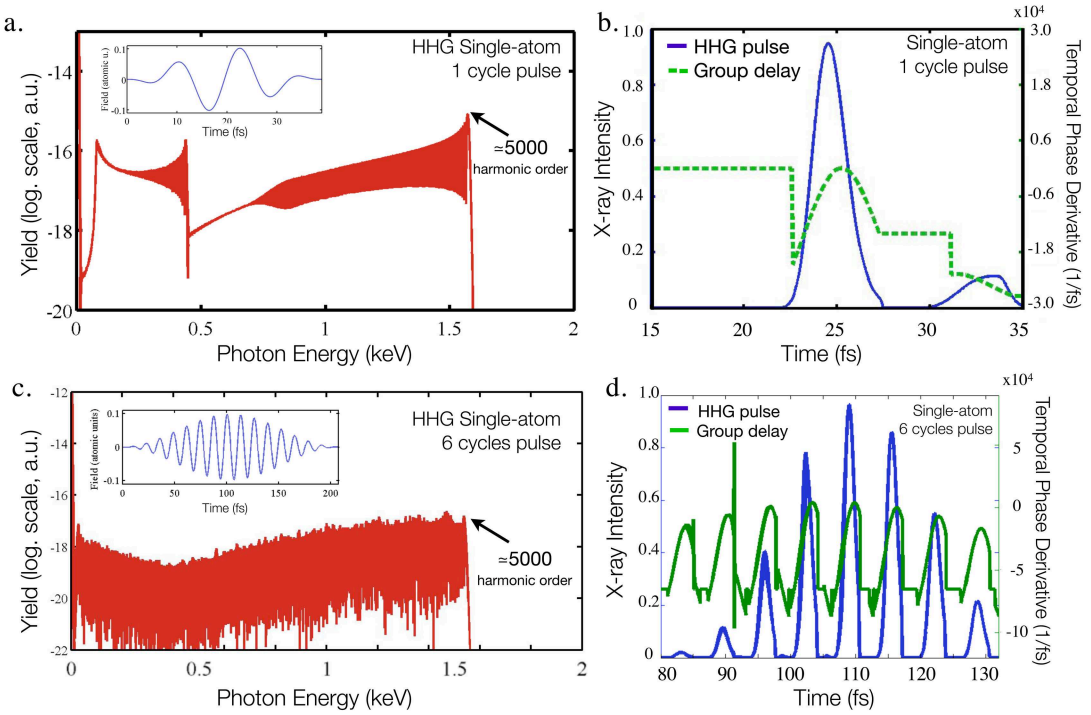

Figure 4.15: Calculated HHG **a c** spectral and **b d** temporal shape for single atom driven by 1 cycle and 6 cycles $\sin^2$ envelope laser pulse, with a wavelength of 3.9 μm and a peak intensity of 4.1 and 3. 3 $\times 10^{14}$ W/cm^2 respectively. The green line in **b** and **d** shows the temporal phase derivative (group delay).

measured extends to $>$ 1.6 keV ($<$ 7.7 Å), corresponding to an extreme $>$ 5000-order nonlinear process. An approximate brightness of 10^5 photons per shot (corresponding to 10^6 photons/s at 20 Hz) is observed in a fractional bandwidth of 1% at 1 keV.

The spatial coherence of the produced X-ray beam was experimentally observed in Young's double-slit diffraction patterns [20]. This spatial coherence measurement demonstrates that coherent diffractive imaging will be possible with near wavelength spatial resolution, as has been achieved using HHG beams and synchrotron sources in the EUV and soft X-ray regions [157, 158]. However, the characterization of the temporal coherence is challenging, as its experimental verification would require the development of characterization methods that can sample ultrabroad bandwidth X-ray waveforms at different photon energies.

To predict the temporal properties of the HHG radiation, we have performed sim-

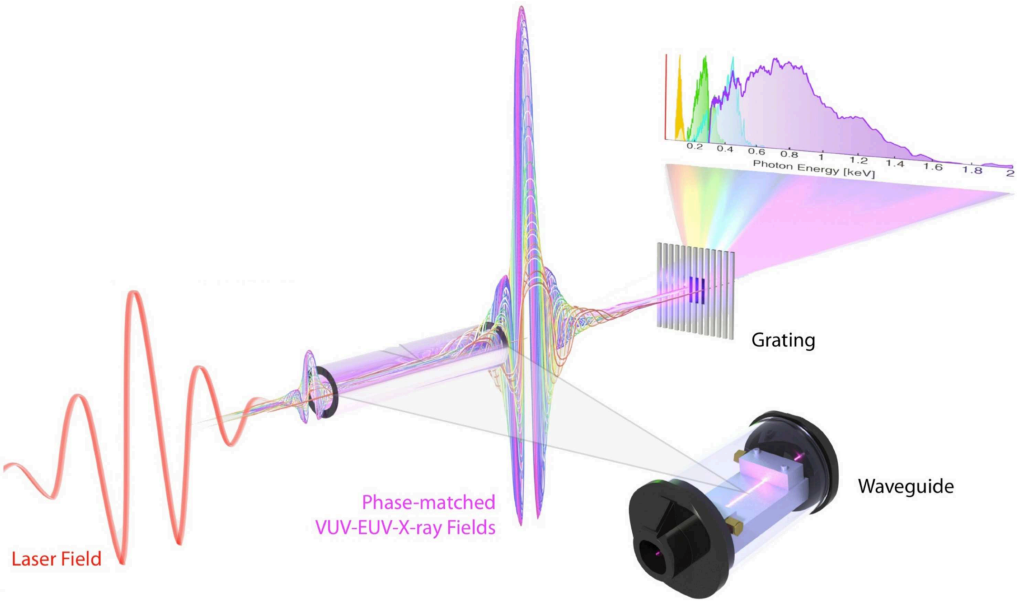

Figure 4.16: Schematic illustration of the coherent kilo-electron volt X-ray supercontinua emitted when a mid-IR laser pulse is focused into a high-pressure gas-filled waveguide. Six-cycle (80 fs) FWHM, 10 mJ pulses, centered at a wavelength of 3.9 μm were focused into a 200 mm diameter, 5 cm long, helium-filled hollow waveguide. Figure taken from [20].

ulations of high-order harmonic propagation. Field propagation is computed from the single-atom response using the scheme based on the discrete dipole approximation (see section 2.5) assuming a plane wave incident field, and including ionization, neutrals and group velocity effects in the fundamental field phase. Assuming a plane wave is reasonable since optimal phase-matching conditions selects an optimal intensity, and, in addition, the multiatmosphere gas pressures required for phase-matched X-ray generation support laser beam self-confinement, giving rise to a high quality, flat-top beam. Absorption was taken into account in the propagation of the harmonics. The attosecond pulses have been computed by Fourier transformation of the harmonic spectrum detected on-axis. The target is modeled as helium gas with a density of 5×10^{19} atoms/cm^3. The disparity of the temporal scales involved in the computations (femtosecond for the driving field and attosecond for the most energetic harmonics) together with the high density used, requires an extremely precise computation. At present we are able to demonstrate good convergence for propagation distances up to 20 μm, which

correspond to the data presented here. In our calculations, the laser pulse is modeled using a $\sin^2$ envelope of 6 cycles FWHM, 3.9 μm wavelength and phase-matching peak intensity of 3.3×10^{14} W/cm^2.

In Fig. 4.17 we show (a) the experimental and (b) theoretical results. Our calculations confirm the femtosecond time scale of the X-ray bursts after propagation. Our calculated phase-matched HHG spectra agree well with those measured experimentally, and show that the HHG chirp is well behaved over the near kilo-electron volt bandwidth that, when compressed, is sufficient to support a single-cycle, 2.5-as pulse in the Fourier limit. For 3.9 μm driving lasers in the single-atom case, contributions from the short and long trajectories lead to a parabolic chirp (see Fig. 4.15), whereas after propagation, the phase-matched short trajectory contribution leads to a positive, quasi-linear chirp, as can be observed in the inset of Fig. 4.17b. The current limit of theory allows us to simulate HHG propagation over 20 μm distances at high pressures and predicts that the uncompressed HHG temporal emission consists of a series of $\simeq$three intense bursts of 1- to 3-fs duration, due to the very long 13-fs period of the multicycle 3.9 μm driving laser field. However, for longer propagation distances, bright HHG emission in the form of a single isolated X-ray burst is expected. This is because phase-matching is transient and favors X-ray emission from a single halfcycle of the laser pulse where the phase-matching is optimal. This has been verified experimentally in the EUV, even without stabilizing the carrier wave with respect to the pulse envelope [42, 159]. Interestingly, this work and past work predict that the HHG bursts are chirped, where the amount of chirp scales inversely with laser wavelength for a given spectral bandwidth [40].

On the other hand, as it was predicted in section 4.2, our simulations confirm that the duration of each X-ray burst still spans femtosecond durations due to the increased phase-matched HHG bandwidth, which scales almost as the square of the laser wavelength.

As a conclusion, here we have demonstrated that the X-ray bursts obtained by ultra-high order harmonic generation driven by mid-IR sources, exhibit temporal coherence. The chirped X-ray supercontinua represent a promising multiple-atomic site probe with sub-femtosecond time resolution, analogous to the chirped white light (visible) continua used to probe many absorption features simultaneously, perfectly synchronized to the driving laser.

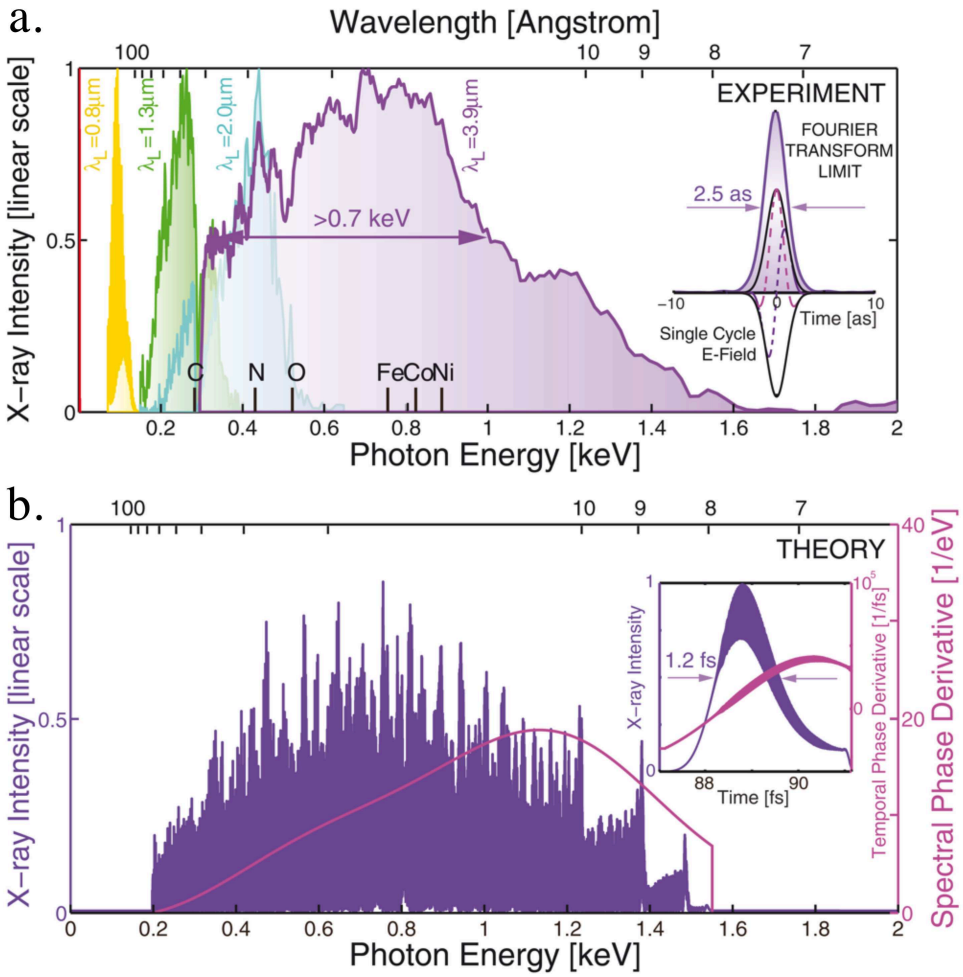

Figure 4.17: **a** Experimental HHG spectra emitted under full phase-matching conditions as a function of driving-laser wavelength (yellow, 0.8 μm; green, 1.3 μm; blue, 2 μm; purple, 3.9 μm). (Inset) Fourier transform-limited pulse duration of 2.5 as. **b** Calculated spectrum and temporal structure of one of the phase-matched HHG bursts driven by a 6 cycles FWHM 3.9 μm pulse at a laser intensity of 3.3×10^{14} W/cm^2.

Conclusions

We present in this thesis a novel method to compute high-order harmonic generation (HHG) from the interaction of intense fields with macroscopic targets. Our starting point is the single-atom model developed previously in the group (SFA+), and our objective was to build the bridge from this microscopic level to the macroscopic case, therefore, between fundamental theory to experiments. For this, we have developed an original method to describe the high-order harmonic propagation. Our approach is based in the integral solution of the wave equation, instead of resorting to its numerical integration, as it is usually done. The main advantage of our approach is that it computes directly the far field at the detector, so we can analyze the topology of the HHG process throughout the macroscopic target, in terms of its contribution to the detected field. Moreover, it offers numerical advantages in simplicity and speed, allowing us to present the first results, to our knowledge, on high-order harmonic generation and propagation at mid-infrared wavelengths of 4 μm and above. Using this method, we have approached a series of experimental situations and drawn the following conclusions.

In a first set of simulations, we have studied the propagation of high-order harmonics from near-infrared fields in rare gases. We have analyzed theoretically the phase-matching conditions for different gas jet positions along the propagation axis, and developed the corresponding experiments at the laser facility in the University of Salamanca (under the guidance of Dr. Íñigo Sola). The agreement of our simulations with the experiments, and with other results in the literature, has served as validation of our code.

Once our code was corroborated, we analyzed theoretically the behavior of the attosecond pulses obtained from HHG. In an original work, we have proposed a route to directly compensate the chirp of the attosecond pulses by detecting them at a certain angle from the propagation axis. Performing a time-frequency analysis, we identified

the interference between different quantum paths as the underlying mechanism for this compensation. This was our first insight in how to observe and control the macroscopic signatures of these single-atom processes.

In order to complete our understanding of phase-matching, we have developed a study of the transversal coherence length, which is a concept that, although not new, is usually considered not to be relevant for the understanding of harmonic propagation. For that purpose, we have introduced harmonic-emission spatial maps as an original theoretical tool to understand the phase-matching process. By studying theoretically and experimentally the effect of aperturing the laser beam in the efficiency of the harmonic signal, we have unequivocally identified the relevance of the transversal coherence length for common parameters (i.e. not exotic) in HHG experiments.

In a next step, we have implemented a semi-infinite gas cell geometry in order to give support to the experiments carried by M. Kovačev's group at Universität Hannover (Germany). We found that in this the geometry, harmonic absorption plays a relevant role, selecting the effective intensity at which each harmonic is generated. Different parameters as the gas pressure and focus position were changed to confirm our expectations.

The second part of this thesis was aimed to simulate HHG driven by mid-infrared laser sources. We adapted our method to this regime in collaboration with the theoretical group of A. Becker and A. Jaron-Becker at JILA, University of Colorado (USA). The main result was the description of the keV X-rays obtained by the experimental group of M. Murnane and H. Kapteyn at JILA, University of Colorado (USA), that led a joint collaboration with Technical University of Vienna (Austria), Cornell University (USA) and us. In particular, since the experimental characterization of the temporal coherence in this regime is challenging (it would require the development of characterization methods for ultrabroad bandwidth X-ray sampling), our simulations were used to complement the experiment. As a result, we predicted that the X-rays are generated in femtosecond bursts with a well-behaved chirp, thus demonstrating their temporal coherence.

Finally, in a further exploration of the X-ray bursts driven by mid-infrared laser sources, we found a route for obtaining soft X-ray waveforms in the zeptosecond regime (1 zs=10^{-21} s). This effect is a consequence of the interference between different rescattering orders of the electron wavepacket with its parent ion.

Spanish summary / *Resumen en español*

"Fuentes de luz coherentes de attosegundo basadas en la generación de armónicos de orden elevado: influencia de los efectos de propagación"

Durante las últimas dos décadas, el avance en el campo de los láseres ultraintensos y ultracortos ha mejorado nuestra comprensión de la materia sometida a campos láser intensos. A diferencia de otros campos no perturbativos de la física, la disponibilidad de la tecnología de láseres intensos en laboratorios de tamaño medio a nivel mundial ha proporcionado una fructífera interacción entre la teoría y los experimentos. Esta tesis es un ejemplo de esta interacción.

La radiación electromagnética intensa induce una fuerte respuesta no lineal en la materia. Los electrones atómicos adquieren energía del campo láser, que puede ser posteriormente liberada en forma de radiación coherente de alta frecuencia, en un proceso conocido como generación de armónicos de orden elevado (HHG, procedente de sus siglas en inglés). La ausencia de láseres convencionales a estas frecuencias elevadas ha impulsado el interés tecnológico en el desarrollo de HHG como herramienta para conseguir fuentes coherente de luz de longitud de onda corta. Hasta hace muy poco, la tecnología de láseres ultraintensos se limitaba a longitudes de onda del infrarrojo cercano (alrededor de 800 nm), y la conversión en armónicos de orden elevado se limitaba a la región del ultravioleta lejano (XUV). Actualmente, con la mejoría de las técnicas de inversión paramétrica, este límite se encuentra en los rayos X blandos.

Sin embargo, desde el inicio se reconocieron las aplicaciones potenciales del proceso HHG, más allá de las naturales de una radiación coherente de alta frecuencia. El

espectro de HHG consiste en un peine de armónicos que se extienden hasta la denominada frecuencia de corte. En la región espectral cercana a este corte, los armónicos tienen intensidades similares y, lo que es más interesante aún, su distribución de fase espectral es suave. Con estas dos premisas, tras filtrar el espectro de baja frecuencia, la radiación resultante se corresponde a un tren de pulsos ultracortos en la región XUV, con duraciones en torno a unos cuantos centenares de attosegundos (1 attosegundo = 10^{-18} segundos), espaciadas regularmente cada medio ciclo del láser incidente. Tras su confirmación experimental a comienzos del siglo XXI, éstos son considerados los pulsos de luz coherente más cortos jamás creados. Esta tecnología está dando sus primeros frutos, pues ya se han identificado distintas aplicaciones para discriminar procesos ultrarrápidos (en el régimen de los attosegundos) en la dinámica de sistemas físicos, químicos y biológicos.

El objetivo de esta tesis es realizar una contribución novedosa y original en este campo. El núcleo principal de este estudio consiste en el desarrollo de métodos teóricos para simular los experimentos. Esta estrategia contiene una vertiente doble. En primer lugar, la teoría se utiliza para comprender los resultados obtenidos experimentalmente. Para ello hemos desarrollado nuestros propios experimentos (bajo la dirección del Dr. Íñigo J. Sola) que contrastamos directamente con los resultados teóricos, y, además, hemos colaborado con dos grupos experimentales a nivel internacional con el objetivo de simular sus experimentos. En segundo lugar, hemos aplicado nuestra teoría para predecir nuevos procesos físicos, y de este modo servir de guía para la realización de nuevos experimentos.

El punto de partida de esta tesis se basa en la teoría SFA+, desarrollada previamente en el Área de Óptica de la Universidad de Salamanca, para el cálculo del proceso de generación de armónicos de orden elevado en un solo átomo, a nivel microscópico. Este método, así como una extensa introducción al proceso HHG, se expone a lo largo del capítulo 1. Nuestro primer objetivo ha sido desarrollar un esquema de propagación de los armónicos de orden elevado que permite la simulación del proceso a escala macroscópica, de manera que la teoría sea comparable a los experimentos. Para ello, hemos implementado una nueva técnica de propagación basada en la aproximación dipolar discreta. Esta técnica, así como los fundamentos para la comprensión de la propagación de armónicos de orden elevado, se desarrollan en el capítulo 2. Nuestro método ha sido publicado en *Physical Review A* **82**, 033432-1-11 (2010).

En el capítulo 3 estudiamos la propagación de armónicos de orden elevado generados por campos láser de longitud de onda en el infrarrojo cercano, focalizados en chorros o celdas de gas de baja densidad. Como primer test, hemos analizado teórica y experimentalmente el cambio en las condiciones de ajuste de fases que resulta de situar el chorro de gas en distintas posiciones a lo largo del eje de propagación. Una vez validado nuestro método teórico experimentalmente, proponemos una alternativa para acortar los pulsos de attosegundo, mediante su detección bajo distintos ángulos desde el eje de propagación. Este resultado ha sido publicado en *Journal of Physics B: At. Mol. Opt. Phys.* **45**, 074021 (2012). Posteriormente presentamos un estudio de la longitud de coherencia transversal, comparando nuestros resultados teóricos y experimentales, en un trabajo que ha sido enviado recientemente a la revista científica *Optics Express,* (2012). Finalmente, hemos implementado la geometría de una celda de gas semi-infinita en nuestro código de propagación, con el objetivo de comprender los resultados experimentales obtenidos por el grupo de M. Kovačev, en la Universidad de Hannover (Alemania). El resultado de esta colaboración ha sido enviado a la revista científica *Pyhsical Review A,* (2012).

En el capítulo 4 hemos modificado nuestro método para estudiar la generación armónicos de orden *ultra*-elevado, producidos utilizando láseres de longitud de onda en el infrarrojo medio (aproximadamente de 4 μm), en colaboración con el grupo teórico de A. Becker y A. Jaron-Becker, del JILA, en la Universidad de Colorado (EEUU). El resultado principal de este trabajo consiste en la demostración de la coherencia temporal de los rayos X con energía de kiloelectronvoltio obtenidos en el grupo ex-perimental de M. Murnane y H. Kapteyn en el JILA, Universidad de Colorado (EEUU), que lideró una colaboración internacional en la que también participaron la Universidad Técnica de Viena (Austria), la Universidad de Cornell (EEUU) y nuestro grupo. El resultado fue publicado en la revista *Science* **336**, 1287 (2012). Como continuación a este trabajo, y gracias al desarrollo de nuestros métodos teóricos, hemos derivado un camino para obtener pulsos de luz de rayos X en el régimen de los zeptosegundos (1 zeptosegundo=10^{-21} segundos). Este trabajo, que hemos realizado en colaboración con los grupos teórico y experimental del JILA, ha sido enviado recientemente a la revista científica *Nature Photonics,* (2012).

Capítulo 1. Generación de armónicos de orden elevado y pulsos de attosegundo

Este capítulo está concebido como una introducción a los fundamentos de los fenómenos de campos fuertes, con especial énfasis en aquellos aspectos relevantes para la generación de armónicos de orden elevado (HHG) y la producción de pulsos de attosegundo.

Cuando la materia interacciona con campos suficientemente intensos, su dinámica se convierte en no lineal. Las cargas excitadas, principalmente electrones, radían a frecuencias distintas de las del campo incidente. Cuando la interacción se extiende durante varios ciclos, la emisión de radiación se produce en múltiplos enteros de la frecuencia fundamental, conocidos como armónicos. En la figura S1 presentamos el espectro típico de HHG. Dicho espectro se compone de unos cuantos armónicos de orden bajo cuya intensidad decrece exponencialmente siguiendo una ley perturbativa, seguidos por una amplia región de armónicos con intensidad similar, conocida como *plateau*. El *plateau* se extiende hasta la denominada frecuencia de corte (*cut-off*), que viene dada por

$$\hbar\omega_{max} = I_p + 3.17U_p. \tag{4.1}$$

siendo I_p el potencial de ionización y U_p la energía ponderomotriz.

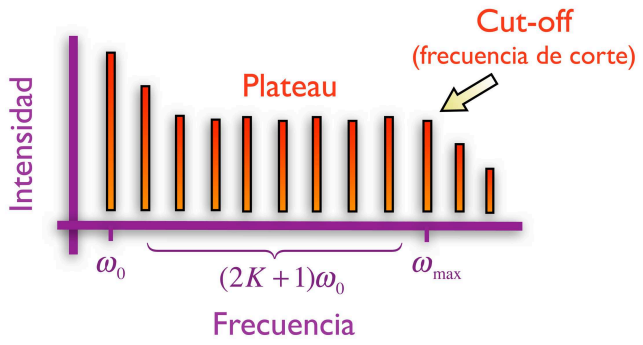

Figura S1. Esquema del espectro de HHG generado en el régimen de ionización túnel, y compuesto por armónicos cuya frecuencia es un múltiplo impar de la frecuencia fundamental. Dicho espectro se compone de unos cuantos armónicos de orden bajo cuya intensidad decrece exponencialmente siguiendo una ley perturbativa, seguidos por una amplia región de armónicos con intensidad similar, conocida como *plateau*. El *plateau* se extiende hasta la denominada frecuencia de corte. La intensidad está representada en escala logarítmica.

En la actualidad, las propiedades básicas del espectro de armónicos de orden elevado son bien conocidas (para más información, recomendamos [4, 5, 6, 7, 8, 9, 10]). Su tratamiento teórico admite distintos niveles de descripción, desde el clásico, al semiclásico o cuántico.

El primer modelo clásico que surgió para explicar el proceso de HHG de una forma intuitiva fue propuesto por Corkum [16] y Kulander y Schafer [45], y es conocido como el modelo de los tres pasos. De esta forma, un electrón es extraído del átomo por medio de ionización túnel en un primer paso. A continuación, el electrón es acelerado por el campo láser, que debido a su carácter oscilante, lo acelera contra el ión del que procede. En un el último paso, el electrón recolisiona con el ión, emitiendo los armónicos de alta frecuencia. Resulta de especial interés el hecho de que en cada medio ciclo del láser incidente, existen dos posibles trayectorias electrónicas que dan lugar a la misma energía cinética en el momento de la recolisión, y por tanto al mismo armónico. Estas trayectorias se conocen, acorde con su tiempo de excursión, como trayectorias cortas y largas. Dado que distintas trayectorias electrónicas recolisionan en tiempos diferentes, la radiación emitida está chirpeada (distintos armónicos se emiten en tiempos diferentes).

Una vez presentadas las características básicas del espectro de HHG, obtenidas a partir del modelo clásico, hay un enorme interés en desarrollar modelos cuánticos para describir de forma más rigurosa el proceso de generación de armónicos. El modelo exacto consiste en resolver la ecuación de Schrödinger dependiente del tiempo (TDSE). Sin embargo, dicha resolución requiere de recursos computacionales muy exigentes, y resulta imprescindible el desarrollo de métodos aproximados. Entre ellos, el más utilizado se basa en el formalismo S-matrix combinado con la aproximación de campo fuerte (SFA) [58]. Este método, combinado con la aproximación semiclásica de punto de silla (*saddle-point*) [63] es el más utilizado en la actualidad.

Sin embargo, nosotros utilizaremos el método cuántico SFA+ desarrollado previamente en la Universidad de Salamanca [41], que además de no incluir la aproximación de punto de silla, incluye el efecto del campo láser sobre el estado fundamental durante la etapa de recolisión, por tanto manteniendo la descripción cuántica del proceso.

Capítulo 2. Cálculo de la propagación de armónicos de orden elevado

El objetivo de este capítulo es establecer la conexión entre la radiación armónica emitida por un solo átomo y la emitida por una muestra macroscópica como ocurre en los experimentos. Este último caso, desde un punto de vista fundamental, se corresponde con la suma coherente de la radiación emitida en cada átomo o molécula de la muestra. Sin embargo, debido a distintos efectos que analizamos en este capítulo, la suma coherente no siempre es óptima, ya que la radiación emitida desde distintos puntos de la muestra puede no estar en fase. Este fenómeno, de vital importancia en los experimentos de HHG, se conoce como ajuste de fases (*phase-matching*).

Para entender de forma sencilla el proceso de ajuste de fases, consideremos un modelo simple formado por dos átomos situados a lo largo del eje de propagación (z) tal y como se indica en la figura S2. Si colocamos un detector a una distancia z_D, el armónico de orden q detectado se corresponde con la interferencia entre la radiación armónica generada en cada átomo, propagada hasta el detector, que vendrá dada por

$$E_{det} = e^{iqk_1 z_1} e^{ik_q(z_D - z_1)} + e^{iqk_1 z_2} e^{ik_q(z_D - z_2)} \propto \cos(\Delta k_q L/2) \tag{4.2}$$

donde $L = z_2 - z_1$ y Δk_q se conoce como el desajuste de fases (*phase-mismatch*). La señal en el detector será máxima cuando $\Delta k_q = 0$, es decir, cuando estemos en condiciones óptimas de ajuste de fase.

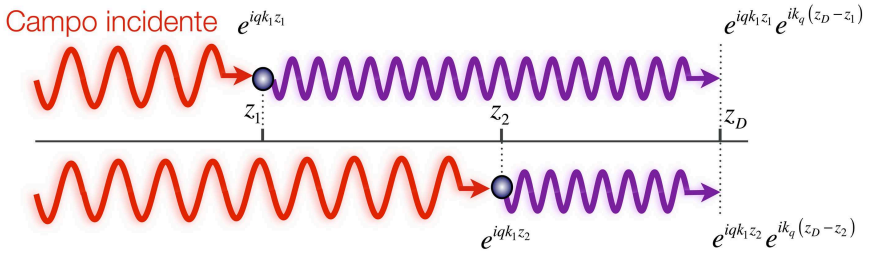

Figura S2. Esquema de dos átomos para entender el ajuste de fases (*phase-matching*) que tiene lugar en la propagación de armónicos de orden elevado.

En un experimento de HHG, el ajuste de fases vendrá dado por distintas contribuciones,

$$\Delta k_q \simeq \Delta k_q^{geom} + \Delta k_q^{f} + \Delta k_q^{b} + \Delta k_q^{int} \tag{4.3}$$

donde Δk_q^{geom} proviene de las variaciones espaciales de la fase debido a la geometría de focalización (como por ejemplo, la fase de Gouy), Δk_q^f está asociado a la presencia de cargas libres en el medio, provenientes de su ionización, Δk_q^b describe el efecto de los átomos neutros en el índice de refracción y Δk_q^{int} se corresponde con la fase del armónico, intrínseca al proceso de generación.

Nuestra principal aportación en esta tesis consiste en la realización de un código de propagación de armónicos. Para ello, en vez de resolver la ecuación de ondas, como se hace normalmente [37, 82, 83], hemos tomado un camino alternativo, en el que considerando su solución integral [89], consideramos el medio de interacción como una suma discreta de emisores de radiación. La radiación de cada uno de los emisores (en nuestro caso, átomos) viene calculada por el método SFA+, descrito en el capítulo anterior. De esta forma, incluimos automáticamente los efectos e geométricos e intrínsecos del ajuste de fases. Para incluir los efectos del índice de refracción en la propagación del campo fundamental (básicamente, cargas libres y átomos neutros), recurrimos a expresiones analíticas. En la figura S3 mostramos un esquema de nuestro método de propagación.

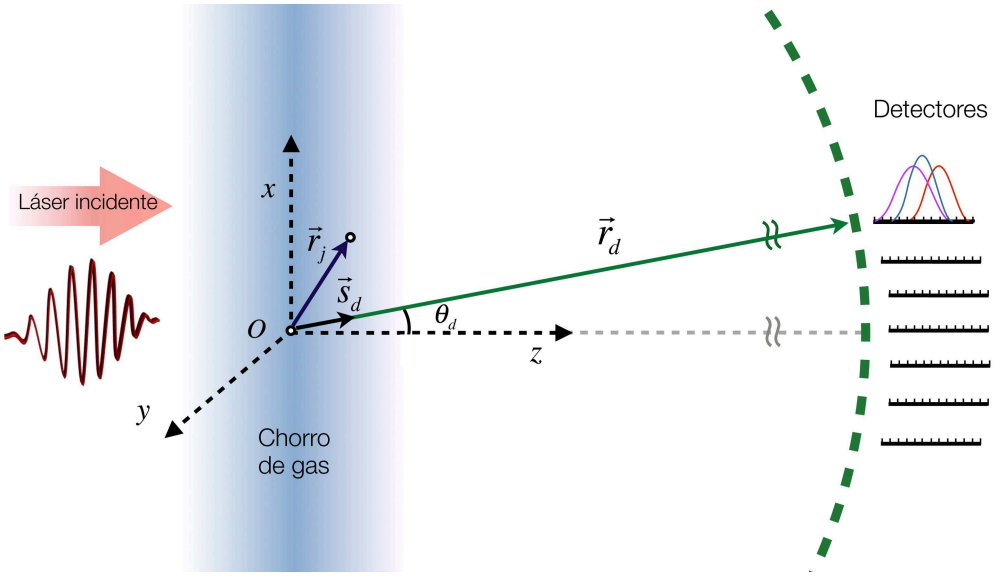

Figura S3. Esquema de nuestro método para calcular la propagación de armónicos de orden elevado. El medio de interacción, en este caso un chorro de gas, se compone de una serie discreta de emisores de radiación, situados en la coordenada $\mathbf{r}_j$. La detección de la radiación tiene lugar a una distancia $|\mathbf{r}_d|$ del centro de la muestra, O, y se conforma de una serie de discreta de detectores situados en distintos ángulos, θ_d.

Incluso para las densidades bajas de gas que se tienen en los experimentos típicos de HHG, el número de emisores es extremadamente elevado (en torno a 10^{12}). A pesar de utilizar métodos aproximados para el cálculo de HHG en un solo átomo, el cálculo para todos los átomos de la muestra se vuelve altamente complicado. Para reducir el número de cálculos, utilizamos la aproximación dipolar discreta [111, 112], que consiste en dividir la muestra en un número discreto de esferas, cada una de ellas conteniendo varios átomos. De esta forma, conseguimos reducir el número de cálculos a 10^5, manteniendo toda la información del proceso.

Capítulo 3. Generación y propagación de armónicos de orden elevado por láseres en el infrarrojo cercano en gases de baja densidad.

En este capítulo estudiamos la generación y propagación de armónicos de orden elevado mediante láseres cuya longitud de onda está en el infrarrojo cercano (principalmente láseres de titanio:zafiro, de 800 nm). En concreto estudiamos dos tipos de geometría del blanco: chorros y celdas de gas de baja densidad (10^{17}-10^{18} átomos/cm^3).

En primer lugar, nos centramos en el estudio de las condiciones de ajuste de fases en un chorro de gas, analizando en detalle la variación de las distintas contribuciones según la posición del chorro respecto al foco. Resulta de especial interés el signo similar u opuesto de las contribuciones de la fase intrínseca y geométrica dependiendo de la posición del chorro. De este modo, si el chorro está situado delante del foco, ambas contribuciones se suman, dando lugar a una mayor variación de la fase a lo largo del eje de propagación. Sin embargo, después de foco se compensan, de forma que nos acercamos más a la condición de ajuste de fases ($\Delta k_q = 0$), y por tanto la señal detectada es mayor. Además, el comportamiento de la fase intrínseca depende de la trayectoria seguida por el electrón (corta o larga). De esta forma, situando el chorro de gas antes del foco, las trayectorias cortas dominan si se detectan en eje, mientras que las largas van ganando peso según aumentamos el ángulo de detección. Por contra, si el chorro de gas está situado después del foco, las trayectorias cortas dominan en todo el espacio angular de detección.

Estas características de ajuste de fases se pueden observar en la figura S4, donde presentamos distintos perfiles angulares del espectro de armónicos, para distintas posi-

ciones del chorro de gas respecto del foco. Cuando el chorro está colocado antes de foco, observamos unos anillos correspondientes a la interferencia entre trayectorias cortas y largas. Sin embargo, después de foco, los perfiles son más uniformes (ya que predominan las trayectorias largas), y además, la señal detectada es mayor, acorde a lo explicado anteriormente.

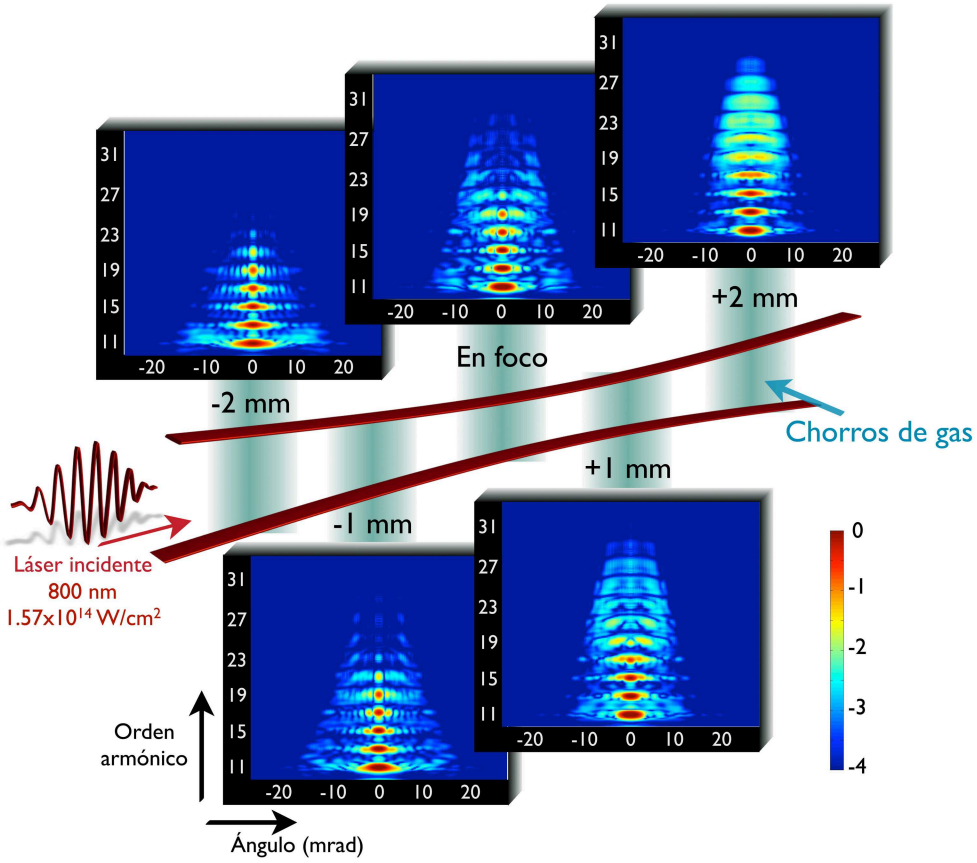

Figura S4. Perfil angular del espectro de armónicos de orden elevado (en escala logarítmica) generados en un chorro de gas de hidrógeno situado en distintas posiciones respecto al foco del haz: -2 mm, -1 mm, 0 mm, 1 mm y 2 mm. En el eje horizontal de cada gráfica representamos el ánglo de detección, mientras que en el vertical el orden armónico. El pulso láser simulado es de 7.7 fs, 800 nm y con intensidad pico de 1.57×10^{14} W/cm^2.

Estas simulaciones teóricas, cuyos resultados reproducen los ya sabidos en la comunidad científica [70, 85, 108, 122], han sido contrastadas satisfactoriamente con nuestros experimentos, llevados a cabo en la Universidad de Salamanca bajo la tutela del Dr.

Íñigo J. Sola. De esta forma, hemos validado nuestro código de propagación.

En segundo lugar, hemos hecho un análisis teórico sobre la reducción de la duración pulsos de attosegundo cuando se detectan a un cierto ángulo. Cuando el chorro de gas está situado antes que el foco, hemos visto que, dependiendo del ángulo de detección, las trayectorias cortas y largas interfieren. Hemos encontrado una situación en la cual las trayectorias largas generadas en un determinado instante de tiempo, interfieren temporalmente con las cortas generadas en el siguiente medio ciclo, dando lugar a la reducción de los pulsos de attosegundo generados, como mostramos en la figura S5.

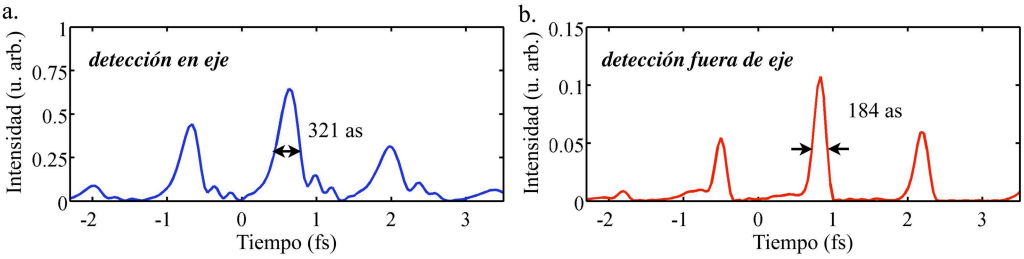

Figura S5. Distribución temporal del tren de pulsos de attosegundo obtenido cuando los armónicos se detectan **a** en eje, y **b** bajo un ángulo de 3.3 mrad, para un chorro de gas situado 1 mm antes del foco. El pulso incidente es de 2.9 ciclos (7.7 fs), 800 nm e intensidad en el foco de $\simeq 2.45 \times 10^{14}$ W/cm^2. Podemos observar cómo la anchura de los pulsos de attosegundo es menor cuando son detectados fuera de eje.

Hasta ahora sólo nos hemos referido al ajuste de fases longitudinal. Con el objetivo de obtener una interpretación más completa de la propagación de armónicos de orden elevado, hemos analizado teórica y experimentalmente la influencia del ajuste de fases transversal. Para ello, hemos diseñado un experimento, en el cual diafragmando el haz láser incidente [134], conseguimos aumentar la eficiencia de los armónicos detectados. Este efecto lo achacamos unívocamente al efecto relevante que tiene el ajuste de fases transversal cuando el haz láser no está diafragmado, gracias al post-análisis realizado teóricamente (ver figura S6).

En último lugar, hemos adaptado nuestro código de propagación para simular HHG en una celda semi-infinita de gas, con el objetivo de dar soporte a los resultados experimentales llevados a cabo en el grupo de M. Kovačev en la Universidad de Hannover. Variando la presión de la celda y la posición del foco en la misma, la mayor o menor absorción selecciona la intensidad con la que se genera un determinado armónico, es

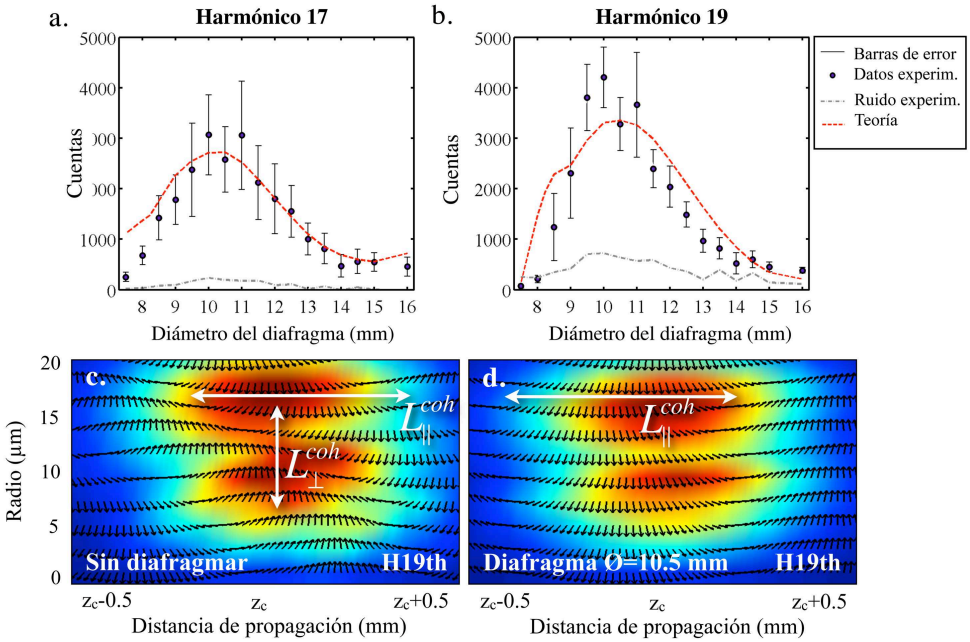

Figura S6. Señal detectada del armónico **a** 17, y del **b** 19, para un chorro de gas situado 2 mm antes que el foco. El resultado experimental se muestra con puntos, mientras que el teórico se corresponde con la línea roja. En la fila de abajo se muestra los mapas de la detección del armónico 19 cuando **c** el haz no está diafragmado, y **d** tras pasar pos un diafragma de 10.5 mm de diámetro. El fondo representa la amplitud del armónico, mientras que las flechas indican su fase, en representación polar. De esta forma podemos identificar la longitud de coherencia como la distancia entre dos flechas de sentido opuesto. Dado que la longitud de coherencia transversal aumenta considerablemente al diafragmar el haz, y la longitudinal se mantiene similar, el aumento de la señal detectada al diafragmar lo achacamos al ajuste de fases transversal.

decir, en qué región del espectro se genera (*plateau* o *cut-off*). Esto tiene una consecuencia directa en la estructura y divergencia del perfil espacial de los armónicos, lo cual ha sido identificado teórica y experimentalmente.

Capítulo 4. Generación y propagación de armónicos de orden ultra-elevado por láseres en el infrarrojo medio en guías de onda.

Como consecuencia del desarrollo de láseres intensos de longitudes de onda en el infrarrojo medio [139], HHG se ha convertido en una herramienta potencial para producir rayos X coherentes. Los avances en la comprensión del ajuste de fases macroscópico [42, 149], han hecho posible generar armónicos de orden ultra-elevado, intensos y coherentes, de energías cercanas al kiloelectronvoltio, gracias a estos láseres en el infrarrojo medio. Este logro ha sido llevado a cabo por una colaboración internacional liderada por JILA (Universidad de Colorado), y en el que también participaron la Universidad Técnica de Viena, la Universidad de Cornell y nuestro grupo [20]. Aunque la intensidad de estos rayos X generados por HHG cae por debajo de las obtenidas con láseres de electrones libres (XFEL), el grado de coherencia es superior, y la fase espectral y la forma del pulso son regulares y repetitivas. En este capítulo nos centraremos en la caracterización de la coherencia temporal de los rayos X obtenidos por HHG, primero mediante la realización de simulaciones de un solo átomo, y, posteriormente, incluyendo la propagación.

El cálculo teórico de HHG utilizando láseres en el infrarrojo medio resulta complejo debido a la excursión del electrón una vez ionizado, que escala con el cuadrado de la longitud de onda. Por ejemplo, usando láseres de 800 nm, la máxima excursión clásica suele ser de 1 nm, mientras que con láseres de 4 μm, unos 40 nm. Este incremento espacial, sumado al incremento temporal (pues el período del láser también aumenta) complica mucho los cálculos, de modo que resulta imprescindible utilizar modelos aproximados. En nuestro caso, hemos utilizado el modelo SFA+ incluyendo la aproximación del punto de silla (*saddle-point*) en el plano transversal.

El estudio que hemos realizado sobre el cálculo de HHG en un solo átomo mediante láseres en el medio infrarrojo (3.9 μm) nos ha deparado varias sorpresas, como se puede observar en la figura S7. Como vemos, al espectro contiene energías de hasta 1.6 keV, pero lo más interesante está en el carácter temporal de la radiación. A pesar de tener un ancho de banda muy extenso (desde 0.2 a 1.6 keV), la radiación se genera en pulsos de femtosegundo, y no de attosegundo debido al *chirp* intrínseco al proceso

HHG. Además, podemos observar una estructura fina (en el régimen de los attosegundos) y regular, superpuesta en cada pulso de femtosegundo. Realizando un análisis tiempo-frecuencia en el que se muestra la correlación del tiempo de emisión con cada armónico generado, hemos identificado estas estructuras como una consecuencia de las recolisiones de orden superior. En el proceso de HHG, un electrón ionizado tiene una cierta probabilidad de recolisión. Si no recolisiona, la trayectoria clásica predice que debido al carácter oscilante del campo, podrá recolisionar el pasar veces posteriores por la posición del núcleo. La probabilidad de que ocurran estas recolisiones de orden superior se incrementa con la longitud de onda del láser [40, 156]. De esta forma, la estructura de attosegundo en la figura S7 es consecuencia de la interferencia entre distintos órdenes de recolisión.

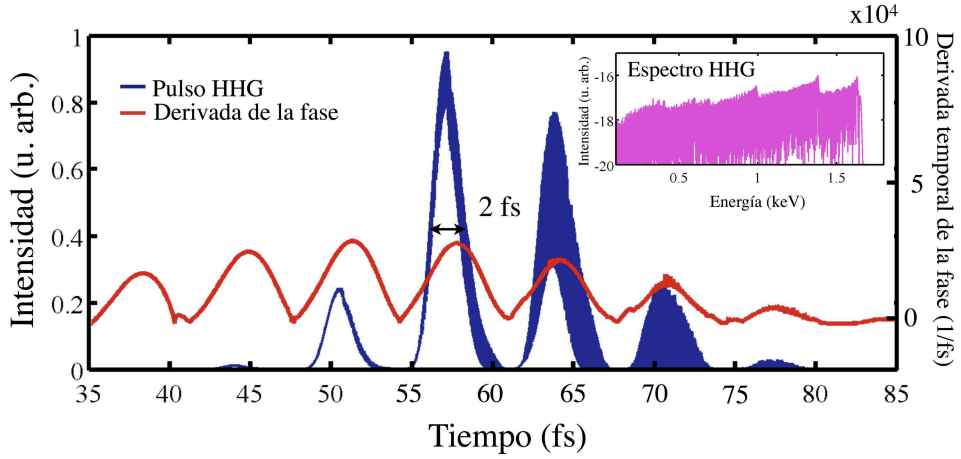

Figura S7. Envolvente de los pulsos de rayos X (línea azul) y su derivada de la fase temporal (línea roja), obtenidos mediante un láser de 3.9 μm, con intensidad pico 3.6×10^{14} W/cm^2, y duración temporal de 2.9 ciclos (37 fs). El espectro de armónicos se presenta en el recuerdo interior (línea rosa).

El contraste de interferencia debido a los eventos de recolisión de orden superior en HHG es suficientemente significativo para modular los pulsos de femtosegundo de rayos X en una forma de onda de pulsos extremadamente cortos. Filtrando adecuadamente las recolisiones de orden superior, demostramos que las formas de onda pueden alcanzar el régimen de los zeptosegundo para láseres de longitud de onda por encima de 7.7 μm. En la figura S8 podemos observar la estructura temporal obtenida en HHG con un pulso de 9 μm y suficientemente corto (1.5 ciclos) para que sólo sean relevantes las

recolisiones de primer y segundo orden. De esta forma, se consigue modular el segundo pulso de femtosegundo en una onda en el régimen de los zeptosegundos.

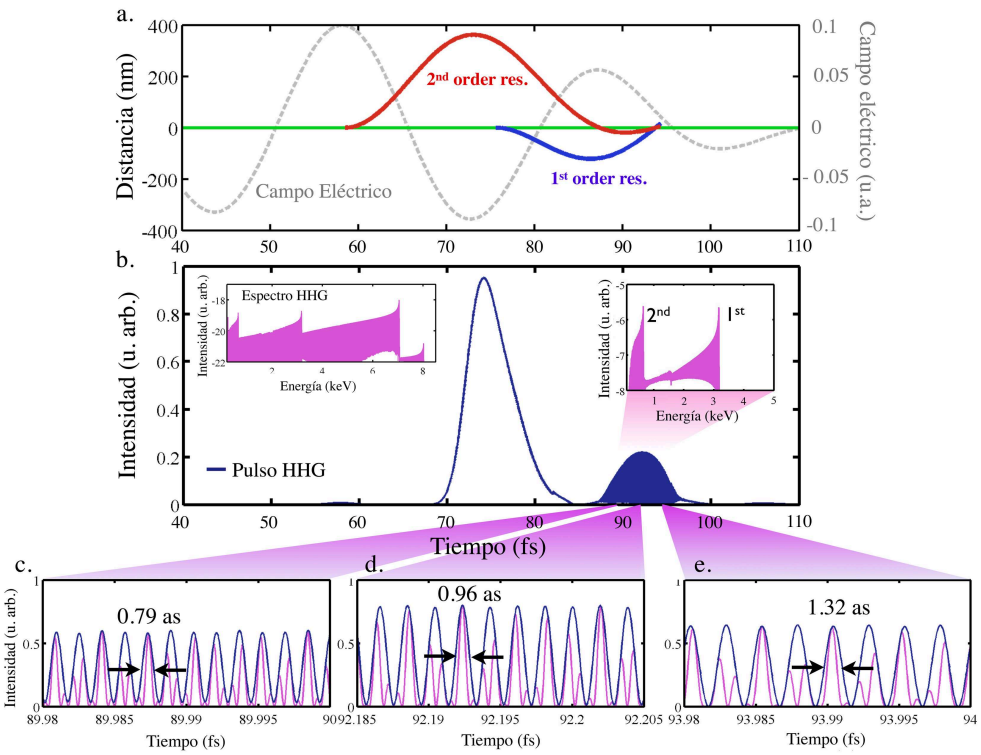

Figura S8. **a** Representación esquemática del láser indicente (línea gris), de 1.5 ciclos, 9μm e intensidad pico 3.4×10^{14} W/cm^2. Se muestran las trayectorias que recolisionan a primer y segundo orden, en el tiempo 94 fs. **b** Envolvente de los pulsos de rayos X obtenidos En el recuadro interno izquierdo se muestra el espectro de armónicos, mientras que en el derecho, el contenido espectral del segundo pulso, mostrando los picos de energía debidos al primer y segundo orden de recolisión. En las gráficas **c** a **e** mostramos en detalle la estructura temporal en el régimen de zeptosegundo del segundo pulso de rayos X.

Finalmente, hemos exprimido al máximo nuestro código para tener en cuenta los efectos de propagación y de esta forma simular los resultados experimentales obtenidos en la colaboración llevada a cabo por los grupos de Kapteyn y Murnane en JILA y Baltuška en Viena. En la figura S9 mostramos los resultados experimentales y teóricos. En primer lugar, el espectro simulado concuerda con el medido experimentalmente. Además, nuestros cálculos predicen que los pulsos de rayos X se generan en la escala de femtosegundo.

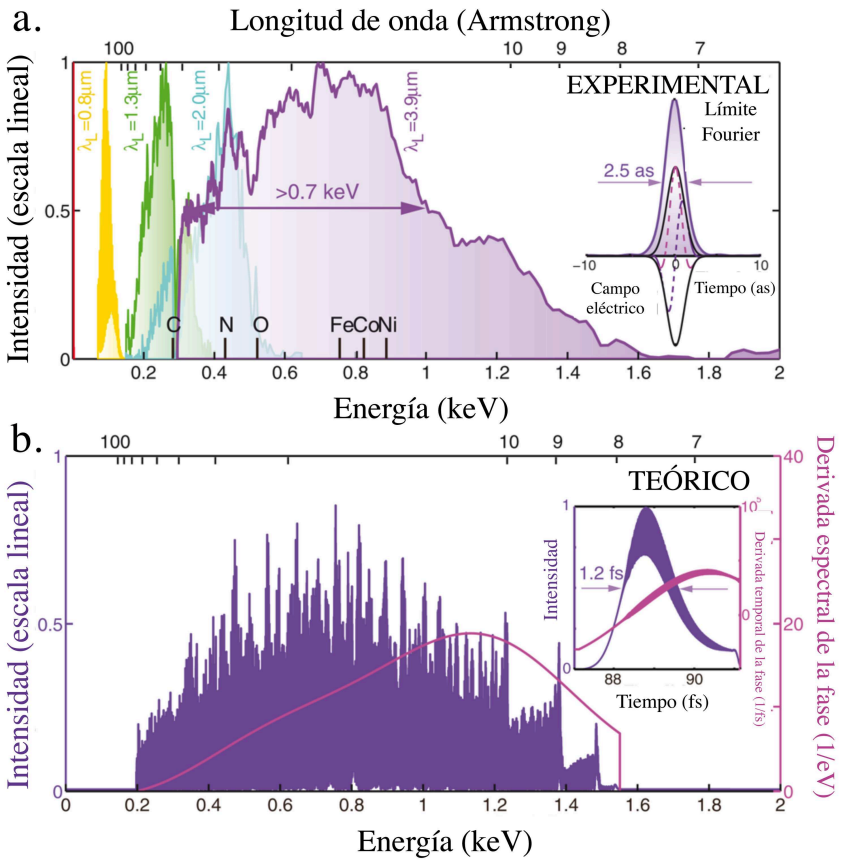

Figura S9. **a** Espectro de armónicos experimental obtenido bajo condiciones de ajusta de fases óptimo para láseres de longitudes de onda: 0.8 μm (amarillo), 1.3 μm (verde), 2 μm (azul), y 3.9 μm (morado). **b** Espectro simulado, así como uno de los pulsos de rayos X generados por un láser de 3.9 μm, 6 ciclos e intensidad pico 3.3×10^{14} W/cm^2.

Como conclusión, en este capítulo hemos demostrado que los pulsos de rayos X obtenidos por generación de armónicos de orden ultra-elevado, exhiben coherencia temporal. Estos pulsos de rayos X representan una herramienta prometedora para explorar procesos físicos ultrarrápidos.

References

[1] J. A. Valdmanis, R. L. Fork, and J. P. Gordon, *Generation of optical pulses as short as 27 femtoseconds directly from a laser balancing self-phase modulation, group-velocity dispersion, saturable absorption, and saturable gain.* Opt. Lett. **10**, 131-133 (1985). 1

[2] R. L. Fork, C. H. Brito Cruz, P. C. Becker, and C. V. Shank, *Compression of optical pulses to six femtoseconds by using cubic phase compensation.* Opt. Lett. **12**, 483-485 (1987). 1

[3] D. Strickland and G. Mourou, *Compression of amplified chirped optical pulses.* Opt. Commun. **56**, 219 (1985). 1

[4] T. Brabec and F. Krausz, *Intense few-cycle laser fields: Frontiers of nonlinear optics.* Rev. Mod. Phys. **72**, 545 (2000). 2, 155

[5] P. Agostini and L.F. DiMauro, *The physics of attosecond light pulses.* Rep. Prog. Phys. **67**, 813-855 (2004). 2, 155

[6] M. F. Kling and M. J. J. Vrakking, *Attosecond Electron Dynamics.* Annu. Rev. Phys. Chem. **59**, 463-492 (2008). 2, 155

[7] F. Krausz and M. Ivanov, *Attosecond physics.* Rev. Mod. Phys. **81**, 163234 (2009). 2, 155

[8] M. Nisoli and G. Sansone, *New frontiers in attosecond science.* Prog. Quan. Electron. **33**, 17-59 (2009). 2, 155

[9] T. Popmintchev, M. Chen, P. Arpin, M. M. Murnane, and H. C. Kapteyn, *The attosecond nonlinear optics of bright coherent X-ray generation.* Nature Photon. **4**, 822 (2010). 2, 10, 73, 135, 155

[10] L. Plaja, R. Torres and A. Zaïr (Eds.), *New trends in attophysics.* Springer, *to be published in 2013.* 2, 155

[11] Th. Maiman, *Stimulated Optical Radiation in Ruby.* Nature **187**, 493-494 (1960). 2

[12] P. A. Franken, A. E. Hill, C. W. Peters, and G. Weinreich, *Generation of optical harmonics.* Phys. Rev. Lett. **7**, 118-119 (1961). 2

[13] A. McPherson, G. Gibson, H. Jara, U. Johann, T. S. Luk, I. A. McIntyre, K. Boyer, and C. K. Rhode, *Studies of multiphoton production of vacuum-ultraviolet radiation in the rare gases.* J. Opt. Soc. Am. B **21**, 595-601 (1987). 2, 7, 73

[14] M. Ferray, A. L'Huillier, X.F. Li, L.A. Lompré, G. Mainfray and C. Manus, *Multiple harmonic conversion of 1064 nm radiation in rare gases.* J. Phys. B: At. Mol. Opt. Phys. **21**, L31-L35 (1988). 2, 7, 73

[15] J. J. Macklin, J. D. Kmetec, and C. L. Gordon III, *High-order harmonic generation using intense femtosecond pulses.* Phys. Rev. Lett. **70**, 766-769 (1993). 2

[16] P. B. Corkum, *Plasma Perspective on Strong-field Multiphoton Ionization.* Phys. Rev. Lett. **71**, 1994-1997 (1993). 2, 9, 155

[17] G. Farkas and C. Toth, *Proposal for attosecond light pulse generation using laser induced multiple-harmonic conversion processes in rare gases.* Phys. Lett. A **168,** 447 (1992). 3, 12

[18] P. M. Paul, E. S. Toma, P. Breger, G. Mullot, F. Augé, Ph. Balcou, H. G. Muller and P. Agostini, *Observation of a Train of Attosecond Pulses from High Harmonic Generation* Science **292,** 1689 (2001). 3, 13

[19] M. Hentschel, R. Kienberger, C. Spielmann, G. A. Reider, N. Milosevic, U. Heinzmann, M. Drescher and F. Krausz, *Attosecond metrology.* Nature **414**, 509 (2001). 3, 13

[20] T. Popmintchev, M.-C. Chen, D. Popmintchev, P. Arpin, S. Brown, S. Ališauskas, G. Andriukaitis, T. Balčiunas, O. Mücke, A. Pugzlys, A. Baltuška, B. Shim, S. E. Schrauth, A. Gaeta, C. Hernández-García, L. Plaja, A. Becker, A. Jaron-Becker, M. M. Murnane, and H. C. Kapteyn, *Bright Coherent Ultrahigh Harmonics in the keV X-ray Regime from Mid-Infrared Femtosecond Lasers.* Science **336**, 1287 (2012). 3, 8, 59, 121, 123, 124, 130, 133, 145, 146, 162

[21] K. Zhao, Q. Zhang, M. Chini, Y. Wu, X. Wang, and Z. Chang, *Tailoring a 67 attosecond pulse through advantageous phase-mismatch.* Opt. Lett. **37**, 3891 (2012). 3, 13, 125

[22] N. B. Delone and V. P. Krainov, *Multiphoton Processes in Atoms*, Springer-Verlag, Berlin, (1994). 3, 4

[23] A. Einstein, *Über einen die Erzeugung und Verwandlung des Lichtes betreffenden heuristischen Gesichtspunkt.* Ann. Phys. **17**, 132 (1905). English translation in A. B. Arons and M. B. Peppard, *Einstein's Proposal of the Photon Concept.* Am. J. Phys. **33**, 367 (1965). 3

[24] M. Göppert-Mayer, *Doctoral dissertation: Uber Elementarakte mit zwei Quantensprüngen.* Ann. Phys. (Leipzig), **9**, 273-94 (1931). 3

[25] M. Gavrila ed. *Atoms in Intense Laser Fields*, Academic Press, Boston, (1992). 4

[26] K. Burnett, V. C. Reed and P. L. Knight, *Atoms in ultraintense laser fields.* J. Phys. B: At. Mol. Opt. Phys. **26**, 561 (1993). 4

[27] P. Moreno, *Doctoral dissertation: Generación de armónicos en H and H_2^+ sometidos a pulsos láser intensos*, (Universidad de Salamanca, 1996). 4

[28] E. Conejero Jarque, *Doctoral dissertation: On the generation and propagation of harmonics in ionizing media*, (Universidad de Salamanca, 1998). 4

[29] M. Protopapas, C. H. Keitel and P. L. Knight, *Atomic physics with super-high intensity lasers.* Rep. Prog. Phys. **60**, 389-486 (1997). 4

[30] M. Büttiker and R. Landauer, *Traversal Time for Tunneling.* Phys. Rev. Lett. **49**, 1739 (1982). 4

[31] K. Rzazewski and L. Roso, *Remark on the Keldysh Adiabaticity Parameter.* Laser Phys. **3**, 310 (1993). 4

[32] L. V. Keldysh, *Ionization in the field of a strong electromagnetic wave.* Sov. Phys. JETP **20**, 1307 (1965). 5

[33] M. V. Amosov, N. B. Delone, and V. P. Krainov, *Tunnel ionization of complex atoms and of atomic ions in an alternating electromagnetic field.* Zh. Eksp. Teor. Fiz. **91**, 2008 (1986). 5, 21, 43

[34] L. A. Lompré, G. Mainfray, C. Manus and J. Thebault, *Multiphoton ionization of rare gases by a tunable-wavelength 30-psec laser pulse at 1.06 μm.* Phys. Rev. A **15**,1604 (1977). 6

[35] P. Agostini, F. Fabre, G. Mainfray, G. Petite and N. Rahman, *Free-Free Transitions Following Six-Photon Ionization of Xenon Atoms.* Phys. Rev. Lett. **42**, 1127 (1979). 6

[36] M. P. De Boer, J. H. Hoogenraad, R. B. Vrijen, R. C. Constantinescu, L. D. Noordam, and H. G. Muller, *Adiabatic stabilization against photoionization: An experimental study.* Phys. Rev. A, **50**, 4085. (1994). 6

[37] X.F. Li, A. L'Huillier, M. Ferray, L.A. Lompré and G. Mainfray, *Multiple-harmonic generation in rare gases at high laser intensity.* Phys. Rev. A **39**, 5751 (1989). 7, 60, 157

[38] J. L. Krause, K. J. Schafer and K. C. Kulander, *Calculation of photoemission from atoms subject to intense laser fields.* Phys. Rev. A **45**, 4998 (1992). 7

[39] L. Lompré, A. LHuillier, M. Ferray, P. Monot, G. Mainfray, and C. Manus, *High-order harmonic generation in xenon: intensity and propagation effects.* J. Opt. Soc. Am. B **7**,754761 (1990). 7

[40] J. Tate, T. Auguste, H. G. Muller, P. Salières, P. Agostini, and L. F. Di Mauro, *Scaling of Wave-Packet Dynamics in an Intense Midinfrared Field.* Phys. Rev. Lett. **98**, 013901-1-4 (2007). 8, 24, 124, 127, 130, 147, 163

[41] J. A. Pérez-Hernández, L. Roso and L. Plaja, *Harmonic generation beyond the Strong-Field Approximation: the physics behind the short-wave-infrared scaling laws.* Opt. Exp. **17**, 9891 (2009). 8, 19, 24, 25, 26, 28, 73, 90, 124, 126, 155

[42] T. Popmintchev, M.-C. Chen, A. Bahabad, M. Gerrity, P. Sidorenko, O. Cohen, I. P. Christov, M. M. Murnane, and H. C. Kapteyn, *Phase matching of high harmonic generation in the soft and hard X-ray regions of the spectrum.* Proc. Natl. Acad. Sci. USA **106**, 10516 (2009). 8, 56, 123, 124, 139, 147, 162

[43] H. B. van Linden van den Heuvell and H. G. Muller, in *Multiphoton Processes*, S. J. Smith and P. L. Knight eds., Cambridge University Press, Cambridge, (1988). 9

[44] T. F. Gallagher, *Above-Threshold Ionization in Low-Frequency Limit.* Phys. Rev. Lett. **61**, 2304 (1988). 9

[45] K. Schafer, B. Yang, L. F. DiMauro, and K. C. Kulander, *Above threshold ionization beyond the high harmonic cutoff.* Phys. Rev. Lett. **70**, 1599-1602 (1993). 9, 155

[46] J. A. Pérez-Hernández, L. Roso, A. Zaïr, and L. Plaja, *Valley in the efficiency of the high-order harmonic yield at ultra-high laser intensities.* Opt. Exp. **19**, 19430-19439 (2011). 12

[47] P. B. Corkum, N. H. Burnett, and M. Y. Ivanov, *Subfemtosecond pulses.* Opt. Lett. **19**, 1870-1872 (1994). 12, 15

[48] P. Antoine, A. L'Huillier and M. Lewenstein, *Attosecond Pulse Trains Using HighOrder Harmonics.* Phys. Rev. Lett. **77,** 1234 (1996). 12, 82, 127

[49] I. P. Christov, M. M. Murnane, and H. C. Kapteyn, *High-harmonic generation of attosecond pulses in the single-cycle regime.* Phys. Rev. Lett **78**, 12511254 (1997). 12, 13

[50] E. Goulielmakis, M. Schultze, M. Hofstetter, V. S. Yakovlev, J. Gagnon, M. Uiberacker, A. L. Aquila, E. M. Gullikson, D. T. Attwood, R. Kienberger, F. Krausz, and U. Kleineberg, *Single-Cycle Nonlinear Optics.* Science, **320** 1614-1617 (2008). 13, 94, 125

[51] Y. Mairesse, A. de Bohan, L. J. Frasinski, H. Merdji, L. C. Dinu, P. Monchicourt, P. Breger, M. Kovacev,1 R. Taïeb, B. Carré, H. G. Muller, P. Agostini and P. Saliéres, *Attosecond Synchronization of High-Harmonic Soft X-rays.* Science, **302,** 1540 (2003). 13, 94

[52] K. Varjú, Y. Mairesse, B. Carré, M. B. Gaarde, P. Johnsson, S. Kazamias, R. López-Martens, J. Mauritsson, K. J. Schafer, Ph. Balcou, A. LHuillier and P. Saliéres, *Frequency chirp of harmonic and attosecond pulses.* J. of Mod. Opt., **52**, 379394 (2005). 13, 23, 94

[53] I. J. Sola, E. Mével, L. Elouga, E. Constant, V. Strelkov, L. Poletto, P. Villoresi, E. Benedetti, J.-P. Caumes, S. Stagira, C. Vozzi, G. Sansone and M. Nisoli, *Controlling attosecond electron dynamics by phase-stabilized polarization gating.* Nature Phys. **2**, 319322 (2006). 15, 82

[54] G. Sansone, E. Benedetti,F. Calegari, C. Vozzi, L. Avaldi, R. Flammini, L. Poletto, P. Villoresi, C. Altucci, R. Velotta, S. Stagira, S. De Silvestri, M. Nisoli, *Isolated Sincle-Cycle Attosecond Pulses.* Science **314**, 443 (2006). 15

[55] H. Vincenti and F. Quéré, *Attosecond Lighthouses: How To Use Spatiotemporally Coupled Light Fields To Generate Isolated Attosecond Pulses.* Phys. Rev. Lett. **108**, 113904 (2012). 15, 125

[56] A. Borot, A. Malvache, X. Chen, A. Jullien, J.-P. Geindre, P. Audebert, G. Mourou, F. Quéré and R. Lopez-Martens, *Attosecond control of collective electron motion in plasmas.* Nature Phys., **8**, 16 (2012). 15, 125

[57] J. A. Wheeler, A. Borot, S. Monchocé, H. Vincenti, A. Ricci, A. Malvache, R. Lopez-Martens and F. Quéré, *Attosecond lighthouses from plasma mirrors.* Nature Phot. (2012). 15, 125

[58] For a review of these techniques, see H. R. Reiss, in Progress in Ultrafast Intense Laser Science, 1 (Springer, 2008). 16, 155

[59] L. V. Keldysh, *Ionization in the Field of a Strong Electromagnetic Wave.* Zh. Eksp. Teor. Fiz. **47**, 1945-1956 (1964) [Sov. Phys. JETP **20** 1307-1314 (1965)]. 16

[60] F. H. M. Faisal, *Multiple absorption of laser photons by atoms.* J. Phys. B **6**, L89-L92 (1973). 16

[61] H. R. Reiss, *Effect of an intense electromagnetic field on a weakly bound system.* Phys. Rev. A **22,** 1786-1813 (1980). 16

[62] A. Becker, L. Plaja, P. Moreno, M. Nurhuda, F. H. M. Faisal, *Total ionization rates and ion yields of atoms at nonperturbative laser intensities.* Phys. Rev. A **64**, 023408 (2001). 16

[63] M. Lewenstein, Ph. Balcou, M. Yu. Ivanov, A. L'Huillier, P. B. Corkum, *Theory of high-harmonic generation by low-frequency laser fields.* Phys. Rev. A **49**, 2117 (1994). 16, 19, 22, 24, 155

[64] M. Lewenstein, P. Salières, and A. L'Huiller, *Phase of the atomic polarization in high-order harmonic generation.* Phys. Rev. A **52**, 4747-4754 (1995). 16, 22, 82

[65] W. Becker, A. Lohr, M. Kleber, M. Lewenstein, *A unified theory of high-harmonic generation: Application to polarization properties of the harmonics.* Phys. Rev. A **56**, 645 (1997). 16

[66] V. P. Krainov, *Ionization rates and energy and angular distributions at the barrier-suppression ionization of complex atoms and atomic ions.* J. Opt. Soc. Am. B, **14** 425 (1997). 18

[67] D. Shafir, H. Soifer, B. D. Bruner, M. Dagan, Y. Mairesse, S. Patchkovskii, M. Y. Ivanov, O. Smirnova and N. Dudovich, *Resolving the time when an electron exits a tunnelling barrier.* Nature, **485**, 343-346 (2012). 21, 82

[68] P. Balcou, A. S. Dederichs, M .B. Gaarde, and A. LHuillier, *Quantum-path analysis and phase matching of high-order harmonic generation and high-order frequency mixing processes in strong laser fields.* J. of Phys. B, **32**, 2973 (1999). 22

[69] A. Zaïr, M. Holler, A. Guandalini, F. Schapper, J. Biegert, L. Gallmann, U. Keller, A. S. Wyatt, A. Monmayrant, I. A. Walmsley, E. Cormier, T. Auguste and P. Salières, *Quantum Path Interferences in High-Order Harmonic Generation.* Phys. Rev. Lett. **100**, 143902 (2008). 22, 24, 82

[70] P. Salières, A. L'Huillier, M. Lewenstein, *Coherence Control of High-Order Harmonics.* Phys. Rev. Lett. **74**, 3776 (1995). 22, 35, 83, 159

[71] P. Salières, B. Carré, L. Le Déroff, F. Grasbon, G. Paulus, H. Walther, R. Kopold, W. Becker, D, Milosevic, A. Sanpera and M. Lewenstein, *Feynman's path-integral approach for intense-laser-atom interactions* Science, **292,** 902 (2001). 23, 82, 88

[72] M. B. Gaarde, F. Salin, E. Constant, Ph. Balcou, K. J. Schafer, K. C. Kulander, and A. LHuillier, *Spatiotemporal separation of high harmonic radiation into two quantum path components.* Phys. Rev. A **59**, 1367 (1999). 23

[73] M. Bellini, C. Lyng, A. Tozzi, M. B. Gaarde, T. Hänsch, A. L'Huillier, and C. Wahlström, *Temporal Coherence of Ultrashort High-Order Harmonic Pulses.* Phys. Rev. Lett. **81**, 297300 (1998). 23, 88

[74] K. Schiessl, K. L. Ishikawa, E. Person, and J. Burgdörfer, *Quantum Path Interference in the Wavelength Dependence of High-Harmonic Generation.* Phys. Rev. Lett. **99**, 253903-1-4 (2007). 24

[75] M. V. Frolov, N. L. Manakov, and A. F. Starace, *Wavelength Scaling of High-Harmonic Yield: Threshold Phenomena and Bound State Symmetry Dependence.* Phys. Rev. Lett. **100**, 173001-1-4 (2008). 24

[76] J. A. Pérez-Hernández, C. Hernández-García, J. Ramos, E. Conejero, L. Plaja and L. Roso, Book Chapter:*Progress in Ultrafast Intense Laser Science VII* (pp 145-162), Springer (2011). 24, 26, 27

[77] J. A. Pérez-Hernández, L. Roso and L. Plaja, *S-Matrix Theory for the High-Order Harmonic Generation beyond the Strong-Field Approximation.* Laser Phys. **19**, 1581-1585 (2009). 28

[78] J. A. Pérez-Hernández, J. Ramos, L. Roso and L. Plaja, *Harmonic Generation Beyond the Strong-Field Approximation: Phase and Temporal Description.* Laser Phys. **5**, 1044-1050 (2010). 28, 32

[79] E. Clementi and C. Roetti, Roothan-Hartree-Fock atomic wavefunctions. Atomic data and nuclear data tables **14**, 177 (1974). 28, 90

[80] X. Tong and C. Lin, *Empirical formula for static field ionization rates of atoms and molecules by lasers in the barrier-suppression regime.* J. of Phys. B **38**, 2593 (2005). 29, 92

[81] C. Granados, *Master's thesis: Estudio de la Generación de Armónicos de Orden Elevado en la Aproximación de ampo Fuerta Extendida (SFA+)*, (Universidad de Salamanca, 2011). 29

[82] A. L'Huillier, X. F. Li and L. A. Lompré, *Propagation effects in high-order harmonic generation in rare gases.* J. Opt. Soc. Am. B, **7**, 527 (1990). 35, 60, 157

[83] A. L'Huillier, P. Balcou, S. Candel, K. J. Schafer, K. C. Kulander, *Calculations of high-order harmonic-generation processes in xenon at 1064 nm.* Phys. Rev. A **46**, 2778 (1992). 35, 60, 157

[84] A. L'Huillier, K. Schafer and K. Kulander, *Higher-order harmonic generation in xenon at 1064 nm: The role of phase matching.* Phys. Rev. Lett. **66**, 2200-2203 (1991). 35

[85] J. Peatross, M. V. Fedorov, K. C. Kulander, *Intensity-dependent phase-matching effects in harmonic generation.* J. Opt. Soc. Am. B **12**, 863 (1995). 35, 83, 159

[86] W. Sellmeier, *Zur Erklärung der abnormen Farbenfolge im Spectrum einiger Substanzen*, Annalen der Physik und Chemie **219**, 272-282 (1871). 39

[87] M. J. Weber, wmphHandbook of optical materials. CRC Press, (2003). 39

[88] B. A. E. Saleh and M. C. Teich, *Fundamentals of Photonics.* John Wiley & Sons, (2007). 41

[89] J. D. Jackson, *Classical Electrodynamics.* John Wiley & Sons, (1999). 43, 60, 157

[90] R. W. Boyd, *Nonlinear Optics.* Academic Press, (2003). 44

[91] C. R. Gouy, *Sur une propriete nouvelle des ondes lumineuses.* Acad. Sci., Paris, C. R. 110, 1251. (1890). 49

[92] F. Lindner, G.G. Paulus, H.Walther, A. Baltuska, E. Goulielmakis, M. Lezius, and F. Krausz, *Gouy Phase Shift for Few-Cycle Laser Pulses.* Phys. Rev. Lett. **92**, 113001 (2004). 50

[93] B. W. Shore, *The theory of coherent atomic excitation.* (ohn Wiley & Sons, (1990), 53

[94] http://physics.nist.gov/PhysRefData/ASD/lines_form.html 53

[95] E. Constant, D. Garzella, P. Breger, E. Mével, Ch, Dorrer, C. Le Blanc, F. Salin and P. Agostini, *Optimizing High Harmonic Generation in Absorbing Gases: Model and Experiment.* Phys. Rev. Lett. , **82**, 1668-1671 (1999). 55

[96] W. Chan, G. Cooper and C. Brion, *Absolute optical oscillator strengths for the electronic excitation of atoms at high resolution: Experimental methods and measurements for helium.* Phys. Rev. A, **44**, 186 (1991). 55

[97] W. Chan, G. Cooper, X. Guo, G. R. Burton and C. Brion, *Absolute optical oscillator strengths for the electronic excitation of atoms at high resolution. III. The photoabsorption of argon, krypton, and xenon.* Phys. Rev. A, **46**, 149 (1992). 55

[98] B.L. Henke, E.M. Gullikson, and J.C. Davis, *X-ray interactions: photoabsorption, scattering, transmission, and reflection at E=50-30000 eV, Z=1-92.* Atomic Data and Nuclear Data Tables **54**, 181-342 (1993). 55, 56, 63, 94, 113, 124

[99] A. Rundquist, C. G. Durfee III, Z. Chang, C. Herne, S. Backus, M. M. Murnane and H. C. Kapteyn, *Phase-Matched Generation of Coherent Soft X-rays.* Science, **280**, 1412 (1998). 55, 56, 73, 123

[100] P. Balcou, P. Salieres, A. L'Huillier, and M. Lewenstein, *Generalized phase-matching conditions for high harmonics: The role of field-gradient forces.* Phys. Rev. A, **55**, 3204 (1997). 56, 82, 104

[101] M. M. Fejer, G. A. Magel, D. H. Jundt, and R. L. Byer, *Quasi-phase-matched second harmonic generation: tuning and tolerances.* IEEE J. Quantum Electron., **28**, 2631-2654, (1992). 56

[102] G. D. Miller, R. G. Batchko, W. M. Tulloch, D. R. Weise, M. M. Fejer, and R. L. Byer, *42%-efficient single-pass cw second-harmonic generation in periodically poled lithium niobate.* Opt. Lett., **22**, 1834-1836, (1997). 56

[103] S. Zhu, Y. Y. Zhu, and N. B. Ming, *Quasi-Phase-Matched Third-Harmonic Generation in a Quasi-Periodic Optical Superlattice.* Science, **278**, 843-846, (1997). 56

[104] I.P. Christov, H.C. Kapteyn and M.M. Murnane, *Quasi-phase matching of high-harmonics and attosecond pulses in modulated waveguides.* Opt. Exp. **7**, 362-367 (2000). 56, 63

[105] A. Paul, R. A. Bartels, R. Tobey, H. Green, S. Weiman, I. P. Christov, M. M. Murnane, H. C. Kapteyn and S. Backus, *Quasi-phase-matched generation of coherent extreme-ultraviolet light.* Nature **421**, 51-54 (2003). 56

[106] E. A. Gibson, A. Paul, N. Wagner, R. Tobey, D. Gaudiosi, S. Backus, I. P. Christov, A. Aquila, E. M. Gullikson, D. T. Attwood, M. M. Murnane and H. C. Kapteyn, *Coherent Soft X-ray Generation in the Water Window with Quasi-Phase Matching.* Science **302**, 95-98 (2003). 56

[107] P. Antoine, A. LHuillier, M. Lewenstein, P. Salières, and B. Carré, *Theory of high-order harmonic generation by an elliptically polarized laser field.* Phys. Rev. A, **53**, 17251745 (1996). 60

[108] M. Gaarde, P. Antoine, A. LHuillier, K. Schafer, and K. Kulander, *Macroscopic studies of short-pulse high-order harmonic generation using the time-dependent Schrödinger equation.* Phys. Rev. A, **57**, 45534560 (1998). 60, 83, 159

[109] T. Auguste, O. Gobert, and B. Carré, *Numerical study on high-order harmonic generation by a Bessel-Gauss laser beam.* Phys. Rev. A. **78**, 033411 (2008). 60

[110] C.G. Durfee III, A. R. Rundquist, S. Backus, C. Herne, M.M. Murnane and H.C. Kapteyn, *Phase Matching of High-Order Harmonics in Hollow Waveguides.* Phys. Rev. Lett. **83**, 2187-2190 (1999). 63

[111] E.M. Purcell, C.R. Pennypacker, *Scattering and absorption of light by nonspherical dielectric grains.* Astrophys. J. **186**, 705 (1973). 64, 158

[112] M.vA. Yurkin, A. G. Hoekstra, *The discrete dipole approximation: an overview and recent developments.* J. Quant. Spectrosc. Radiat. Transfer **106**, 558 (2007). 64, 158

[113] G. Mie, *Beiträge zur Optik trüber Medien, speziell kolloidaler Metallösungen.* Leipzig, Ann. Phys. **330**,377-445 (1908). 66

[114] J. Zhou, J. Peatross, M. M. Murnane, H. C. Kapteyn, I. P. and Christov, *Enhanced High-Harmonic Generation Using 25 fs Laser Pulses.* Phys. Rev. Lett. **76**, 752-755 (1996). 73

[115] K. J. Schafer, and K. C. Kulander, *High Harmonic Generation from Ultrafast Pump Lasers.* Phys. Rev. Lett. **78**, 638-641 (1997). 73

[116] S. Watanabe, K. Kondo, Y. Nabekawa, A. Sagisaka, and Y. Kobayashi, *Two-Color Phase Control in Tunneling Ionization and Harmonic Generation by a Strong Laser Field and Its Third Harmonic.* Phys. Rev. Lett. **73**, 2692 (1994). 82

[117] I. J. Kim, C. M. Kim, H. T. Kim, G. H. Lee, Y. S. Lee, J. Y. Park, D. J. Cho, and C. H. Nam, *Highly Efficient High-Harmonic Generation in an Orthogonally Polarized Two-Color Laser Field.* Phys. Rev. Lett. **94**, 243901 (2005). 82

[118] T. Siegel, R. Torres, D. J. Hoffmann, L. Brugnera, I. Procino, A. Zaïr, J. G. Underwood, E. Springate, I. C. E. Turcu, L. E. Chipperfield, and J. P. Marangos, *High harmonic emission from a superposition of multiple unrelated frequency fields.* Opt. Exp. **18**, 6853 (2010). 82

[119] M. Kitzler and M. Lezius, *Spatial Control of Recollision Wave Packets with Attosecond Precision.* Phys. Rev. Lett. **95**, 253001 (2005). 82

[120] N. Dudovich, J. Levesque, O. Smirnova, D. Zeidler, D. Comtois, M. Yu. Ivanov, D. M. Villeneuve, and P. B. Corkum, *Attosecond Temporal Gating with Elliptically Polarized Light.* Phys. Rev. Lett. **97**, 253903 (2006). 82

[121] J.A. Pérez-Hernández, D. J. Hoffmann, A. Zaïr, L. E. Chipperfield, L. Plaja, C. Ruiz, J.P. Marangos, and L. Roso, *Extension of the cut-off in high-harmonic generation using two delayed pulses of the same colour.* J. of Phys. B **42**, 134004 (2009). 82

[122] H. Merdji, M. Kovacev, W. Boutu, P. Salières., F. Vernay and B. Carré, *Macroscopic control of high-order harmonics quantum-path components for the generation of attosecond pulses.* Phys. Rev. A, **74** 043804 (2006). 83, 94, 159

[123] J. L. Krause, K. J. Schafer, and K. C. Kulander, *High-order harmonic generation from atoms and ions in the high intensity regime.* Phys. Rev. Lett. **68**, 3535 (1992). 83

[124] A. L'Huillier, M. Lewenstein, P. Salières, Ph. Balcou, M. Yu. Ivanov, J. Larsson and C.-G. Wahlström, *High-order Harmonic-generation cutoff.* Phys. Rev. A **48**, R3433 (1993). 83

[125] F. Schapper, M. Holler, T. Auguste, A. Zaïr, M. Weger, P. Salières, L. Gallmann, and U. Keller, *Spatial fingerprint of quantum path interferences in high order harmonic generation.* Opt. Exp. **18**, 2987-94(2010). 88

[126] C.-G. Wahlström, J. Larsson, A. Persson, T. Starczewski, S. Svanberg, P. Salières, Ph. Balcou and A. L'Huillier, *High-order harmonic generation in rare gases with an intense short-pulse laser.* Phys. Rev. A, **48**, 4709 (1993). 88

[127] J.L. Schwob, A.W. Wouters, S. Suckewer, and M. Finkenthal, *High-resolution duo-multichannel soft x-ray spectrometer for tokamak plasma diagnostics.* Rev. Sci. Instrum. **58**, 1601-1615 (1987). 90

[128] B.J. MacGowan, J.A. Koch, and S. Mrowka, *A simple method for overcoming spatial resolution limitations in soft x-ray spectrograph/detector systems.* Rev. Sci. Instrum. **63**, 5122-5123 (1992). 90

[129] M. B. Gaarde and K. J. Schafer, *Space-Time Considerations in the Phase Locking of High Harmonics.* Phys. Rev. Lett., **89**, 213901 (2002). 94, 127

[130] T. Ruchon, C. P. Hauri, K. Varjú, E. Mansten, M. Swoboda, R. Lopez-Martens and A. LHuillier, *Macroscopic effects in attosecond pulse generation.* New. J. Phys. **10**, 025027, (2008). 94

[131] Y. Mairesse, A. de Bohan, L. J. Frasinski, H. Merdji, L. C. Dinu, P. Monchicourt, P. Breger, M. Kovačev, T. Auguste, B. Carré, H. G. Muller, P. Agostini, and P. Salières, *Optimization of Attosecond Pulse Generation.* Phys. Rev. Lett. **93**, 163901 (2004). 94

[132] Cheng Jin, Anh-Thu Le, Carlos A. Trallero-Herrero, and C. D. Lin, *Generation of isolated attosecond pulses in the far field by spatial filtering with an intense few-cycle mid-infrared laser.* Phys. Rev. A, **84**, 043411 (2011). 94

[133] L.E. Chipperfield, P.L. Knight, J. W. G. Tisch and J. P. Marangos, *Tracking individual electron trajectories in a high harmonic spectrum.* Opt. Comm. **264**, 494501 (2006). 104

[134] S. Kazamias, F. Weihe, D. Douillet, C. Valentin, T. Planchon, S. Sebban, G. Grillon, F. Augé, D. Hulin and Ph. Balcou, *High order harmonic generation optimization with an apertured laser beam.* Eur. Phys. J. D **21**, 353-359 (2002). 106, 111, 160

[135] A. Dubrouil, Y. Mairesse, B. Fabre, D. Descamps, S. Petit, E. Mevel and E. Constant, *Controlling high harmonics generation by spatial shaping of high energy femtosecond beam.* Opt. Lett. **36**, 2486-4288 (2011). 106

[136] N.A. Papadogiannis, C. Kalpouzos, E. Goulielmakis, G. Nersisyan, D. Charalambidis, F. Augé, F. Weihe and Ph. Balcou, *Kilohertz extreme-ultraviolet light source based on femtosecond high-order harmonic generation from noble gases.* Appl. Phys. B, **73**, 687-692 (2001). 113

[137] D.S. Steingrube, T. Vockerodt, E. Schulz, U. Morgner and M. Kovačev, *Phase-matching of high-order harmonics in a semi-infinite gas cell.* Phys. Rev. A, **80**, 043819 (2009). 115, 118

[138] M. Kretschmar, C. Hernández-García, D. S. Steingrube, L. Plaja, U. Morgner and M. Kovačev, *Spatial contributions of electron trajectories to high-order harmonic radiation originating from a semi-infinite gas cell. Submitted to* Phys. Rev. A (2012). 117, 118

[139] G. Andriukaitis, T. Balčiunas, S. Ališauskas, A. Pugzlys, A. Baltuška, T. Popmintchev, M.-C. Chen, M. M. Murnane and H. C. Kapteyn, *90 GW peak power few-cycle mid-infrared pulses from an optical parametric amplifier.* Opt. Lett. **36**, 2755 (2011). 121, 123, 144, 162

[140] M. T. Asaki, C.-P. Huang, D. Garvey, J. Zhou, H. C. Kapteyn, and M. M. Murnane, *Generation of 11 femtosecond pulses from a modelocked Ti:sapphire laser.* Opt. Lett. **18,** 977 (1993). 122

[141] A. Baltuška, Th. Udem, M. Uiberacker, M. Hentschel, E. Goulielmakis, Ch. Gohle, R. Holzwarth, V. S. Yakovlev, A. Scrinzi, T. W. Hänsch, and F. Krausz, *Attosecond control of electronic processes by intense light fields.* Nature **421,** 611 (2003). 122

[142] J. Itatani, J. Levesque, D. Zeidler, Hiromichi Niikura, H. Pépin, J. C. Kieffer, P. B. Corkum, and D. M. Villeneuve, *Tomographic imaging of molecular orbitals.* Nature **432,** 867 (2004). 122

[143] S. Baker, J. S. Robinson, C. A. Haworth, H. Teng, R. A. Smith, C. C. Chirila, M. Lein, J. W. G. Tisch and J. P. Marangos, *Probing Proton Dynamics in Molecules on an Attosecond Time Scale.* Science **312,** 424 (2006). 122

[144] E. Gagnon, P. Ranitovic, X.-M. Tong, C. L. Cocke, M. M. Murnane, H. C. Kapteyn, A. S. Sandhu, *Soft X-ray Driven Femtosecond Molecular Dynamics.* Science **317**, 1374 (2007). 122

[145] N. L. Wagner, A. Wüest, I. P. Christov, T. Popmintchev, X. Zhou, M. M. Murnane, and H. C. Kapteyn, *Monitoring molecular dynamics using coherent electrons from high harmonic generation.* Proc. Natl Acad. Sci. USA **103**, 13279 (2006). 122

[146] W. Li, X. Zhou, R. Lock, S. Patchkovskii, A. Stolow, H. C. Kapteyn and M. M. Murnane, *Time-Resolved Dynamics in N_2O_4 Probed Using High Harmonic Generation.* Science **322**, 1207 (2008). 122

[147] R. M. Lock, S. Ramakrishna, X. Zhou, H. C. Kapteyn, M. M. Murnan1, and T. Seideman, *Extracting Continuum Electron Dynamics from High Harmonic Emission from Molecules.* Phys. Rev. Lett. **108**, 133901 (2012). 122

[148] J. Seres, P. Wobrauschek, C. Streli, V. S. Yakovlev, E. Seres, F. Krausz, and C. Spielmann, *Generation of coherent keV x-rays with intense femtosecond laser pulses.* New J. Phys, **8**, 251-251 (2006). 122, 123, 124

[149] E. J. Takahashi, T. Kanai, K. L. Ishikawa, Y. Nabekawa, and K. Midorikawa, *Coherent Water Window X Ray by Phase-Matched High-Order Harmonic Generation in Neutral Media.* Phys. Rev. Lett. **101**, 253901 (2008). 124, 162

[150] T. Popmintchev, M.-C. Chen, O. Cohen, M. E. Grisham, J. J. Rocca, M. M. Murnane, and H. C. Kapteyn, *Extended phase matching of high harmonics driven by mid-infrared light.* Opt. Lett. **33**, 2128 (2008). 124

[151] S. Gordienko, A. Pukhov, O. Shorokhov and T. Baeva, *Relativistic Doppler Effect: Universal Spectra and Zeptosecond Pulses.* Phys. Rev. Lett. **93**, 115002 (2004). 125

[152] L. Plaja, L. Roso, K. Rzazewski and M. Lewenstein, *Generation of attosecond pulse trains during the reflection of a very intense laser on a solid surface.* J. Opt. Soc. Am. B **7**, 1904 (1998). 125

[153] B. Dromey, M. Zepf, A. Gopal, K. Lancaster, M. S. Wei, K. Krushelnick, M. Tatarakis, N. Vakakis, S. Moustazis, R. Kodama, M. Tampo, C. Stoeckl, R. Clarke, H. Habara, D. Neely, S. Karsch and P. Norreys, *High harmonic generation in the relativistic limit.* Nature Phys. **2**, 457 (2006). 125

[154] Y. Mairesse, A. de Bohan, L. J. Frasinski, H. Merdji, L. C. Dinu, P. Monchicourt, P. Breger, M. Kovačev,1 R. Taïeb, B. Carré, H. G. Muller, P. Agostini and P. Salières, *Attosecond Synchronization of High-Harmonic Soft X-rays.* Science **302**, 1540 (2003). 127

[155] R. López-Martens, K. Varjú, P. Johnsson, J. Mauritsson, Y. Mairesse, P. Salières, M. B. Gaarde, K. J. Schafer, A. Persson, S. Svanberg, C.-G. Wahlström, and A. LHuillier, *Amplitude and Phase Control of Attosecond Light Pulses.* Phys. Rev. Lett. **94**, 033001(2005). 127

[156] D. D. Hickstein, P. Ranitovic, S. Witte, X.-M. Tong, Y. Huismans, P. Arpin, X. Zhou, K. E. Keister, C. W. Hogle, B. Zhang, C. Ding, P. Johnsson, N. Toshima, M. J. J. Vrakking, M. M. Murnane and H. C. Kapteyn *Direct Visualization of Laser-Driven Electron Multiple Scattering and Tunneling Distance in Strong-Field Ionization.* Phys. Rev. Lett. **109**, 073004 (2012). 130, 163

[157] M. D. Seaberg, D. E. Adams, E. L. Townsend, D. A. Raymondson, W. F. Schlotter, Y. Liu, C. S. Menoni, L. Rong, C.-C. Chen, J. Miao, H. C. Kapteyn, and M. M. Murnane, *Ultrahigh 22 nm resolution coherent diffractive imaging using a desktop 13 nm high harmonic source.* Opt. Exp. **19**, 22470-22479 (2011). 145

[158] C. G. Schroer, P. Boye, J. M. Feldkamp, J. Patommel, A. Schropp, A. Schwab, S. Stephan, M. Burghammer, S. Schöder, and C. Riekel, *Coherent X-Ray Diffraction Imaging with Nanofocused Illumination.* Phys. Rev. Lett. **101**, 090801 (2008). 145

[159] I. Thomann, A. Bahabad, R. Trebino, M. M. Murnane and H. C. Kapteyn, *Characterizing isolated attosecond pulses from a hollow-core waveguide using multi-cycle driving pulses.* Opt. Exp. **17**, 4611 (2009). 147